

# Exploring The Relation Between Galaxy Evolution and Galaxy Interaction

David Patrick O’Ryan



Physics

Department of Physics

Lancaster University

July 10, 2024

A thesis submitted to Lancaster University for the degree of  
Doctor of Philosophy in the Faculty of Science and Technology

*Supervised by Dr Brooke Simmons*

# Abstract

Hierarchical models and observations show that galaxy interaction and merging is of paramount importance to galaxy assembly and evolution. However, the relationship between these physical processes and the characteristics of the galaxies involved is unclear. In this thesis, we make direct constraints between the physical processes occurring in galaxy interaction - increased star formation, nuclear activity, and morphological disturbance - and the underlying parameters of galaxies - their interaction stage, stellar masses, kinematics, and orientation parameters.

To constrain these relations, we require large samples of interacting galaxies which are representative of the full underlying parameter space. A clear signature of interaction or merger activity is through the morphological distortion of a galactic system. We search for such signatures through the entire *Hubble Space Telescope* science archive with a Bayesian convolutional neural network. In total, we classify 92 million sources into interacting and non-interacting galaxies. We find 21,926 disturbed and interacting galaxy systems; the largest interacting galaxy sample morphologically classified to date.

We use this new sample to explore the relationship between the dynamical timescale of interaction and galactic parameters. We match our new sample with the Cosmic Evolutionary Survey and find ancillary data for a volume limited sample of 3,378 interacting galaxies. We break this sample into four distinct stages aimed at capturing different parts of the dynamical timescale of interaction. We find evolution in the star formation rate with stage which cumulates in the complete disappearance of the red sequence at the merging stage. We find that

the fraction of galaxies with an active galactic nuclei is constant with interaction stage, except at the point of coalescence where we find it increases from a measured value of  $0.059 \pm 0.003$  to an enhanced value of  $0.071 \pm 0.005$ . By investigating the relationship between these fundamental processes and stage, we show that there is a direct relation between the interaction stage and the physical processes we observe. However, we require methods to more precisely probe the dynamical timescale of an interaction to make further constraints.

Thus, we introduce a new algorithm which will be capable of exploring this relationship. We utilise a three-body numerical simulation with an Markov-Chain Monte Carlo (MCMC) algorithm to directly map the parameter space to tidal features. We constrain the underlying parameters of a sample of 51 synthetic images representing different observed interacting systems. We are able to recover the true parameters within a confidence interval of 86.4%. We apply this methodology to a subset of observational data, and explore the algorithm's potential as well as its limitations.

The results of this thesis demonstrates the complex nature of the relationship between galaxy evolution and interaction, with larger samples and catalogues needed to constrain it. With the use of ESA Datalabs, building such samples is not just limited to interacting galaxies. It will allow the largest general galaxy morphology catalogues to date to be created. This, therefore, requires ever larger catalogues of ancillary data or the development of methods to efficiently create it. The introduction of a new algorithm to further investigate the relationship of interaction and its underlying parameters provides us a unique way to link interaction and evolution. The limitations of this algorithm are primarily due to the computational expense such a MCMC approach costs. We explore how this method can be developed, from bypassing the computational expense entirely with simulation based inference to new methods of optimisation with graphical processing units.

This thesis is dedicated to those who took the time to listen to a wee  
boy talk about the stars.

## Acknowledgements

For as long as I can remember I have aspired to be an astrophysicist. While I have never lost that passion for astronomy, it would not remain so resolute without the support of those around me. I offer my sincere gratitude and thanks to:

My supervisor Brooke Simmons. Your guidance, enthusiasm and support over these many years have made this work possible. I left every single meeting inspired and encouraged, ready to work harder than before.

My examiners John Stott and Stephen Serjeant. Your comments on this work greatly improved its quality.

My many collaborators: Bruno Merin, Chris Lintott, Mike Walmsley, Becky Smethurst, Tobias Geron, Sandor Kruk, Kameswara Mantha, Karen Masters, and the whole Galaxy Zoo team who were all incredibly supportive, insightful and inspiring throughout my PhD.

The academics in the observational astrophysics department: Julie Wardlow, Isobel Hook, Mathew Smith, Young-Lo Kim and Sam Oates. Your help and guidance, especially in the final months of my PhD, was essential to my success.

The ESA trainee cohort of 2022. When my love for astronomy was wavering and commitment to this path in doubt you showed me a wonderful, inquisitive and welcoming environment that brought my passion back.

The team at 1715Labs. Working with you was a brilliant experience, and gave me a taste of life in industry.

Those in the PhD office, who made it such a welcoming place. To Jamie Dumayne, Brenda Zambrano and Izzy Garland for many nights of drinks, movies, dinners and laughter. To Heather Wade and Tom Cornish for introducing me to Lancaster. To Rahul Rana, Pascale Desmet, Jon Carrick, Nick Amos, Harry Stevenson and Andrew Milligan for excellent scientific discussion, advice and summer BBQs.

My house mates: Amy Hewitt, Matthew Thorne, Nikita Mehta and Zach Mason. I hope that we will meet again. Until then, I wish you all the success in the world.

To my parents. You fanned those initial flames that gave me a passion for astronomy that has never left me. Your support then, and now, drives me forward.

My brother and sister, Michael and Ruth. Thank you for putting up with me all these years.

To Calum Cooper and Ronan Duff, who have supported me completely since the day we met. Although my path led me to leave you in Glasgow, you remain my closest friends.

To the University of Glasgow, where I aspired to learn throughout my childhood. Being taught there gave me the tools to complete and, hopefully, excel at my PhD.

This research was funded by the Science and Technology Facilities Council of the UK.

Finally, to Abby. Know your unwavering support made all of this possible. Your selflessness has left an impact on me that will persist for the rest of my life.

## **Declaration**

This thesis is my own work and no portion of the work referred to in this thesis has been submitted in support of an application for another degree or qualification at this or any other institute of learning.

The research presented in Chapter 2 has been published in the relevant scientific journals in paper format and can be found as O’Ryan et al. (2023, ApJ, 948, 1). The contents of Chapter 3 and 4 have been written in the style of journal papers as they will be submitted for publication in due course.

---

*The grand and bold thing is what we [ought] to do.*

- Rich Kron

\*

*I shall be telling this with a sigh  
Somewhere ages and ages hence:  
Two roads diverged in a wood, and I—  
I took the one less traveled by,  
And that has made all the difference.*

- Robert Frost,  
The Road Not Taken

\*

*To an old wine or a new idea, he cannot say no.*

- Berthold Brecht,  
The Life of Galileo



# Contents

<b>List of Figures</b>	<b>x</b>
<b>1 Introduction</b>	<b>1</b>
1.1 What is a Galaxy? . . . . .	2
1.2 Galaxy Assembly Across Cosmological Time . . . . .	4
1.3 Galaxy Morphology & Galactic Properties . . . . .	7
1.4 Categorisation of Mergers . . . . .	13
1.5 Effects of Galaxy Interaction . . . . .	15
1.5.1 Morphological Distortion: Tidal Features . . . . .	16
1.5.2 Star Formation Enhancement . . . . .	19
1.5.3 Ignition of Active Galactic Nuclei . . . . .	20
1.5.4 Quenching of Galactic Systems . . . . .	21
1.6 Identifying Interacting and Merging Galaxies . . . . .	22
1.7 Cosmological Effects . . . . .	26
1.8 This Thesis . . . . .	27
<b>2 Creating a Large Sample of Interacting Galaxies</b>	<b>29</b>
2.1 Introduction . . . . .	29
2.2 Data . . . . .	32
2.2.1 The <i>Hubble</i> Archives & ESA Datalabs . . . . .	32
2.2.2 The Shapely Python Package . . . . .	34
2.3 Utilising a Convolutional Neural Network . . . . .	34
2.3.1 Zoobot . . . . .	35
2.3.2 Transfer Learning . . . . .	36

---

2.4	Creating the Training Set . . . . .	37
2.4.1	Interacting Galaxies and Galaxy Zoo . . . . .	38
2.4.2	One Active Learning Cycle . . . . .	42
2.5	Diagnostics . . . . .	43
2.5.1	Model Performance . . . . .	43
2.5.2	Duplication Removal . . . . .	49
2.5.3	Bad Predictions & Removal . . . . .	50
2.6	Results & Discussion . . . . .	55
2.6.1	An Interacting Galaxy Catalogue . . . . .	55
2.6.2	The Gems . . . . .	57
2.6.3	Source Redshifts and Photometry . . . . .	60
2.7	Conclusion . . . . .	67
<b>3</b>	<b>Timescales for the Effects of Interactions on Galaxy Properties and SMBH Growth</b>	<b>70</b>
3.1	Introduction . . . . .	70
3.2	Data: Catalogue Matching & Secondary Identification . . . . .	72
3.2.1	The COSMOS2020 Catalogue . . . . .	72
3.2.2	Secondary Identification . . . . .	75
3.2.3	Finding Additional Systems . . . . .	78
3.2.4	Creating the Volume Limited Sample . . . . .	80
3.3	Method: Environment, AGN and Interaction Stage . . . . .	82
3.3.1	Classifying Stage of Interaction . . . . .	82
3.3.2	Matching to Environment Catalogue . . . . .	89
3.3.3	Classifying AGN . . . . .	91
3.3.4	Summary of Selection Process and Source Counts . . . . .	92
3.3.5	Visual Classification: Sources of Contamination . . . . .	93
3.3.6	Aside: Mass Ratios in Sample . . . . .	103
3.4	Star Formation and AGN Evolution with Interaction Stage . . . . .	103
3.4.1	Controlling for Interaction Stage . . . . .	103
3.4.2	Projected Separation and Star Formation Enhancement . . . . .	114
3.5	Nuclear Activity with Interaction Stage . . . . .	117
3.6	Discussion . . . . .	123

---

3.6.1	Interaction Stage and Projected Separation . . . . .	123
3.6.2	Interaction Stage and AGN . . . . .	125
3.7	Conclusions . . . . .	127
<b>4</b>	<b>An Infrastructure to Constrain Underlying Interacting Galaxy</b>	
	<b>Parameters</b>	<b>130</b>
4.1	Introduction . . . . .	130
4.2	Data . . . . .	132
4.2.1	Sample of Major Interacting Galaxies . . . . .	132
4.2.2	Observation Preparation . . . . .	133
4.3	Simulating Galaxy Interaction . . . . .	135
4.3.1	APySPAM . . . . .	135
4.3.1.1	Restricted Three-Body Simulation . . . . .	135
4.3.1.2	Stellar Population Evolution . . . . .	137
4.3.1.3	Extending Flux Distribution . . . . .	141
4.3.1.4	Impact on Computation Time . . . . .	142
4.3.2	Creating Test Images . . . . .	144
4.4	Constraining Interaction . . . . .	144
4.4.1	The Parameter Space of Interaction . . . . .	147
4.4.2	Defining the Likelihood Function . . . . .	148
4.4.2.1	MCMC & Bayes Theorem . . . . .	148
4.4.2.2	Simplifying the Prior . . . . .	150
4.4.2.3	Simplifying the Likelihood Function . . . . .	151
4.5	Results & Discussion . . . . .	152
4.5.1	Testing on a Synthetic Image . . . . .	153
4.5.2	Diagnostics of Pipeline . . . . .	161
4.5.3	Inputting 3D Information . . . . .	164
4.5.4	Running on Full Idealised Sample . . . . .	166
4.5.5	Applying to Observations . . . . .	173
4.5.6	Limitations . . . . .	178
4.5.6.1	Resolution & Depth Effects . . . . .	178
4.5.6.2	Computational Expense . . . . .	180
4.6	Conclusions & Future Work . . . . .	181

---

<b>5</b>	<b>Summary and Future Work</b>	<b>184</b>
5.1	Summary . . . . .	184
5.2	Future Work . . . . .	186
5.2.1	Catalogues of Galaxy Morphology with Ancillary Data . .	186
5.2.2	Constraining Interacting Galaxy Parameters . . . . .	188
	<b>Appendix A Model Diagnostics &amp; Further Identified Objects</b>	<b>190</b>
A.1	Further Model Diagnostics . . . . .	190
A.2	Examples of Sources with 3-Band Information . . . . .	191
A.3	Unknown Objects . . . . .	191
A.4	Acknowledging PIs . . . . .	196
	<b>References</b>	<b>197</b>

# List of Figures

1.1	The declining merger rates from $z = 3$ to $z = 0$ . . . . .	6
1.2	The Hubble tuning fork. . . . .	8
1.3	The distribution of galaxies in colour-colour space showing two distinct populations in a clear bi-modal structure. . . . .	11
1.4	Examples of a major, a minor and a micro interaction. . . . .	15
1.5	Examples of a collisional ring galaxy and a system containing shells. . . . .	18
2.1	Example images of the labelled interacting galaxy systems used to train <b>Zoobot</b> . . . . .	40
2.2	Example images of the labelled non-interacting galaxy systems used to train <b>Zoobot</b> . . . . .	41
2.3	The distribution of prediction scores given to our validation set of 3,270 labelled sources set aside by <b>Zoobot</b> in training. . . . .	44
2.4	A measure of accuracy and purity against prediction score. . . . .	45
2.5	Confusion matrices of four different cutoffs of prediction score defining a binary classification of interacting galaxy or not. . . . .	47
2.6	Flow diagram of our contamination and duplication removal process. . . . .	48
2.7	The representation distribution of 54,757 candidate interacting galaxies. . . . .	52
2.8	Scatter plot showing the precise distribution of each representation of sources in the remaining 54,757 sources. . . . .	53
2.9	An example of 50 of the final interacting systems found with <b>Zoobot</b> . . . . .	56
2.10	Sky Distribution of our catalogue, with marked positions of well known deep surveys conducted by <i>HST</i> . . . . .	59

2.11	The redshift distribution of a subsample of our catalogue. . . . .	63
2.12	The distribution of redshift with magnitude for all sources with available data. . . . .	64
2.13	The colour-magnitude distribution of sources with a redshift measurement associated. . . . .	66
3.1	Comparison of the measures of stellar mass and SFR using either LePhare or EAzy photometric codes to calculate them. . . . .	74
3.2	An example of each visual classification made on the cross matched sample. . . . .	76
3.3	Where a secondary could be identified at different stages in the interaction. . . . .	77
3.4	The mass distribution of the paired interacting galaxy sample and the control sample. . . . .	79
3.5	Redshift vs Mass distribution for each stage of interaction we have defined. . . . .	81
3.6	Examples of the four stages we split our interacting galaxy sample into. . . . .	84
3.7	The progression through an interaction using our stage definitions. . . . .	87
3.8	The projected separations of the confirmed galaxy pairs in our sample. . . . .	88
3.9	The measured distribution of projected separation with redshift. . . . .	90
3.10	The scatter in photometric redshifts of our paired sample. . . . .	94
3.11	The change in found interaction type across our redshift distribution. . . . .	97
3.12	The density about each of our sources matched with the Darvish et al. (2017) catalogue. . . . .	100
3.13	The fraction of galaxies in each stage in different environments. . . . .	101
3.14	The distribution of environment classifications through our sample. . . . .	102
3.15	The distribution of mass ratios in our paired sample and across each stage of interaction. . . . .	104
3.16	The LePhare stellar mass against the EAzy SFR across the different stages of the interaction. . . . .	106
3.17	The stellar mass distribution across the four stages. . . . .	108

3.18 SFR distribution weighted by mass across each stage. . . . .	109
3.19 Stellar mass against the ratio of measured SFR to the expected SFR if the galaxy was on the SFMS. . . . .	112
3.20 The change in fraction of different galaxy classifications from the fraction of SFR to the expected SFR on the SFMS. . . . .	113
3.21 The projected separation against the SFE in average star formation at different bins of projected separation. . . . .	116
3.22 The distribution of AGN through stage with SFR and stellar mass.	119
3.23 The change in AGN fraction with stage. . . . .	120
3.24 The distribution of both AGN and SFGs which have been matched our confirmed galaxy pairs. . . . .	122
4.1 Our mock observations of each interacting system. . . . .	146
4.2 The example system used to test our MCMC: the Arp 240 inter- acting system. . . . .	154
4.3 Corner plot showing the constraints made on all thirteen parame- ters we are exploring. . . . .	155
4.4 Same as Figure 4.3, but reduced to only corresponding parameters.	156
4.5 Simulations from the areas of parameter space that lay within the 11.8% CI of our constraints. . . . .	160
4.6 Steps taken by each walker in our MCMC chain to constrain the Arp 240 best fit simulation. . . . .	163
4.7 The reduced corner plot of the synthetic Arp 240 system with a velocity map also used for constrained. . . . .	165
4.8 Second example of our best fits from our methodology is represen- tative of the simulated image of Arp 172, a stage 3 system. . . . .	167
4.9 Third example of our best fits from our methodology is represen- tative of the simulated image of Arp 290, a stage 2 system. . . . .	167
4.10 First example of our worst fits. . . . .	168
4.11 Second example of our worst fits. . . . .	168
4.12 Third example of our worst fits. . . . .	169

4.13	The distribution of parameter values used to create our synthetic interaction images and the best-fit values we recover from our algorithm. . . . .	170
4.14	Reduced corner plot of the constraints made on the observational image of Arp 240. . . . .	175
4.15	Reduced corner plot of the constraints made on the observational image of Arp 172. . . . .	176
4.16	Reduced corner plot of the constraints made on the observational image of Arp 256. . . . .	176
4.17	Reduced corner plot of the constraints made on the observational image of Arp 290. . . . .	177
4.18	Reduced corner plot of the constraints made on the observational image of the Heart system. . . . .	177
A.1	The Receiver-Operator and Precision-Recall Curve for the Zoobot model that was used to explore the Hubble archives. . . . .	192
A.2	The F1 score found during the diagnostics of the model used in this work. The F1 score is a measure combing the measure of accuracy and purity into one metric. . . . .	193
A.3	Example of six interacting systems in the catalogue with full 3-band imagery. . . . .	194
A.4	The six unknown systems found in this work. . . . .	195



# Relevant First Author Publications

## Chapter 2

- Harnessing the Hubble Space Telescope Archives: Creating a Catalog of 21,926 Interacting Galaxy, O’Ryan et al., ApJ, 2023, 968, 40

## Relevant Co-Author Publications

- Galaxy Zoo DESI: Large-Scale Bars as a Secular Mechanism for Triggering AGN, I. Garland et al., submitted (O’Ryan: 12<sup>th</sup> of 15 authors)
- Galaxy Zoo DESI: Detailed Morphology Classifications for 8.7M Galaxies in the Legacy Imaging Surveys, M. Walmsley et al. (O’Ryan: 12<sup>th</sup> of 16 authors), MNRAS, 2023, 526, 3
- Zoobot: Adaptable Deep Learning Models for Galaxy Morphology, M. Walmsley et al. (O’Ryan: 13<sup>th</sup> of 17 authors), JOSS, 2023, 5312, 85
- The most luminous, merger-free AGNs show only marginal correlation with bar presence, I. Garland et al. (O’Ryan: 14<sup>th</sup> of 17 authors), MNRAS, 2023, 522, 1
- Galaxy and Mass Assembly: Galaxy Morphology in the Green Valley, Prominent Rings and Looser Spiral Arms, D. Smith et al. (O’Ryan: 17<sup>th</sup> of 18 authors), MNRAS, 2022, 517, 3
- Preparing for low surface brightness science with the Vera C. Rubin Observatory: Characterization of tidal features from mock images, G. Martin et al. (O’Ryan: 20<sup>th</sup> of 52 authors), MNRAS, 2022, 513, 1
- Gems of the Galaxy Zoos-A Wide-ranging Hubble Space Telescope Gap-filler Program, W. Keel et al. (O’Ryan: 16<sup>th</sup> of 16 authors), AJ, 2022, 163, 4

- Quantifying the Poor Purity and Completeness of Morphological Samples Selected by Galaxy Colour, R. J. Smethurst et al. (O’Ryan: 9<sup>th</sup> of 10 authors), MNRAS, 2022, 510, 3
- Origin of the Local Group Satellite Planes, I, Banik, D., O’Ryan & H. Zhao, MNRAS, 2018, 466, 4

# Chapter 1

## Introduction

In the context of the large scale structure of the Universe, galaxies represent a fundamental building block of matter. Their evolution through cosmic time leads to the local Universe as we see it today (Springel et al., 2005). A key part of its evolution is that of mutual interactions between galaxies. Our best cosmological model,  $\Lambda$ -Cold Dark Matter, dictates that galaxies assembled hierarchically (White & Rees, 1978; White & Frenk, 1991). Therefore, we must understand the effects of mutual interaction to not just understand galaxy evolution but to better understand our theories of cosmology.

We have come to understand that interaction has multiple impacts on the evolution of galaxies. The first, and most obvious, effect is that it leads to the distortion of the galaxies involved and the formation of distinct tidal features. Early numerical simulations had excellent success recreating, and thus proving, these distortions to the galaxies were from tidal interactions between galaxies (Toomre & Toomre, 1972). Thus, tidal features became the primary method by which to identify interacting galaxies. However, it was found that datasets identified in this way contained high levels of contamination. Often, pairs of systems which appeared interacting or distorted were found to be at very different redshifts; their peculiar morphologies caused by other processes. These were close pairs by projection rather than physically close together in space (e.g Ackermann et al., 2018; Blumenthal et al., 2020; Pearson et al., 2022). A paramount

requirement for the identification of interacting pairs became redshift information, to ascertain their 3D distances from each other. However, spectroscopic information is not available across many of the millions of close pairs to classify.

From the systems we have reliably identified, we have found mutual interaction has further effects on galaxies than morphological disturbance. It has been found that interaction also causes an increase in the measured star formation (Bushouse, 1987; Mihos et al., 1992), higher fractions of active galactic nuclei (Ellison et al., 2008; Satyapal et al., 2014) and evidence for quenching of the systems involved (Schweizer & Seitzer, 1992; Gabor et al., 2010). This is particularly true of interactions between gas-rich galaxies where the fuel for star formation is readily available and quickly used. Rejuvenation of galaxies can also occur due interactions between gas-rich and gas-poor systems (Schweizer & Seitzer, 1992; Hopkins et al., 2009).

The scale, change and impact of these effects is dependent on a host of underlying parameters of the galaxies involved. These include the galactic masses, the orientation of the galaxies and velocity of the encounter. This link between these parameters and the characteristics of the final system have been poorly explored. In this work, we create a large sample of interacting galaxies using a new machine learning algorithm - *Zoobot* - and use it to investigate this relationship. We then describe a new software to extract their underlying parameters for further study. For now, however, it would be prudent to begin this discussion by exploring the definition of a galaxy, and outline the major work already conducted into linking galaxy interaction to its underlying parameters and, furthermore, with galaxy evolution.

## 1.1 What is a Galaxy?

For the purposes of this work, a galaxy will be the smallest unit of mass we will consider. A galaxy is a gravitationally bound system of gas, dust, stars and dark matter. The orbits and kinematics of each of these components leads us to different classifications of galaxies. At the galactic centre, there is often a supermassive blackhole (SMBH). While almost all examples of galaxies have a

SMBH at their centre, there are some examples where it is speculated they do not (Gebhardt et al., 2001). If the stars, gas and dust orbiting the galactic centre of mass have been unperturbed for a long period of time they flatten into a disk. The disk is split into a thick and thin component. Their general sizes are dictated by the history of the galaxy, and whether they have interacted or merged with many other galaxies in their history. Such harassment by other galaxies leads to heating of this disk. This heating takes the form of increased peculiar motion in the stellar orbits. This heating contributes not only to the thick disk, but can also lead to the growth of a bulge component in the galaxy (Hopkins et al., 2010; Bell et al., 2017). The bulge can be grown by other, secular, processes but we will focus on interaction and merging.

The bulge component is composed of stars whose orbit has been heated by changes in the gravitational potential due to galaxy interaction and harassment. This leads to new orbits that form a spherical bulge component around the galactic centre. This leads the galaxy to have a bulge and disk component, with the bulge composed of a spherical component of stars while the disk is formed of stars and gas continuing in unperturbed orbits. This is the simple view of a classic disk galaxy. Many disk galaxies do not show bulges at all, or show a pseudobulge (Gadotti & Kauffmann, 2009). This remains, at least partially, dependent on the merger history of the galaxy. If a galactic interaction leads to a strong enough merger the entire galactic disk is heated and can be destroyed. This leads to a completely spheroidal galaxy called an elliptical galaxy (Toomre, 1977; De Lucia et al., 2006). Between these two galaxy types - disk and elliptical - lie lenticular galaxies. These are systems that have used most of their gas across their disk and are beginning to exhibit the same features as elliptical galaxies. Whether this is due to mergers (Christlein & Zabludoff, 2004; Burstein et al., 2005) or via environmental and secular effects (Mathieu et al., 2002; Rizzo et al., 2018) remains debated. What this demonstrates, however, is the stellar dynamics of galaxies is complex and determined according to the assembly history of each.

The stars, gas and dust are embedded in a much larger, spherical halo. This galactic halo has two different matter components: baryonic and non-baryonic. The baryonic component is formed of very diffuse, ancient stars that form the stellar halo, stellar streams or globular clusters which orbit around the galaxy.

The non-baryonic component is formed of dark matter. What dark matter is precisely is still debated, but this spherical dark matter halo extends out to many times the luminous matter of the galaxy. In general, all examples of galaxies are embedded in a dark matter halo (although there are some debated exceptions as described in van Dokkum et al., 2018). This dark matter halo has also been imperative to our understanding of how galaxies form, evolve and interact.

For much of the history of extragalactic astrophysics, the idea that galaxies could interact and merge was thought to be very improbable except in dense clusters. The small radii (and, therefore, cross section) of the luminous matter in galaxies led astronomers to believe that the probability of an interaction was close to 0 and that galaxies were island universes (Kant, 1755; Curtis, 1917). However, with the development of the idea of the dark matter halo, it was realised that the probability of galactic systems interacting in the field was reasonable. Over time the idea that galaxy interaction and merging would have a significant impact on galaxy evolution was developed. Today, merger rates through cosmic time is a well studied concept and test of our cosmological models.

## 1.2 Galaxy Assembly Across Cosmological Time

Galaxies throughout cosmic history have been assembling and accreting matter. Studies at high redshifts reveal that galaxy structure is significantly different compared to the local volume. Initially, galaxies were very small systems that formed from gravitational instability throughout the early cosmos (Lacey & Cole, 1993). These instabilities were generated by the physical processes of the very early Universe brought about by its small scale. From these initial density perturbations arose small systems which accreted from the surrounding gas. These galaxies had peculiar morphologies (Elmegreen & Elmegreen, 2005) with disk galaxies beginning to dominate at  $z \approx 3 - 6$  (Ferreira et al., 2022). These early systems formed stars at a much higher rate than the present day. While these systems were accreting much of their matter to gain mass, the Universe was expanding. At this time the rate of galaxies interacting and merging was also greater than today (Hopkins et al., 2010; Lotz et al., 2011), reaching as high as 50% at  $z \approx 6$

(Conselice & Arnold, 2009; Bluck et al., 2009). This provided a peak in the cosmic star formation history through  $1 < z < 3$  where approximately half of all stellar mass was formed (Bundy et al., 2005).

However, it is not clear that the only driver of this higher star formation rate in the early universe was mergers. More recent works have shown that secular processes may have also played a significant role. It has been noted that the fraction of clumpy galaxies was significantly higher at these times (Swinbank et al., 2012; Cheng et al., 2020; Vayner et al., 2023). Clumps within galaxies are large, star forming regions which form due to violent disk instabilities. The size, and longevity of the clumpy region is found to correlate closely to the gas fraction of the galaxy it is in (Fensch & Bournaud, 2021). This points to disc galaxies in the early Universe containing much higher gas fractions (Tacconi et al., 2010; Scoville et al., 2023) than their local counterparts. Therefore, not only was the merger fraction higher at earlier epochs, but the internal properties of galaxies differed and were much more extreme.

However, as stated, the merger rate was also changing throughout this epoch of the Universe. Figure 1.1 shows the changing merger rate through cosmic time. As shown, the merger rate has been decreasing with redshift, while the internal environment of galaxies has become less extreme, which has had profound effects on both the star formation density of the Universe and the morphology of those galaxies within it. From  $z = 1$ , the once massive galaxies with rapid star formation have transformed into bulge-dominated galaxies (Brown et al., 2007). At lower redshifts we find that the majority of the stellar mass is contained within bulge dominated systems. These galaxies are dominated by old stellar components and have little ongoing star formation (Hogg et al., 2002; Bell et al., 2004).

This gives us an avenue by which to link observed galaxy morphologies to their merger histories. We split them into two distinct populations. One is of galaxies with an intense merger history, leading to the complete destruction of their disks and their domination by older stellar populations. The other is of those with a relatively non-violent merger history. These non-destructive interactions and mergers served to feed the gas within the galactic disks and increase their mass, while maintaining their star formation rates. These systems are dominated by

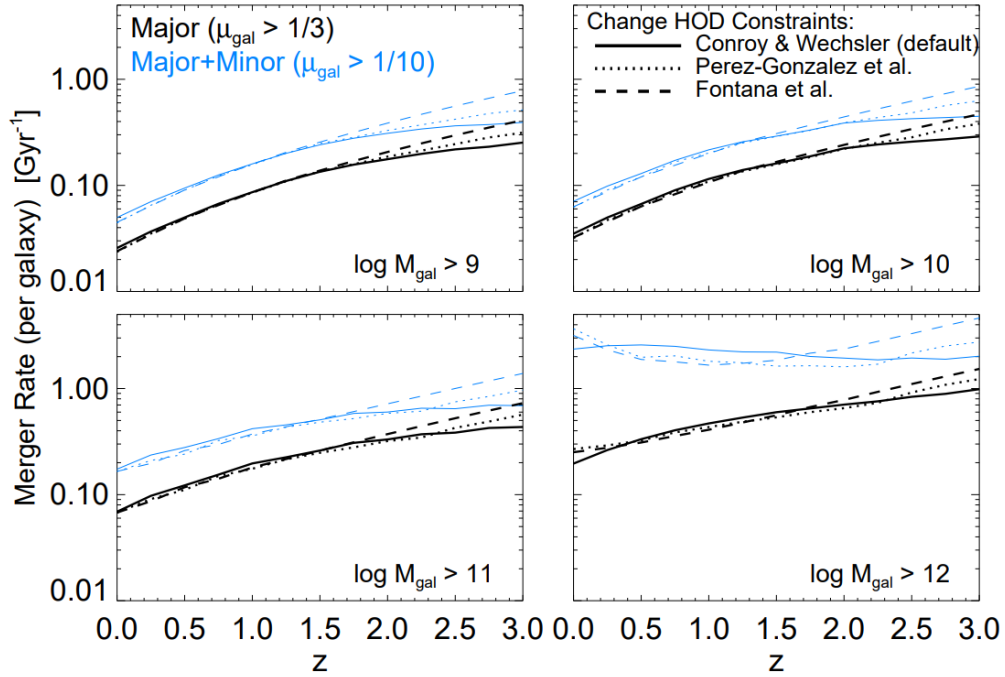


**Figure 1.1:** The clearly declining merger rates from  $z = 3$  to  $z = 0$ . This is Figure 3 of Hopkins et al. (2010). This study looked at the history of a simulated set of galaxies of various stellar mass, and investigated the decrease in the merger fraction as a function of redshift and baryonic mass. As shown, for all mass bins and methods of identifying mergers (the different lines) the merger rate decreases. This is only not true for mergers between very high mass systems and low mass systems (in the bottom right of this plot). Thus, mergers between high and low mass systems may still have some driving force in the cosmic star formation rate density.



younger stellar populations, with star formation continuing to the present epoch. Thus, starting from the observations of morphology, we can make assumptions about the internal gas content, star formation and, therefore, colour of galaxies.

## 1.3 Galaxy Morphology & Galactic Properties

Galaxy morphology, and its change with time, is the study and measure of a galaxy's shape and features. A striking distinction in galaxy morphology is between disk and elliptical galaxies, the primary breakdown in the famous 'Hubble tuning fork' shown in Figure 1.2 (Hubble, 1936). This mapped the complexity of galaxy morphology, with simple early-type elliptical galaxies on the left and complex late-type disk and spiral galaxies on the right. Elliptical galaxies are spheroidal systems, with high internal velocity dispersions. Such systems are often created as the result of mergers and cannibalism of smaller systems to interactions with counterparts of a similar mass (Baugh et al., 1996; De Lucia et al., 2006). Disk galaxies, on the other hand, are rotationally-dominated systems with a central bulge whose size is crucially dependent on the merger history (Barnes, 1992; Hopkins et al., 2010; Bell et al., 2017). In fact, galaxies that appear to have no bulge component at all likely have had no merger event in the last few Gyrs (Martig et al., 2012).

This is also reflected in the observed colour of disk and elliptical galaxies. Observational colours in this context are the comparison of flux in two different wavelength ranges: one capturing the flux of young, star forming regions while the other captures the flux from old, low mass stars. In combination, these young and old stars, constitute a stellar population. Stellar populations have well defined spectral energy distributions (SEDs) based on their age and, indirectly, to a galaxy's star formation rate (SFR) and gas mass. When star formation is occurring rapidly, and the SFR is very high, lots of young, luminous OB-type stars form. The flux from these stars falls mainly in our blue filters, in the rest wavelength of ultraviolet. These stars have lifetimes of only a few million years and, therefore, die very quickly. Thus, if stars are forming slowly, and the SFR is very low, these OB-type stars will die and not be replaced. This leaves an older

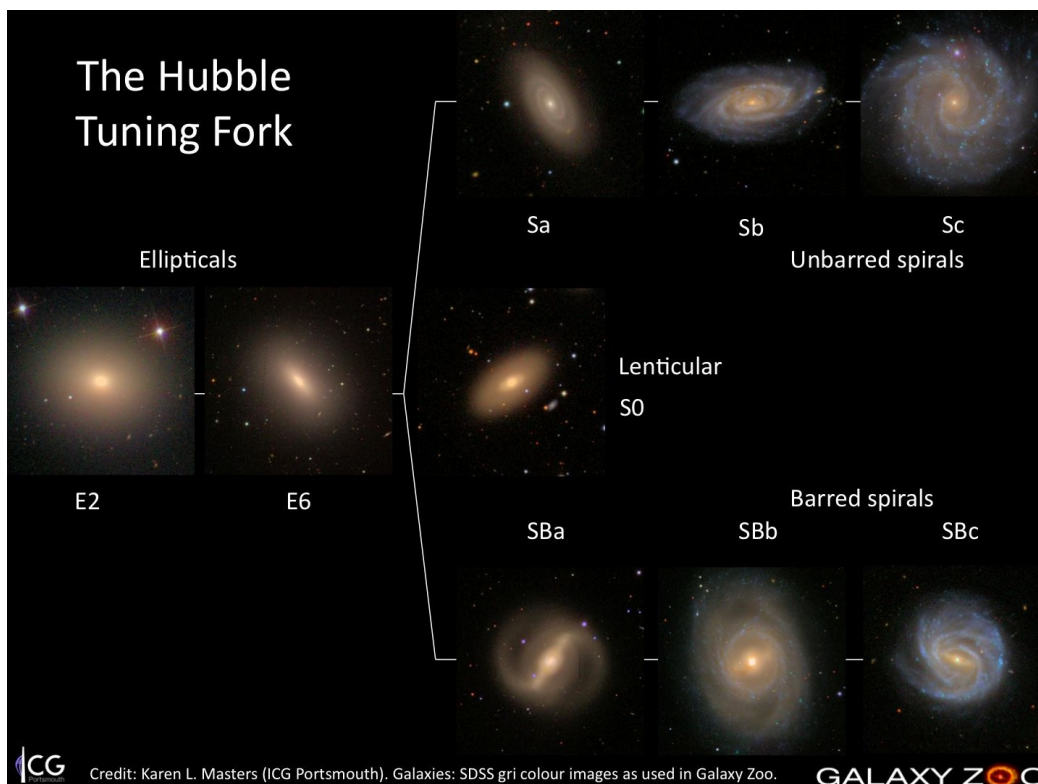


**Figure 1.2:** The Hubble tuning fork. Credit goes to the Galaxy Zoo collaboration (and specifically Karen Masters) for the creation of this figure. On the left, we have elliptical systems - so called early-type galaxies - which are often ‘red and dead’ systems. They have an intense merger history, which has destroyed their disk component and caused them to use the majority of their gas in star formation. On the right, we have two different kinds of disk galaxies. Ignoring the bar or un-barred part of this, they are systems which have a less intense merger history and have only accreted smaller systems into them. This serves to enhance their gas disk, and preserve their disk component.

stellar population, mainly composed of G- to M-type stars which lie primarily in our green and red filters, with wavelengths in the optical.

A secondary method to measure the time since active star formation is by using the 4000Å break (Balogh et al., 1998). This is a large step in an observed galaxies spectra at around 4000Å caused by the absorption of high energy radiation from metals in stellar atmospheres. These metals are formed in high luminosity stars and then injected into the population via supernovae. So, the higher metallicity (and older) a stellar population is, the larger the 4000Å break will be and the longer it will have been since active star formation and the redder the population. Thus, the SFR and age of the dominant stellar population of a galaxy influences their observed colour.

The SFR, then, is highly dependent on the gas mass present in the galaxy. This gas must be cold, molecular gas, with little energy so it is able to form massive clouds that fragment and undergo collapse (Goldreich & Lynden-Bell, 1965; Quirk, 1972). From models of individual clouds, it was noted that the cold gas density was related to the density of star formation in galaxies (Schmidt, 1959). This was further refined to be a global law in disk galaxies in particular in Kennicutt (1998). In this, it was shown that the surface area of star formation is directly related to the surface area of cold gas by

$$\Sigma_{SFR} \propto \Sigma_{Gas}^n. \quad (1.1)$$

This relation has been found to be  $n \approx 1.3$ . Thus, two things are happening here, if a galaxy has cold gas, it has star formation and if it has star formation with little dust, it will be observed to be blue and vice versa.

When observing populations of red galaxies, those dominated by older stellar populations, it has been found they are often elliptical galaxies (Bower et al., 1992). These galaxies have a more violent merger history that has destroyed the ordered rotationally dominated component of a galactic disk and, in the process, either removed or used the gas within the galaxy (Faber & Gallagher, 1976). As a result of this, the current gas mass and density are very low which leads to the SFR being also low.

The opposite is true for disk galaxies. As stated previously, these systems have had a less tumultuous merger history - particularly since  $z \approx 1$ . An indicator of the merger or interaction history in disk galaxies is the size and shape of the bulge component (Emsellem et al., 2011). However, because of the plentiful gas, dust and ordered rotation in the galactic disk the SFR within is larger than elliptical galaxies. The surface density of gas within the disk is much larger than in elliptical galaxies providing the ideal for star formation. Spiral arms can exist in such galaxies, containing large filaments of gas and dust. They contain areas where large molecular clouds can condense, fragment and then collapse into new stars. These star forming regions will be young enough that massive OB-type stars will form, which in turn changes the underlying SED of the galaxy that we observe. The blue filter will contain more flux, and therefore, the galaxy appears blue when comparing the red and blue filters.

This gives rise to two distinct populations of galaxies: old, red elliptical galaxies and young, blue disk galaxies. When plotting colour-colour or colour-magnitude diagrams, there is clear bi-modality which separates these two populations with the ‘green valley’ running between them (Strateva et al., 2001). Figure 1.3 shows the colour-colour distribution if the two populations. In this Figure, we clearly can see the blue population - blue cloud - and the red population - red sequence - beneath it with the green valley in between. The green valley is a disputed area of this distribution. Some works claim that it is a rapid transition phase (Schiminovich et al., 2007; Smethurst et al., 2015), where galaxies are moving between the two populations due to different processes. Others, meanwhile, show that the picture is much more complicated, with morphology and environment playing an important role that dictates the decline in star formation (Schawinski et al., 2014). However, the rule elliptical galaxies are always red and disk galaxies are always blue is not universally true (Smethurst et al., 2022). Examples of blue ellipticals and red spirals do exist (Schawinski et al., 2009; Masters et al., 2010; Keel et al., 2022) and they are the subject of intense debate and study in the current field. However, as a general guideline for the expected properties of a galaxy the colour and morphology are deeply interdependent on one another.

There are also many types of systems that do not fit this simple morphological definition of galaxies. Starburst galaxies are often very morphologically irregular

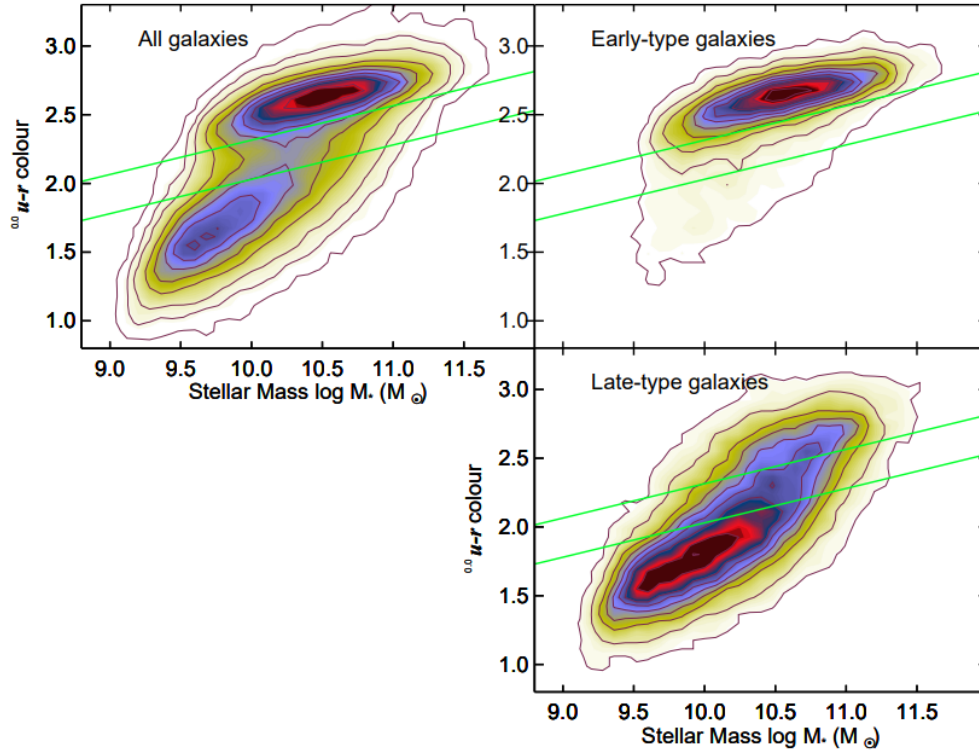


**Figure 1.3:** The distribution of galaxies in colour-colour space showing two distinct populations in a clear bi-modal structure. This is using the u-band and r-band filters and, therefore, the closer to 0 on the y-axis the bluer the galaxy. Left plot: the top population is the blue cloud, primarily composed of disk galaxies with young, star forming stellar populations. The bottom population is the red sequence, primarily composed of more massive elliptical galaxies which are gas poor and quiescent. Between these two populations lies the green valley, marked by the green lines. This is believed to be a transitional population moving between the blue cloud and red sequence for debatable reasons. To further show the split with morphology, the panels on the right split the colour-mass space into early-type (elliptical) galaxies and late-type (disk) galaxies. Note, this is Figure 2 of Schawinski et al. (2014)

and have measured SFRs far in excess of expectation for their mass. These then lead into post-starburst galaxies and merger remnants, who are the complete opposite and have measured very low SFRs. Thus, a parameter such as the SFR of the system is highly dependent on its merger histories and, as we will find, its surrounding environments (Pawlik et al., 2018; Hani et al., 2020). In fact, it has been found that in cluster environments, the fraction of disk galaxies drops to  $\leq 10\%$  when compared to  $\approx 60\%$  in the field.

The effect of the galactic environment on a galaxy should also not be understated. There are many ways to define the galactic environment, but it is most commonly associated with the number density of galaxies about them (Eisenstein et al., 2003; Balogh et al., 2004). There are three broad classifications of environment: field, filament and cluster. A field galaxy is one with neighbours, and is in relative isolation. A filament galaxy has some neighbours, but their influence is minimal. A cluster galaxy is one in which a large number of other galaxies are bound in large galactic super-structures. In such an environment, SFRs are suppressed (Baldry et al., 2006) by ram pressure stripping and the dominant morphologies are elliptical and irregular galaxies due to constant interaction and harassment. In such environments, the relation between galaxy morphology and the underlying processes is almost completely broken by interference from the environment.

Galaxies in the field or in filaments are of particular interest. Here, we can study the direct link between morphology and the underlying processes of galaxies. And these, in turn, are highly dependent on galaxies underlying merger and interaction histories. So, what is this relation? As stated previously, the influence of interaction and merging accelerates the evolution of rotational systems to dispersion dominated systems. However, there are many more subtle effects that can be attributed to galactic merging and interaction. For instance, two galaxies can be brought into a state of starbursting due to merging (Martig & Bournaud, 2008). This completely changes the SED of the galaxy, and can lead to the rapid quenching both systems (Violino et al., 2018; Ellison et al., 2022). Depending on when we observe such a galaxy, we can find either a much bluer or redder galaxy than expected (Di Matteo et al., 2007). However, these effects are also debated, with some studies finding that galaxy interaction does not induce

significant change in the SFR, and therefore, the underlying SED of the galaxy population (Bergvall et al., 2003). So, why is this? It transpires that the effects of a galaxy merger or galaxy interaction is dependent on the underlying parameters of the galaxies themselves. This leads to multiple classifications of galaxy interactions which each lead to different outcomes for the galaxies involved.

## 1.4 Categorisation of Mergers

The effects of galaxy interaction and merging is dependent on multiple factors and underlying parameters. A key parameter to the destruction or survival of a disk is the mass ratio between the two systems (Bournaud et al., 2005; Cox et al., 2008). The impact parameter also has significant influence over the final morphology over the system, however, we will discuss this further in Section 1.5. The gas content of each galaxy also has an effect on the changes of the internal SFR of the systems. The large change in the systems we see based on these parameters gives rise to many different categorisations of galaxies. For the mass ratio, we define a major, a minor and a micro interaction. These are the ratios of the primary galaxy mass (the more massive galaxy) and the secondary galaxy mass (the less massive galaxy).

These are then further sub-divided into two separate categories based on their gas content: a wet merger or a dry merger. This refers to the gas mass and colour of both galaxies. A wet merger involves galaxies which have a high gas fraction, and therefore, lots of resultant star formation. Both of the involved galaxies are often disk-dominated galaxies. A dry merger involves little gas, and is often the merger of massive, red elliptical galaxies. There are also intermediate categorisations based on the amount of gas, such as damp mergers (where there is some gas, but not enough to dramatically increase star formation) and mixed mergers (mergers between gas-poor and gas-rich systems), however, we will focus on the binary definition of wet and dry mergers.

Depending on the classification, an interaction leads to specific outcomes for the interacting galaxy system. A major interaction is when the galaxies involved have a mass ratio of approximately 1:1. Some definitions vary, however, and allow

this limit to go down to 1:3. For the purposes of this work, they must have a mass ratio of at least 1:3. Major interactions are the most devastating to the morphology of the systems involved, with the forces upon them causing severe morphological distortion and the formation of tidal features (described further in the following Chapter). If the two systems merge, there is complete destruction of the disks in both galaxies and the post-merger remnant will be highly irregular. If this is also a wet merger we would also expect a significant increase in the SFRs of both galaxies (Mihos & Hernquist, 1994, 1996; Woods et al., 2006). We also find that wet major mergers have an increased AGN fraction, which suggests that such a merger may play a role in starting nuclear activity (Alonso et al., 2007; Ellison et al., 2011; Koss et al., 2012). The opposite of this is true when a major interaction is dry, where only a small increase in SFR is found in the nuclear region of the galaxies (Sánchez et al., 2004; Bell et al., 2006).

A minor interaction has less catastrophic consequences for the morphology of one of the two galaxies. This is defined as an interaction where the mass ratio is less than 1:3 but greater than 1:10. Due to this large mass disparity, the morphology of the primary galaxy is relatively unaffected by such an interaction. However, the secondary galaxy will be almost completely destroyed by the encounter. If only an interaction occurs, the secondary will be highly disrupted forming a long and stretched tidal tail as it moves through the orbit. When these systems merge, we observe small increases in the SFR of the primary. There is ongoing work investigating whether such mergers were actually a primary driver of star formation in galaxies across cosmic time through rejuvenation of gas reservoirs within the primary galaxy (Bournaud et al., 2007; Kaviraj, 2014b; Jackson et al., 2022). Finally, a micro interaction is one in which the mass ratio between the primary and secondary galaxies is less than 1:10. This sees the complete destruction of the secondary galaxy, whether a flyby or a complete merger. These can form stellar streams about their primary galaxy and are often absorbed by the primary with very little change in its morphology.

Figure 1.4 displays examples of each of the different merger categories we have defined here. These, from left to right, are the Arp 240, Arp 188 and NGC 5907 systems. They each show a major, minor and micro interaction, respectively, and demonstrate the change in effect the mass ratio has on the morphology of





**Figure 1.4:** Examples of a major, a minor and a micro interaction. Each of these are wet interactions, containing lots of gas and therefore, increases the rate of formation of stars. These are the Arp 240, Arp 188 and NGC 5907 systems, respectively. Here, we show the famous double looped stellar stream of NGC 5907 but point out that the existence of the second loop is in dispute and that we only show it here for illustrative purposes (van Dokkum et al., 2019). From major to micro interactions, we see decreasing impact and change in the morphology of the primary galaxies but always the complete destruction of the secondary.

the galaxies involved, from Arp 240, with the complete distortion of the galactic disks and formation of tidal features to NGC 5907 where the primary galaxy is barely disturbed at all. Thus, the different categories of interactions and mergers have very different impacts on the systems involved. We will now discuss, in depth, the effects that interaction has on these galaxies and specifically explore the formation of morphological disturbances like tidal features, changes in the SFR and the increase in AGN fraction.

## 1.5 Effects of Galaxy Interaction

Until the work of Toomre & Toomre (1972), the probability that two galaxies would encounter each other and interact was thought to be negligible. We now understand that galaxy interaction plays an important, and fundamental role in the evolution of galaxies. As stated previously, they have multiple effects upon the systems undergoing the interaction. The specific effects of interaction rests on a host of parameters. We have discussed the mass ratio and gas content and mentioned the impact parameter but there is also the orientation of the interaction, the relative sizes of the galaxies and the point in the dynamical history of the interaction we are observing. Thus, in this Chapter, we will explore how

these different underlying parameters link to the physical processes we observe in interacting and merging galaxies.

### 1.5.1 Morphological Distortion: Tidal Features

As previously discussed, galaxies are large gravitationally bound systems of stars, gas, dust and dark matter. Upon a close encounter between two galactic systems, these components experience strong gravitational forces which disrupt their ordered layout. As the galaxies move through their relative orbits, the gravitational potential changes at an accelerating rate. This imparts energy into the ordered components of the galaxies, and causes thermalization of their internal motions. This leads to violent relaxation, where the stellar orbits are so altered they no longer follow their prior orbits. However, the energy in the system must be conserved. Thus, as the internal stellar motions within the galaxy thermalizes, the energy in the galaxies orbits decay via dynamical friction. If this decay is large enough, the energy in the galaxies orbit may be sufficiently reduced to no longer escape from one another and they will eventually coalesce to leave a single merger remnant.

The changing gravitational fields as the two galaxies encounter each other leads to radial distortion of each galaxy. If stellar material, including gas, dust and stars, is close to the edge of the galaxy a combination of the galactic rotation and radial elongation lead to it being sheared off and away from the galaxy. This forms two ‘tidal tails’ in the system, one leading and one preceding the motion of the galaxy. Dependent on the geometry of the encounter, the trailing tail of one galaxy and the preceding tail of the other can form a ‘tidal bridge’ - a linking of the two systems. An example of both of these is the interacting pair Arp 240, shown in left hand plot of Figure 1.4.

The geometry of the bulk motion of the galaxy is very important in forming these tidal features. To maximise the shearing of material, the internal galaxy rotation and direction of the two galaxies in the orbit must match. Thus, the formation of tidal tails and tidal bridges is only possible in a prograde interaction whereas a retrograde interaction suppresses them. Further, depending on the relative velocities of the galaxies these tidal tails can be split off from the galaxy

as the encounter continues. This can lead to the formation of ‘tidal debris’ about the galaxies.

The confirmation that features such as these were from a tidal origin came primarily from simulations of interactions of different systems. The first restricted numerical simulations were conducted by Toomre & Toomre (1972) who successfully modelled the features of four different systems using distributions of test particles. Numerous works since have recreated tidal features using numerical simulations (Salo & Laurikainen, 1993; Petsch & Theis, 2008; Barnes & Hibbard, 2009; Wallin et al., 2016). These have also been expanded to include a range of other properties in hydrodynamic simulations (Hopkins et al., 2013; Moreno et al., 2019, 2021; Sparre et al., 2022), and investigated in cosmological simulations (Kaviraj et al., 2015; Rodríguez Montero et al., 2019; Hani et al., 2020; Das et al., 2023b). In these more advanced simulations the key to linking the simulations to observations is the morphology of the tidal features. This is often from either direct comparison or from searching for analogues through a suite of interaction simulations in cosmological simulations.

While the most striking tidal features to form in galactic encounters are these tidal tails and bridges, we also see the formation of many other features. These include ‘stellar streams’ (previously discussed), shells and rings forming in the galactic disk. As stated, stellar streams are likely smaller galactic systems that have been destroyed while passing the primary galaxy. This leaves a faint stream of material about the galaxy. The right plot of Figure 1.4 shows an example of a stellar stream with the NGC 5907 system. Shells, on the other hand, are formed around galaxies and can be present in as many as 10% - 20% of elliptical and lenticular galaxies (Malin & Carter, 1983; Atkinson et al., 2013). The right panel of Figure 1.5 shows an example of shell in the elliptical galaxy NGC 1344. Investigation of the formation shells shows they are primarily composed of stars (Quinn, 1984). There are often numerous shells in a single galaxy. Shells are formed from the disruption of a small satellite around a significantly more massive galaxy - i.e, in a minor to micro interaction. This then forms a stellar stream which, over time, condenses to a cloud of stars orbiting the primary galaxy. This then either forms into an X-shaped structure or a annulus which, in the 2D projection of the sky, appears as a shell. Thus, observing a stellar stream or a

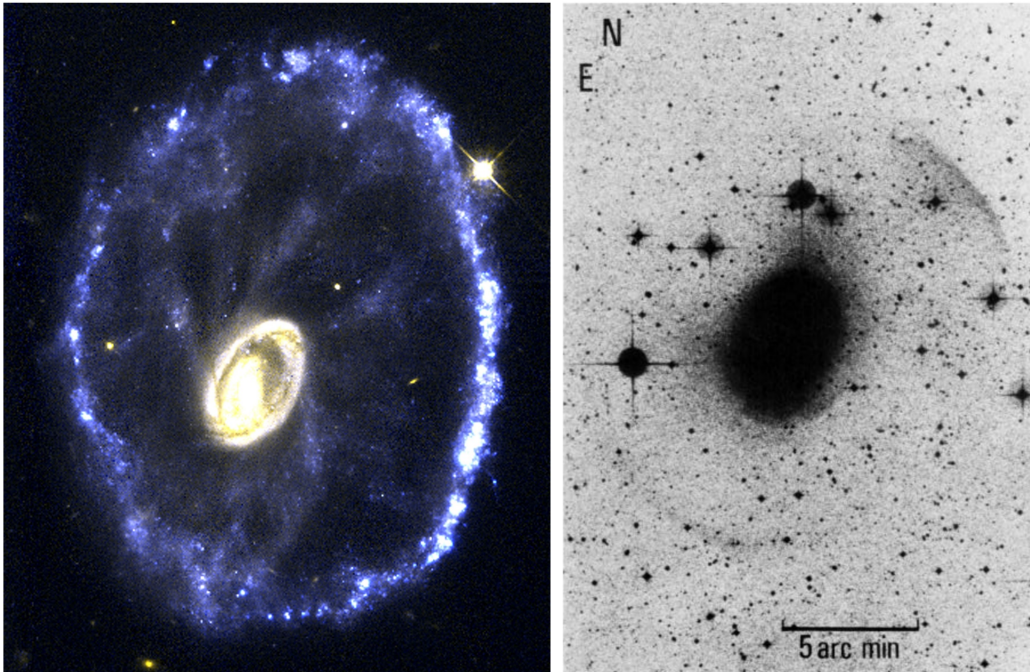


**Figure 1.5:** Examples of a collisional ring galaxy and a system containing shells. Left: The Cartwheel galaxy, the most famous ring galaxy to date. Ring galaxies can only be formed by a direct collision between two galaxies. The ring itself is composed of a region of the disk undergoing intense star formation due to the density wave passing through the disk from the impact of the secondary galaxy. Right: The system NGC 1344, showing two shells of stellar material surrounding it. This is formed by the condensation of stellar streams into clouds of stars. Cartwheel Galaxy Image: NASA / Hubble, NGC 1344 Image: Malin & Carter (1983)

shell is highly dependent on the time in the dynamical history of the encounter that we are observing.

Finally, we find rings can form from galaxy interaction. These systems are often called ring galaxies or collisional ring galaxies. Figure 1.5's left panel shows the Cartwheel Galaxy: a famous example of a ring galaxy. This ring is formed of young, hot stars and is formed only from the head-on collision with another system (Lynds & Toomre, 1976). The interaction to form this is so intense, that it causes a density wave to pass through the galactic disk which triggers intense star formation at its wake.

From the example of a ring galaxy, we see that interaction not only affects the stellar distribution of the galaxy, but also has direct impacts on the gas within

it. As we have stated in previous sections, interaction and merging can induce enhancements in star formation and even lead to a starburst in a galaxy which brings about the complete quenching of the system.

### 1.5.2 Star Formation Enhancement

As noted earlier, it is often observed in interacting and merging galaxies that the star formation is enhanced in some way. While to what level this enhancement is often debated between observations (Barton Gillespie et al., 2003; Li et al., 2008a; Patton et al., 2011; He et al., 2022) and simulations (Di Matteo et al., 2007; Cox et al., 2008; Hopkins et al., 2013; Moreno et al., 2021), the underlying processes that lead to enhancement are well understood. First, by star formation enhancement we mean that the SFR either globally or in different regions of an interacting galaxy is higher when compared to isolated galaxies. Thus, some property of interaction is causing an increase in the star forming activity of the galaxies involved.

The rate at which stars form is known to be directly related to the surface density of gas at any given point within the galaxy, shown in equation 1.1. Due to an interaction the torques and gravitational forces upon the gas clouds leads to a loss of angular momentum. This causes the gas clouds to drift inwards, toward the galactic centre. As more gas clouds fall into the centre, the surface density of gas in this region increases. This in turn increases the SFR.

This is a simple explanation, and an easy idea to hold about driving the increase in star formation in interacting galaxies. As the morphology of the galaxy is compressed into a tidal feature, we see the same increase in the surface density of gas which leads to a further increase in the SFR. This movement and compression of gas into the galactic centre also has a secondary effect on the SMBH at the galactic centre. Increasing the gas density begins the feeding of the SMBH which causes the ignition of nuclear activity.

### 1.5.3 Ignition of Active Galactic Nuclei

The presence of an active galactic nuclei (AGN) in a galaxy is easy to identify observationally. When viewed them face on, the AGN is so luminous that it often outshines the entire bulge and disk of the galaxy. The AGN dominates the SED of the galaxy, and we must carefully remove it using models to decouple the SED of the galaxy and the AGN. The bright flux we observe is from a long and complicated process of accretion of material onto the SMBH at the galactic centre (for an excellent breakdown of the structure and evolution of AGN see Beckmann & Shrader, 2012). The structure of material about the black hole is also complex, and results in many observational oddities.

Surrounding the black hole is an accretion disk of material. As this material accretes, it causes the SMBH to project powerful jets of radiation perpendicular to the accretion disk plane. These jets are highly luminous, and we observe them in the radio, optical, infrared and X-ray. Two populations of AGN have been discovered, containing narrow and broad emission lines, named Seyfert 1 and Seyfert 2 AGN respectively. While at first thought to be two distinct types of AGN, these are believed to be one AGN population viewed from different angles (for a review of the unification, see Netzer, 2015). This is possible as surrounding the accretion disk, there are gas clouds which are either within or outside the nuclear region. Where these gas clouds are gives rise to the narrow and broad line emission observed in AGN spectra.

When we observe only narrow lines we are viewing the accretion disk through low density clouds. The gas of these clouds are photo-ionised by the continuum emission from the central source itself. These are outside of the nuclear region and moving slowly (on the order a hundred km/s). The broad lines are observed when viewing the accretion disk through high density clouds which are located within the nuclear region close to the accretion disk. These clouds are moving fast (doppler broadening is observed to thousands of km/s). Putting this in the context of our AGN classifications, we only observe narrow line emission in Seyfert 2 AGN, so we are observing the nuclear region through low density, slow moving gas clouds out. When we observe Seyfert 1 galaxies, we are viewing the nuclear region through dense gas clouds which lie close to the central engine. This entire

system is encased in a dusty torus of material. We cannot observe the nuclear region through this torus, thus, hiding emission lines from our observations at perpendicular viewing angles.

There are many other categories of AGN beyond Seyfert 1 and 2's. As we move to higher luminosities, we get further populations of AGN such as blazars, quasars, radio-quiet and radio-loud systems. These classifications are all dependent upon the inclination at which we are viewing the AGN system and the material in the line of sight.

From this description of an AGN structure we can see how galaxy interaction increases the likelihood of nuclear ignition. AGN require large volumes of gas and dust to be present at the galactic core, a surge of which is caused by interaction (Hopkins et al., 2008, provides an excellent summary of this process from the point of view of simulations). However, what is often surprising from observations of samples of interacting systems is the meagre increase in the AGN fraction within them. There have been many hypotheses as to why this might be, from a delay in the AGN ignition (Ellison et al., 2011) to AGN flickering (Schawinski et al., 2015). A delay in AGN ignition would make sense, again, in the context of the structure we have just discussed. As gas and dust are moved into the galactic core, they do not necessarily immediately move directly around the SMBH and may take time to get there. There may be other mechanisms at work within the AGN itself that causes suppression of ignition for some time. This could also produce the AGN flickering, where material may be periodically cut off from the SMBH.

It cannot be disputed that the sudden movement of gas into the galactic centre during interaction appears like an obvious way for AGN activation to occur. However, this movement of gas around the galaxy and use in star formation and use or ejection by an AGN can start the quenching of the galaxy.

#### 1.5.4 Quenching of Galactic Systems

During the interaction of two galaxies there is significant movement of gas, AGN activation and large increases in star formation across the galaxy. However, a galaxy only has a limited reservoir of gas available to it. Therefore, this sudden

increase in gas usage in multiple different processes leads to the gas being used in a shorter timescale than expected. Once the gas is used, and the gas density drops significantly, star formation and AGN will rapidly cease and the colour of the galaxy will change to red. This process is called quenching.

This rapid quenching of systems is different to what is expected for isolated galaxies. Galaxies gradually use their gas over long periods of time forming stars and slowly quench as the average gas density across the disk reduces to the point of very low SFRs (Peng et al., 2010b) in ‘mass quenching’. A system can also be quenched by the environment in ‘environment quenching’. However, by concentrating gas and increasing the gas density in an interaction, even if a galaxy had previously stopped forming stars it is able to commence star formation again and use the remaining gas entirely. Thus, we often see increases in the SFR during and immediately after an interaction but then the sudden shut off of SFR shortly after it (Ellison et al., 2022).

The gas is not only used in star formation, but also from stellar feedback around the areas where the stars are forming. As these new stellar populations form OB-type stars very quickly die and cause an increase in the rate of supernova. This, in turn, creates strong shocks and winds that drive the molecular gas out of the galaxy at very high speed (Bolatto et al., 2013; Geach et al., 2018). A similar process can occur due to the AGN in the galaxy. These objects drive strong winds across the galactic system. These winds can also act to drive out gas (Cicone et al., 2014; Cheung et al., 2016; Baron et al., 2018) and cause the cessation of star formation.

## 1.6 Identifying Interacting and Merging Galaxies

We have described and explored the effects of interaction and merging across the galaxy population. We have described the basic properties of galaxies and how these differ when compared to interacting galaxies. However, we are only able to fully understand these differences by using samples of interacting galaxies and comparing them to control samples.



The first samples of interacting galaxies were identified by eye. The earliest interacting galaxy catalogue was the Arp (1966) Atlas of Peculiar Galaxies. This contained 166 interacting systems. This was quickly added to with a 2-part edition of the Vorontsov-Velyaminov (1977) catalogue, providing a further 268 systems to the original Arp (1966) catalogue. Both of these catalogues contained major interactions, where clear tidal features easily put them into the interacting galaxy classification. These samples were also not large enough to make statistical, representative statements about the interacting galaxy population. Thus, larger catalogues had to be created.

Later catalogues often used visual classification to find interacting and merging galaxies. A very successful example is from the Galaxy Zoo collaboration which created a catalogue of 3,003 interacting galaxies identified by citizen scientists based on morphology (Darg et al., 2010a). However, a limitation was found when visually classifying interacting galaxies. With no information on the redshift, and therefore of 3D distribution of a galaxy pair, it is very difficult to distinguish ‘close pairs’ from truly interacting pairs. A close pair, in this context, is two galaxies which appear to be very close together in the sky in the 2D projection of the sky but are actually at different redshifts. This means they are not actually close together in 3D space and cannot be interacting. Many interacting galaxy samples created by visual classification must discard large numbers of false positives from their sample (Blumenthal et al., 2020; Pearson et al., 2022). As machine learning algorithms started to be used in galaxy classification, this problem of contamination by close pairs continued.

Neural networks play an increasingly central role in galaxy classification. As the size of observational samples has increased (e.g. RC3, with  $\sim 20,000$  galaxies, de Vaucouleurs et al. 1991; 2dF, with  $\sim 200,000$  galaxies Colless et al. 2001; SDSS,  $\sim 1,000,000$  galaxies with spectra, York et al. 2000; Abazajian et al. 2009; Legacy Survey of Space and Time, with  $\sim 20,000,000,000$  galaxies expected, Ivezić et al. 2019), so has the challenge of visually classifying each galaxy individually. Rather, a neural network can now be trained to make morphology classifications of galaxies using a much smaller subset of visually classified galaxies.

A neural network is a layered structure of interconnected nodes which can pass information to one another. Each node has a weight assigned to it which allows it to alter the input and then pass on the weighted output. If the weighted output is above or below some value, the output is set zero. The input in this context can be some information about a galaxy, a section of an image or an underlying parameter estimation. These nodes all interconnect through many different layers where they all perform operations on their input and provide weighted outputs. The weighted outputs from the final layer are then passed to a classification layer which outputs either a formal classification or some value that can be mapped to a classification by a user.

A formal classification can be made in this way by training the neural network to recognise certain features of an image. Training a neural network in supervised learning involves providing it with a training set of fully annotated data so it can ‘learn’ classifications. If the training set is sufficiently large, it is split into batches that the neural network will iterate over. To train, the neural network is fed each batch of the training set and makes classifications upon each item within them. It iterates through each batch until it has made classifications on the entire training set. A loss function is then used to measure how accurate the model was based on how many classifications were correct and incorrect. The weights of the model are then updated by back propagating through the model. Once this is completed, an epoch of the training has been completed. This process is repeated through many epochs with model weights being tweaked each time and the a loss function being minimised. Once this has been achieved, the model is able to make accurate classifications on data similar to the training set. Thus, it is important that the training set is large and is representative of the unclassified dataset.

In morphology classification, the workhorse neural network is the convolutional neural network (CNN; examples include Banerji et al., 2010; Huertas-Company et al., 2015; Walmsley et al., 2020; Tian et al., 2023). A CNN takes an image and breaks it down into smaller subsections in its convolutional layers. These are the layers immediately after the input layer, and reduce the dimensions of the image by applying a convolutional filter of a specified size to the image. This conducts the dot product between a group of the pixels in the image and the filter. This returns a single integer which represents a group of pixels in the

image. This integer is then passed to the next layer of the CNN. This is applied across the entire image, and reduces the dimensionality of the image by a factor of the size of the convolutional filter. A ReLU activation is applied immediately after this and setting all negative integers equal to zero. After the convolutional layer, there is a pooling layer. This layer dramatically reduces the dimensionality of the output of the convolutional layer by pooling it by a specified filter and dimension.

This can be repeated many times, depending on the dimensions of the image. The aim is reduce the dimensionality of the image for passing to the fully connected layers while maintaining the representation of the image. These representations - essentially integers representing different sections of the image - are passed through the neural network operations as described previously. The output features from the fully connected layer then go to a classification layer, often a `Softmax` or `Logistic` layer, which returns the classification to be interpreted. The power of a CNN such as described is that it is able to recognise features in an images. For instance, tidal features, AGN or the whole morphology of the galaxy such as ellipticals or disks (e.g Ackermann et al., 2018; Ghosh et al., 2020; Tarsitano et al., 2022; Tian et al., 2023).

However, using a CNN for the purposes of identifying interacting galaxies still introduces the same problems as using visual identification. While the classifications it makes on the morphology of interacting galaxies, or on two galaxies being near each other in an image, it faces the same contamination from close pairs.

New methods combining CNNs with morphological parameterisations of a galaxy are being developed to overcome this issue. This has found some success in correctly identifying interacting galaxies from morphology alone (Ren et al., 2023). Other works have turned to training CNNs on simulated data, where the training set could be controlled and large enough to span the entire parameter space of interaction. These training sets would also have the advantage of being completely free of contamination. However, when applied to observational data it was found that the accuracy of such models breaks down (Bottrell et al., 2019; Ćiprijanović et al., 2020). Thus, creating large and pure interacting galaxy samples remains a task to complete, and the method being it an open question.

The effectiveness of using morphology, and the existence of tidal features, is not uniform across redshift however. Galaxies at higher redshifts they are found to have both dimmer surface brightnesses and smaller angular sizes. This is not due to evolutionary effects, but from cosmological effects and has direct consequences for this classification method. We will lose sensitivity to detecting tidal features about interacting and merging galaxies as their redshift increases and our interacting galaxy samples will become biased toward those systems with high surface brightnesses.

## 1.7 Cosmological Effects

A fundamental obstacle to successfully identifying interacting and merging galaxies are two cosmological effects: surface brightness dimming of a galaxy and the changing angular size of a galaxy. Both of these are a result of the Universe expanding. For instance, we would expect that the luminosity per unit area of a galaxy would remain constant if the Universe was static. However, because the Universe is expanding three things are changing with time: the photon arrival rate, the wavelengths of the photons and the angular size of the galaxy.

The surface brightness is defined as the luminosity within some defined area, in this case angular size on the sky. So, because the angular size is changing while the luminosity remains the same, the surface brightness is decreasing. This relation between the surface brightness and redshift was originally derived by Tolman (1930, 1934). If we have a galaxy at redshift,  $z$ , its surface brightness will be dimmed by

$$I_0 = \frac{I_e}{(1+z)^4} \quad (1.2)$$

where  $I_0$  is the observed surface brightness of an object and  $I_e$  is its intrinsic surface brightness. Due to this, a galaxy observed at  $z = 1$  will be 16 times dimmer than the same galaxy observed in the local Universe ( $z \sim 0$ ).

We use the detection of tidal features to classify interacting and merging systems. These features often lie in the low surface brightness regime. Therefore, even in the local Universe, we are observing them at the very limiting magnitudes of many of our telescopes. So, when attempting to make classifications at high

redshifts and where surface brightness dimming begins to take an effect, we will lose the ability to detect the tidal features of an interacting galaxy. Therefore, we risk being biased only those galaxies with a surface brightness (Calvi et al., 2014), or mis-representing the underlying structure of a galaxy entirely (de Albernaz Ferreira & Ferrari, 2018).

## 1.8 This Thesis

The primary focus of this thesis is investigating and constraining the relationship between galaxy interaction and evolution. The list of unresolved questions about galaxy interaction is long and complex, but we will focus on the following questions here:

- What is the relation between galaxy interaction and the enhancement in star formation?
- What is the relation between galaxy interaction and the fraction of AGN?
- At what point in an interaction do we find enhancement in star formation and a change in fraction of AGN compared to non-interacting galaxies?
- What is the conclusive relationship between the dynamical timescale of interaction, the formation of tidal features and the above effects?

To fully answer these questions three components are required: first, a large statistically significant sample of interacting galaxies; second, available ancillary data of these systems to make inferences between the underlying processes in interaction and their parameters; and thirdly, the tools to constrain the dynamical timescales of each system. This thesis details methodologies which achieve these goals. First, in Chapter 2, we create the largest interacting galaxy catalogue to date through combining morphological classification with novel methods of machine learning, data extraction and analysis. We then use this catalogue, in Chapter 3, by matching to existing ancillary catalogues and conduct our own inferences about the relationship between galactic parameters and underlying

processes. However, we find that we can only constrain this relationship to a very general point. We require tighter constraints on the dynamical timescale of the interactions in our sample to further explore the relationship between galaxy evolution and interaction. In Chapter 4, we describe software we have built that will conduct such constraint in the context of Bayesian statistics and galactic parameterisation. We will describe the results we have found by applying it to a small, well constrained, interacting galaxy sample and then describe the limitations of the approach in terms of computational efficiency. Finally, in Chapter 5 we summarise our results, describe them in the context of current works and speculate about the future work to advance them.

Where necessary, we use a Flat  $\Lambda$ CDM cosmology with  $H_0 = 70\text{kms}^{-1}\text{Mpc}^{-1}$  and  $\Omega_M = 0.3$ . Hereafter in this thesis, when referring to an interacting galaxy we are referring to a galaxy which has undergone one or multiple flybys by a secondary galaxy and caused a tidal disturbance. A merging galaxy is the final state of these flybys, where two or more systems have coalesced to form a highly morphologically irregular system.

# Chapter 2

## Creating a Large Sample of Interacting Galaxies

### 2.1 Introduction

Interacting and merging galaxies are important to our current theory of  $\Lambda$ CDM cosmology, in which structure typically assembles hierarchically (Abadi et al., 2003; Springel et al., 2005; De Lucia & Blaizot, 2007; Guo & White, 2008). Galaxy interaction leads to highly disturbed morphologies (Toomre & Toomre, 1972; Hernández-Toledo et al., 2005; Wallin et al., 2016), intense starbursts (Mihos & Hernquist, 1996; Springel, 2000; Saitoh et al., 2009; Moreno et al., 2021) and, potentially, quenching of some systems (Hopkins et al., 2013; Smethurst et al., 2018; Hani et al., 2020; Das et al., 2023a). In general, galaxies undergoing interaction are observed to have higher star formation rates than those that exist in the field (Ellison et al., 2008; Scudder et al., 2012; Pearson et al., 2019b). Interaction also has a direct impact on the gas angular momentum within each galaxy, causing it to decrease. This, potentially, leads to funnelling of gas into into their nuclear regions and igniting activity. This could be a connection with active galactic nuclei (Ellison et al., 2008; Li et al., 2008b; Ellison et al., 2011; Comerford et al., 2015). However, such a connection remains debated (Alonso

et al., 2007; McKernan et al., 2010; Marian et al., 2020). Thus, understanding galaxy interaction is crucial to testing theories of galaxy evolution itself.

Interacting galaxies have long been explored with different samples of galaxies. Examples include constraining merger rates as a function of redshift (Lotz et al., 2008b), inferring the contribution of minor mergers to the cosmic star formation budget (Kaviraj, 2014b,a), and examining interactions as a function of their local environments, internal properties and AGN activity (Darg et al., 2010b). These studies (and many others; for further examples, see Barton et al., 2000; Alonso et al., 2004; Ellison et al., 2013; Holincheck et al., 2016; Silva et al., 2021) illustrate the complex parameter space involved in understanding the role of interaction in galaxy evolution. Thus, to effectively study interacting galaxies, we need observed datasets of such a size that they can sample a wide range of various parameters of interest.

The first large-scale catalogues of interacting galaxies are from the mid 20th century (Arp, 1966; Vorontsov-Velyaminov, 1959, 1977, hereafter VV). These catalogues primarily used visual inspection to identify mergers (e.g., de Mello et al., 1997; Nair & Abraham, 2010) and generally found from hundreds to thousands of systems. The largest set of interacting galaxies identified by a single expert classifier contains 2,565 relatively nearby systems (Arp & Madore, 1987). Citizen science techniques can extend this number, as was presented by Darg et al. (2010b) who used them to find a catalogue of 3,003 interacting galaxies.

The inclusion of automated classification shows promise to continue this expansion. The use of machine learning in classifying galaxy morphology is well established (Ardizzone et al., 1996; Abd El Aziz et al., 2017; Barchi et al., 2020; Ghosh et al., 2020; Cheng et al., 2021). The workhorse algorithm is the convolutional neural network (CNN; for an introduction, see O’Shea & Nash, 2015), most often used in image recognition and feature extraction. CNNs can be used for general classification (e.g. early- versus late-type galaxies) or to extract specific morphological features of galaxies, such as bars, spiral arms, etc. Many works have demonstrated their effectiveness at this (e.g. Ackermann et al., 2018; Jacobs et al., 2019; Bickley et al., 2021; Buck & Wolf, 2021; Walmsley et al., 2022a). Pearson et al. (2022) demonstrated the power of CNNs for finding in-



interacting and merging galaxies specifically, finding 2,109 in 5.4 deg<sup>2</sup> of Hyper Suprime-Cam imagery - a large sample for the small area covered.

However, issues with using CNNs in classifying interacting galaxies have been found on numerous occasions. The primary concern, is that - without due care - classifying interacting galaxies by morphology alone can be highly contaminated. For example, CNNs often confuse chance alignments of galaxy pairs on the sky for interacting systems. This leads to many predicted interacting systems being thrown away after visual inspection (in some cases up to 60%; Bottrell et al. (2019); Pearson et al. (2022)).

In this work, we aim to use machine learning to create a large, high-confidence catalogue of interacting systems, drawn entirely from existing astronomical imagery. We search through the European Space Agency's *Hubble Space Telescope* Science Archive<sup>1</sup> using a CNN to predict whether an image contains an interacting system, from among the 126 million extended objects in the *Hubble* Source Catalogue (HSC; Whitmore et al., 2016). This catalogue is composed of source detections across a range of filters using the **Source Extractor** algorithm (Bertin & Arnouts, 1996). The limiting magnitudes of the HSC in the *F606W* and *F814W* were found to be the 26th magnitude.

The feature extraction we implement is focused on finding tidal features or morphological disturbance caused by the interaction. The tidal features prioritised include tidal tails, tidal bridges or tidal debris. As stated previously, this runs the risk of introducing high levels of contamination by close pairs. We thus implement further automated and manual methods, which significantly reduce this. The systems we find are often in the background of previous deep surveys (such as the Cosmic Evolution Survey, COSMOS, Scoville et al. 2007; the Great Observatories Origins Deep Survey, GOODS, Giavalisco et al. 2004; and the Panchromatic Hubble Andromeda Treasury Survey, PHAT, Dalcanton et al. 2012), where spectroscopic coverage varies. Therefore, while our final catalogue reduces contamination to  $\sim 3\%$ , definitively removing all contamination by close pairs remains a challenge following this work.

This Chapter is laid out as follows: Section 3.2 describes the HSC and all the criteria we applied to create the images we predict over. This Section also

---

<sup>1</sup>See <http://hst.esac.esa.int/ehst/>

introduces ESA Datalabs<sup>1</sup>; a new platform which allows the user to directly access the *Hubble* Science Archive. Section 2.3 gives an in depth description of the *Zoobot* CNN we utilise for our predictions, and how it differs from a commonly used CNN. Section 2.4 explains the process of creating the training set for our CNN to find interacting galaxies, with Section 2.5 showing how well it performed and providing the diagnostics of the CNN. We also use this Section to investigate the contamination in our catalogue. Section 2.6 describes our results and discusses the final catalogue as well as define interesting systems or objects that we have found. We also explore some basic properties of the catalogue here. Finally, Section 3.7 summarises our results and conclusions.

## 2.2 Data

### 2.2.1 The *Hubble* Archives & ESA Datalabs

The observational data is directly from the *Hubble* Science Archive and is accessed from the new ESA Datalabs platform. The repository contains approximately 100TB of data from the *Hubble Space Telescope* (*HST*). This repository spans all *HST* instruments and filters. ESA Datalabs provides a direct interface between users and the data. On this platform, every observation's FITS file can be accessed. To streamline our pipeline, we applied criteria to the observations as not all filters have the same number of observations, some instruments are not as sensitive to the low surface brightness regime as others or the field of view of certain instruments would not be ideal for measuring galaxy morphology. Finally, we do not conduct source extraction from each FITS file ourselves but use the *Hubble* Source Catalogue (Whitmore et al., 2016, hereafter HSC) to define the centre of each source cutout.

The criteria we apply are: the observational data must be from the Advanced Camera for Surveys (ACS), it must be final product data of *HST* (i.e. within a .drc file, where the data has been drizzle (Avila et al., 2015) combined and had charge-transfer-efficiency corrections applied), observed within the *F814W*

---

<sup>1</sup><https://datalabs.esa.int/>

filter and must be flagged as an extended source in the HSC. This offloads sky subtraction, cosmic ray rejection and charge efficiency calculations to the original *HST* pipeline and removes costly steps from our cutout creation process. We utilise all final product data of the *F814W* filter from *HST* as this was the filter which contained the most FITS files, and therefore observations. The *F814W* filter contained 9,527 final product FITS files which could be used for source extraction, whereas the closest second (the *F606W* filter) contained  $\approx 6000$ . By using the filter with the most files, we are confident that we cover a majority of the HSC. Applying this criteria gives 126 million sources to predict over.

We must create 126 million source cutouts from 9,507 different FITS files. Creating a dataset of cutouts at this magnitude in conventional methods (such as `AstroQuery` or Table Access Protocol (TAP) services) would be impractical due to making many network calls and long FITS file download times. Instead, we use the ESA Datalabs platform, which is due to be released in Q4 of 2024. This platform has been developed to allow us to ‘mount’ the *Hubble* Science Archive onto it. In practice, providing access to the entire *Hubble* Science Archives as local files for the user to manipulate while on the platform. This bypasses network calls to servers to download our required FITS files, a process which could have taken minutes per download. Having direct access to the files, and quickly matching source coordinates to FITS files (described in Section 2.2.2) allows us to open a FITS file and create all source cutouts from it without having to close or reopen it. Therefore, we were able to create on the order of 10k cutouts in the same order of time taken to download a single file.

The source cutouts were created as *F814W* gray scaled 150x150 ( $7.5'' \times 7.5''$ ) pixel images using the HSC source coordinates as the centre. The image size was set and standardized to streamline the pipeline. The majority of cutouts are centred on the source but, in a minority, misalignment between source and image centre occurs. This is a result of the drizzling process, with incorrect alignment sometimes being significant. However, the target source was always present in the cutout and we, therefore, did not attempt to rectify this. We scale the image using a `ZScaleInterval` with a set contrast of 0.05 and a `LinearStretch` following the default parameters in the `Astropy` (Astropy Collaboration et al., 2013a, 2018a) package. These were binned to  $300 \times 300$  pixels (pixel resolution is  $3.25'' \times 3.25''$ )

with a linear interpolation from the `CV2` python package. The images were created at  $150 \times 150$  to minimise storage required on the early version of ESA Datalabs being used. Creating the images at half the size allowed us to scale up to  $300 \times 300$  pixels without any effects of the interpolation.

### 2.2.2 The Shapely Python Package

A large computational expense in our pipeline was matching FITS files to sources. Conventionally, the `Astropy` `CONTAINS` function would be used to match source coordinates to the FITS file WCS. We instead use the `Shapely`<sup>1</sup> Python package. `Shapely` is a geometry orientated package primarily focused on geospatial data. We found converting the FITS image footprints into `Shapely` Polygons and the source coordinates to `Shapely` Points and then checking if they overlapped had significant speed up. Per iteration, `Astropy`'s `CONTAINED_BY` function matches a source to a FITS file on the order of 500ms. Using `Shapely`'s `CONTAINS` function, the same process is on the order of  $6\mu\text{s}$ .

## 2.3 Utilising a Convolutional Neural Network

We must choose a CNN which would best suit our needs to classify them into interacting galaxies or not. We select the newly developed CNN `Zoobot` (Walm-sley et al., 2022a, 2023). `Zoobot` is a CNN specifically trained to classify galaxies based on morphology into many different types (spiral, disk, elliptical, barred, non-barred, etc). We retrain it to only classify galaxies into interacting or non-interacting. Instead of training `Zoobot` from scratch and creating a new model, we use transfer learning to finetune existing `Zoobot` models to classify our data for our particular question. This allows us to retain information from `Zoobot`'s previous training. More importantly, it requires a significantly smaller training set to achieve high accuracy.

---

<sup>1</sup>Shapely docs: <https://shapely.readthedocs.io/en/stable/manual.html>

### 2.3.1 Zoobot

The version of `Zoobot` we use is a deep CNN which was trained on Galaxy Zoo volunteer classifications over three different Galaxy Zoo: DECaLS (GZD)(Dark Energy Camera Legacy Survey, described in Dey et al., 2019) campaigns. These were GZD-1, GZD-2 and GZD-5 - each number corresponding to the DECaLS data release. For training `Zoobot`, DECaLS imaging was selected using the NASA-Sloan Atlas (NSA), which was itself constructed with SDSS Data Release 8 (DR8) images. This also introduced implicit cuts to the training data, as SDSS can not get to the depths of DECaLS. This introduces implicit magnitude and redshift cuts on the training data. Specifically, SDSS DR8 and the NSA cover galaxies brighter than  $m_r > 17.77$  and closer than  $z < 0.15$ . In Section 2.3.2 we describe using transfer learning to use `Zoobot` effectively outside of this magnitude and redshift range.

Walmsley et al. (2022a) use the 249,581 volunteer classifications from GZD-5 campaign to train `Zoobot` to answer all 34 questions (example shown in Figure 4 of Walmsley et al., 2022a) in the remaining campaigns. GZD-5 was used as it had a slightly different volunteer decision tree, having an expanded question on potential different galaxy merger stages. Each galaxy image had been shown to volunteers as a 3-colour (g,r,z) of  $424 \times 424$  cutout. Each images pixel scale was an interpolation between the measured Petrosian 50%- and 90%-light radius. The measured full Petrosian radius had to be at least  $3''$  to be shown to the volunteers. When inputting into `Zoobot`, these cutouts were scaled and grayscale to  $300 \times 300 \times 1$  images, averaging over the 3-colour channels to remove colour information and avoid biasing the morphology predictions. `Zoobot` utilised the Adam (Kingma & Ba, 2014) optimizer to train.

By training `Zoobot` in this way, combining the approach of answering many questions at once with Bayesian representation learning, it learns a generalisable summary of many types of galaxies. These generalised summaries are lower-dimensional descriptions of galaxy types and are referred to as representations. These representations change depending on the galaxy type, morphology or environment in an image and lead to similar images being closer together in a representation space than dissimilar ones. This representation approach on a

very broad classification problem is found to increase accuracy and generality of *Zoobot*, giving it an edge over conventional CNNs. A more detailed breakdown of this approach, as well as further details about *Zoobots*' architecture, can also be found in Walmsley et al. (2022a).

*Zoobot* was trained to give a prediction score to an image of a galaxy based on the question it is answering. The type of prediction score is set by the users choice of the model final layer in *Zoobot*. We elect to use a `SOFTMAX` output, which returns an output score as a float between 0 and 1. This prediction score is not a probability score, although it may seem analogous. A well behaved prediction score will map to probability, though not necessarily linearly. The mapping between prediction score and probability is not considered in this work, and we use the prediction score as an indicator of *Zoobot*'s confidence a source is an interacting galaxy.

We are only interested in the 'Is the galaxy merging or disturbed?' question from the Galaxy Zoo: DECaLS workflow, where the answer can be 'merging', 'major disturbance', 'minor disturbance' or 'None', and only want our version of *Zoobot* to return the answer to this. Our version of *Zoobot* is also not trained to predict over *HST* data which differs from DECaLS data (different resolutions, filter bandwidths, etc). If we were to use our version of *Zoobot* as downloaded we would likely lose accuracy. We utilise transfer learning to optimise accuracy of just our question as well as to classify *HST* data. Since this work, *Zoobot* has been trained on *HST* data so the transfer learning step would not be needed in future with the new models. How we apply transfer learning is discussed in the following Section, but an excellent review and discussion of applying transfer learning for detecting galaxy mergers can be found in Ackermann et al. (2018).

### 2.3.2 Transfer Learning

Transfer learning (or finetuning) is a method of applying the same machine learning model to a similar problem that it was originally trained on. Rather than having to completely retrain all parameters in a model and essentially create a new one, we can use the original model architecture and the parameters it has learned from its previous training. In the case of *Zoobot*, we keep the parameters

it has learned from training on the DECaLS dataset and freeze all sections of the model responsible for feature extraction and recognition.

We construct a classification section that maximises accuracy and only allow the weights of this section to change. As the classification section has fewer parameters than the feature extraction section (the classification section contains 86,209 parameters compared to the feature extraction sections' 4,048,989 parameters) we need significantly less data to completely retrain it (in our case, a factor of 15 less). Once this retraining is complete, the weights of the feature extraction sections of the model can be unfrozen and tweaked using our smaller dataset with a very low learning rate to further boost overall model accuracy.

An example of taking an existing model and applying it to a new problem with transfer learning is shown in Walmsley et al. (2022b). Here, they take the trained model and finetune it to finding ring galaxies. They retain an accuracy of 89% while only needing to train the model on  $10^3$  ring galaxies. This significantly reduces computational expense and training time of the model, while keeping the required training set very small. Interacting galaxies are rare, and interacting galaxy catalogues not expansive. So retraining the full network on hundreds of thousands of interacting galaxies is not feasible. Using transfer learning, and following the example from Walmsley et al. (2022b), we only need to create a training set of  $10^3$  -  $10^4$  interacting galaxies to achieve an accuracy of  $\approx 90\%$ .

## 2.4 Creating the Training Set

We create a large training set of interacting galaxies following the criteria described in Section 3.2 to train our model. Therefore, we need a large, labelled set of interacting and non-interacting galaxies. We elect to follow the methodology of finetuning as described in Walmsley et al. (2022b), and aim to create a balanced training of 50% interacting and 50% non-interacting galaxies. This has the advantage that it significantly improves the performance and accuracy of machine learning classifiers, but the disadvantage that it can bias our final model if few interacting galaxies exist compared to the general population. However, such a bias will be mitigated by using a high prediction cutoff to define an interacting

galaxy. This is discussed in Section 2.5.1. To create this large training set we use the Galaxy Zoo collaboration (initial data release described in Lintott et al., 2008).

### 2.4.1 Interacting Galaxies and Galaxy Zoo

The data in Galaxy Zoo is volunteer classifications on galaxy images spanning multiple projects. We incorporate classifications from all major Galaxy Zoo projects; Galaxy Zoo 1 (Lintott et al., 2008), Galaxy Zoo 2 (Willett et al., 2013), Galaxy Zoo: *Hubble* (Willett et al., 2017), Galaxy Zoo: CANDELS (Simmons et al., 2017) and Galaxy Zoo: DECaLS (Walmsley et al., 2022a). These projects contain a total of 1,367,760 labelled galaxy images that we must extract the interacting galaxies from. We only use labels that are from citizen scientists, and no labels generated by previous versions of Zoobot. We apply three criteria to each interacting or non-interacting label. Firstly, it must have greater than 20 volunteer votes on it. Applying this allows us to use a statistically robust weighted vote from a crowd answer rather than trusting any volunteers individually. Secondly, the calculated weighted vote (i.e. the combination of the 20 or greater votes) must then be greater than 75% in favour of being an interacting galaxy or less than or equal to 25% for it not to be; this ensured purity in our training set. If the question given to volunteers was more specific (such as ‘Is this a minor disturbance?’ and ‘Is this a major disturbance?’) then if either answer was the majority vote we classified it as an interacting galaxy. Thirdly, the object must exist in the *Hubble* footprint so that we could make a cutout of it.

Checking if each training source existed in the *Hubble* footprint was only possible in an efficient way because of ESA Datalabs. Rather than having querying every coordinate and make network calls to TAP services, we extract every final product *F814W* observation footprint and check if each labelled galaxy exists in at least one file. We make this check by creating a `Shapely` Polygon for each observational footprint and a `Shapely` Point for each labelled galaxy central coordinate. Using the `Shapely` Polygon `CONTAINS` function, we check if a labelled galaxy’s Point overlaps with an observations’ footprint Polygon. This returns a list of files which contain the training source. If a training source was not found



in any observational footprint we discard it. We make no attempt here to check if our sources have other photometry available to them, and only create 1-colour images with the  $F814W$  data. We provide the images to `Zoobot` as 1-colour grayscale cutouts.

Upon applying these criteria we find 3,167 labelled interacting galaxies in Galaxy Zoo: *Hubble* project, the largest contribution to our training set. These were paired with 3,167 labelled non-interacting systems (following the previous criteria) to balance the training set. From all other projects, we find 869 labelled interacting systems which fitting the creation criteria. The primary limiting factor for Galaxy Zoo’s 1 and 2 was that many found interacting galaxies did not exist in the Hubble footprint. For Galaxy Zoo: CANDELS and Galaxy Zoo: DECaLS the limiting factor was the required calculated weighted vote. These labelled interacting systems were then paired with 869 labelled non-interacting systems, ensuring that each labelled non-interacting system came from the same project as its labelled interacting system counterpart.

Each of these projects has a varied redshift range: Galaxy Zoo: *Hubble* is  $z < 1$ , Galaxy Zoo: CANDELS  $1 < z < 3$  and Galaxy Zoo’s 1, 2 and DECaLS are  $z < 0.15$ . This introduces a redshift bias into our model, where the morphology and brightness of interacting sources changes with a  $z > 1$ . This is only partially rectified by including Galaxy Zoo: CANDELS, which provided 322 labelled interacting systems.

From all Galaxy Zoo projects, we find a training set of 4,036 labelled interacting galaxies and combine them with their matched 4,036 labelled non-interacting galaxies giving a total training set size of 8,072. Figures 2.1 and 2.2 show six examples of our labelled interacting and non-interacting galaxy training set. As we require `Zoobot` to learn to weight tidal features or disturbances highly, it is important that such structures dominate the training set. Previous works, such as Pearson et al. (2019b), have found that final catalogues produced by CNNs are often heavily contaminated by sources which are simply close pairs by projection effects and chance alignment in the sky. By focusing our CNN on tidal features, we aim to minimise this contamination. We ran an initial test of the prediction pipeline on the first 500,000 sources that had been created from the HSC to initially test our `Zoobot` model. We investigate any source which was

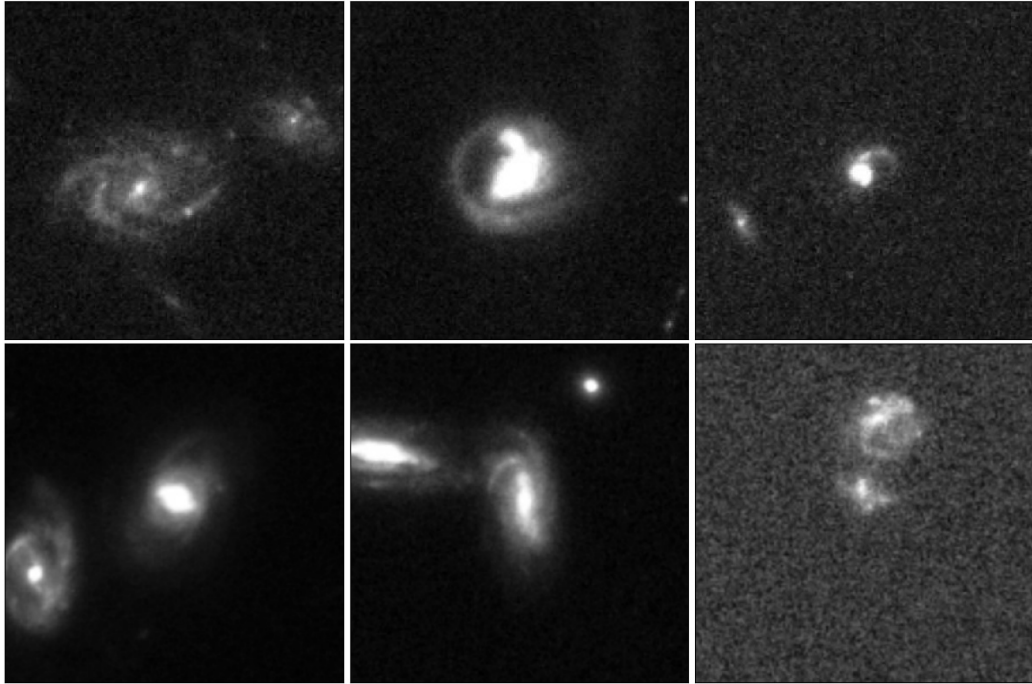


**Figure 2.1:** Example images of the labelled interacting galaxy systems used to train Zoobot. Each galaxy had a weighted vote fraction  $\geq 0.75$  in Galaxy Zoo. *Top Row:* Three examples from the Galaxy Zoo: *Hubble* project of the training set. *Bottom Row:* Three examples from the other Galaxy Zoo projects. These are, from right to left, Galaxy Zoo 2, Galaxy Zoo CANDELS and Galaxy Zoo DECaLS. The priority with this training set was that the interactors had clear tidal features and disruption so Zoobot would learn to highly weight them and not misclassify close pairs.

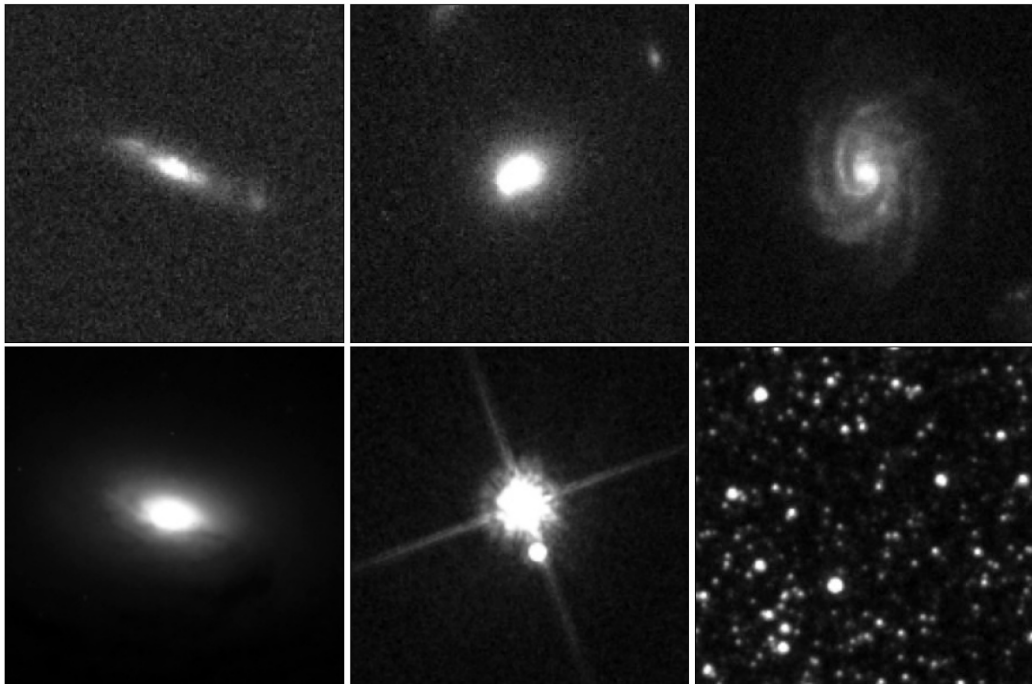


**Figure 2.2:** Example images of the labelled non-interacting galaxy systems used to train Zoobot. *Top Row:* Three examples from the Galaxy Zoo: *Hubble* project of the training set. *Bottom Row:* Three examples from the other Galaxy Zoo projects. These are, from right to left, Galaxy Zoo 2, Galaxy Zoo CANDELS and a starfield from the active learning cycle. Starfields/globular clusters/open clusters existed throughout the HSC flagged as extended sources. 1,000 images of starfields were added to the training set so Zoobot would give them a very low score.

given a prediction score  $\geq 0.75$  and, to further increase the size of our training set, conduct one step of active learning.

### 2.4.2 One Active Learning Cycle

To enlarge our training set further, we conduct one step of active learning to find interacting galaxies. An active learning cycle involves an ‘expert’ checking the predictions made by the model, correcting any incorrect predictions and then feeding it back into the model as additional labelled images to a training set. We complete finetuning of `Zoobot` on our initial training set of 8,072 galaxies and make predictions on the first 500,000 sources from the HSC (created under the criteria previously discussed). We visually inspect the sources `Zoobot` gives a prediction score  $\geq 0.75$  and correct any wrong predictions. These corrected labelled sources and those `Zoobot` correctly labelled are then added to the training set. Not only does this step allow us to add more labelled interacting galaxies to the training set, but it also allows us to evaluate `Zoobot`’s behaviour and check if it consistently predicts a type of source or galactic morphology incorrectly.

From the first 500,000 sources, a total of 6,198 sources were given a prediction score of  $\geq 0.75$ . We correct the predictions `Zoobot` made and balance this set to 5,698. During this cycle, a large number of globular clusters/starfields/open clusters were given a very high prediction score. Figure 2.2 shows an example of these contaminating star fields. We created sources of 1,250 star fields and added these into the training set, labelling them as non-interacting. Adding the balanced 5,698 sources plus the 1,250 starfields to our training set gave us an unbalanced training set of 15,020 sources. To then balance the training set, we took 1,250 labelled interacting galaxies from the Galaxy Zoo: *Hubble* project and made random image augmentations with the `TensorFlow` Python package. These augmentations were simple rotations, cropping and resizing. With these extra sources, our training set contains 16,270 sources. Of these, 50% (8,135) were labelled images of interacting galaxy systems.

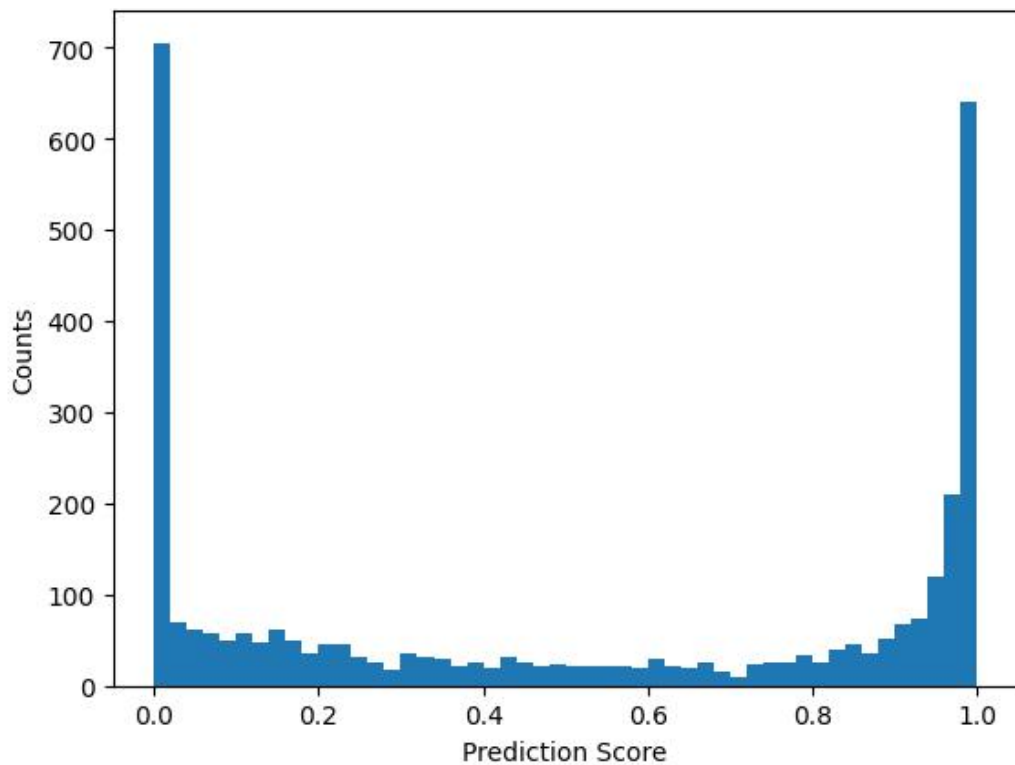
## 2.5 Diagnostics

### 2.5.1 Model Performance

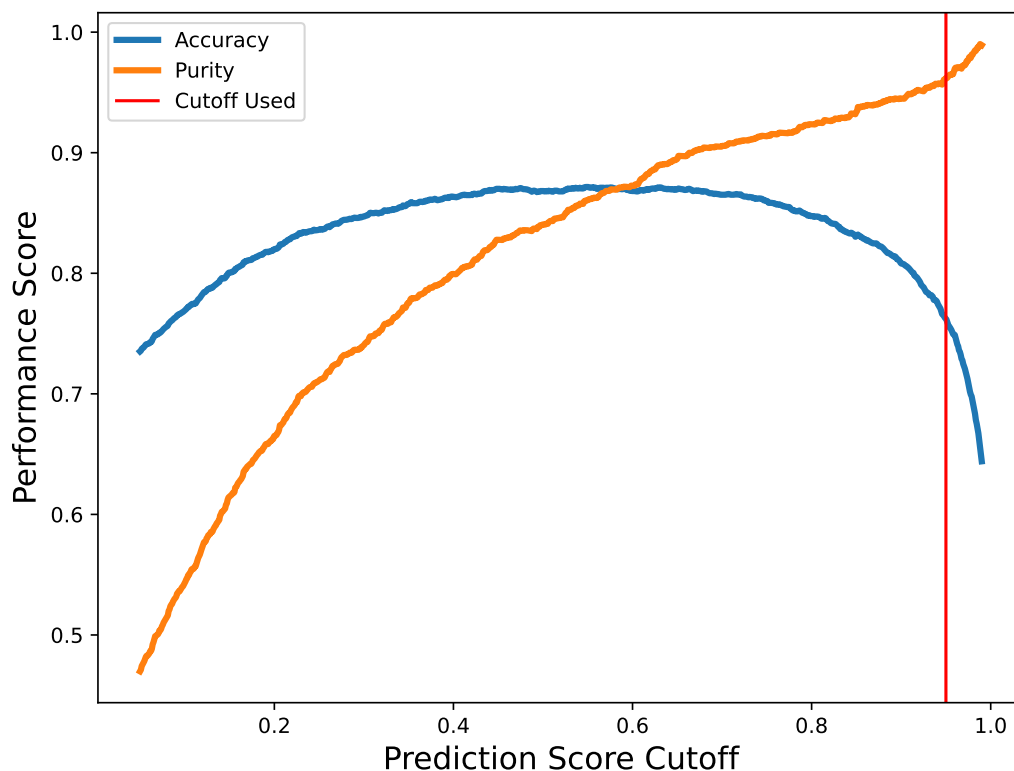
Upon finetuning `Zoobot` we validate its performance. We reuse the validation set that `Zoobot` automatically creates when training. This set is created by putting aside a random set of 20% of the training set. `Zoobots` then uses it to validate its performance in training. We record which images `Zoobot` selected, and extract these from the training set for further diagnostics. This provides us with a validation set of 3,270 images, containing 1,648 non-interacting galaxies and 1,622 interacting galaxies.

`Zoobot` gave a prediction score between 0 and 1 to each of the validation images, Figure 2.3 shows the resulting distribution. This distribution shows that our model has high confidence in what is or isn't an interacting system due to the high counts at very low and very high probability scores. It is likely the use of a balanced training set, and the very low volunteer score needed to define a source as non-interacting that leads to a strongly bi-modal prediction score distribution. Using a balanced training set is an intrinsic trade off between ease of training, and potential biases introduced. Having a balanced dataset does not reflect reality, and leads `Zoobot` to over-predict interacting galaxies. Using very stringent volunteer classification cutoffs also leaves few ambiguous systems in the validation set, further enhancing this bi-modality.

The prediction score must be reduced to a binary classification for our problem. We use Figure 2.3 to define a prediction score above which a source is classified as an interacting galaxy. We measure the accuracy of `Zoobot` for different cutoffs, where the accuracy is the fraction of labels correctly predicted over the total number of labels predicted on. Figure 2.4 shows this change in accuracy. We find that our model is most accurate with a prediction score cutoff of 0.55 with an accuracy of 88.2%. Figure 2.4 also shows the change in the purity of our catalogue with changing prediction cutoff. Here, purity is the ratio of number of true interacting galaxies to total sources in the final catalogue. These scores can be combined into the F1 score of our model, shown in Figure A.2 in the Appendix.



**Figure 2.3:** The distribution of prediction scores given to our validation set of 3,270 labelled sources set aside by Zoobot in training. These were split into 1,648 non-interacting sources and 1,622 interacting sources. As can be seen from the distribution, our model is often confident when a source does or does not contain an interacting galaxy by the strong bi-modality. This is likely due to the very stringent vote weightings used when selecting the training set. Using this distribution, we decide the prediction score to use as a cutoff to give us our final binary classification: interacting galaxy or not.



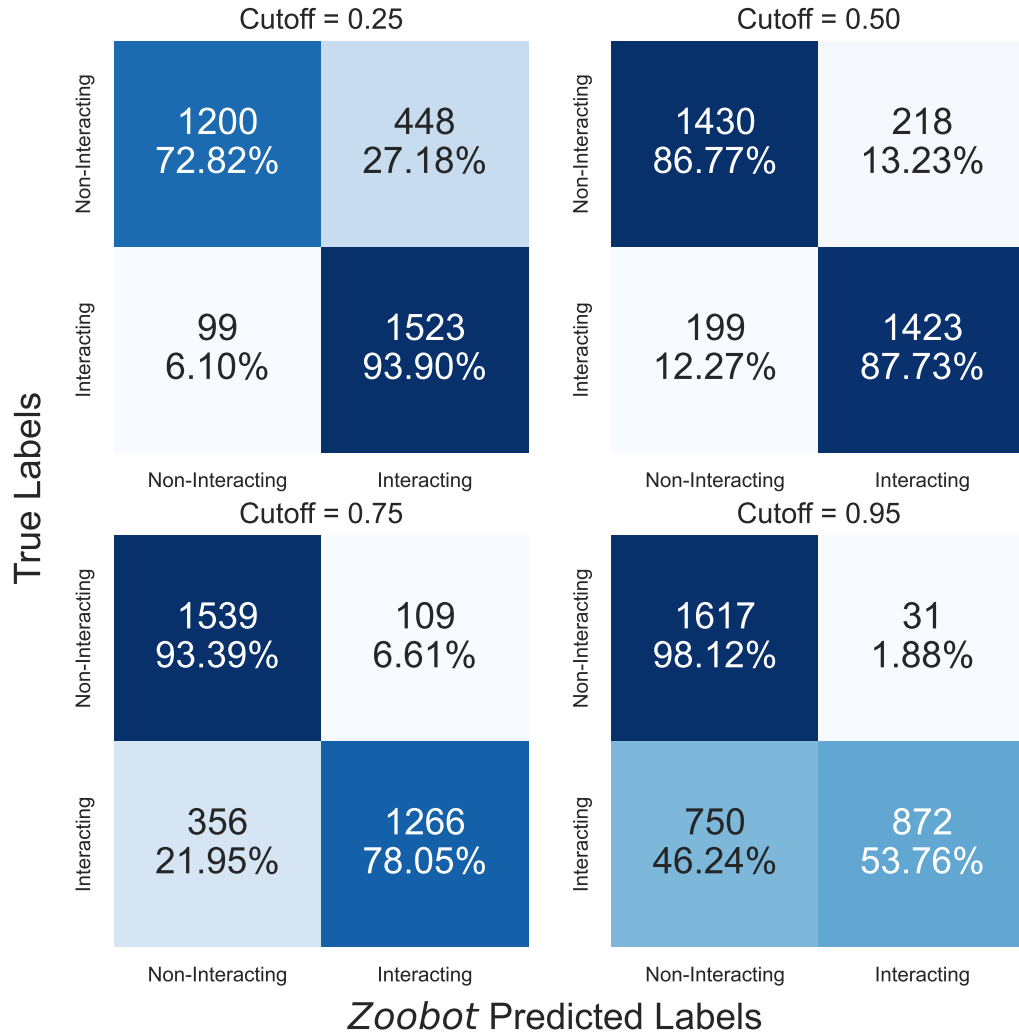
**Figure 2.4:** A measure of accuracy and purity against prediction score. The accuracy (in blue) is a direct measure of the number of sources *Zoobot* correctly predicted vs the total number of predictions made. The measure of purity (in orange) is the the number of predictions *Zoobot* correctly made vs the total number of predictions for an interacting galaxy. The cutoff score (in red) shows the point above which we would define an interacting galaxy and below which we would not. At this point, the accuracy appears lower due to *Zoobot* making many false negative predictions while successfully making true negative predictions. This is confirmed by the maximisation of purity. Due to the number of sources *Zoobot* is predicting over, the size of the catalogue will exceed any previous catalogues. Therefore, we use this very conservative cutoff to maximise purity over the completeness of our catalogue. These measures can also be shown with the F1 score. Figure A.2 shows this change with prediction cutoff in the Appendix.

Figure 2.5 also shows a measure of accuracy for our model at different cutoffs using confusion matrices. Importantly, it also shows how our model is getting labels wrong: either giving false positives (where a labelled non-interacting galaxy is predicted to be interacting) or false negatives (where a labelled interacting galaxy is predicted to be a non-interacting). The number of incorrect positive and negative predictions change based on the prediction cutoff, with a very low cutoff giving many false positives and a very high cutoff giving many false negatives. Figure 2.5 shows that with a cutoff of 0.50, we would return a high level of contamination in our final catalogue. Of the 1,622 galaxies predicted to be interacting, 218 would be non-interacting systems - approximately 13%. Our main aim in this work is to present a highly pure, large interacting galaxy catalogue that can be used for statistical exploration of interacting galaxy parameter space. Therefore, we use a very stringent cutoff of 0.95.

Using a cutoff of 0.95 reduces contamination significantly. Figure 2.5 shows the final contamination in our validation catalogue would be  $\approx 2\%$ , where Figure 2.4 shows that we are maximising the purity in our sample at the expense of accuracy. The aim of this work is not to create a general tool to be used by the community, but to find a large catalogue of interacting galaxies. As we are investigating 126 million sources, despite removing  $\approx 50\%$  of interacting galaxies from the final catalogue, we are certain that we can find a catalogue larger than previous works.

Using such a high cutoff also reduces any risk of any biases introduced by using a balanced training set. While using such a training set often increases the accuracy and speeds up training, it can bias the model toward one conclusion. In our case, the true rate of interacting galaxies will be much smaller than 50%. Therefore, our model will be biased to labelling a source as an interacting galaxy. This will be particularly true for edge cases, which could be ambiguous to even an expert classifier. By using such a high cutoff score, this bias will be mitigated by only labelling the most clearly interacting objects as interacting.





**Figure 2.5:** Confusion matrices of four different cutoffs of prediction score defining a binary classification of interacting galaxy or not. Confusion matrices break down our accuracy measurement into how *Zoobot* is misclassifying sources. At a cutoff of 0.50, the accuracy is highest at 88.2%. However, at this cutoff,  $\approx 10\%$  of our final catalogue would contain contamination. We elect to use the very stringent prediction cutoff of 0.95 for the rest of this work as it will return the lowest contamination.

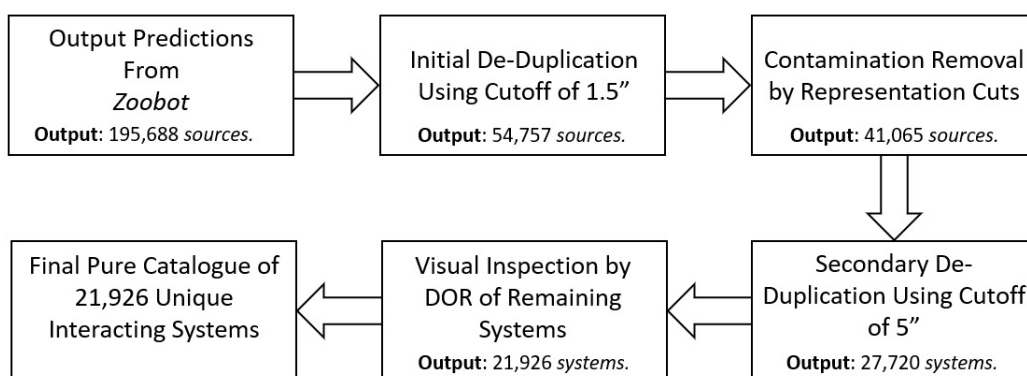


**Figure 2.6:** Flow diagram of our contamination and duplication removal process. De-duplication used agglomerative clustering based on sky separation. The first step of de-duplication uses a cutoff of  $1.5''$ . This significantly reduced duplication in the catalogue, as well as the size of the catalogue to 54,757 interacting galaxies. We then applied contamination removal to this de-duplicated catalogue. Upon visual inspection, a small number of duplicated systems still existed in the catalogue. To ensure a pure catalogue of unique systems, we applied a agglomerative clustering again with a cutoff of  $5''$ . This gave us a catalogue of 27,720 unique interacting systems. The final step to ensure purity was visual inspection by DOR, removing any remaining contamination. This gave the final pure catalogue of 21,926 unique interacting systems.

## 2.5.2 Duplication Removal

The fully trained `Zoobot` made predictions on  $\approx 126$  million extended sources from the HSC that had passed our creation criteria. Of these, 195,688 sources were given a score of 0.95 or greater,  $\approx 0.2\%$  of the total number of sources. Upon visually inspecting a subset of sources, it is clear that our `Zoobot` model had predicted for an interacting galaxy even if it was not the central (and, therefore, target) source in the image. This is due to the misalignment of sources from the centre in the training set as described in Section 2.4. `Zoobot` learned to classify an image as an interacting galaxy if it contained one, and not just if it was the central source. Therefore, many interacting systems were duplicated in our final catalogue, appearing in cutouts where the central source was not interacting.

Another source of further duplication was the HSC itself. In the HSC, many extended objects have multiple source IDs applied to them. This is due to bright clumps in extended sources being assigned a new ID, sources which had been found but did not exist in reality or background sources which existed in extended systems. We find that of the 195,688 Source IDs given a prediction score of 0.95 or greater, approximately 3.6 Source IDs were matched to a single real object. To refine the catalogue and remove the duplication we use spatial clustering of each source with agglomerative clustering (an introduction and description of hierarchical clustering, including agglomerative clustering, can be found in Nielsen, 2016).

Agglomerative clustering is a method of hierarchical clustering based on a distance metric between the sources. We set the maximum distance between points to define a cluster. i.e. any sources within a defined distance on the sky from each other will be merged under one source ID. This approach means we do not need any knowledge of how many clusters of sources exist in the dataset or the level of duplication within it, as would be the case in many other clustering approaches. We create distance matrices of the angular separation of every source using the `Astropy` Python package. These projected sky separations are then used as a euclidean distance in the clustering algorithm with an `EUCLIDEAN_LINKAGE`. The new ID of a cluster is the first source ID in the cluster.

Initially, we utilise a limiting sky separation of  $1.5''$  (corresponding to 0.03kpc to 65.01kpc from  $0.001 < z < 8$ ) to remove the duplication. This reduced the size of our potential catalogue to 54,757 interacting galaxy candidates. We then applied contamination removal as described in Section 2.5.3. Once contamination removal was completed, the catalogue size was 41,065 interacting galaxies. Visual inspection found further duplication, so our initial de-duplication had not been aggressive enough. To ensure the catalogue was of unique systems, we opted to use a final aggressive limiting sky separation of  $5''$  (corresponding to 0.10kpc to 216.70kpc from  $0.001 < z < 8$ ) completely removing the duplication in our catalogue. This aggressive de-duplication further reduced the size of our catalogue to 27,720 candidate interacting systems. However, we could be certain that each of these candidate systems was unique. Figure 2.6 shows a full breakdown of the steps in our de-duplication and contamination removal process.

### 2.5.3 Bad Predictions & Removal

After the initial step of de-duplication we begin removal of contamination from the catalogue. A major, and expected, source of contamination is by close pairs of galaxies. These are systems where chance alignment in the sky appears that galaxies are close together but are actually at different redshifts. Other sources of contamination include large central galaxies with satellite galaxies about them, star fields with extended sources in them and objects with strange morphologies that *Zoobot* predicted were tidal features.

Upon applying the clustering by sky projection of  $1.5''$ , the catalogue contained 54,757 candidate interacting galaxies. Our primary concern is contamination by close pairs. Creating catalogues of interacting galaxies with CNNs are notorious for suffering from this problem, where a significant number of candidates must be removed from otherwise large final catalogues (Bottrell et al., 2019; Pearson et al., 2022). The decisive way to remove this contamination is to compare redshift measurements of each galaxy in the candidate interacting system. However, this is impractical for our catalogue where the majority of candidates have no redshift measurements. To find close pairs, and remove them effectively,

we take advantage of the representations `Zoobot` learns of each image. As described previously, `Zoobot` was trained to answer every question in Galaxy Zoo: DECaLS simultaneously for every galaxy. It therefore learns a generaliseable representation of many kinds of galaxies. In this representation space, morphologically similar galaxies will exist close together in clusters while those that are dissimilar will be further apart. We extract the features `Zoobot` has learned of each candidate, and plot its representation.

We remove the classification head of `Zoobot` and directly output the final layer of the feature learning section of the model. This gives 1,280 features (the representations) for each of our 27,720 candidate systems. However, there will be much redundant information in this very high dimensional feature space. We compress this using incremental principal component analysis (PCA) (Ross et al., 2008). An excellent demonstration of using this approach can be found in Walmsley et al. (2022b). We reduce the dimensionality from 1,280 to 40 (as in Walmsley et al. (2022b)), and input the resultant components into the Auto-Encoder UMAP (McInnes et al., 2018). UMAP projects the 40 dimensional components of each candidate system onto a 2 dimensional manifold. The position of each galaxy on this manifold is directly linked to its visual morphology. Close pairs have similar visual features which will then appear as a cluster in our representation space.

Figure 2.7 shows the representation distribution of our 54,757 candidates after compression with UMAP. A random image in each bin has been selected to show the morphology of the objects within the bin. There are three clear gradients that exist in the representation distribution: one of source size, one of the source inclination and one of image contrast between the source and the background. The gradient of source size is clear from left to right. This is also true of contrast between the source and background. The gradient of source inclination is from top to bottom. The top shows very inclined sources, and even the diffraction spikes of stars, while along the bottom we find face on sources which take up a larger part of the cutout centre. At the very bottom of the figure (away from the main body) a cluster of very poorly contrasted sources with the background that are face on are found. The gradients of inclination and source size are expected while that of contrast is less so. This gradient is likely a result of how we created

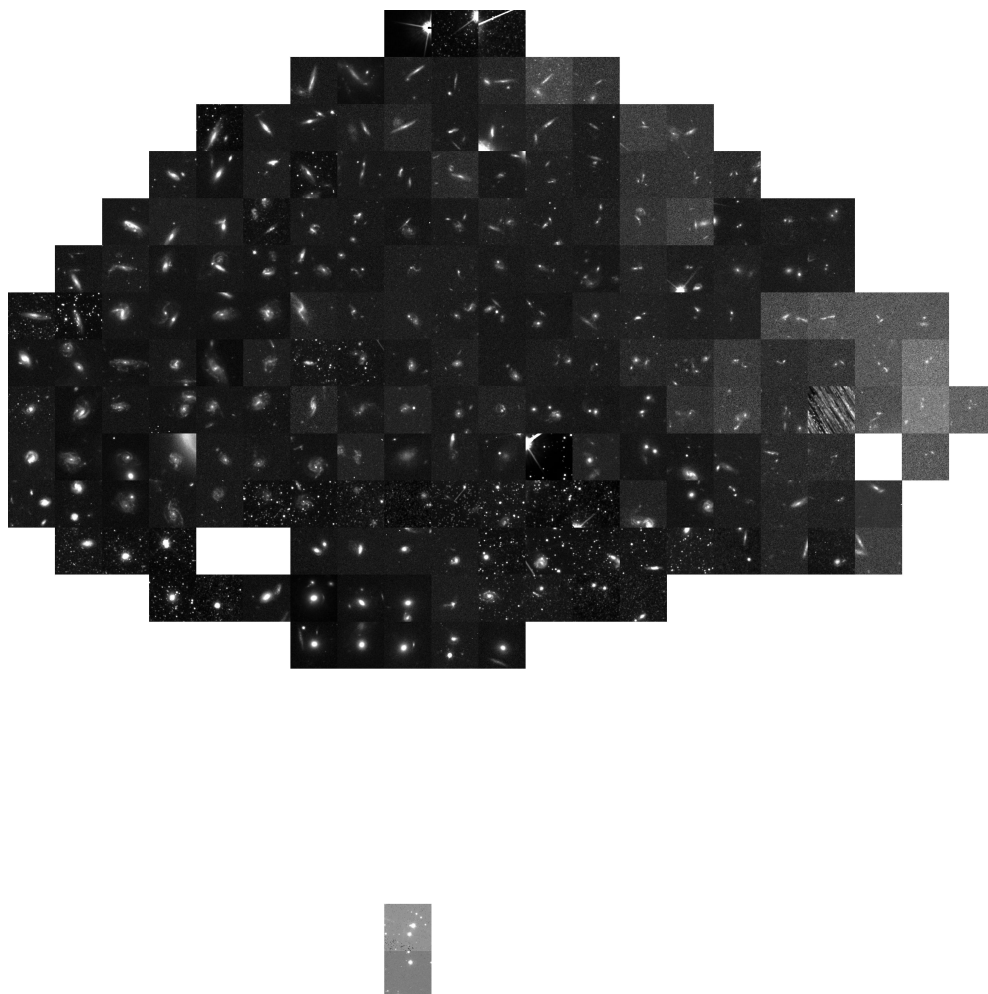


**Figure 2.7:** The representation distribution of 54,757 candidate interacting galaxies. This distribution is the compressed 2D representation of the 1,280 dimensional representation that Zoobot has learned of each image. Each image is a randomly selected one from sources within each bin in the distribution. The X and Y axis on this plot are the 2D mapping on the manifold given by UMAP for the 40 dimensional principal components of each source, and not physical parameters. Three gradients are clear in this distribution: first; from the left to right there is a distinct gradient in the contrast of the images. The images to the left are local galaxies with low redshift, while those on the right are dimmer sources at much higher redshift. This is an effect of how the images are created using a linear scaling function and a fixed contrast. The second feature, also from left to right, is a gradient of larger source size to smaller source size. This is a feature Zoobot has learned based on the redshift of the source as well. The third, from top to bottom, is a gradient of the inclination of the source. With the most inclined (and even diffraction spikes) of the sources appearing at the top, while at the bottom the sources are face on. Along the bottom of the representation plot, there are close paired sources as well as many star fields. Along the very top, there is contamination in the form of isolated stars in star fields. Thus, we make aggressive cuts along the top and bottom of our representation space to remove as much contamination in a general way. The full representation plot, with all sources and the cuts, is shown in Figure 2.8.

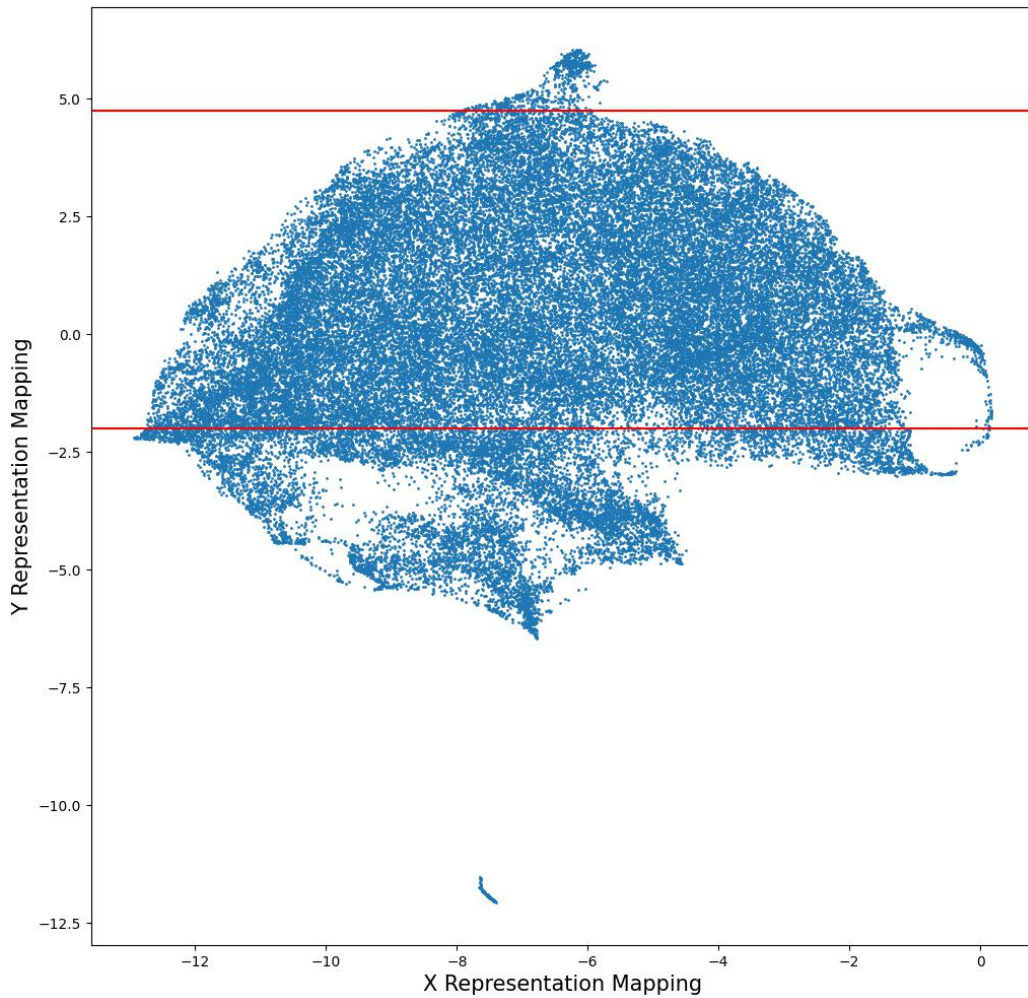


**Figure 2.8:** Scatter plot showing the precise distribution of each representation of sources in the remaining 54,757 sources. This is the unbinned version of Figure 2.7. The two red lines show the cutoffs utilised to remove the majority of close pairs by projection as well as the very obvious contamination of stars and stellar fields at the top of the representation distribution. The number of candidate interacting systems in the catalogue was reduced to 41,065 systems.

our images using a Linear Stretch with fixed contrast. The effect of this is that dimmer sources have brighter backgrounds, a particular issue at high redshift.

Figure 2.7 has many areas of similar morphology. On the left, we have isolated objects: disturbed spirals or large galaxies with tidal disturbance to them. Along the bottom, we see isolated bright objects with satellites about them. On the bottom right, we see our area of representation space dominated by close pairs. In the centre, we see the population of interacting galaxies that `Zoobot` was trained to find. The areas of representation space which are dominated by clear sources of contamination are cut. Figure 2.8 shows a scatter plot of the representation distribution and the cuts we make. They are made such that any source with a  $Y$  Mapping of  $-2 \leq Y \leq 4.75$  will be kept in the catalogue. The choice of these cuts has been made by eye, and then bootstrapping the remaining images to check contamination removed. After applying these cuts, we retain 41,065 systems in our catalogue.

We estimate  $\approx 25\%$  of sources in the greater than 0.95 prediction bin are close pairs. This may seem lower than previous works, but is due to our very conservative prediction cutoff. The general cuts to our population based on their position in representation space makes it very likely that we retain some close pairs in the catalogue, while also removing interacting galaxy systems.

As described in Section 2.5.2, we then apply a  $5''$  to the 41,065 remaining candidates, further reducing our catalogue to 27,720 systems. With such an aggressive sky projection cut, many individual interacting galaxies are now identified under the same ID as the secondary galaxy in the system. To remove remaining contamination in the catalogue, a final visual classification step was conducted. This visual inspection was conducted by DOR. Any systems removed at this stage were classified into three categories: interacting system, contamination and gems. The gems sub-category became necessary as many sources of contamination that were being removed were objects of other astrophysical interest, and is described in Section 2.6.2.



## 2.6 Results & Discussion

### 2.6.1 An Interacting Galaxy Catalogue

Upon de-duplication and contamination removal described in Sections 2.5.2 and 2.5.3, our final catalogue contains 21,926 interacting systems. Figure 2.9 shows a random sample of 50 of the systems from our catalogue. In these examples we can see highly distorted or currently interacting systems, precisely what we trained *Zoobot* to highly predict. Some cutouts are of the full interacting system, containing both the primary and secondary galaxies in the interaction. Some source cutouts only show one of the interacting galaxies, though these systems remain highly disturbed. Due to the constraints in our training set, so highly weighting disturbance or tidal features in our predictions, we are sampling interaction from all epochs except the approach to the initial pass. At this initial stage, there will be no tidal features formed or disturbance in the disks as the two galaxies approach each other. Separating them from close pairs would be difficult without kinematic or redshift information, not available for the majority of these sources.

We investigate which of the systems in our catalogue have previous references in the astrophysical literature. To search the literature, we use the *AstroQuery* Python package with a coordinates based search of cutoff radius 5". We search the astronomical databases Simbad (Wenger et al., 2000), the NASA Extragalactic Database (NED; Helou et al., 1991) and ViZieR (Ochsenbein et al., 2000) for references to our interacting systems. These return either a list of references, or an empty list showing no references associated with the system. We find that 7,522 of our systems have at least 1 reference associated with them, while 14,404 do not. A flag exists in the catalogue data release which shows whether a system has references associated with it or it could be considered a ‘new’ system. We, however, do not claim that these systems are discovered by ourselves. These systems have always existed in the backgrounds of large surveys or observations and been discovered by others, it is only with ESA Datalabs that we can apply a methodology such as in this work to extract those systems from these observations. We also do not claim that these unreferenced systems are particularly interesting or phenomenal. It is most likely that these systems are the very faint

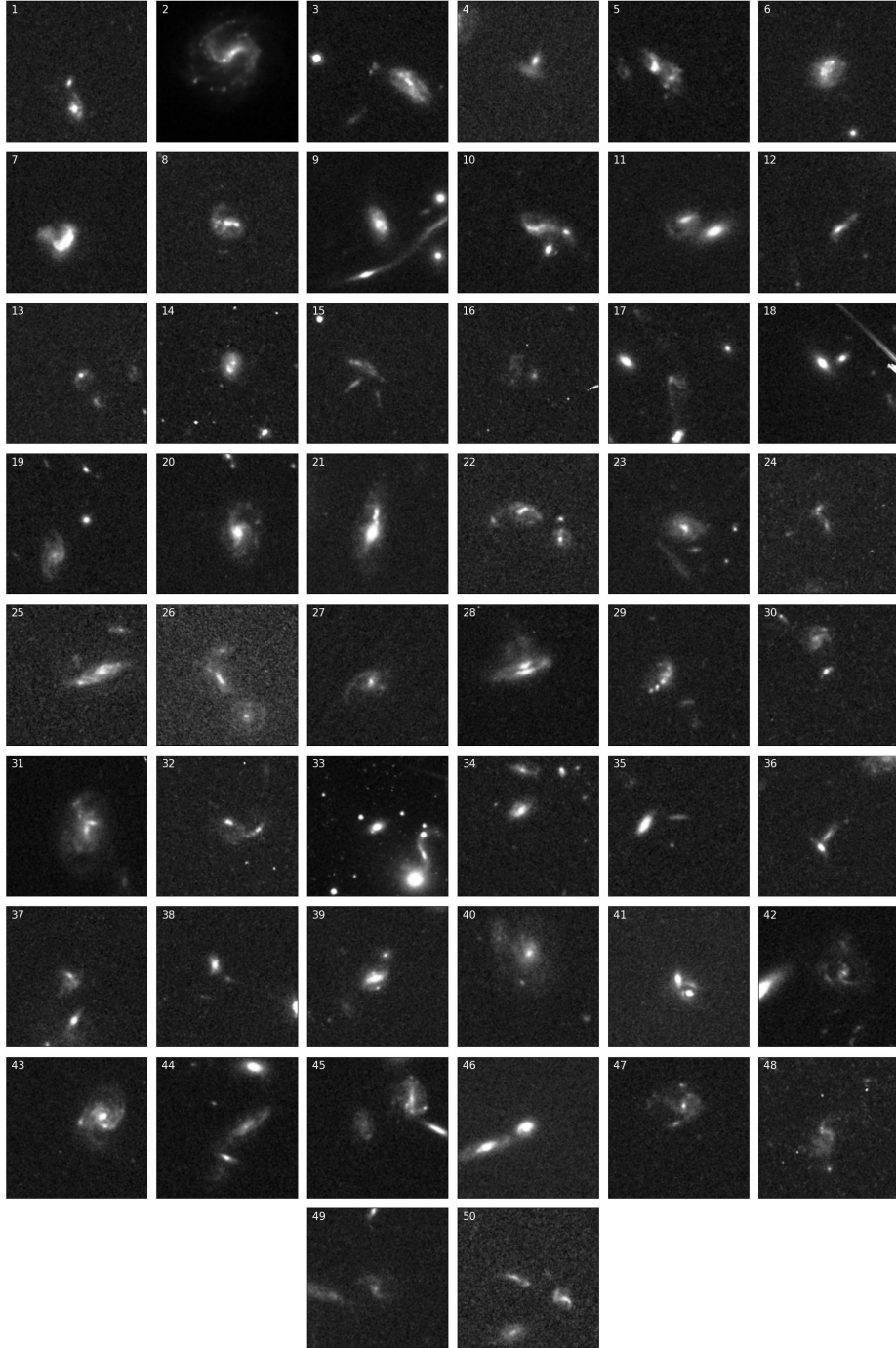


**Figure 2.9:** An example of 50 of the final interacting systems found with Zoobot. These were selected randomly from the de-duplicated and de-contaminated 21,926 sources. Each of these examples have extended tidal features and distortion. Not all of the final interacting systems have two galaxies within them (for example, image 2), but are clearly very disturbed by a tidal event. These were kept in as they would form a large part of the interacting galaxy population and would be flagged as disturbed or interacting in Galaxy Zoo. Each of these images is a 1-colour image using the  $F814W$  *HST* filter.

background galaxies in surveys or observations whose main objective was something other than finding interacting galaxies. This will be further discussed in Section 2.6.3.

Figure 2.10 shows the distribution of our catalogue in the sky. The *HST* is able to observe the majority so the catalogue sources are scattered throughout it. We find that the sources cluster in different parts of the sky which correspond to major surveys conducted using the *HST* involving ACS and the *F814W* filter. We also mark the centres of the seven surveys which correspond to the major clustering of interacting systems in the sky. These were the COSMOS, the GOODS North, GOODS South, PHAT, CANDELS, AEGIS and Spitzer Space Telescope FLSv Region (Morganti et al., 2004) surveys.

The full catalogue and data product are found on Zenodo at the following DOI where it is freely accessible to the community: doi:10.5281/zenodo.7684876. Table 2.1 shows an example of the data and format of the 50 sources shown in Figure 2.9. We also bootstrap the final catalogue as an estimate of contamination remaining. As described in Section 2.5.3, the final step of contamination removal was visual inspection by DOR of the 27,720 candidate interacting systems to remove the remaining 5,794 contaminants from the final catalogue. Visual inspection by a single expert at this scale is not perfect. We extract random sources from the catalogue in batches of 500 and manually re-classify them again. This bootstrapping reveals that  $\approx 3\%$  of our interacting system in the final catalogue remains contamination.

## 2.6.2 The Gems

By conducting a visual inspection of the 27,720 candidate systems we were able to directly identify many other objects of astrophysical interest. As *Zoobot* was trained to highly predict objects with irregular morphologies, we also find many other astrophysical objects with strange morphologies which may be of interest to the community. We call these sources of contamination gems. We make 16 sub-categories of these: active galactic nuclei (AGN)/quasars, submillimetre galaxies, galaxy groups, high redshift galaxies, jellyfish galaxies, galaxy jets, gravitational lenses/lensing galaxies, Lyman- $\alpha$  Emitters, overlapping galaxies, edge on proto-

## 2.6 Results & Discussion

Image No.	SourceID	RA (deg)	Dec (deg)	Interaction Prediction	References	Status
1	4001014298177	261.292845	37.162387	0.983999	No entry	Unreferenced
2	4001444190958	183.527536	33.183451	0.998016	[1994PASP..106..646K]	Referenced
3	4000809226818	93.960150	-57.813401	0.982266	[2019ApJ...878...66C]	Referenced
4	4553390202	73.581297	2.903528	0.968280	No entry	Unreferenced
5	4000907600174	259.037474	59.657617	0.999978	No entry	Unreferenced
6	4575187799	150.001883	2.731942	0.974649	[2007ApJS..172...99C]	Referenced
7	4000717342023	149.527791	2.126945	0.993912	[2007ApJS..172...99C]	Referenced
8	4001174802281	28.593114	-59.643515	0.982890	No entry	Unreferenced
9	4182689774	186.709991	21.835419	0.973232	[2016ApJS..224....1R, 2011ApJS..193...8B]	Referenced
10	4000958398690	186.719496	23.961225	0.999288	No entry	Unreferenced
11	4266881925	344.730228	-34.799824	1.000000	No entry	Unreferenced
12	4001084105393	150.128198	2.623949	0.982739	[2018ApJ...858...77H, 2007ApJS..172...99C]	Referenced
13	4000961670486	345.337556	-38.985521	0.954961	No entry	Unreferenced
14	4000719687395	338.173538	31.189718	0.974724	No entry	Unreferenced
15	4001435343326	331.771500	-27.826175	0.986885	No entry	Unreferenced
16	4001268932937	8.856781	-20.271978	0.986329	No entry	Unreferenced
17	4651336656	149.836709	2.141702	0.984389	[2007ApJS..172...99C]	Referenced
18	4000877021787	116.211231	39.462563	0.979178	No entry	Unreferenced
19	4000878525229	149.834893	2.516816	0.963694	[2007ApJS..172...99C, 2009ApJS..184..218L]	Referenced
20	6000290755870	186.774907	23.866311	0.981961	No entry	Unreferenced
21	4000806637434	210.253419	2.854869	0.960790	No entry	Unreferenced
22	4001215753971	135.898809	50.487130	0.998386	No entry	Unreferenced
23	4000813961830	163.678042	-12.776815	0.958405	[2005ApJ...630..206F]	Referenced
24	4001200639012	54.037618	-45.170026	0.991404	No entry	Unreferenced
25	4000921402261	150.417634	2.313781	0.990775	[2018ApJ...858...77H, 2012ApJ...753..121K]	Referenced
26	4001224732336	337.217339	-58.444885	0.955972	No entry	Unreferenced
27	4000781402752	216.968619	34.575819	0.974076	No entry	Unreferenced
28	4001283017901	120.202582	36.058927	0.994169	[2016ApJS..224....1R]	Referenced
29	4000833486119	116.260049	39.457642	0.971092	No entry	Unreferenced
30	4000949659908	146.342493	68.730869	0.961113	No entry	Unreferenced
31	4000982920478	53.084832	-27.765379	0.983472	[2010A&A...512A..12B]	Referenced
32	4001189505548	192.492491	2.436292	0.992574	No entry	Unreferenced
33	4001060882070	89.700725	-73.049783	0.962839	No entry	Unreferenced
34	4000889750512	151.176470	41.214096	0.962205	No entry	Unreferenced
35	6000322363510	53.149367	-27.823945	0.963889	[2016ApJ...830...51S]	Referenced
36	4000722901091	28.257843	-13.928090	0.982778	No entry	Unreferenced
37	6000198293960	264.488431	60.101798	0.986865	No entry	Unreferenced
38	4001095660911	258.587670	59.970358	0.955193	No entry	Unreferenced
39	4000972775076	330.960020	18.796346	0.989131	No entry	Unreferenced
40	4001132466571	126.545810	26.456196	0.997077	No entry	Unreferenced
41	4000933395648	312.810365	2.288410	0.976252	No entry	Unreferenced
42	4000932940918	218.066960	32.997228	0.990737	No entry	Unreferenced
43	4001048433104	93.880689	-57.754746	0.957755	No entry	Unreferenced
44	4001039919651	53.111470	-27.673717	0.994424	[2011ApJ...743..146C]	Referenced
45	4001282607544	333.765783	-14.006097	0.999520	No entry	Unreferenced
46	4000922341052	260.723839	58.849293	0.995477	No entry	Unreferenced
47	4000731518210	194.869144	14.146223	0.994651	No entry	Unreferenced
48	4001082523786	311.703084	-12.869002	0.976454	No entry	Unreferenced
49	4000767041112	149.784518	2.172233	0.991335	[2007ApJS..172...99C]	Referenced
50	4001024667142	150.661685	1.718587	0.967865	[2007ApJS..172...99C]	Referenced

**Table 2.1:** An example of the format of the final catalogue for the 50 example images presented in this paper.

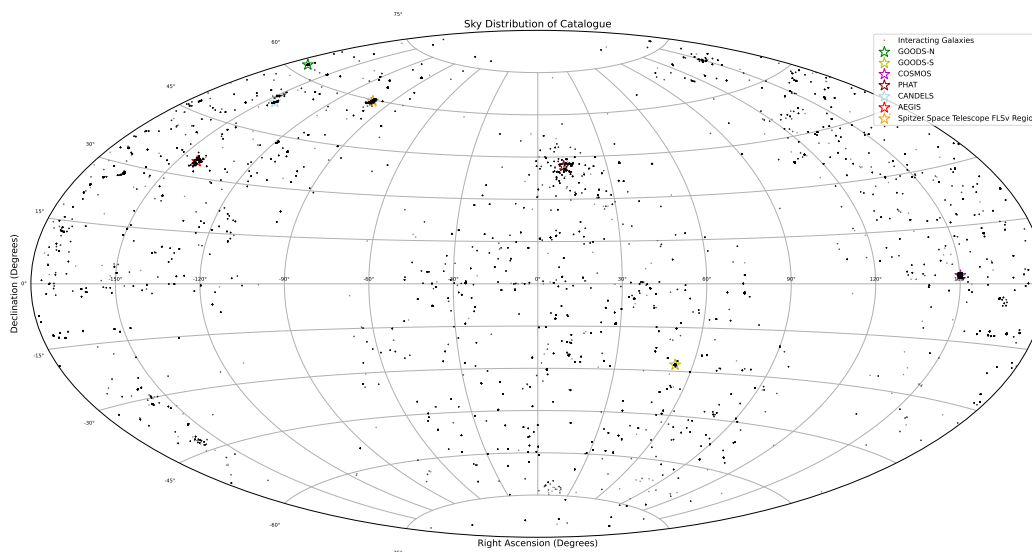


**Figure 2.10:** Sky Distribution of our catalogue, with marked positions of well known deep surveys conducted by *HST*. *HST* is able to observe almost the entire sky and therefore the interacting galaxies are scattered throughout. Large clusters of sources are found in the locations of surveys. This shows that often our sources are in the background of larger surveys and observations.

planetary disks, radio halos, ringed galaxies, supernova remnants, transitional young stellar objects, young stellar clusters and unknown objects.

Each sub-category has been defined by checking Simbad and VizieR for references within a  $5''$  radius of each source and using the astrophysical literature for a definition of the source. DOR classified any unreferenced objects by morphological similarity to other defined objects. The platforms ESASky<sup>1</sup>(Merín et al., 2017), NASA Extragalactic Database (NED) and the Sloan Digital Sky Survey were also used to investigate any unreferenced objects. ESASky was of paramount importance to these classifications. This platform allows us to easily access observations across a range of observatories across a range of wavelengths. Most importantly, it allows us to easily find the source using the *HST F814W* observations, and then switch seamlessly to the same coordinates in a different observatory.

Switching observatories allowed us to classify objects in more wavelengths. For example, we confirmed the unreferenced AGN/quasar candidates by investi-

<sup>1</sup>ESASky: <https://sky.esa.int/>

gating the source in Chandra or XMM-Newton for hard or soft X-Ray emission. We would find the source in the *F814W* observation, and then switch the ESASky viewer to XMM or Chandra. This would reveal a high signal in X-Ray at the source, and allow us to make our prediction. The same was done for the submillimetre candidates. They were located in *F814W* observation, and then swapped to Herschel or Planck measurements. If there was a positive signal in their positions, they were classified as such. Further work will be needed to confirm these classification.

The final category which required further inspection was that of the unknown objects. These are objects which have unusual morphology which mark them out from the rest of the sample, but no references associated with them in Simbad or VizieR. They also did not appear in NED, meaning they could not be confirmed to be galaxies. These objects are shown in appendix A.3.

Table 2.2 shows a breakdown of the total number of objects found and the number of which were referenced or unreferenced. We have released catalogues of each sub-category in the same format as that of the main catalogue without the interaction prediction column. Each of these catalogues can also be found at the same Zenodo link.

### 2.6.3 Source Redshifts and Photometry

We investigate the redshift distribution and photometric properties of sources in our catalogue. We extract all sources with pre-existing data, querying Simbad, VizieR, the HSC via the Milky Way Archive for Space Telescopes (MAST) and NED. Our queries use a  $5''$  search radius within the Python package `AstroQuery`. The existing data from each of these databases has undergone heterogeneous selection and analysis procedures by the various studies we extract them from; we do not try to reconcile these here. Rather than a detailed physical analysis of these sources, our priority in this subsection is to highlight how to explore and use this catalogue, as well as any difficulties which may arise.

Of the 21,926 interacting systems in our high-confidence sample, 3,037 of the 7,522 referenced sources have a measured redshift. Figure 2.11 shows the redshift distribution of this subset of our catalogue. 42.5% of the sources have a redshift  $z \leq 0.5$ , 45.1% have a redshift  $0.5 < z < 1$  and 12.4% have a redshift  $z > 1$ . In

Category	Total Found	Referenced	Unreferenced
AGN/Quasars	35	21	14
Submillimetre Galaxies	11	8	3
Galaxy Groups	6	6	0
High Redshift Galaxies	10	7	3
Jellyfish Galaxies	18	5	13
Galaxy Jets	25	10	15
Gravitational Lenses/Lensing Galaxies	189	64	125
Lyman-Alpha Emitters	1	1	0
Overlapping Galaxies	221	92	129
Edge-on Protoplanetary Disks	9	2	7
Radio Halos	1	1	0
Ringed Galaxies	6	1	5
Supernova Remnants	4	3	1
Transitional Young Stellar Objects	2	1	1
Unknown Objects	6	0	6
Young Stellar Clusters	2	1	1

**Table 2.2:** A breakdown of gems found in the visual inspection stage of contamination. Each gem category has been classified based on the references associated with each object.

fact, a small fraction (15) of these sources are found to be at  $z \geq 5$ . Upon investigation of these sources two of their redshifts have been measured photometrically, while the remaining 13 sources did not have the method of measurement recorded in the archive. Therefore, this finding of very high redshift interacting galaxies are uncertain at best.

It is important to note that the small sample with redshift information is affected by the selection biases of the combined studies publishing these values, and therefore the distribution may not be representative of the full sample. In addition, above redshift  $z = 1$  the  $F814W$  filter begins to only capture rest-frame UV flux, and therefore  $z > 1$  galaxies with low star formation rates are more likely to fall below the flux limits of our detection images. Sampling only the rest-frame UV also changes a galaxy’s observed brightness and morphology (e.g., Ferreira et al., 2022) – the latter being how Zoobot identifies interacting galaxies. For example, tidal features whose initial starburst has faded may be undetected; conversely, a single galaxy with irregular star-forming clumps may appear to be multiple interacting galaxies, which we noted as a particular source

Filter (s)	Sources Covered
F814W	100%
F606W + F814W	45.0%
F475W + F814W	11.0%
F475W + F606W + F814W	6.1%

**Table 2.3:** Percent of sources in the final catalogue which have observations in the relevant *Hubble* filter.

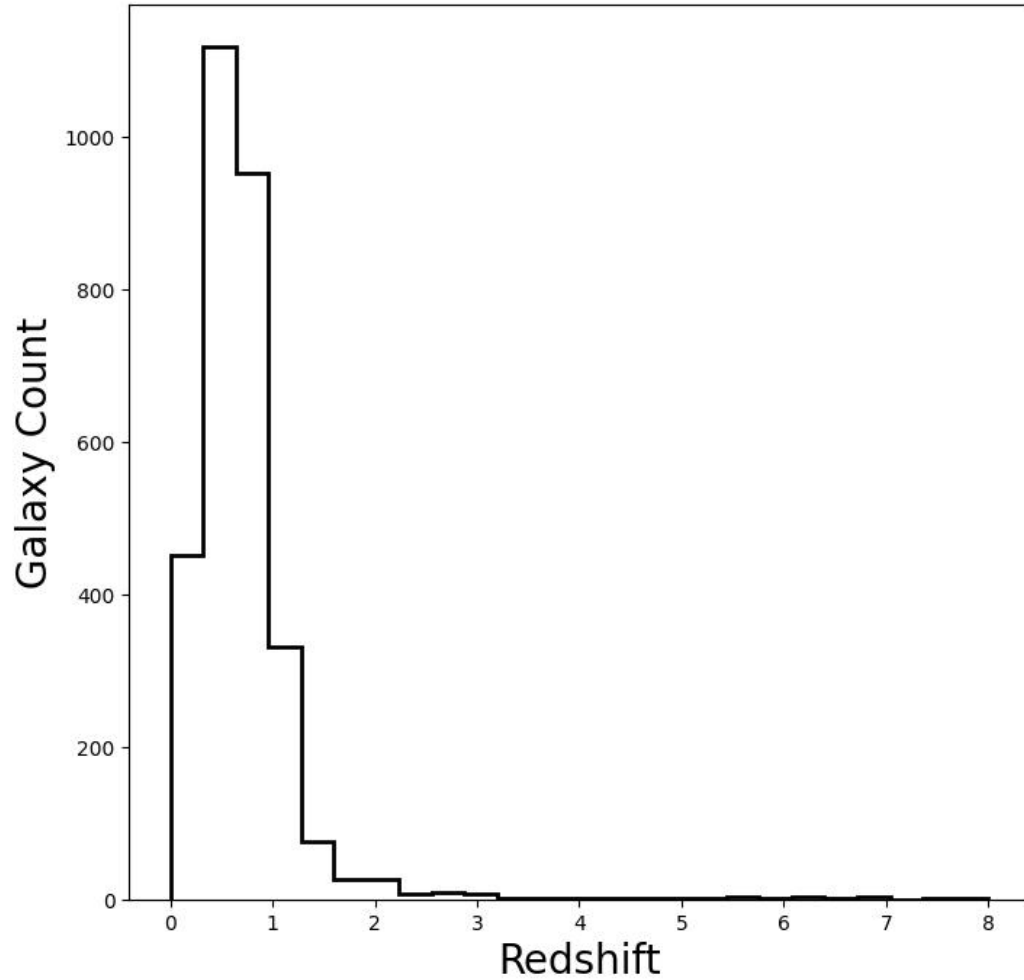
of contamination during the visual inspection stage. High-redshift interacting galaxies that are detected initially by Zoobot but have unusual morphologies compared to  $z \sim 1$  sources may be removed during prediction (Section 2.3), given that finetuning is based primarily on the  $z \lesssim 1$  imagery of Galaxy Zoo: *Hubble*. Therefore, the currently measured redshift distribution in Figure 2.11 is likely due to some combination of selection bias and training bias.

Figure 2.12 shows the basic parameter space sampled by the sub-sample of the catalogue with existing photometry and redshifts. We show the distributions of redshift with the measured apparent  $F814W$  magnitude and the calculated absolute  $F814W$  magnitude. The faintest objects are, as expected, observed at approximately the limiting magnitude of the deepest observations in our catalogue. Other observations have brighter limits; those wishing to select a uniform or volume-limited sample from our catalogue must consider the variable flux limits across the sample.

We finally focus on sources from our high-confidence sample that have multi-band photometry, focusing on commonly-observed filters. By construction, 100% of the sample has  $F814W$  measurements, with 45% of the catalogue having  $F606W$  and only 11% having measured fluxes in  $F475W$ . Table 2.3 summarizes the filter coverage of our catalogue. 6.1% (1336 sources) have complete 3-band photometric information in the HSC. We use these to create examples of colour images from the catalogue (using the algorithm of Lupton et al., 2004). We used a scaling factor  $Q = 2$  and  $\alpha = 0.75$ , with  $(F814W, F606W, F475W)$  as RGB channels and multiplicative factors of (1.25, 0.95, 2). The resultant images are shown in Appendix A.2.

We extract the measured magnitudes of the  $F606W$  and  $F814W$  filters, giving us two-band photometry for 9,876 sources. Cross referencing with each source





**Figure 2.11:** The redshift distribution of a subsample of our catalogue. Of the 7,583 referenced systems, 3,037 of them had redshift measurements in the NED, MAST or Simbad. This redshift distribution shows that our model confidently predicted interacting systems primarily for  $z < 1$  systems. This was anticipated, as the model was primarily trained on systems at these redshifts. There are fifteen sources with a reported  $z > 5$ .

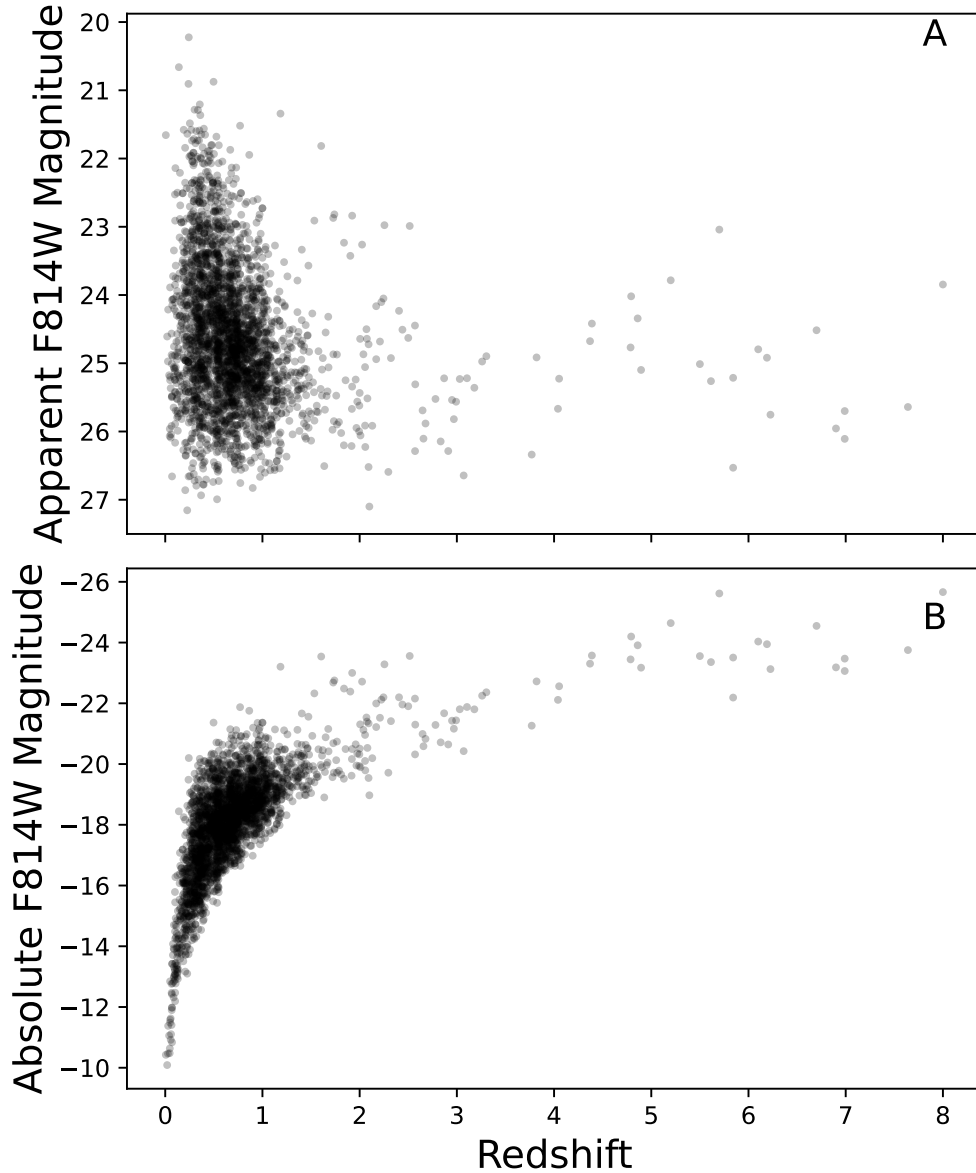


**Figure 2.12:** The distribution of redshift with magnitude for all sources with available data. This shows the parameter space we are sampling in this catalogue. Panel A shows that the majority of our sources are dim, background sources at low redshift. Panel B shows the faintest objects we find are at the limiting magnitudes of the different surveys this data is from. While we find many galaxies at high redshift in this sample, these are measured only with photometric redshifts. Therefore, we would be hesitant to claim finding galaxies at such high redshift values.

that had a redshift yields 2,993 sources from our catalogue. We calculate the colour of each source and plot it against the absolute magnitude in the  $F814W$  filter. Figure 2.13 shows the resulting colour-magnitude distribution in Panel A. The resultant distribution is very hard to interpret due to the high scatter of the sources. We extrapolate from this panel that there is little contamination from sources other than galaxies. If levels of contamination were high we would expect a second locus of sources with a very different colour-magnitude distribution.

Plotting the colour-magnitude distribution in this way captures a wide range of rest-frame wavelengths in the observed filters, which is the primary reason that panel A of Figure 2.13 is hard to interpret. In this first-look study, we do not have full spectral energy distributions (SEDs) of most sources, so K-correction of individual colours within this sample would involve assuming a template SED for each galaxy. Given that a high fraction of galaxies in our sample of mergers may deviate from standard SED templates, we wish to avoid this method. Instead, we choose redshift ranges within which to examine subsamples, such that the observed  $F606W$  and  $F814W$  bands cover consistent rest-frame colours within that subsample. Figure 2.13B shows only sources with  $z < 0.18$ , within which the observed filters can be taken to be approximately rest-frame filters, which we define as at least 50% of the flux captured in the observed band being emitted at rest-frame wavelengths covered by that band. At  $0.24 < z < 0.56$ , the observed  $F606W$  filter captures at least 50% rest-frame  $F475W$  flux, and the observed  $F814W$  filter captures at least 50% rest-frame  $F606W$  flux, so Figure 2.13C is approximately a rest-frame  $F475W - F606W$  vs  $F606W$  plot. At  $0.62 < z < 1$ , Figure 2.13D is approximately a rest-frame NUV-Blue plot ( $F336W - F475W$  vs  $F475W$ ).

The galaxies in Panel B are observed in approximately the rest frame  $F606W$  and  $F814W$  filters. Nearly all are blue systems (by general definitions at various redshifts, *e.g.*, Kauffmann et al., 2003; Whitaker et al., 2012; Schawinski et al., 2014). This is expected for interacting systems with enough gas to fuel a starburst. The lack of many red systems is due to few gas-poor (“dry”) interactions in the (relatively) local volume (López-Sanjuan et al., 2009). In Figure 2.13C, the  $F606W$  and  $F814W$  filters are still detecting rest-frame optical ( $F475W$  and  $F606W$ ) emission, and we find a much broader population. There are both blue

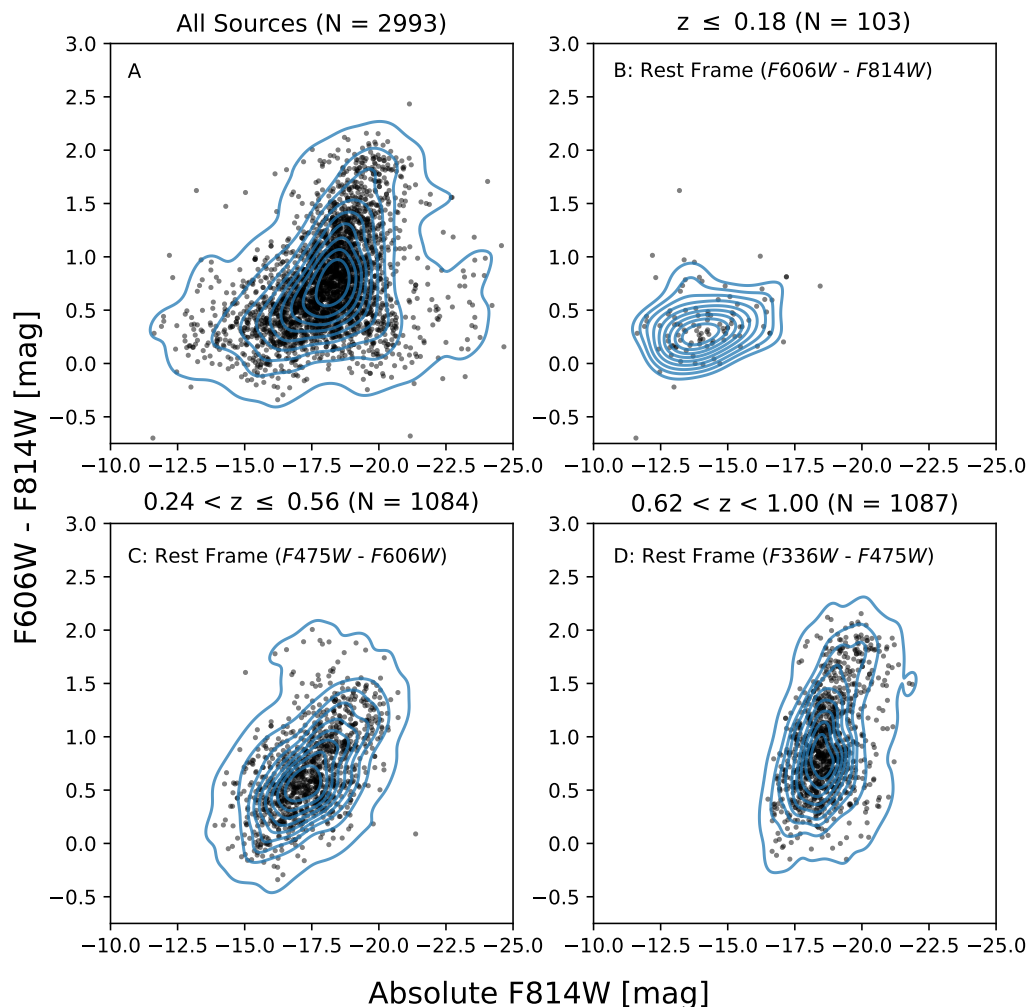


**Figure 2.13:** The colour-magnitude distribution of sources with a redshift measurement associated. Panel A shows the distribution of all galaxies, without controlling for redshift or dust extinction. The remaining panels then split these sources into distinct redshift bins where the  $F606W$  and  $F814W$  filters are observing in different rest frames. Panel B shows the colour-magnitude distribution in the local Universe, where the rest frame observations are  $F606W$  and  $F814W$  flux. This bin reveals a blue population. Panel C shows the redshift bin where 50% - 100% of observed  $F606W$  and  $F814W$  flux is rest frame  $F475W$  and  $F606W$  flux. This bin reveals a larger distribution of interacting galaxies, with a dominating population of blue systems and a minor population of red systems. Panel D shows the redshift bin where 50% to 100% of observed  $F606W$  and  $F814W$  flux is rest frame  $F336W$  and  $F475W$  flux. These filter bands are very sensitive to star formation, and reveal a broad distribution in colour of red and blue systems.

and red interacting systems, with the redder mergers occurring in more luminous (likely higher mass) systems, broadly consistent with expectations (van Dokkum, 2005; Lotz et al., 2008b). The rest-frame filters approximately captured in Panel D (*F336W* and *F475W*) sample emission across the 4000 Å break. Sensitivity to NUV means this panel effectively splits systems according to very recent star formation history (Schawinski et al., 2014; Smethurst et al., 2015). There is a significant spread in colour, with equivalent red and blue systems. We, therefore, find many young blue systems undergoing star formation and bright brighter, elliptical, massive systems also undergoing interaction in this bin.

This initial examination of the subsample of systems with easily retrievable redshifts has revealed that the interacting galaxies in the sample broadly agree with previous studies of colours in merging systems. This demonstrates the underlying promise of the catalogue. A detailed study is beyond the scope of this work, but there is considerable potential for new astrophysical insights using this high-confidence catalogue with nearly an order of magnitude more sources than those previously published.

## 2.7 Conclusion

We present a large, pure catalogue of 21,926 interacting galaxy systems found from the *Hubble* Source Catalogue. This catalogue is a factor of six larger than previous works. Each interacting system was found using the European Space Agency’s new platform ESA Datalabs, which allowed us to directly apply an advanced CNN - *Zoobot* - to the entire *Hubble* science archive. This corresponds to predicting over 126 million sources. The compiled catalogue has a contamination rate of  $\approx 3\%$  as found by bootstrapping. Table 2.1 shows an example of 50 entries in our new catalogue, Figure 2.9 showing the corresponding images. The new catalogue and all corresponding images can be downloaded from Zenodo: doi:10.5281/zenodo.7684876.

Each of our interacting galaxies were given a prediction score  $\geq 0.95$  by *Zoobot*, with such a conservative score chosen to limit contamination and maintain purity in the catalogue. Contamination was removed by applying cuts in representation space (shown by Figure 2.8) and visual inspection. Upon visual inspection, many

contaminating images were found to be objects of other astrophysical interest. These have been compiled into separate catalogues, and Table 2.2 shows a breakdown of the objects found. These sub-catalogues have been released alongside our interacting galaxy catalogue. With the priority of purity in this catalogue creation, we will aim in future work to use it in the statistical analysis of interacting galaxies and begin linking the underlying parameters of interaction to the complex physical processes that occur in them. A secondary purpose of this catalogue is to serve as a training set for future models which may wish to search for interacting or merging galaxies.

With the use of ESA Datalabs, this project was conducted quickly. The entire process, from creating the source cutouts, to training Zoobot, to making predictions on 126 million sources took three months to complete. Using conventional methods, such as **AstroQuery** or TAP services, downloading the data would have likely taken on this timescale. By bringing the user to the data, rather than vice versa, catalogues of a similar size - and many times larger than previous catalogues - of many different objects can be created quickly.

None of the the interacting systems in this work are ‘new’; every one of them exists in the background of large scale *HST* surveys and observations since their release. However, the method to directly search for them has been impractical until the release ESA Datalabs. By directly applying machine learning to existing astrophysical data repositories, a new method to creating significantly larger catalogues has been achieved.

This shows the importance of archival work, and the power that ESA Datalabs will bring to the field of astronomy. ESA Datalabs is expected to be released in Q4 2024 and with it, the ability for large scale exploration of archival data. It will be released with introductory tutorials, step-by-step guides and different Python environments for ease of use for different telescopes and instruments the ESA is involved in. It will have a full cluster of GPUs at its disposal and a storage capability in the range of hundreds of Terabytes. In future, this entire project - from training set creation to predictions - could be conducted on ESA Datalabs.

Such a setup as ESA Datalabs also allows the creation of large observational catalogues, comparable to that we create from cosmological simulations. This is incredibly important to further constraining already existing results. In the

current period of astronomy where large survey instruments are awaiting first light, or the beginning of future telescopes is uncertain, the ability to get ever more information out of the archives is paramount.

# Chapter 3

## Timescales for the Effects of Interactions on Galaxy Properties and SMBH Growth

### 3.1 Introduction

To fully map out the effect of galaxy interaction, we must understand its impact through various merger histories and across the full dynamical timescale of the interaction. The dynamical timescale is the full time of the interaction, from the two galaxies approaching each other to flying by and escaping or merging. We cannot observe a full, continuous interaction and have to rely on many observations to provide snapshots of the dynamical timescale we can piece together. This, however, makes it difficult to conclusively link the dynamical timescale to physical processes. Often, observational samples are too small to be fully representative or deep studies of individual systems are required to identify the dynamical timescale (Barton et al., 2000; Lambas et al., 2012; Wild et al., 2014). We gain insights from works focused on simulations, where the dynamical timescale can be directly recorded. They find sudden increases in star formation occurs at the mid-point of the dynamical timescale, as the two systems flyby (Cox et al.,



2008; Rodríguez Montero et al., 2019; Moreno et al., 2021). However, confirming this observationally remains elusive (Ren et al., 2023). Observational confirmation is also difficult with nuclear activation and quenching of interacting systems (Ellison et al., 2011; Goulding et al., 2018; Steffen et al., 2023).

While we cannot directly measure the full dynamical timescale for individual systems, we can create large samples of interacting galaxies contain systems spanning the full dynamical history. Attempts to create such a sample have been either by machine learning classification (Pearson et al., 2019a; Suelves et al., 2023), visual classification by citizen scientists (Darg et al., 2010a) or by photometric parameterisation (Lotz et al., 2004; Nevin et al., 2023). However, as stated previously, each sample has always been plagued by contamination and a loss of statistical significance when broken down into stages.

An alternate approach to directly measuring the dynamical timescale of an interaction has been to infer it from the projected separation between the two systems. Early works showed that there was significant star formation enhancement (SFE) in galaxy pairs with small separations (Lambas et al., 2003; Li et al., 2008a; Ellison et al., 2008; Shah et al., 2022). A connection was also found between the projected separation in galaxy pairs and the AGN fraction where, once again, the AGN fraction appears to increase with decreasing projected separation (Rogers et al., 2009; Ellison et al., 2011; Gordon et al., 2017; Silva et al., 2021). However, using projected separation as a proxy for the stage in dynamical time of an interacting history overlooks which part of the dynamical history the interaction is. For instance, if a galaxy pair is found to have small projected separation, without visually confirming the morphology, it is difficult to ascertain if the galaxies are just approaching each other or have just passed each other. Extended morphological tracers can help break this degeneracy, which is critical to our understanding of the effects of interaction.

In this Chapter, we split our large sample of interacting galaxies found in Chapter 2 into four specific stages based on their morphology. Each stage is designed to capture different parts of the dynamical time of an interaction. The stages range from galaxies being close pairs, to overlapping and disturbed, to disturbed and distinct to finally coalescing. This follows the classification methods

of developing algorithms for staging of interaction (Bottrell et al., 2019; Chang et al., 2022).

We focus here on the subset of our sample in the Cosmic Evolutionary Survey (COSMOS) survey<sup>1</sup>. This provides us with ancillary data which contains many galactic parameters of interest and we explore how they evolve with our defined stages of interaction. We primarily focus on the evolution of the stellar masses, star formation rates and AGN classification from various COSMOS catalogues. We use the photometric redshifts available from COSMOS to confirm a set of interacting galaxies and close pairs to draw on trends with projected separation.

This Chapter is laid out as follows. In Section 3.2 we briefly summarise the COSMOS catalogue, and describe the process of catalogue matching especially focused on accurate de-duplication and cross-matching. Section 3.3 describes the methods by which we split the interacting systems into stages, and how we identify the secondary galaxies in each pair. In Sections 3.4 and 3.5 we show our results of star formation and active galactic nuclei evolution with interaction stage and present an initial discussion. These are followed in Section 3.6 where we compare to previous works and put our results in the context of the field. Finally, in Section 3.7 we make concluding remarks and discuss future work to better our constraints.

## 3.2 Data: Catalogue Matching & Secondary Identification

### 3.2.1 The COSMOS2020 Catalogue

The COSMOS survey is a deep, wide field survey centred on coordinates (+150.1192°, +2.20583°). It covers a 2 square degree area about this central point and has been observed with many major space and ground based observatories. These include *HST*, Spitzer, GALEX, XMM, Chandra, Herschel and NuStar from for space based observatories and a host of ground based telescopes

---

<sup>1</sup>DOI: 10.26131/IRSA178

including Keck, Subaru, the Very Large Array, the European Southern Observatory Very Large Telescope, etc. This gives it unprecedented wavelength coverage from the radio to the X-Ray wavelengths. The original survey overview is fully described in Scoville et al. (2007), which initially used *HST* observations with the *F814W* band, reaching a  $5\sigma$  depth of 27.2AB. Since this initial release, there have been many photometric catalogues from the COSMOS team using different fitting software across the host of photometric information they have available to them. This information has only grown as almost all major astrophysical observatories have observed this field.

Each COSMOS dataproduct release contains multiple catalogues of galactic parameters such as star formation rates (SFR), stellar masses and line emissions. We elect to specifically use the COSMOS2020 catalogue (Weaver et al., 2022). This catalogue has a wealth of ancillary information for approximately 1.7 million sources. Each source has been analysed with well known astronomical software (for our purposes, primarily **LePhare**, Arnouts et al. 1999; Ilbert et al. 2006, and **EaZY**, Brammer et al. 2008). These provide estimates of the physical parameters of each source based on its measured broadband photometry. For our purposes, the parameters of interest are the stellar masses and the estimated star formation rates of each source. For the stellar mass we use the best fit **LePhare** measurement and for the star formation rates we use the best fit **EaZY** measurements. We compare the output masses and SFRs for our sources in Figure 3.1. As shown, there can be wide scatter and disagreement between the two algorithms. We tested different combinations of **EaZY** and **LePhare** stellar masses and SFRs to find which would be best to use in this work. We found that using the same algorithm in both parameters revealed the degeneracies of using discrete templates to fit the broad band photometry in the underlying parameter space. Therefore, we elect to inter-mix the algorithms and use the best fit **LePhare** stellar mass and best fit **EaZY** SFR measurement.

Our sample of interacting galaxies has been de-duplicated, but the COSMOS2020 catalogue is not specifically a de-duplicated merger catalogue. We cross match between our sample and the COSMOS2020 catalogues using a position search within  $10''$  of our sample coordinates. Once we have identified the nearest COSMOS2020 source for each interacting galaxy ID, we de-duplicate

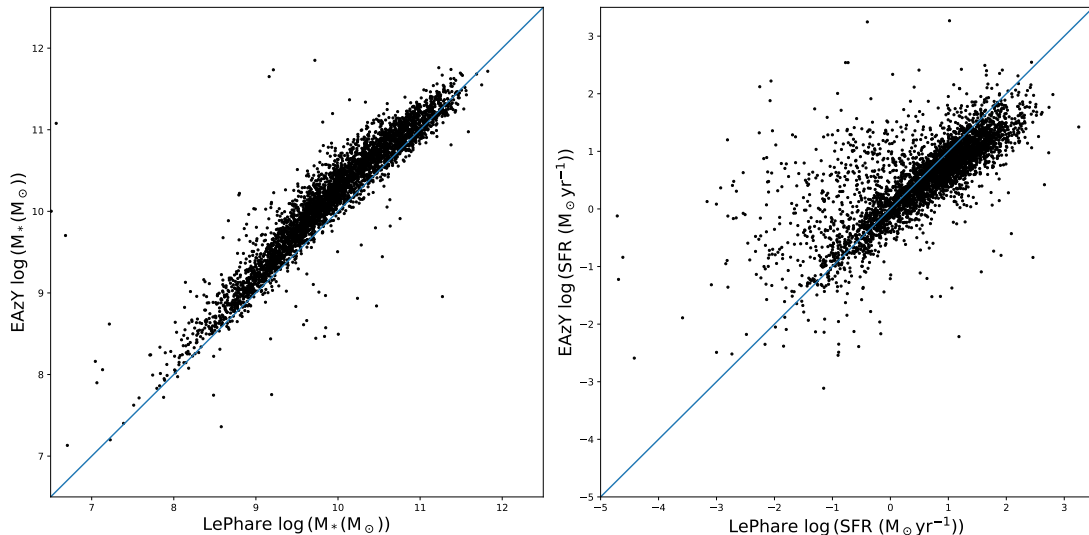


**Figure 3.1:** Comparison of the measures of stellar mass and SFR using either LePhare or EAzy photometric codes to calculate them. If the algorithms agreed perfectly, the sources would lie on the blue 1:1 line. *Left:* The scatter in the stellar masses between softwares. As shown, EAzy often seems to find larger stellar masses when compared to LePhare. *Right:* Scatter in SFRs when measured with LePhare or EAzy.

based on COSMOS2020 ID and redo the coordinate matching process with any duplicate matches. If no further COSMOS2020 sources were within 1" of the source, then we classify the source as not in the COSMOS2020 catalogue. We find 3,786 of our sources exist in the COSMOS2020 catalogue.

Once matched, we remove any sources with non-physical photometric measurements for the stellar mass or star formation rates. We then further reduce our sample by only keeping sources within a mass range of  $6.5 \leq \log_{10} M_*(M_\odot) \leq 12.5$  and a star formation rate range of  $-5 < \log_{10} \text{SFR}(M_\odot \text{yr}^{-1}) \leq 3.5$ . We also opt to institute a redshift cut of  $z \leq 1.2$ . Beyond this redshift, we find that identification of tidal features becomes difficult due to surface brightness dimming and we risk mis-identifying the stages of the interacting galaxies. This also matches the redshift cut applied to the environment catalogue we cross match with in Section 3.3.2. Applying these cuts reduces our sample size to 3,689 interacting galaxies.

### 3.2.2 Secondary Identification

As the catalogue described in Chapter 2 only contains source coordinates and IDs, we must also manually identify the secondaries of many of our interacting systems. To find the secondaries, we apply three steps. First, a cutout surrounding each source was created. These cutouts were from the COSMOS cutout service, selecting HST-ACS tiles in the  $F814W$  filter. Each cutout was  $30'' \times 30''$  (corresponding to  $1001 \times 1001$  pixels). The original cutout from Chapter 2 was also displayed next to the enlarged cutout. We annotate each cutout with each sources' COSMOS2020 ID and measured photometric redshift and error. By annotating each cutout with the sources photometric redshift and ID, we visually assessed each cutout and gave one of the four following classifications to each: system disturbed but secondary could not be identified; secondary could be identified; cannot confirm galaxy is interacting; null redshift (0 or NaN); incorrect primary assigned.

To associate a secondary galaxy for each primary, the galaxy had to be within the cutout we were visually assessing and within the recorded error of the primary photometric redshift. Using photometric redshift cutoffs in this way is often done when calculating environment parameters (e.g Baldry et al., 2006) or defining interacting galaxies by close pairs (e.g Shah et al., 2022). A null redshift is defined as the primary galaxy out with our redshift limits, 0 or NaN. A minority of the cutouts we visually assessed were found to have the incorrect primary at the centre. In these cases, we record the correct primary galaxy ID and extract the ancillary data from the COSMOS2020 catalogue. We then attempted to find the secondary galaxy again for the corrected primary.

Using these definitions, we find that of the 3,689 original systems cross-matched with COSMOS2020 2,283 could not have their secondary identified, 834 had a clear secondary, 446 could not be reliably classified as an interacting galaxy, 248 had a null redshift and 149 were the incorrect primary. Figure 3.2 shows an example of each of our classifications. Each secondary we identify was added to our sample, increasing our sample size to 3,829.

While initially surprising that the majority of our systems could not have a secondary identified, we found that it was mostly due to limitations in the COS-

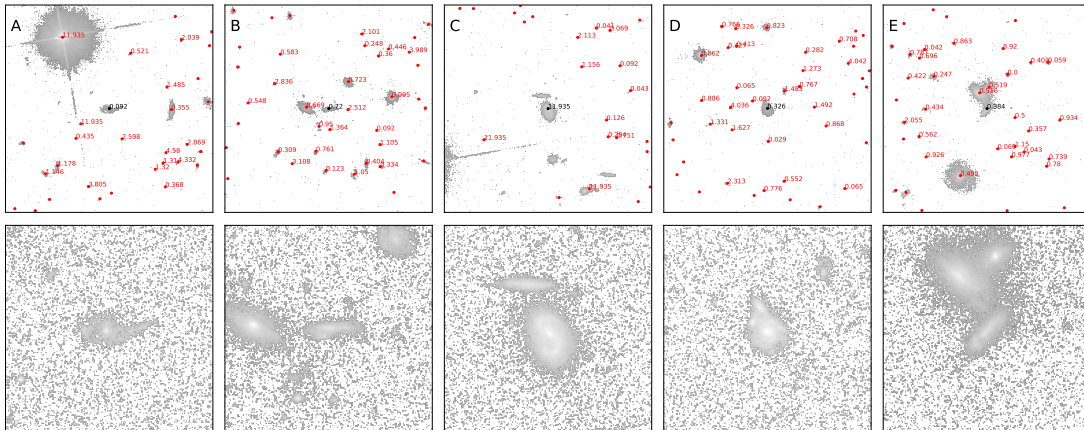


**Figure 3.2:** An example of each visual classification made on the cross matched sample. These are: (A) where the secondary could not be identified, (B) the primary had a clear secondary, (C) the primary could not be reliably classified as an interacting galaxy, (D) the redshift of the primary was null and (E) the incorrect primary was identified. Based on these classifications, we either add the secondary galaxies to the sample or we remove the contamination from it. These images are  $30''$  across using the COSMOS cutout service, selecting HST/ACS tiles as the basis for the observations in the  $F814W$  filter.

MOS catalogue or the way in which we conduct our secondary identification. Each potential secondary must have a COSMOS ID associated with it, however, when two systems are very close together and small enough they were identified under a single COSMOS ID despite being two separate systems. The same also occurred when two systems were merging or interacting. The tidal features connecting the systems or coalescing systems would only be identified under one ID in the catalogue. Figure 3.2 panel (C) shows an example of two systems being close enough together that they have been identified under a single COSMOS2020 entry. Figure 3.3 shows this disparity with the different types of interaction we observe.

Those galaxies which were found to be contamination (i.e., could not be reliably classified as interacting as they showed little tidal distortion or had no neighbouring systems at a matching redshift or having a redshift of 0) were removed from our sample. Galaxies that could not be reliably classified as interacting were also removed. These systems were often overlapping but at different redshifts, or were systems with irregular morphologies of spiral arms or a clumps

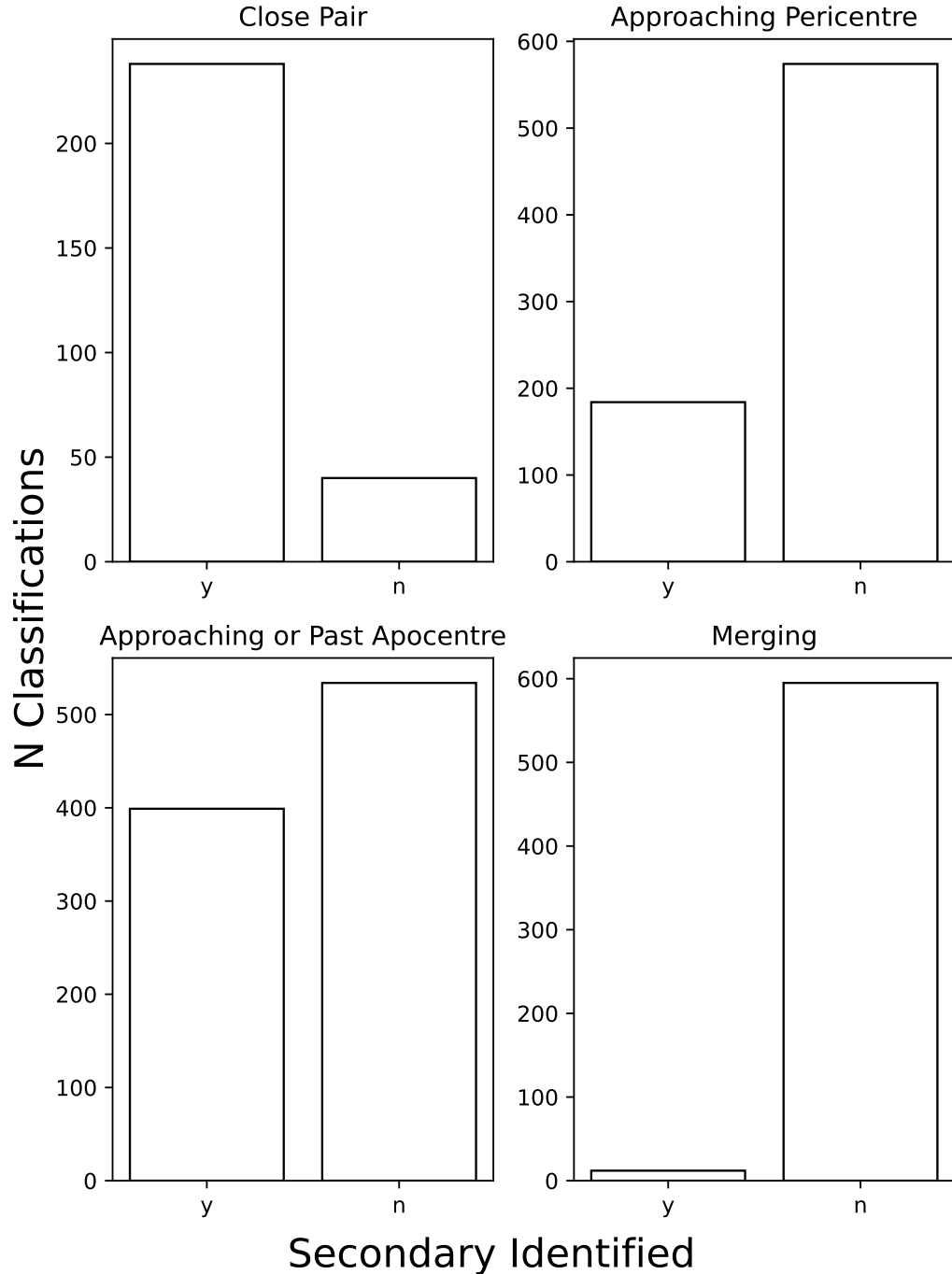


**Figure 3.3:** Where a secondary could be identified at different stages in the interaction. The reasoning for such disparity in secondaries identified is due to the relative distance each the secondary would be from the primary at each stage. For a close pair, we often found the secondary galaxy, but a minority of these were so close together that the entire system was given a single COSMOS ID. The same was true for those interacting systems approaching pericentre or merging. When the secondary was near apocentre, often it would be outside the cutout we were using for visual classification.

were present. There was also many systems that were at high redshift ( $z > 1$ ) where the resolution of the cutouts meant that features could not be discerned visually.

Our final classification type was that the incorrect galaxy had been identified as the primary galaxy. This was the case for 149 systems. These were systems where the interacting galaxies were clearly in the cutout but some tidal debris or some nearby system had been matched from COSMOS. We reassign these systems to the correct COSMOS IDs and then take them through the secondary identification process.

By the end of this selection method, we find a sample size of 3,829 interacting galaxies. We conduct a de-duplication based on the COSMOS2020 ID, which reduces the sample back down to 3,547 interacting galaxies. The remaining systems are each visually confirmed interacting and disturbed galaxies based on their morphology and photometric redshift as measured in the COSMOS2020 catalogue.

For each galaxy in our sample, we define a mass- and redshift-matched control galaxy to investigate differences in their galactic parameters. We find these control galaxies from the COSMOS2020 catalogue. All galaxies within 0.01 dex of our samples stellar mass are selected from the catalogue, and within a  $\pm 0.01$  redshift slice. We then define the control galaxy as the system furthest from our interacting galaxy. Each control galaxy is then visually confirmed to be non-interacting and have no nearby pairs. We also confirm that it does not already exist in the catalogue, and ensure there is no duplication in the control sample. Figure 3.4 shows the mass distribution of our paired sub-sample of galaxies and their control, showing a mass distribution which is approximately the same as the interacting sample. With the previously defined cuts, we find a control galaxy for all but one of our interacting galaxies.

### 3.2.3 Finding Additional Systems

As a result of using visual classification to find the secondary galaxy in each interaction, we were able to also confirm other interacting systems which had not been found in our catalogue. Primarily, these extra interacting galaxies are



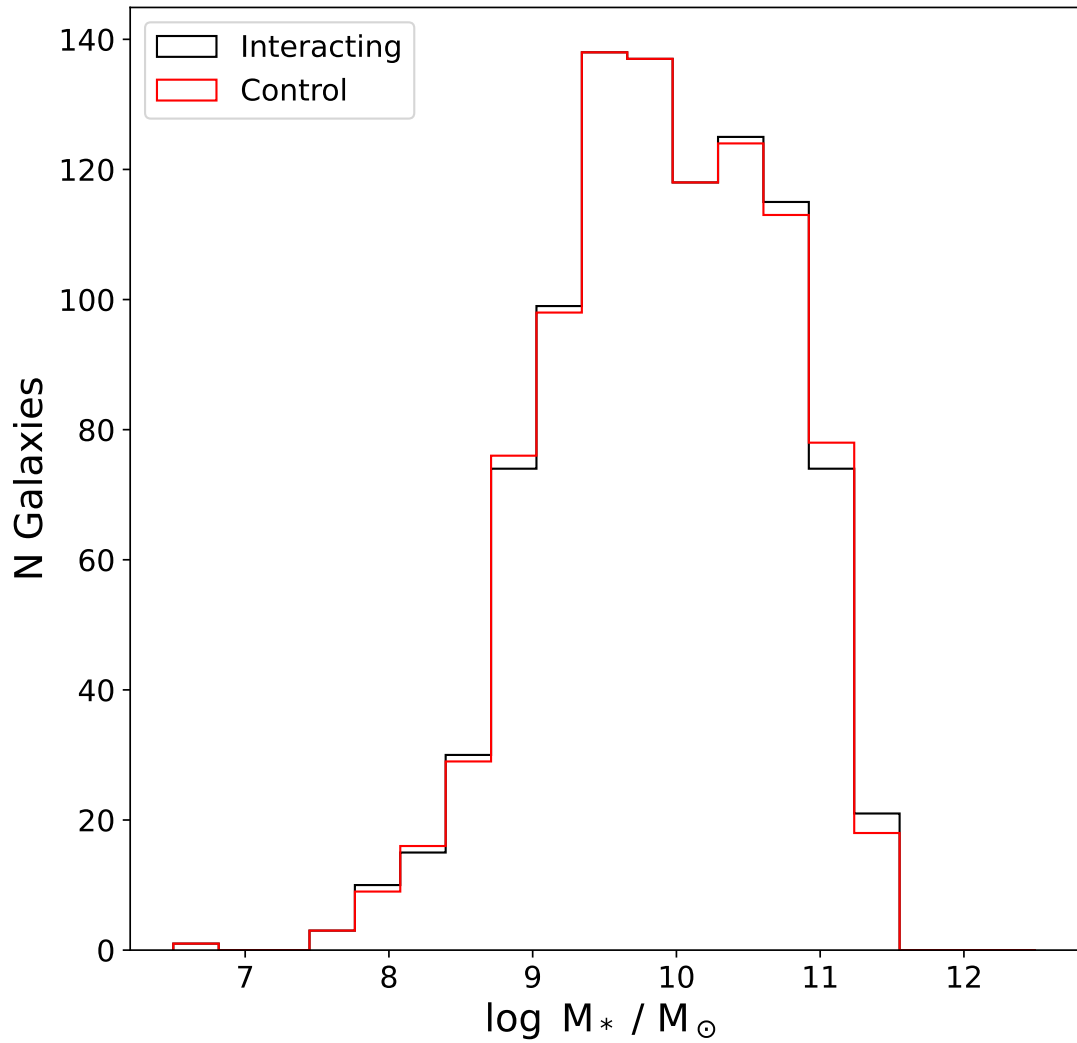


**Figure 3.4:** The mass distribution of the paired interacting galaxy sample and the control sample. Both primary and secondary galaxies are within this distribution.

from systems which had more than two galaxies involved in the interaction. Our selection process was built to only find a primary and secondary galaxy and, therefore, we add these extra systems into our sample manually. Other interacting galaxies that were added were low redshift systems which would have appeared to completely fill the cutout of the classification process in Chapter 2. By looking at the larger COSMOS2020 cutouts, we are able to recover these galaxies and add them to this sample.

In total, we found an extra 841 interacting systems that we could add to our sample. Upon conducting a de-duplication of these with the sample already found, this was reduced to 634 interacting systems. This gives us a total flux-limited sample size of 4,181.

### 3.2.4 Creating the Volume Limited Sample

We now investigate the distribution of our sample between mass and redshift. Figure 3.5 shows the resultant distribution from our flux limited sample. In order to ensure that our results are not biased by a redshift-dependent mass/luminosity limit, we institute a cut in the mass of the interacting systems. Thus, creating a mass limited sample. We elect to use a mass cut of  $\log(\frac{M}{M_{\odot}}) \geq 9.25$ , shown by the blue dashed line in Figure 3.5. Note, if one galaxy in a pair is below this volume cut, then we remove both galaxies from the sample. This ensure that our pairs are volume limited, and not just individual galaxies. This specific cut is motivated by two reasons. First, this is the lowest mass system which is still observed in our the coalescing sample at  $z = 1.2$ . The second reason is that such a mass cut is approximately the one made in the environment catalogue we will describe later in Section 3.3.2. There we make a cut of  $\log(\frac{M}{M_{\odot}}) \geq 9.6$ , we find that decreasing the mass cut to  $\log(\frac{M}{M_{\odot}}) \geq 9.25$  does not make major differences to our results. Thus, we opt to use a lower mass cut to increase the number of galaxies in our sample. Making such a cut reduces our flux-limited sample of 4,181 to a mass-limited sample of 3,384 interacting galaxies.

Throughout this Chapter, we will use our volume limited sample in our analysis. This gives us uniform sensitivity across our volume. However, we also conducted the same analysis described below with the flux-limited sample and

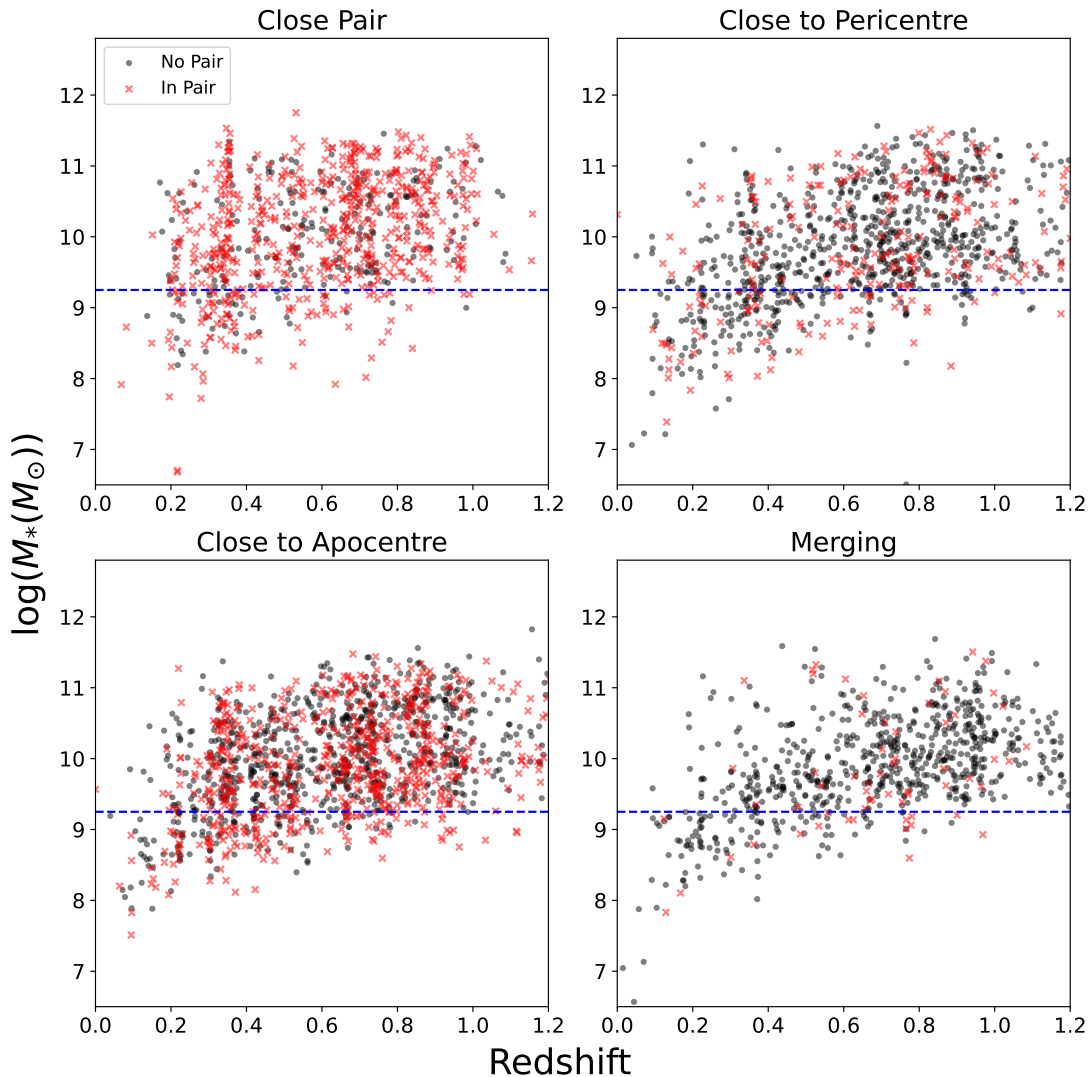


**Figure 3.5:** Redshift vs Mass distribution for the four stages of interaction. We separate those systems with an identified secondary (in red) from those where no secondary could be found. The dashed blue line shows the mass cuts we make for our mass-limited sample and is set at  $\log(\frac{M}{M_{\odot}}) \geq 9.25$ . As shown here, the distribution of systems across redshift and mass is consistent for all stages in our sample. This is important as we use tidal distortion and the existence as tidal features as a fundamental for our classification methodology. Therefore, we are likely not affected by this in our analysis. We find that our ability to identify pairs is primarily affected by stage and not redshift.

the qualitative conclusions of this Chapter did not change. For a full summary of our selection process, and the source counts after each step, see Section 3.3.4. This also will summarise our environment and AGN selection which is described below.

### **3.3 Method: Environment, AGN and Interaction Stage**

A primary aim of this work is to investigate the evolution of different galactic parameters with stage of the interaction. Each stage is defined to capture a different part of the dynamical time and merger history. This stage also relates to the projected separation of galaxies with an identified secondary. Here, we define the shorthand for the interaction stages and which part of the dynamical time they cover. We also describe how we find AGN in our full sample and find measurements of the environment about each. The parameters required to calculate the AGN fraction are not found in the COSMOS2020, and we therefore must cross match with other catalogues to find the required parameters. We also describe the catalogue we use to define the environmental density about each of our sources. This is important to consider, as it is well known that measured SFRs of galaxies can be affected by environment, as well as existing biases in where interacting and merging galaxies reside. We, therefore, need to check that we have not introduced any environmental biases into our definition of interaction stage.

#### **3.3.1 Classifying Stage of Interaction**

The primary goal of this work is to find if a relation exists between a host of galactic parameters, underlying physical processes and the stage of the interaction. Each stage covers a different part of the dynamical history in an interaction and, in this case, we define it based on the morphology and projected separation between systems. We have already encountered the four stages we will investigate

in Figures 3.4 and 3.5 and now define a short hand name to refer to them as well as fully describe the part of the dynamical history they represent. These are:

- Separated: Systems which are well-separated with little to no morphological disturbance (Close pairs).
- Pericentre: Close pairs showing morphological distortion while still in a pair or show a physical connection by tidal features.
- Apocentre: Well separated pairs with morphological disturbance or isolated galaxies with clear tidal features.
- Merging: Highly disturbed systems with a secondary core present.

Our four stage approach is not a new one, and many other works have utilised it to differentiate different parts of the dynamical history of a galaxy interaction (e.g Chang et al., 2022; Garay-Solis et al., 2023).

Figure 3.6 shows the original source cutouts used in Chapter 2 to give an example of each stage. There are degeneracies associated with this staging system, however. In this context, we define a degeneracy as when the interacting galaxies may be at two or more parts of the dynamical timescale and we have no way to tell without further information on the system.

The separated stage of the interaction captures the first approach of the two systems and they are observed as a galactic pair. This sample comes from a combination of the remaining contamination in the OR23 catalogue (approximately 4% as described in Chapter 2), or were found to be real galaxy pairs in the de-contamination step described there. They have little to no morphological disturbance and, in our sample, are most often those galaxies with distinct disks. At this point, we would expect no change in the underlying processes of the galaxies from their control samples. Interaction has not taken place yet, and the two systems are morphologically intact. By definition, this stage requires an identified secondary galaxy and therefore has the highest number of identified secondaries with every system having a secondary that can be visually classified. This is also the least degenerate part of the dynamical time we are sampling due

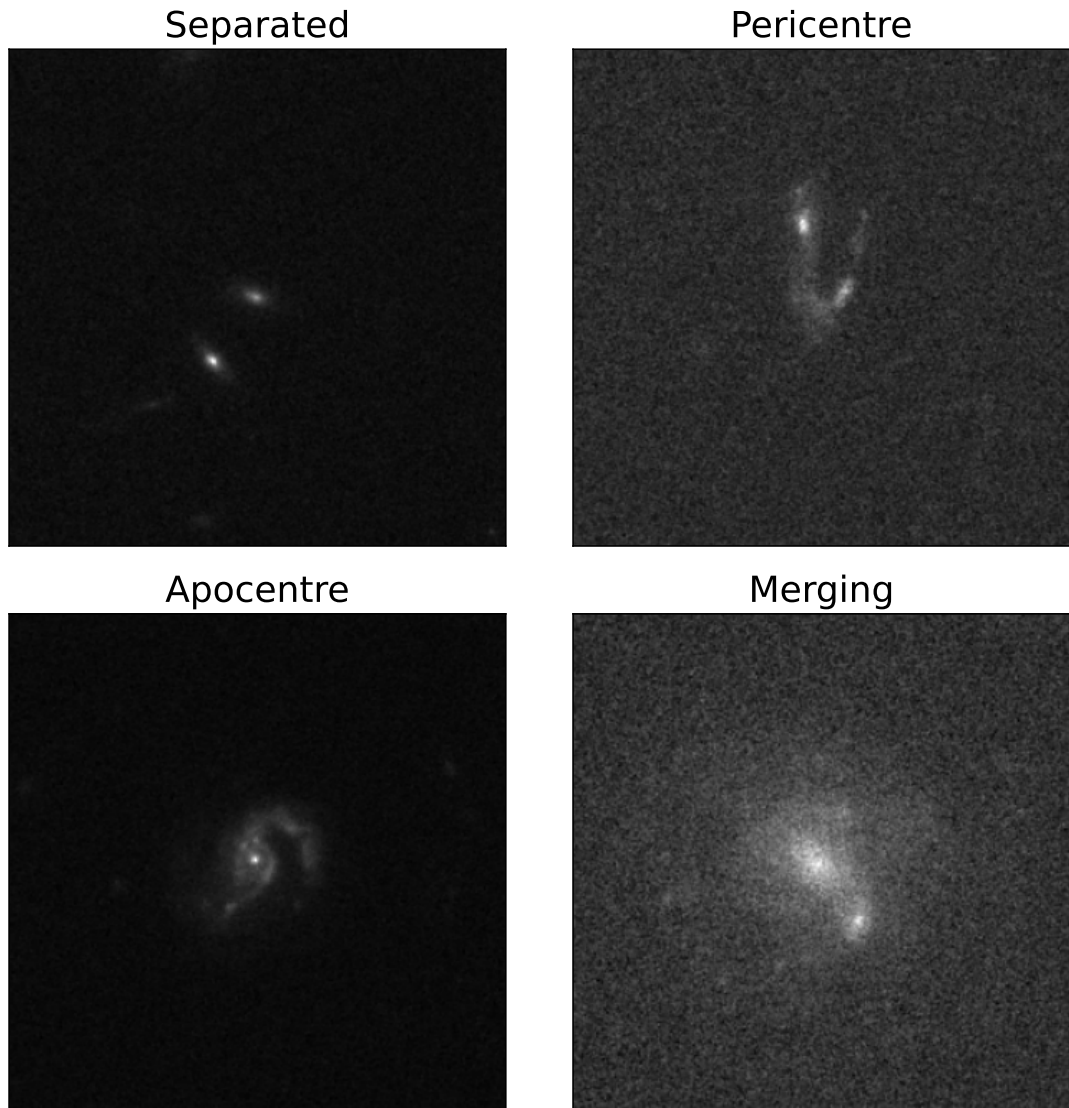


**Figure 3.6:** Examples of the four stages we split our interacting galaxy sample into. Separated: A close pair with confirmed redshift matching. Pericentre: Two distinct systems interacting with tidal features forming. Apocentre: A tidally disturbed system with no secondary present, likely at apocentre. Merging: A galaxy with multiple cores while highly disturbed. At the final stage before coalescence.

to a criteria of no morphological disturbance. Therefore, it is unlikely that the galaxies have already made a passage.

The pericentre stage of the interaction is defined as the point where the two galaxies in the interaction are at or just passing the pericentre of the tidal encounter. At this point, we find the beginning of morphological disturbance, the beginning of the formation of tidal features and some tidal debris. Due to the two systems having to overlap or connect via tidal features - by definition - this is the stage that suffers most from limited identification of the secondary galaxy. The COSMOS2020 catalogue often defines these two systems as a single system, and therefore, we lack information about their secondary. This stage is also highly degenerate in the context of the dynamical timescale of the interaction. Without further information, we are unable to define whether the galaxies involved at this stage are at the first, second, third, etc passage of the tidal encounter. We also do not know if they are approaching or have just passed pericentre.

The apocentre stage describes those interacting systems where the two disks are fully separated and distinct from one another. They have some morphological disturbance associated with them, but do not require a secondary galaxy to be put into this stage. If the galaxies have sufficient velocity they would escape from each other and, therefore, their secondary could be beyond our COSMOS2020 cutouts used to visually identify them. This is reflected in an even distribution of finding the primary and secondary in this stage. This stage also defines a large part of the dynamical timescale. It spans from separating from the secondary and after pericentre, to moving out to the apocentre of the interaction (or escaping with sufficient velocity), to falling back in toward the secondary galaxy again. Without velocity information, we have no way of finding if the galaxy is moving away or moving toward its secondary.

Finally, the merging stage represents the final step of a galaxy interaction. If the two galaxies do not have sufficient velocity to escape one another they coalesce and ultimately merge. We define this stage through the severe morphological disturbance of the galaxy involved as well as the existence of a second core within it. While we attempt to capture only pre- or ongoing-coalescing systems, it is important to note that this stage is degenerate to post-merger remnants which will also be accepted by our criteria. Post-merger remnants are systems where

coalescence has been completed and immediately after will be highly morphologically disturbed and difficult to distinguish from those systems with merging ongoing. At this stage, we would expect the interaction will be at its most violent with complete disruption of both galactic disks and likely increased star formation across the galaxy.

We have noted the degeneracy of each stage as we have described them. Thus, we can now put this fully into the context of the dynamical timescale. Over a typical interaction, we would expect the galaxy pair to move from being separated to the pericentre of the interaction in the early times of the dynamical timescale. Then, dependent on the velocity of the system, the galaxy pair will either move straight into the merging stage of classification and begin to coalesce or it will move toward the apocentre stage. This change from pericentre to apocentre can then take two branching paths dependent on the velocity in the system. If the galaxies have sufficient velocity, the apocentre stage will be their end state until the tidal features slowly dissipate. If they do not have enough velocity to escape on another, the system will move from the apocentre stage back into the pericentre stage. This could then happen for many cycles until finally the galaxies enter the merging stage and coalesce. Figure 3.7 shows the branching paths that the galaxies can take through each stage. These images are created using the Advanced Python Stellar Animation Module restricted numerical simulation, described in Chapter 4, and are for illustrative purposes only here.

As described previously, in the literature, rather than using the stage of an interaction based on morphology the projected separation of the two systems is used. To explore the difference between using our staging system and the projected separation, as well as to ensure we recover the expected relations, we measure the projected separations of our confirmed galaxy pairs. Figure 3.8 shows the stage classification with projected separation between the two pairs. We measure this by taking the average of the best fit photometric redshifts between the two galaxies, and converting their angular separation to a physical one. The most distinct projected separation ( $s_{\text{proj}}$ ) in stages is between the pericentre and apocentre stages. Here, we see that the pericentre stage is dominated by systems with  $s_{\text{proj}} < 35\text{kpc}$  while the apocentre stage is dominated  $25 \leq s_{\text{proj}} \leq 100\text{ kpc}$ . The pericentre stage is visually classified as systems which are highly morphologically



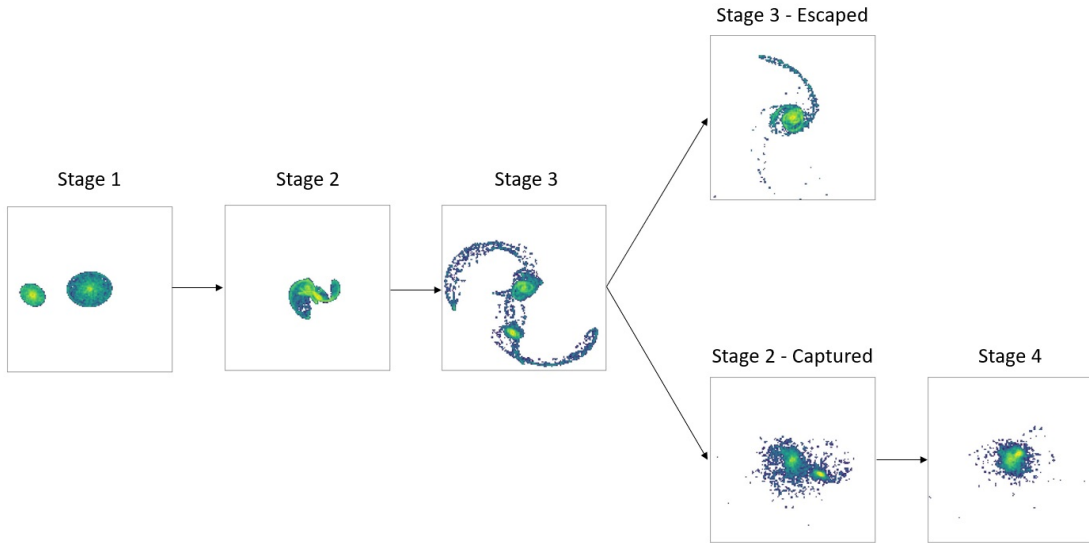


**Figure 3.7:** The progression through an interaction using our stage definitions. In the separated stage, we have two systems that are approaching each other but exhibit no tidal features. This is before the point of closest approach has occurred. This is followed by an initial pericentre stage: the systems are approximately at their closest approach. This stage is often mistaken, in the COSMOS catalogue, for being of only one source. Clear tidal features exist with major disturbance in the two disks. This is followed by the apocentre stage, where there are two distinct cores with clear tidal features. However, after this point, there are two outcomes to the system depending on the galactic velocities. If the secondary has the escape velocity, the system will remain an apocentre stage interaction until the tidal features dissipate (and no longer are in our sample). If they do not have enough energy, the system will return to the pericentre stage of the encounter and then begin to coalesce in the merging stage. Images are from the Advanced Python Stellar Particle Animation Module interacting galaxy algorithm described in Chapter 4 and based on the stellar particle animation module algorithm described in Wallin et al. (2016).

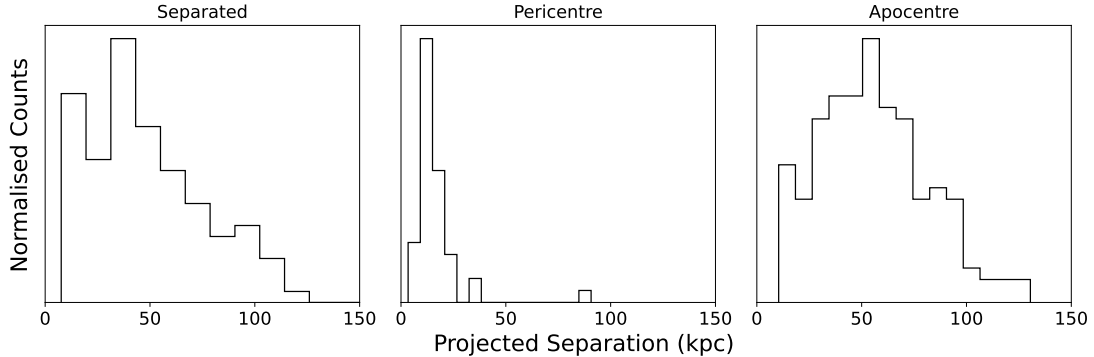


**Figure 3.8:** The projected separations of the confirmed galaxy pairs in our sample. This conforms with other works the definition of our different stages. The separated stage can be at any projected separation, however, we have visually confirmed that these sources are not morphologically disturbed. The pericentre stage is dominated by systems with small projected separation as, by definition, they must be morphologically linked or overlapping. Those systems at larger separation are very large systems whose morphology categorise them as at the pericentre stage. Finally, apocentre stage galaxies are those which are visually confirmed to be fully morphologically separated and tidally disturbed. The bulk of these lie in a range of 25 - 100kpc in projected separation from each other. There is some overlap between the pericentre and apocentre stages in projected separation, as their visual classification is also dependent on the system size.

disturbed, while either being morphologically linked to each other or overlapping. Those galaxy pairs with large projected separations are pairs which are very large in angular size, while still overlapping or morphologically linked. If this criteria is not met, then the system becomes an apocentre stage interaction where the two galaxies in the pair are completely distinct. There is some overlap between the projected separations of the pericentre and apocentre stage as this is somewhat dependent on the angular size of the two systems involved in the interaction.

Figure 3.9 shows the overlap between our four stages in projected separation. It also shows the limitations in our sample of finding the secondary galaxy in the interaction. This, primarily, is at low redshift where a larger projected separation represents a larger angular separation on the sky. This is a limitation of using visual confirmation of the secondary within a cutout of limited angular size. Thus, we see at low redshift ( $z < 0.2$ ) we only identify pairs of galaxies with projected separation below  $50kpc$ . Toward our limiting redshift, however, we are

able to identify galaxy pairs down to a projected separation of 10kpc, as well as out to 200kpc. However, due to the size limitation of the original cutout classified by `Zoobot`, we find a second bias at low redshift. As the projected size of the cutout gets smaller at low redshift, we lose systems which are at larger projected separations. There are systems beyond this cutoff, but these are likely separated systems which had their secondaries identified with the much larger COSMOS2020 cutouts used in the visual confirmation stage.

We will use the projected separation to investigate relations between AGN activity and if we observe enhancement in star formation. The SFR is already present in the COSMOS2020 catalogue as measured using `EaZY`. To ensure that any enhancements are from interaction alone, we must ensure that there is no large bias in the environment of our sample. First, we describe how we classify the environment of each of our matches.

### 3.3.2 Matching to Environment Catalogue

It is well known that the environment has a direct impact on the observed SFR of galaxies. A galaxy in a cluster environment has, on average, a higher SFR than those in the field (Baldry et al., 2006). Thus, if any of our stage classifications are biased towards one environment or another, it could impact our results.

There is no measure of the environmental density in the COSMOS2020 catalogue. Such a measure is often calculated in numerous ways, such as the N-nearest neighbour (Baldry et al., 2006), different Bayesian metrics (Cowan & Ivezić, 2008) or estimating it from Voronoi Tessellation (Vavilova et al., 2021). However, in this Section, we use the existing environmental density catalogue produced by Darvish et al. (2017). This catalogue was created specifically for the COSMOS survey, and has a measured density for all sources with mass  $\log(\frac{M}{M_{\odot}}) \geq 9.6$  and  $z \leq 1.2$ . Darvish et al. (2017) calculate not only the density, but also the density parameter  $\delta$  and assign each source to a field, filament or cluster classification. For a full description of how they calculate the environment and density field see Darvish et al. (2015) and Darvish et al. (2017), but we will briefly describe it here.

To build the density field throughout the COSMOS field, Darvish et al. (2017) first construct a set of overlapping redshift slices. Within each slice, a subset of the

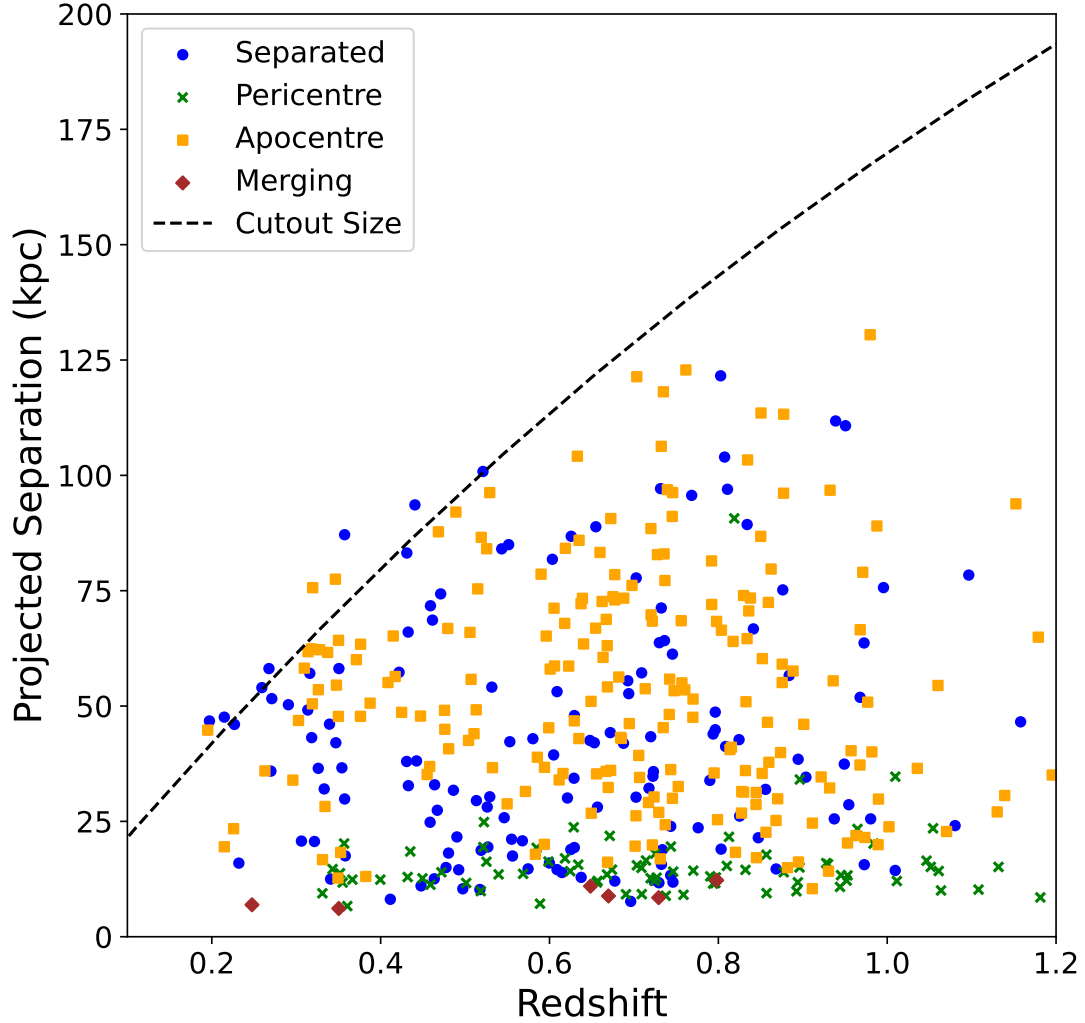


**Figure 3.9:** The measured distribution of projected separation with redshift. As we have made redshift cuts out to  $z = 1.2$ , we investigate the limitations on the projected separations we can successfully identify across our volume. We find that we can successfully identify secondary galaxies and their projected separations down to 10kpc to  $z = 1.2$ . This is true across defined interaction stage. We find, because of the defined size of our cutouts, the limitation of finding the secondary galaxy is at low redshifts where the projected separation size of the two systems will begin to be larger than the projected size of the cutout. The changing cutout size with redshift is shown as the dashed black line.

galaxies are selected such that the median of the probability distribution function (PDF) of their photometric redshift is within it. Then, from this subset, they calculate the weighted surface density within the redshift slice. The weighting is based upon the PDF of the photometric redshift present within the redshift slice. These weights significantly reduce the effects of projection effects. They then apply a weighted adaptive kernel smoothing using a 2D Gaussian kernel whose width changes based on the found local density of galaxies. Once this density field is created, the density around the sample galaxies can simply be interpolated across the density field based on the angular position and the redshift slice the sample galaxy is in (based on its photometric redshift PDF).

The result of this process, and the cuts defined previously, is a catalogue of  $\approx 45,000$  galaxies with their densities accurately measured. We remove any sources which are flagged as uncertain from the catalogue (a flag in it) providing us with  $\approx 39,000$  sources with which to cross match the sample from Chapter 2. We apply the same cuts to our sample as applied in Darvish et al. (2017), and only consider those systems with a mass  $\log(\frac{M}{M_{\odot}}) \geq 9.6$ . To cross match with our sample, we use the COSMOS2015\_ID which exists in both the COSMOS2020 catalogue and the Darvish et al. (2017) catalogue. Upon applying the mass cut to our sample, we find 2,800 matches to the Darvish et al. (2017) catalogue. Upon matching based upon the COSMOS2015 ID, we find that 628 sources in our sample do not exist in the environment catalogue. This reduces our sample to 2,172 galaxies with confirmed and reliable environment density measurements.

### 3.3.3 Classifying AGN

We will also investigate the effect of interaction stage on AGN activity throughout our sample. As the COSMOS2020 catalogue does not contain the relevant parameters to make this calculation, we turn to the Chandra COSMOS Legacy Survey Multiwavelength Catalogue (Marchesi et al., 2016) and the COSMOS VLA 3GHz survey (Smolčić et al., 2017; Delvecchio et al., 2017). Both of these catalogues span the entire COSMOS area, and contain detailed classifications of the sources they find. The Chandra survey spans the X-ray range of wavelengths,

and successfully identified numerous X-ray AGN. The VLA 3GHz survey is a radio survey, and we use this to find the radio AGN through our sample.

Our matching process is similar to previously described matching processes. We use the previously identified COSMOS2020 source coordinates and select the nearest source within a  $10''$  matching radius. We first find matches of radio AGN using the VLA 3GHz survey catalogue and then search the Chandra survey. At every step, if we find a match in the relevant catalogue, we remove it from subsequent searches in other catalogues and take the first classification as the correct one.

Applying our matching criteria, we find 1,140 matches in the VLA 3GHz survey and 155 in the Chandra survey. From existing flags within the catalogues, these were split into 833 star forming galaxies and 462 AGN. We also investigate cross matching with the MPA-JHU catalogue (Kauffmann et al., 2003; Brinchmann et al., 2004; Salim et al., 2007), however, found that all matches were already represented by the VLA and Chandra surveys. We also use the COSMOS XMM-survey and, again, find no new sources to add to our sample. While the ratio of AGN to star forming galaxies in our sample seems large compared to other works, it is important to note that this is a result of limited matching between the catalogues. Of the 4,181 galaxies in our sample, only 1,295 appeared at all in either the VLA or Chandra catalogues.

#### 3.3.4 Summary of Selection Process and Source Counts

We summarise our source selection in a single table. Table 3.1 shows the breakdown of the number of sources added or removed at each selection and we describe it here. First, we cross match 3,346 sources from the OR23 catalogue to the COSMOS2020 catalogue. We then conduct visual inspection of each source with additional photometric redshift measurements. We use these to confirm secondary galaxies, or other interacting systems, in the COSMOS field, finding 803 more systems. Of these 4,181 sources visually confirmed 845 were confirmed pairs. Cross matching our found 4,181 sources with the Darvish et al. (2017) environment catalogue of the COSMOS survey provides us with 2,225 sources with environment measurements. We then volume limit the sample and apply cuts of

### 3.3 Method: Environment, AGN and Interaction Stage

Selection Process	Sources	Confirmed Pairs	Environment Measurements	AGN & SFG Classifications
In COSMOS	3,689	-	-	-
Visual & Secondary Identification	3,829	-	-	-
Deduplication	3,547	-	-	-
Extra Found Systems	4,181	845	982	1,295
Volume Limited	3,378	1,214	607	802

**Table 3.1:** Source counts at each stage of our selection process.

stellar mass cuts of  $9.25 \leq \log_{10} \frac{M_*}{M_\odot} \leq 12.5$  and a redshift cut of  $0 < z < 1.2$ . This provides us with a volume limited sample of 3,378 sources with 566 confirmed pairs and 2,214 with environment classifications.

This volume limited sample was then cross matched with the VLA and Chandra catalogues which existed in the COSMOS archives and the MPA-JHU catalogue. Of our flux limited sample of 4,181 sources 1,295 sources were cross matched with these catalogues. Applying the volume limitation to this sample, we find 802 sources with classifications of AGN or star forming galaxy.

#### 3.3.5 Visual Classification: Sources of Contamination

Throughout the description of our sample, we have identified these interacting systems by a combination of visual classification and the best-fit photometric measurements from the COSMOS2020 catalogue. This introduces limitations which could bias or contaminate our sample. We identify three serious areas of bias or contamination: 1) error inherent from using only photometric redshift measurements, 2) failure of identification of tidal features at higher redshifts due to surface brightness dimming and reduction in angular size, and 3) misidentification of tidal features as disturbances caused by other processes. In this subsection, we will address each of these points and quantify how they affect our sample. We will also discuss any how we mitigate these effects where appropriate.

First, there is always an inherent error in using the photometric redshift measurements of galaxies. We briefly mentioned this when describing pericentre stage systems. There, we found  $\sim 50$  systems which were clearly morphologically disturbed with linking tidal features, but their photometric redshifts were such that they couldn't possibly be interacting. It is also possible that we have missed pair identifications in the separated stage (where no tidal features are expected) due to

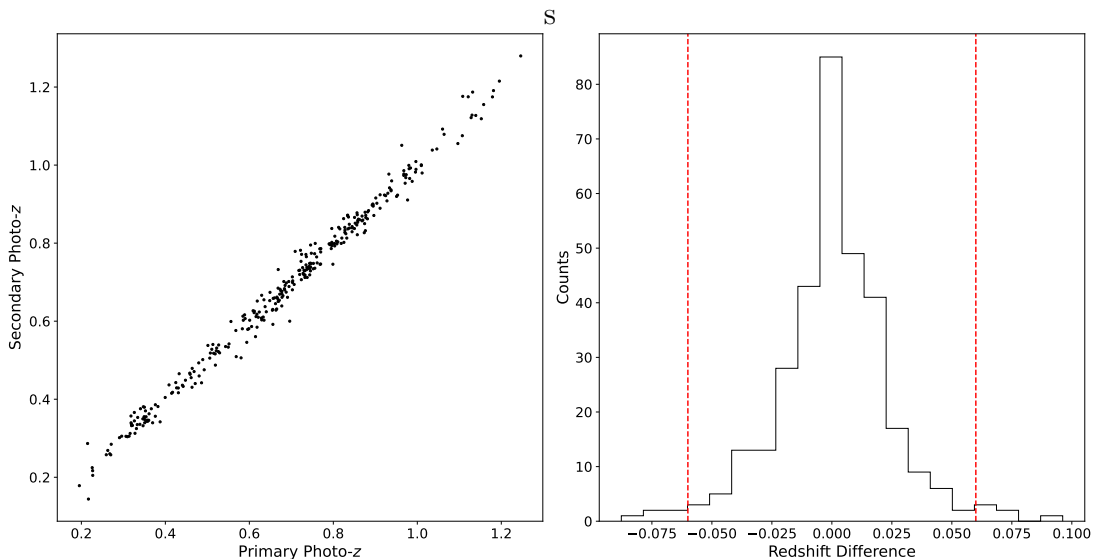


**Figure 3.10:** The scatter in photometric redshifts of our paired sample. Left shows the scatter in the primary and secondary photometric redshift measurements. Right the measured difference in the primary and secondary photometric redshifts found in the left panel. The red dashed lines show the expected error at the maximum redshift of our sample. As shown, the bulk of the sample lies within this region.

incorrect photometric redshifts. We wish to quantify both these effects. Weaver et al. (2022) quantify the error in their photometric redshift calculations (which we use here) as  $< 1\%$  for our redshift and flux range. They quantify the scatter in the distribution of photometric to spectroscopic redshifts is  $0.025(1+z)$  within our redshift and flux range. Therefore, the maximum error we would expect on our photometric redshifts in our sample is  $\pm 0.06$ .

To investigate the affected systems, we therefore look at the redshift distribution of our paired sample. Figure 3.10 shows the scatter in our found pairs as well as the difference between them from our visual classification. During the visual classification, we instituted a cut that each interacting pair must be within a photometric redshift difference of  $\pm 0.1$ . To estimate our completeness, we apply a bootstrapping test to our sample and see the number of systems we may have removed from our sample with this cut. We create a simulated paired sample of 10,000 systems and apply an error measurement based on the photometric redshift errors. This gives a paired sample across our redshift sample at slightly different redshifts. We then apply our cut, and check how many systems we would



remove due to the photometric error from the COSMOS2020 catalogue. We find that we would retain  $\approx 91\%$  of the sample with this cut, given the photometric redshift error. This is a lower limit on what we have retained, as we have not considered possible tidal features that would have caused us to keep the system in our sample. Therefore, we are unlikely to have removed a large percentage of interacting galaxies due to the photometric redshift error and the cuts we have applied.

The resultant scatter in photometric redshifts between the primary and secondary in our paired sample is shown on the left panel of Figure 3.10. The right hand panel shows the distribution of the difference measured between the primary and secondary photo- $z$ s, with the red dashed lines showing the maximum expected error on the photometric redshift measurement at the highest redshift of our sample. As shown, the bulk of our paired sample lies at very low redshift difference, meaning we are unlikely to have removed too many systems. This leads us to conclude that our pair selection process has been robust. The second limitation of our approach is the failure of identifying interacting systems at high redshift due to missing the tidal features of the system. This would be a combined result of the affects of surface brightness dimming of their disks and tidal features at high redshift and while also having a small angular size.

The change in angular size is more difficult as we have a standardised cutout size which does not depend the redshift, or angular size of the system. This means that if a system were at redshift 1.2, our pixel resolution corresponds to roughly  $0.5\text{kpc pix}^{-1}$  limiting the tidal features we would be able to identify. With such a scale we are able to identify extended tidal features away from the galactic disk such as tidal arms, but lack the resolution to those features which would be much closer to the disk. Thus, those interacting systems which have formed features such as shells, small tidal bridges or stellar streams will be missing from our samples at higher redshifts. Thus, at high redshift, we are most sensitive to the separated, apocentre and merging stage interacting systems while lacking the required resolution to pickup more intermediate tidal features at the pericentre stage.

We attempt to mitigate surface brightness dimming by making reasonable choices with our volume limitation. We elect to make redshift cuts of  $0 \leq z \leq 1.2$

and a mass limit of  $9.25 \leq \log \frac{M}{M_{\odot}} \leq 12.5$  following similar works exploring galaxy morphology (Conselice et al., 2007, 2009; Martin et al., 2022; Khalid et al., 2024). In the context of identifying interacting galaxies, Blumenthal et al. (2020) studied the reliability of making visual classifications by tidal features alone with examples from the IllustrisTNG simulation. They found that relying on tidal features alone biased their sample to higher environments, stellar masses and interactions near the time of the closest approach in the dynamical timescale. This was due to these conditions leading to increased visibility of tidal features and disturbed morphologies across redshift.

To investigate this, we look at the change in found fraction of micro, minor and major interactions across our redshift range. The effect of surface brightness dimming will be related to the type of interaction we are observing, and the resultant flux distribution of the tidal features. For instance, a stream formed in a minor interaction will be significantly dimmer than a tidal tail formed in a major interaction or merger (Sola et al., 2022). To get an idea of how we are affected, we split our pair sample into its constituent interaction types based on the mass ratio. We define the mass ratio such that the primary galaxy contains the highest stellar mass in the pair. If there is more than two galaxies involved in the interaction, we take the primary galaxy to be the galaxy with the highest stellar mass in the system. We define three different interaction types based on the mass ratio: micro (where the mass ratio is less than 1:10), minor (where the mass ratio is between 1:10 and 1:3) and major (where the mass ratio is greater than 1:3). For the  $F814W$  filter, we would expect the surface brightness to decline by  $(1+z)^3$ , and therefore that the surface brightness will decline by a maximum of a factor of 10 at  $z = 1.2$ .

Figure 3.11 shows the distribution of interaction types across redshift. The bottom panel shows the distribution in galaxy counts across redshift for the volume-limited sample. The top panel shows the change in the fraction of each interaction type we find in each redshift bin. For the minor and major interactions, we see that there is little change in the fractions across our redshift distribution. However, as expected, with micro interactions we see a gradual decline in the found fraction with increasing redshift. This shows a loss in sensitivity to this interaction type but over our redshift distribution there is not significant change

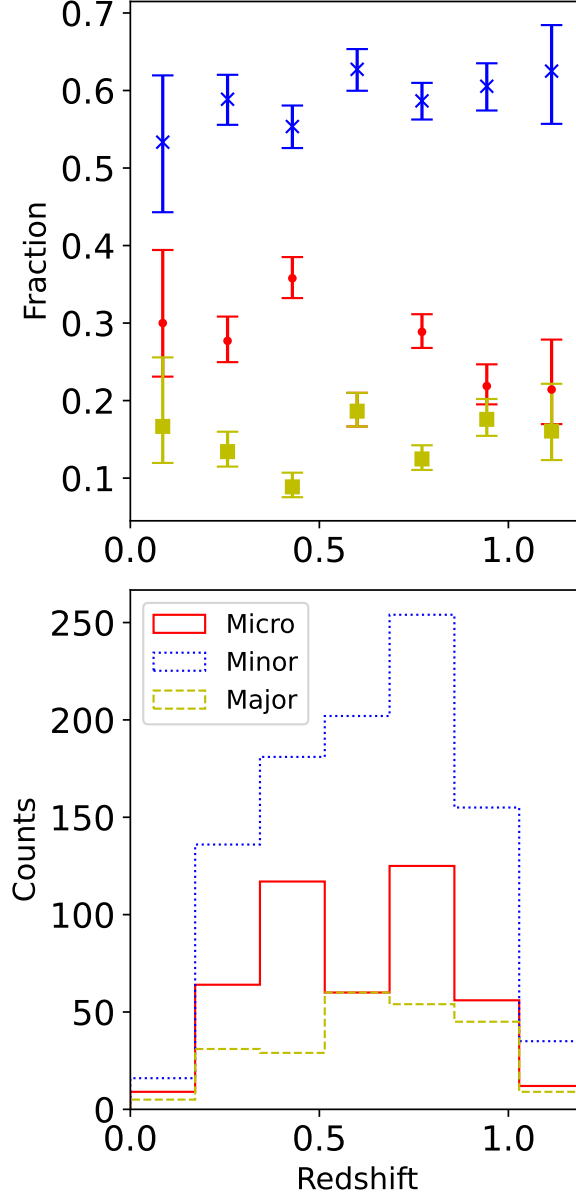


**Figure 3.11:** The change in found interaction type across our redshift distribution. We define interaction types from the mass ratio of paired galaxies in our paired sample. *Bottom:* The distribution of different interaction types across redshift. *Top:* The change in the fraction found of different interaction types with redshift. As expected, the minor and major interaction fractions remain consistent with redshift but the micro interaction fraction declines. This is a result of surface brightness dimming on the tidal features formed in the interactions. In a micro interaction, we would see the complete destruction of the secondary into stellar streams about the primary galaxy. Such a tidal feature would be in the low surface brightness regime, and quickly be lost at increasing redshift. However, the change in fraction we find across our redshift range is not high enough to alter our conclusions.

that could change our conclusions. Therefore, we show this as a warning to those who might use our methodology over a wider redshift distribution.

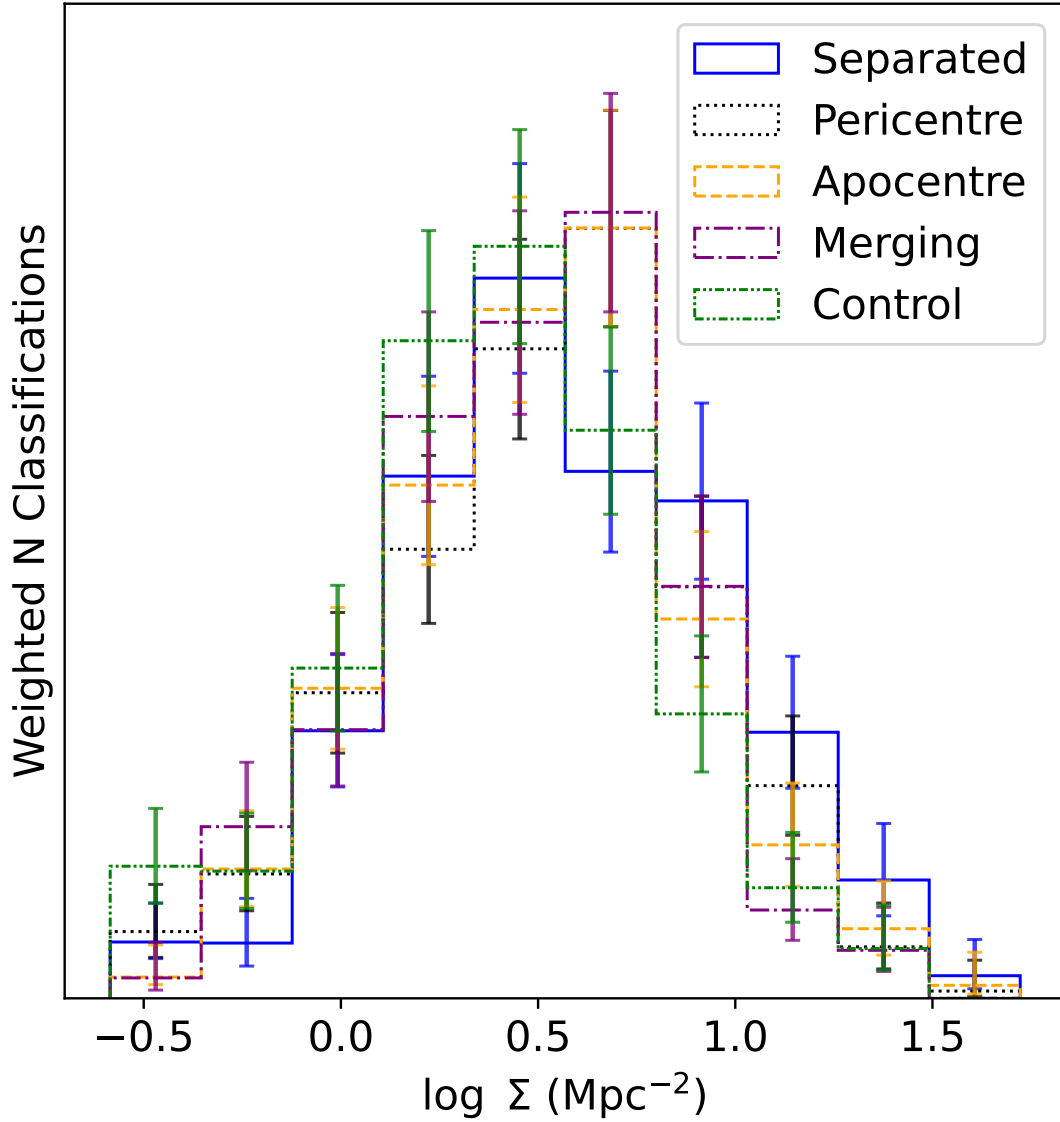
The final limitation of our approach we discuss is of relying on visual classification to identify interacting galaxies. Besides the issue of close pairs (described in previous sections) there is also assuming the disturbance of the systems is due to interaction, and not from other processes. The most obvious process which could mimic tidal disturbance is that of ram pressure stripping (RPS). RPS is an effect of the galactic environment stripping out the gas within a galaxy, and causing the formation of what appears like debris about the galactic disk. It can also cause major disturbance and irregular morphology. Thus, this could easily be a form of high contamination in the apocentre and merging stages of our sample. The environment that RPS is most prevalent is that of a cluster environment. Therefore, if we are highly contaminated to identifying RPS galaxies as interacting galaxies, we would see a bias in the environment of our sample toward galaxy clusters. To check this, we measure the distributions of our galaxies in each environment with stellar mass. We use the sample matched to Darvish et al. (2017) as described in Section 3.3.2.

Figure 3.12 shows the distribution of our matched samples with their density values with Figure 3.13 showing the change in environment fraction with stage. It is important to note that Darvish et al. (2017) has a higher mass cutoff than we have implemented in our underlying sample. Therefore, this is showing the density of all systems  $\log M_*/ M_\odot \geq 9.6$ . We conduct weighted Kolmogorov-Smirnov (KS-test; Kolmogorov, 1933) and Anderson-Darling (AD-test; Stephens, 1974) tests on the environment distributions. The KS-test is excellent at comparing different weighted distributions and indicating if they are drawn from the same parent sample. The AD test tests for this similarity as well, and we use both to ensure consistency and robustness in our measurements. We conduct this calculation based on the mass weighted counts in each stage and with the control sample. We find reasonable  $p$ -values  $\geq 0.85$  between each sample, meaning each stage sample is likely drawn from same parent sample of environment measures. However, when we compare to the control, we get a significantly smaller  $p$ -value. This is  $\sim 0.1$ , with a calculated significance difference of 2. Figure 3.12 shows the mass weighted distributions of each of our interacting stage samples as well as our

control sample. The errors are calculated as the  $2\sigma$  Poisson Confidence Interval based on the counts in each bin (Gehrels, 1986). We can see that the control distribution peaks at a lower number density when compared to the interacting sample. While this will not affect our comparison between the samples of different interaction stages, it is important to note that our sample has a slight bias toward higher density environments when compared to the control, as expected.

We also check the SFR-stellar mass relation between our four interacting stage samples and environment, and show these in Figure 3.14. This shows that there is no ordered structure, or bias, in our sample with environment across our four stage samples and further reinforces that the galactic environment is not responsible for effects we may find from interaction. The majority of our sample lie either within filaments or in the field. The environment which would have the most effect upon the SFRs of our sample is a cluster environment. However, the fraction of our sample within a cluster is never greater than  $\sim 20\%$ . Therefore, the lack of information here does not have a large impact on this measurement.

Another source that could be of major contamination is in our merging stage sample. We have identified the merging stage as those systems with a disturbed disk and containing more than one core. Another such system that could be recognised by this description is that of a clumpy galaxy. Clumpy galaxies are systems with internal regions undergoing intense star formation. These regions appear like multiple other ‘cores’ throughout the galactic disk which are actually clumps of young stellar populations. To avoid such contamination, we apply multiple criteria to mitigate the potential impact they might have. First, our redshift range spans a sufficient range that the found fraction of clumpy galaxies declines rapidly compared to the merger rate, settling at a fraction of  $2.38^{+0.33}_{-0.30}\%$  in  $0.02 < z < 0.15$  (Adams et al., 2022). The decline in the fraction of clumpy galaxies is particularly true at  $0.15 \leq z \leq 3$ , where the fraction drops from  $> 40\%$  at  $z \sim 3$  to  $15\%$  by  $z \sim 0.5$  (Guo et al., 2015). Other works have found the peak of the fraction of clumpy galaxies at  $z \sim 2$  (Murata et al., 2014; Guo et al., 2018), well beyond our redshift range before this rapid decline occurs to  $z \sim 0.5$ . There are also two morphological distinctions that we use to our advantage to discern between merging and clumpy galaxies. Clumpy galaxies often exhibit more than one clump at different radii across the galactic disk (with Adams et al., 2022,



**Figure 3.12:** The density about each of our sources matched with the Darvish et al. (2017) catalogue. As shown, there is no existing bias in the distribution of galactic environments throughout our stages. We also plot the weighted density distribution of the control sample. Here, we find that the peak in density is at a lower value  $0.5 \text{ Mpc}^{-2}$  compared to our interacting sample. Errors are found by calculating the Poisson confidence interval for each bin. Therefore, that we have identified primarily tidal affects and not environmental ones.

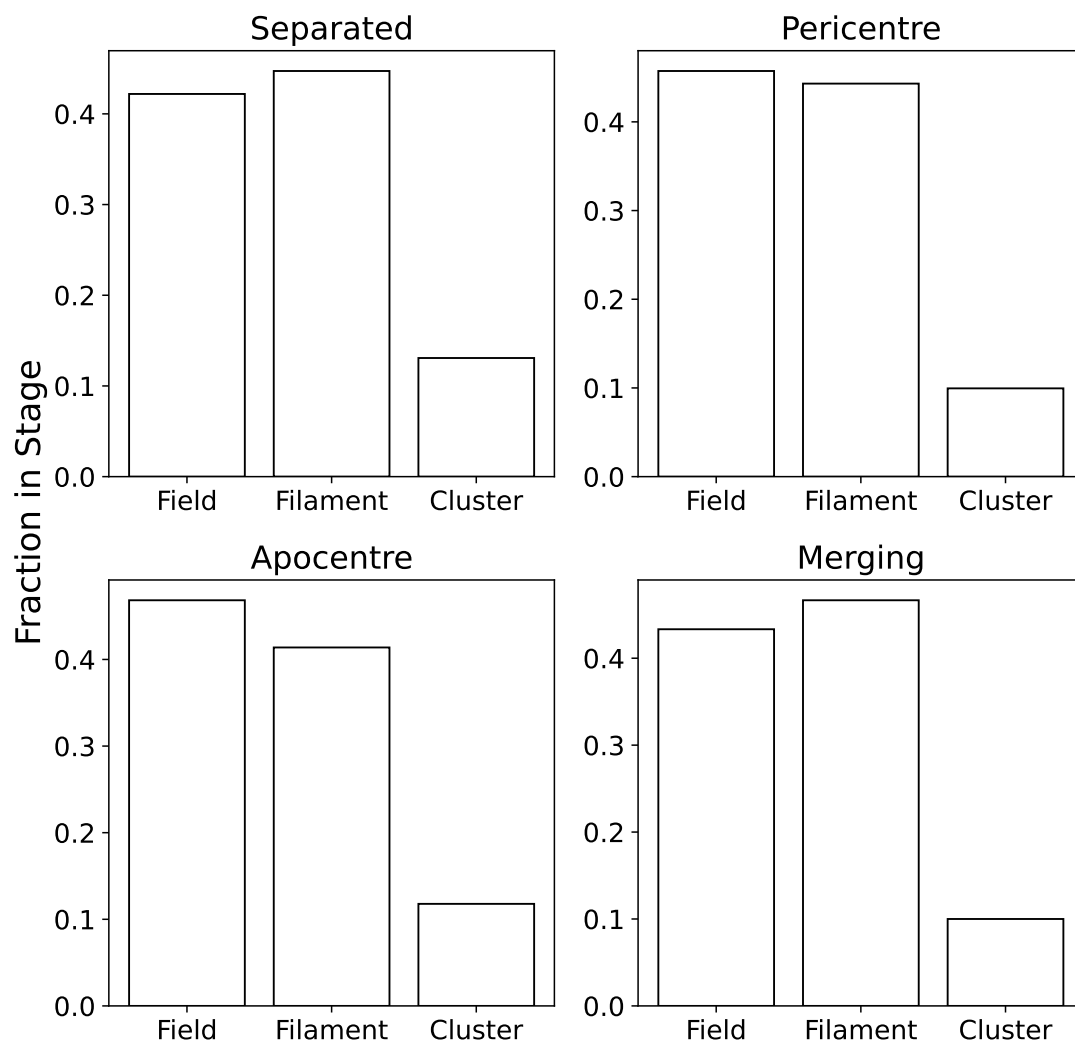


**Figure 3.13:** The fraction of galaxies in each stage in different environments. This reinforces that there is no overarching bias between our samples for the cluster environment. In the cluster environment, RPS could lead to morphologies which appeared like tidal disturbance.

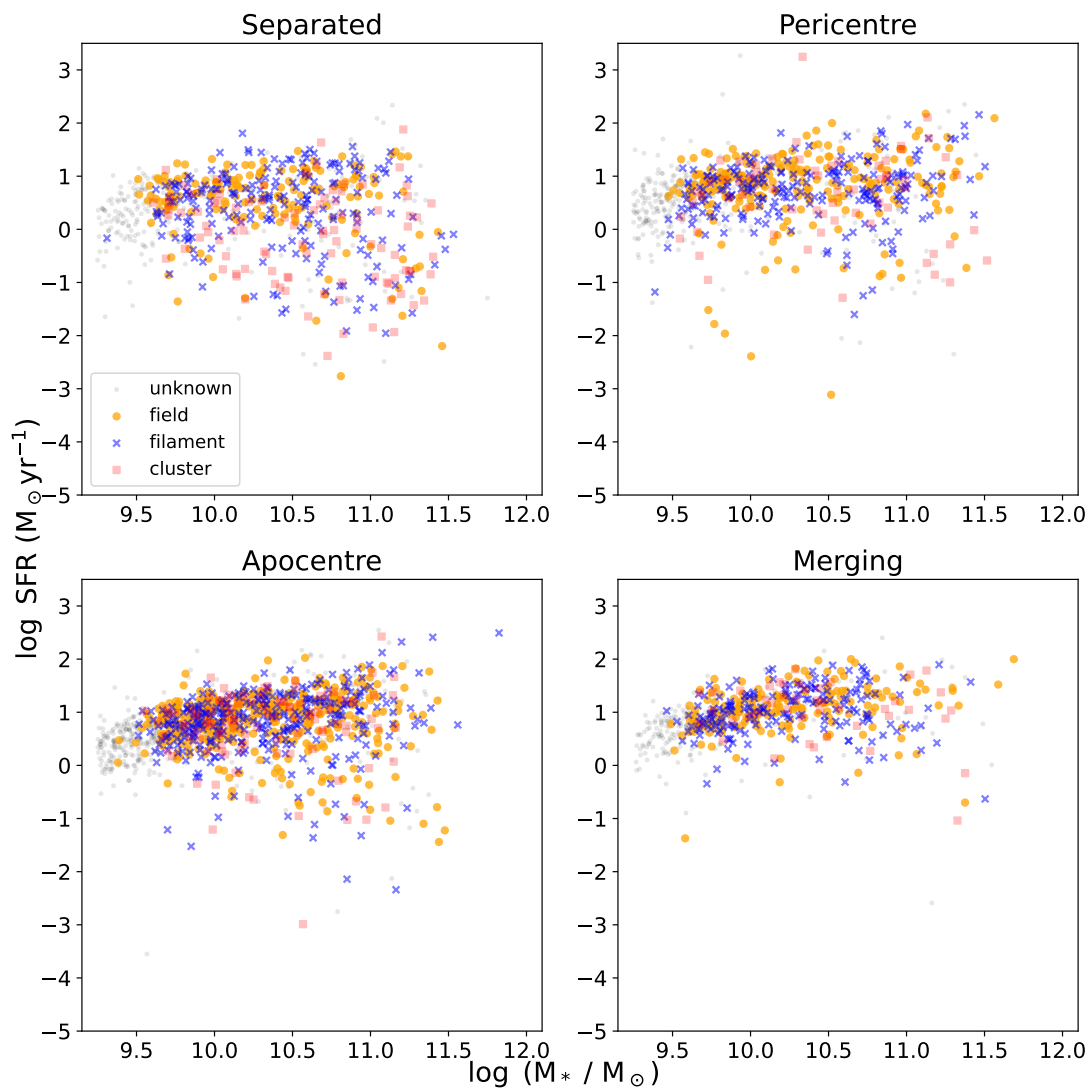


**Figure 3.14:** The distribution of environment classifications through our sample. This is only for sources with a  $\log M_* / M_\odot \geq 9.6$ . However, from this subsample, we see that there is no trend with environment and that the distribution is random throughout each stage.



finding a mean of 3.16 clumps per galaxy), making them easy to differentiate from a second core which would be close to the centre of a perturbed disk. We therefore remove potential merging galaxies which appear to have more than one ‘core’ at different places of a non-perturbed disk ( $\sim 25$ ). With the low fraction of clumpy galaxies in our redshift range and an increased number of cores compared to mergers we are confident we have separated out potential contamination by clumpy galaxies.

### 3.3.6 Aside: Mass Ratios in Sample

Here, we briefly discuss the mass ratios we find of our identified pairs of interacting galaxies. Figure 3.15 shows the distribution of interaction types through our subsample. We find that our sample is dominated by micro and minor interactions.

The mass ratio is known to have a direct impact on the potential enhancements we see in SFR and in AGN fraction. While we do not focus on the mass ratio throughout this work, due to the limited pair galaxy size, knowing that we are dominated by micro and minor interactions will inform us of the relations we expect to uncover from our analysis. This assumes, of course, the subsample of galaxy pairs is representative. With this note on the distribution of interaction types based on mass ratio in mind, we now look at the relation between the stellar mass of our systems and the SFRs through interaction stage.

## 3.4 Star Formation and AGN Evolution with Interaction Stage

### 3.4.1 Controlling for Interaction Stage

With our mass-limited sample selected, we investigate the change in multiple parameters with stage of the interaction. First, we show the results of breaking down our sample into stages with relation to the SFR and stellar mass of our sample. We use the estimates of these parameters that exist in the COSMOS2020

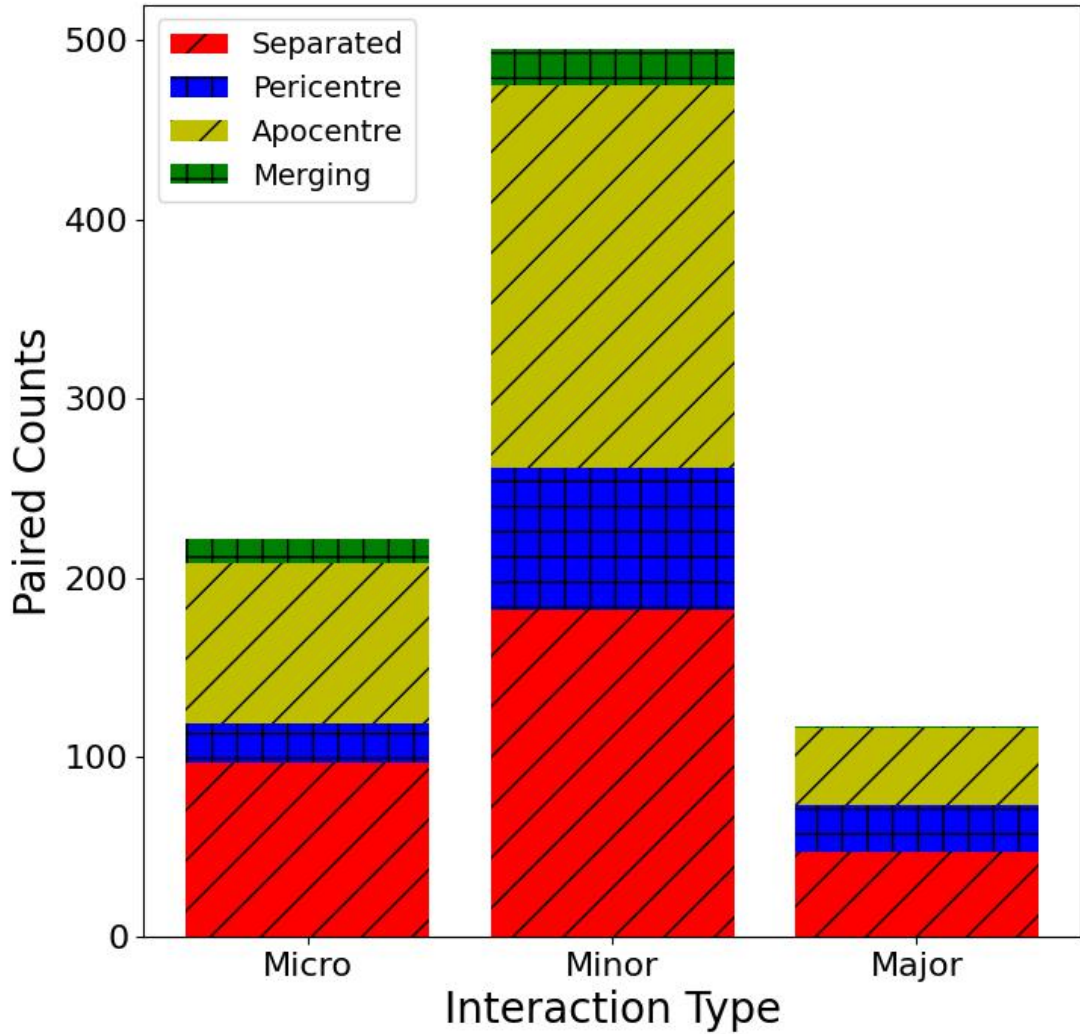


**Figure 3.15:** The distribution of mass ratios in our paired sample and across each stage of interaction. The ratio has been calculated as the mass of the least massive galaxy in the pair divided by the mass of the more massive galaxy in the pair. These are separated into our previously defined interaction stages and the interaction type (based on mass ratio). We find that, overwhelmingly, our sample is dominated by micro and minor interactions. These are where the two systems have very different stellar masses.

catalogue itself. Then, we use our subsample of galaxy pairs to recover the relationship between projected separation and star formation enhancement (SFE). We then further break this measure down into its component stages.

Figure 3.16 shows the breakdown of stellar mass and SFR with stage. On a population scale, there is clear evolution in the star formation rate from the separated stage through to the merging stage. In the separated stage, where the galaxies are distinct from one another with no clear morphological disturbance, we clearly see two populations of galaxies. These are the blue, star-forming galaxies and red sequence of galaxies. The blue contours in Figure 3.16 show increasing number density in the population into the blue cloud. In the pericentre stage, when the galaxies are actively interacting and overlapping, this red sequence remains but is highly diminished while there is no change in the blue cloud. The apocentre stage shows a similar effect, where the red sequence reduces again before finally in merging the red sequence completely disappears. Through these, the blue cloud remains highly populated and hosts the majority of galaxies in the stage.

However, this result could also be due to many other factors rather due to interaction stage. For instance, if the mass distribution of our sources evolves as well, we could simply be selecting higher mass systems as we increase stage. This would have the result of systems in the merging stage having, on average, higher SFRs than those in the separated stage and appearing like we had evolution in the star forming population with stage. Another effect that could cause this relation to appear would be our selection was highly dependent on galactic environment. However, we have already explored this possibility in Section 3.3.2 and found no bias in environment between the stages. While there is a slightly higher fraction of cluster galaxies in our separated stage, we find in Figure 3.12 they are scattered across our sample with relation to SFR and stellar mass. Therefore, this is likely not the cause of a larger red sequence in our separated stage.

We can quantify the similarity of the mass distributions, and then the SFR distributions, using well known statistical tests. We opt to conduct tests: KS and AD-tests. First, we create weighted distributions of stellar mass. The weighting scheme we use balances the distributions such that each bin could be assumed to have the same number of sources within it. Therefore, any bins with fewer than a

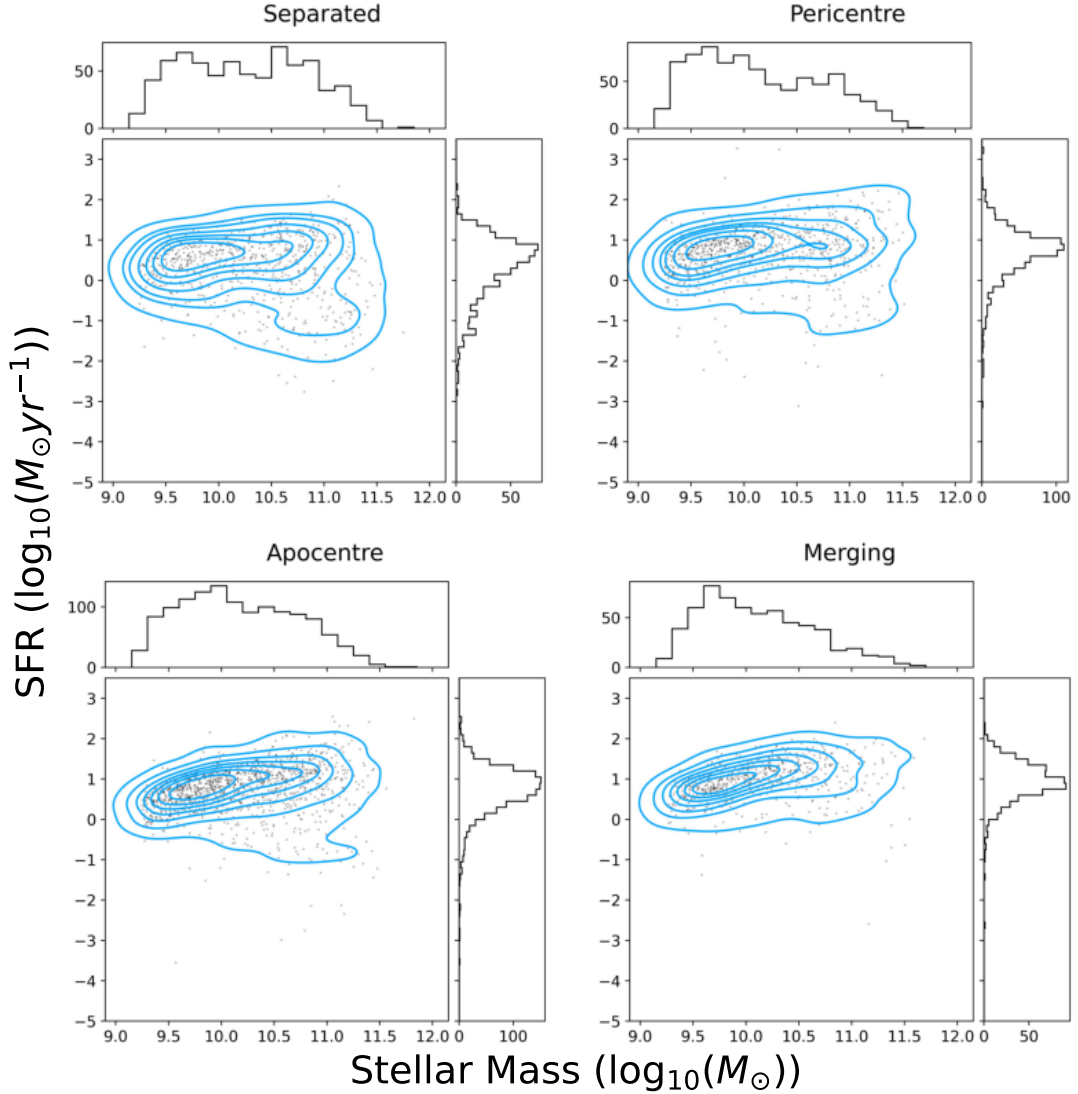


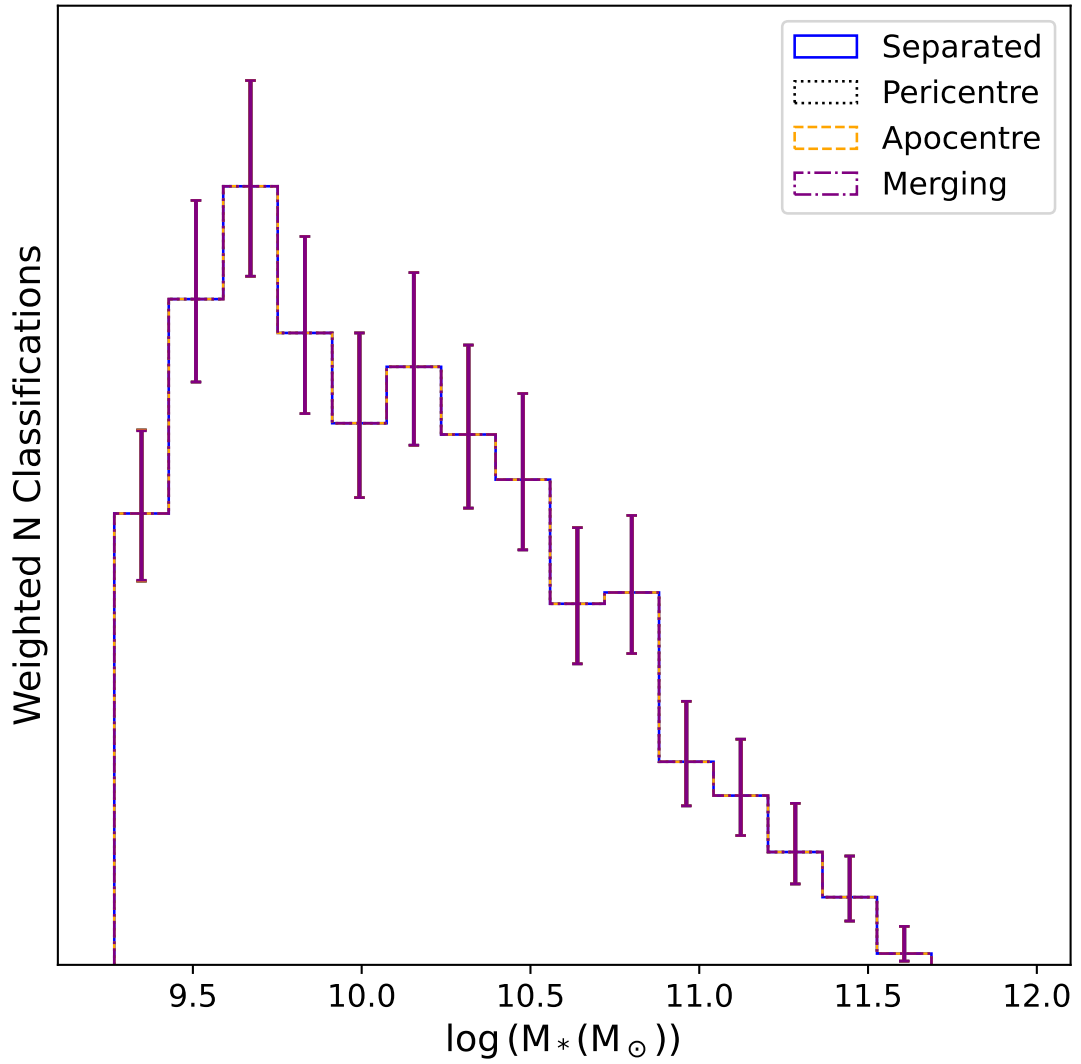
**Figure 3.16:** The LePhare stellar mass against the EAzy SFR across the different stages of the interaction. The blue contours are 8 levels of density of the underlying populations in each frame. *Top left:* The stellar mass and star formation rate of the separated stage of our sample. Here, the interacting galaxies are simply close pairs with little to no morphological disturbance. There are clearly two populations here: a main, star forming sequence forming the main population and a smaller red sequence. *Top right:* pericentre stage of the interaction, where the two galaxies are close to pericentre. The star forming sequence remains, but the red sequence is reduced significantly. *Bottom left:* apocentre stage of the interaction, where the galaxies are close to apocentre or escaped. Here, we see the almost complete disappearance of the red sequence. *Bottom Right:* merging stage of the interaction, where the two systems are close to or have coalescence. The red sequence of galaxies has completely disappeared.

certain number of sources will be weighted up while those bins with more will be weighted down. These weights applied to the mass distribution are then applied to the SFR distribution as to control for stellar mass in this distribution.

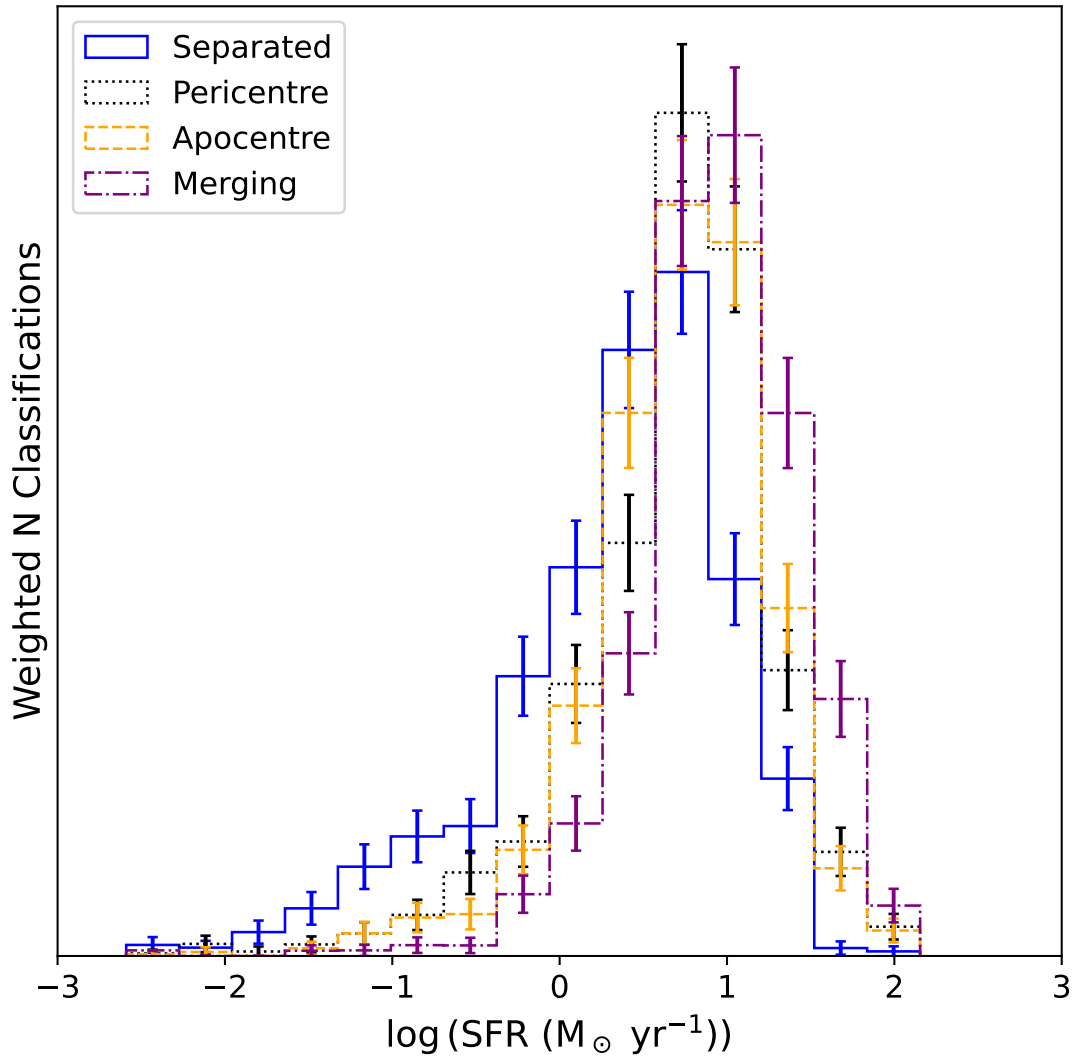
Figure 3.17 shows the weighted mass distributions through the four different stages. By design, the weighted distribution has identical counts, with the error calculation being conducted as an estimate of the  $2\sigma$  confidence interval assuming an underlying Poisson distribution. This is the same as done for the environment distributions. We statistically measure the similarity we apply our KS- and AD-tests to them. We chain the KS and AD test through each distribution and calculate the value of the test values and a  $p$ -value. This  $p$ -value represents the probability that each distribution is drawn from the same parent distribution. For each mass distribution, we find that  $p$ -value of both tests is  $\approx 1$ . Thus, this proves that the distribution in stellar mass though each stage is likely drawn from the same parent sample.

Figure 3.18 shows the SFR distributions while being weighted by stellar mass. When comparing the separated and pericentre, separated and apocentre, separated and merging, pericentre and merging and apocentre and merging stages, the  $p$ -values are  $\ll 0.05$ . This allows us to reject the null hypothesis for these distributions and assume they are from different parent samples. However, for comparing pericentre and apocentre stages, the  $p$ -value = 0.74. Thus, while these distributions are likely to be not identical, they are very similar in the parent sample they have been drawn from. For the same mass distribution through each stage of interaction, the star formation distribution changes from separated to pericentre stage and from apocentre to merging stage, while remaining similar from the pericentre to apocentre stage.

Putting this result into the context of the dynamical timescale of an interaction, it shows there are distinct points at which the SFR changes in these systems. The first is when the interacting system moves from being a close pair to actually morphologically disturbing each other in a close flyby. This difference, most likely enhancement, then persists through to the apocentre stage - where the galaxies remain highly disturbed but are no longer overlapping with their secondary. The SFR distribution remains approximately the same between these two, meaning the forces that drive and affect star formation remain equivalent between these



**Figure 3.17:** The stellar mass distribution across the four stages. Each bin is weighted based on the counts in the smallest sub-sample in stage: the merging stage of the interaction. These counts have been weighted so that there are equivalent counts in each distribution. The error bars are calculated by estimating the  $2\sigma$  confidence interval on the underlying Poisson distribution.



**Figure 3.18:** SFR distribution weighted by mass across each stage. This weighting is based on our sample of merging stage.

two stages. Finally, the SFR changes again when we approach the merging or post-merger stage of the interaction. We can also say that this change is likely an enhancement in the SFR of the galaxies through the interaction due this change being driven by the disappearance of the red sequence through each stage.

We further examine this result by controlling for redshift and making specific classifications of galaxy star formation class. While the red sequence is significantly reduced across across each stage, it is difficult to ascertain the change in the galaxies within the blue cloud. We expect that, due to an interaction, the population of starbursting and quiescent galaxies will change. Therefore, we define a star forming main sequence (SFMS) across redshift. This allows us to classify each source based on its SFR independently of redshift. To define the star forming main sequence, we follow the example of Aird et al. (2019). There, they define the star forming main sequence as a function of galactic stellar mass and redshift as

$$\log \text{SFR}_{\text{MS}}(z)[M_{\odot} \text{yr}^{-1}] = -7.6 + 0.76 \log \frac{M_{*}}{M_{\odot}} + 2.95 \log(1 + z). \quad (3.1)$$

This finds the expected main sequence SFR of a galaxy at a given stellar mass,  $M_{*}$ , and redshift,  $z$ .

The ratio of the measured galaxy SFR and the expected main sequence SFR is then taken. We then use this fraction to classify each galaxy into distinct bins. These bins are:

- (i) Starburst galaxies. Here, the galaxy SFR is highly elevated compared to the SFMS. We follow Aird et al. (2019) and define a cutoff of  $\log \text{SFR}/\text{SFR}_{\text{MS}} > 0.4$ .
- (ii) Main sequence galaxy. The galaxy is within 0.4 dex of the SFMS and approximately has the expected SFR, defined as  $-0.4 < \log \text{SFR}/\text{SFR}_{\text{MS}} < 0.4$ .



- (iii) Sub-main sequence galaxy. A galaxy whose SFR is below the majority of the SFMS, but likely not quiescent, defined as  $-1.3 < \log \text{SFR}/\text{SFR}_{\text{MS}} < -0.4$ .
- (iv) Quiescent (High) galaxy. A galaxy with an SFR in the top  $\approx 50\%$  of the quiescent galaxy population, defined as  $-2.3 < \log \text{SFR}/\text{SFR}_{\text{MS}} < -1.3$ .
- (v) Quiescent (Low) galaxy. A galaxy with low SFR and very likely completely quenched, defined as  $\log \text{SFR}/\text{SFR}_{\text{MS}} < -2.3$ .

We split our sample into its different stages and apply these criteria. Figure 3.19 shows the ratio between the expected SFMS SFR and the measured SFR in COSMOS2020. This clearly shows a large increase in galaxies classified as starburst from the separated to merging stages and a large reduction in the number of quenched systems. Figure 3.20 shows the change in fraction of the different galaxy classifications through stage, reflecting the results found in Figure 3.16. Initially, in the separated stage, we find that the majority of our galaxies lie on the SFMS or just below it. There also exists a small population of galaxies which are classified as starburst with a population of quiescent galaxies that is roughly double the starburst fraction. We find some of these quiescent galaxies exist in cluster environments, but not to a significant extent to affect our results. As we move through the interaction stage, we see that the quiescent galaxy fraction gradually decreases to the point of almost non-existence in the merging stage galaxies. The inverse is true in our starburst fraction. We find this almost quadruples over the course of the different stages of interaction. The fraction of galaxies on the SFMS remains dominant throughout, however, we do find the fraction of sub-MS galaxies significantly reduced. We find that, in general, the SFR of these galaxies is increasing with interaction stage (though, not in the pericentre to apocentre stage). It appears to have sub-MS and quiescent galaxies move up and join the SFMS (as it remains dominant). But, many galaxies from the SFMS are moved upwards and into a starbursting phase.

It is important to note the parameter space that we are searching in these examples. We are probing interactions between galaxies of high mass, where the resultant tidal features that form would be classifiable in an image. The

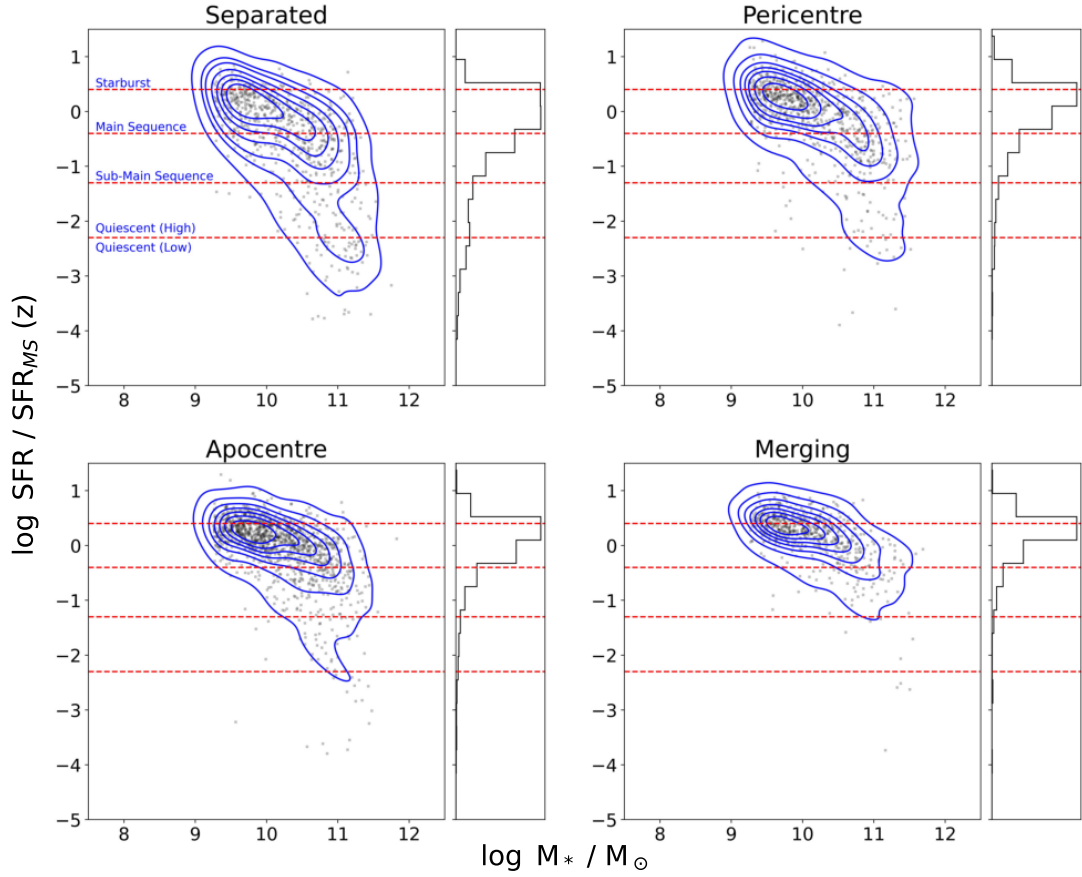


**Figure 3.19:** Stellar mass against the ratio of measured SFR to the expected SFR if the galaxy was on the SFMS. This is of all galaxies in our sample. Black points are the individual sources, while the blue contours are as in Figure 3.16. The red dotted lines show the cutoffs for different galaxy classifications based on their SFR, with each cut off being defined by the text in blue. The histograms beside each plot show the change in counts. We find that through interaction stage, the quiescent galaxy population significantly reduces while the starburst population rapidly increases. As these cutoffs are also dependent on redshift, we find that this evolution in SFR with interaction stage is independent of redshift.

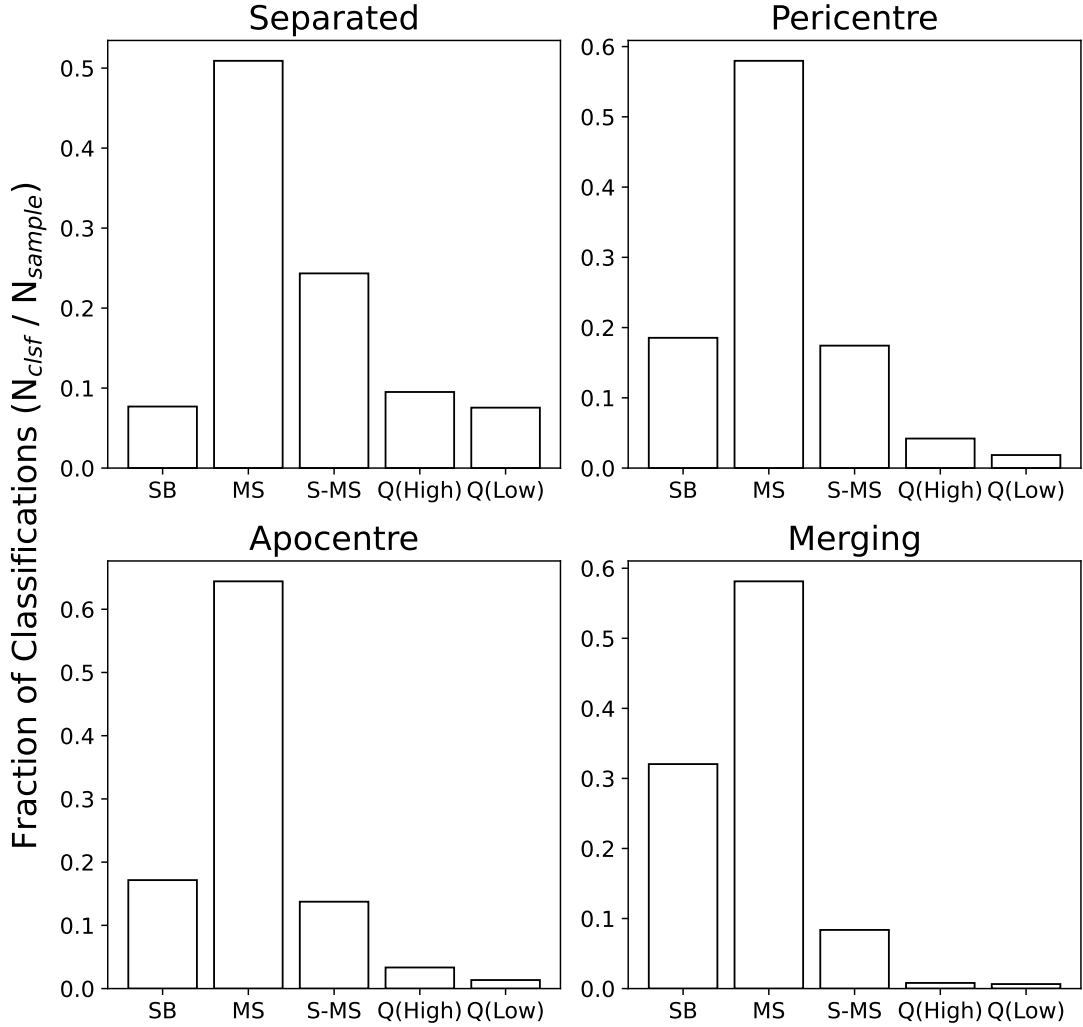


**Figure 3.20:** The change in fraction of different galaxy classifications from the fraction of SFR to the expected SFR on the SFMS. While galaxies on the SFMS remain dominant through each sample across interaction stage, there is significant change in the starburst and quiescent populations. The starburst galaxy population moves from being roughly half the size of the quiescent population in the separated stage to completely dominating it in the merging stage. This is occurring while the quiescent population is significantly reduced to almost non-existence in the merging stage.

majority of our sample is minor interactions where one of the two systems is very highly perturbed by the interaction. In this parameter space, we would expect large increases in the SFRs. However, we do not see a significant increase in the starbursting population until we the two galaxies begin to actually coalesce. Thus, the effect of the interaction itself may be to only enhance the SFR, while at coalescence we find the dramatic starburst. This can be argued from our results of clear, statistically robust change and evolution of a galaxy's SFR with interaction stage. The SFR changes dramatically from the separated to pericentre stage and apocentre to merging stage - after the initial passage of closest approach and at the point of coalescence of the interaction.

### 3.4.2 Projected Separation and Star Formation Enhancement

We directly investigate the relation between the SFE and the projected separation using our confirmed sub-sample of galaxy pairs. This sample is significantly smaller than our non-pair sample: containing 607 pairs or 1,214 galaxies. Upon sub-dividing this into different stages we find 253 separated pairs, 94 pericentre pairs and 241 apocentre pairs. Only 19 merging galaxies were in our confirmed galaxy pair sub-sample, and therefore we do not attempt to make inferences about this population.

To measure the SFE of our galaxy pairs, we directly compare to the mass- and redshift-matched control sample that was also created with this sub-sample and defined in Section 3.2.2. We separate our galaxy pairs into different bins based on the projected separation between them. We find that the bulk of our sample has a projected separation between the two galaxies of  $\leq 50$  kpc. Therefore, we sample from this region of the parameter space with high precision and smaller bin widths before we increase the bin widths at larger projected separations. We define a cutoff that each bin must contain at least 10 counts to be included in this plot and, therefore, by changing the bin widths with projected separation we are able to maintain some level of statistical robustness. We define our bins as [0.5, 10, 20, 50, 100, 125] kpc.

We create two projected separation distributions: one of interacting galaxies and the other of our control galaxies. We then take the average of each bin. By taking the average of each bin, we find the total excess of the SFR caused by interaction alone and then compare it to what we would expect from non-interacting galaxies in the same bin. Note that the control galaxy relation to the projected separation is meaningless as they are not paired. The control galaxies are simply mass and redshift matched to each interacting galaxy and used as a reference for what SFR we would expect of it had it not been interacting. Finally, we divide the averaged interacting SFR distribution by the averaged control SFR distribution. This provides us with a measure of the excess star formation due to interaction, and the SFE when compared to the isolated population.

Figure 3.21 shows star formation enhancement between our interacting and control binned SFRs and the projected separations between each galaxy pair. On the left of the plot, we have the distribution for the full galaxy pair sample, without taking account of stage. The errors on our measurements are following the methodology of Cameron (2011) and briefly described in Section 3.4.1. The dashed black line represents no enhancement in SFR, as the average SFR in the interacting galaxy sample would be equal to the average SFR in the control sample. We find at very small projected separation a SFR enhancement of 1.74 which gradually decreases with projected separation down to approximately 1 at 117.5kpc.

On the right, we break the galaxy pair sample into different stages and plot out the resultant enhancement in star formation. This shows very different behaviour in enhancement dependent on the stage of the interaction. In the separated stage, we find that the star formation is very weakly enhanced, and with no overall structure. The enhancement moves around 1 through the distribution, with some enhancement being a result of low number counts in the bin. This is not unexpected. The separated stage represents when the two galaxies are close pairs, but with no morphological disturbance. Therefore, we would not expect significant, if any, enhancement in the SFR based on the projected separation. This is the stage with the lowest enhancement across projected separation.

In the pericentre stage, we see consistent enhancement with projected separation. It is also much larger than the separated stage, with it being approximately

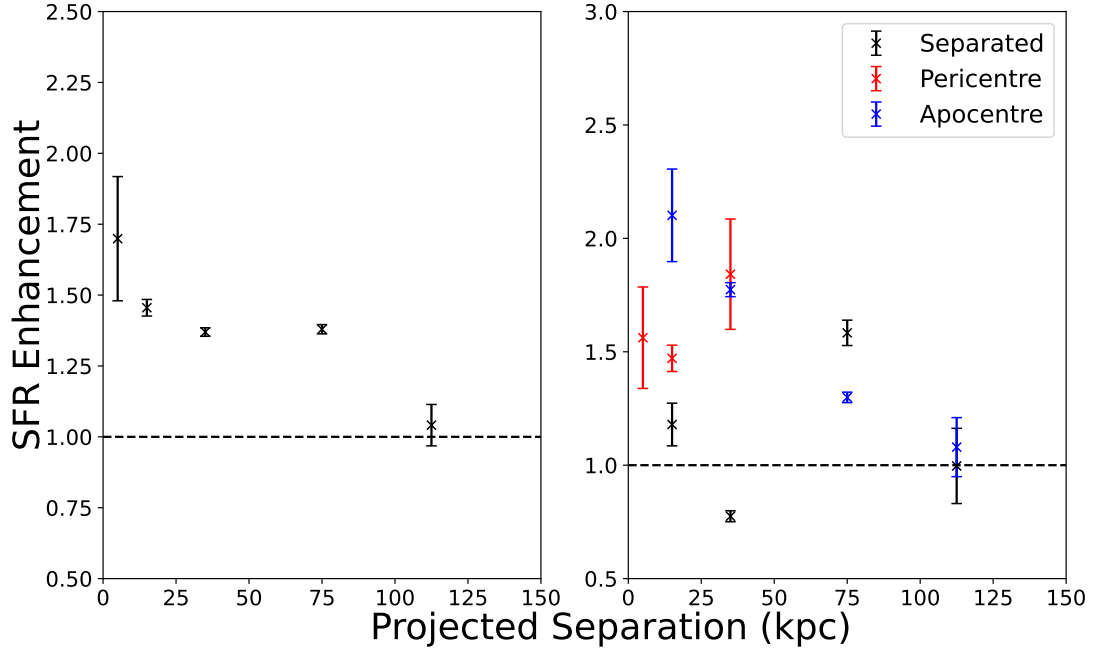


**Figure 3.21:** The projected separation against the SFE in average star formation at different bins of projected separation. Each bin must contain at least 10 counts to be considered. As the bulk of our galaxy pair sample is at low projected separation, we heavily sample from this region of the parameter space. The bins are: [0.5, 10, 20, 50, 100, 125] kpc. As we move to higher projected separation, the bins increase in width to maintain statistical significance in our sample. *Left:* The star formation enhancement found in the entire galaxy pair sample. As expected, we see a gradually decreasing enhancement. *Right:* As left but broken up into different stages of the interaction. Black markers are the separated stage, red the pericentre stage and blue the apocentre stage. We limited our investigation to the separated, pericentre and apocentre stages as only three galaxy pairs were identified in the merging stage. We find a generally decreasing star formation enhancement with projected separation but very different individual behaviour dependent on the stage classification.

1.6. In fact, the measured enhancement increases across the 50kpc of projected separation. However, accounting for the errors on these measurements and the declining counts in each bin, it is likely that the enhancement remains constant as the projected separation increases. We see a very large enhancement in the overlapping apocentre stage galaxies which overlap with the pericentre stage measurements. The enhancement in apocentre stage galaxies then rapidly declines as we move to higher projected separations. After 150kpc, our galaxy pair sample does not have the counts to make robust estimates of the SFE. However, it is important to note that this result has been found with a sample of 607 pairs. No merging stage galaxies have been represented and in numerous projected separation bins the counts are small enough to have conclusion altering error bars. Therefore, it is imperative that future works, with larger sample sizes not only look at the projected separation of the systems but the morphology as well.

### 3.5 Nuclear Activity with Interaction Stage

We now use our AGN sample matched with the AGN catalogues described in Section 3.3.3. As stated previously, we find matches of 802 AGN and star forming galaxies (SFGs) in our volume limited sample. These are from both the sample of primary and secondary galaxies. The breakdown of number of classifications per stage is shown in Table 3.2. Figure 3.22 shows distribution of stellar mass to SFR with stage, with the confirmed AGN and SFGs marked. We find no major changes in AGN with stellar mass or SFR with stage in our sample. Galaxies containing AGN appear throughout the starburst, the SFMS and red sequence across each stage. There is no obvious bias in stellar mass or SFR for hosting an AGN. We do, however, see a concentration of AGN in the separated stage on the red sequence at higher masses. This changes as we increase interaction stage, with the bulk of the AGN beginning to appear at lower masses in the apocentre and merging stages. Finally, in the merging stage we see AGN and SFGs distributed almost evenly across the star forming main sequence with little bias in distribution with mass.

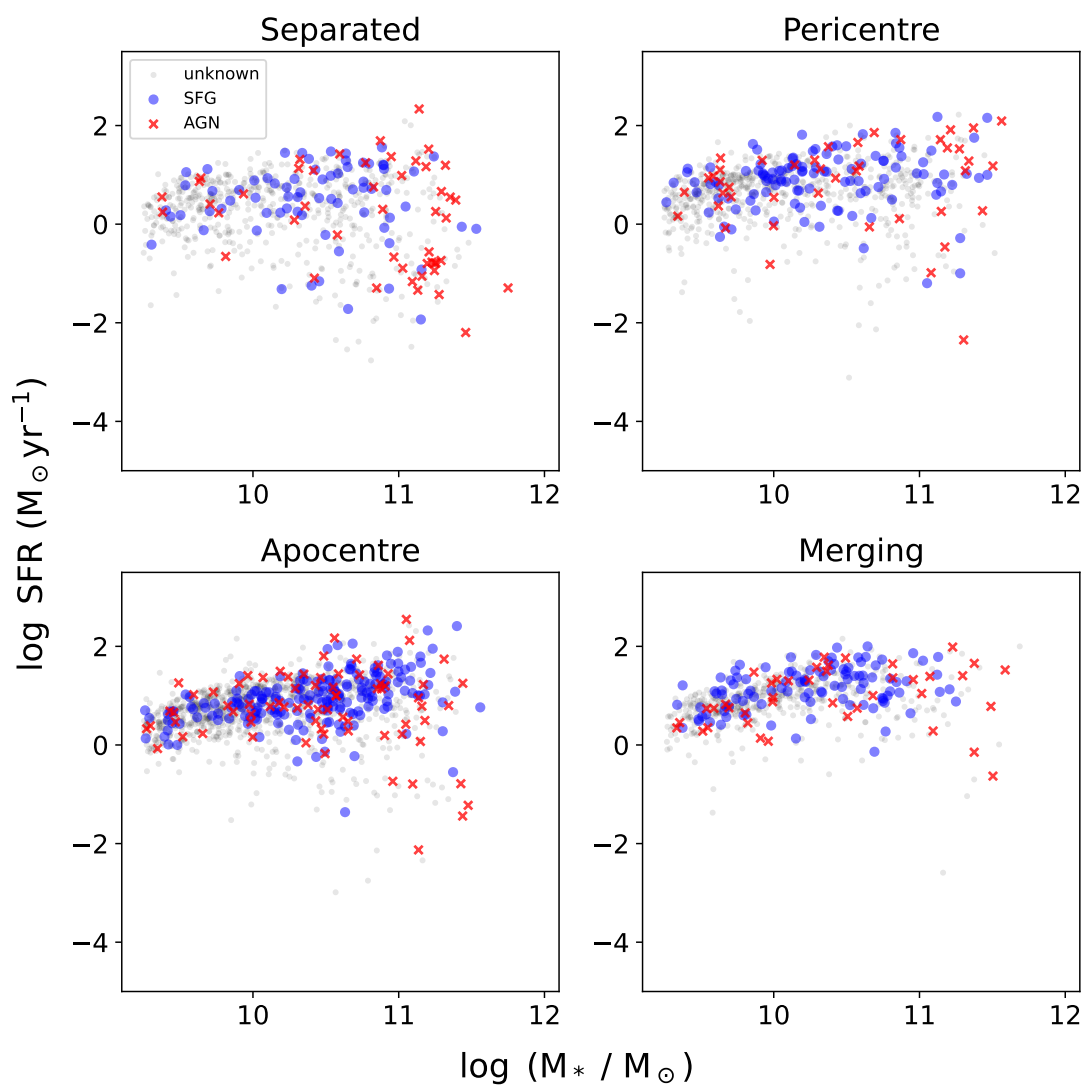
	Separated	Pericentre	Apocentre	Merging
SFG	79	135	216	121
AGN	58	55	88	50

**Table 3.2:** Breakdown in number of classified AGN and SFGs per stage. With our counts so low in this sample, it is difficult to make concrete conclusions about the evolution of AGN during interaction.

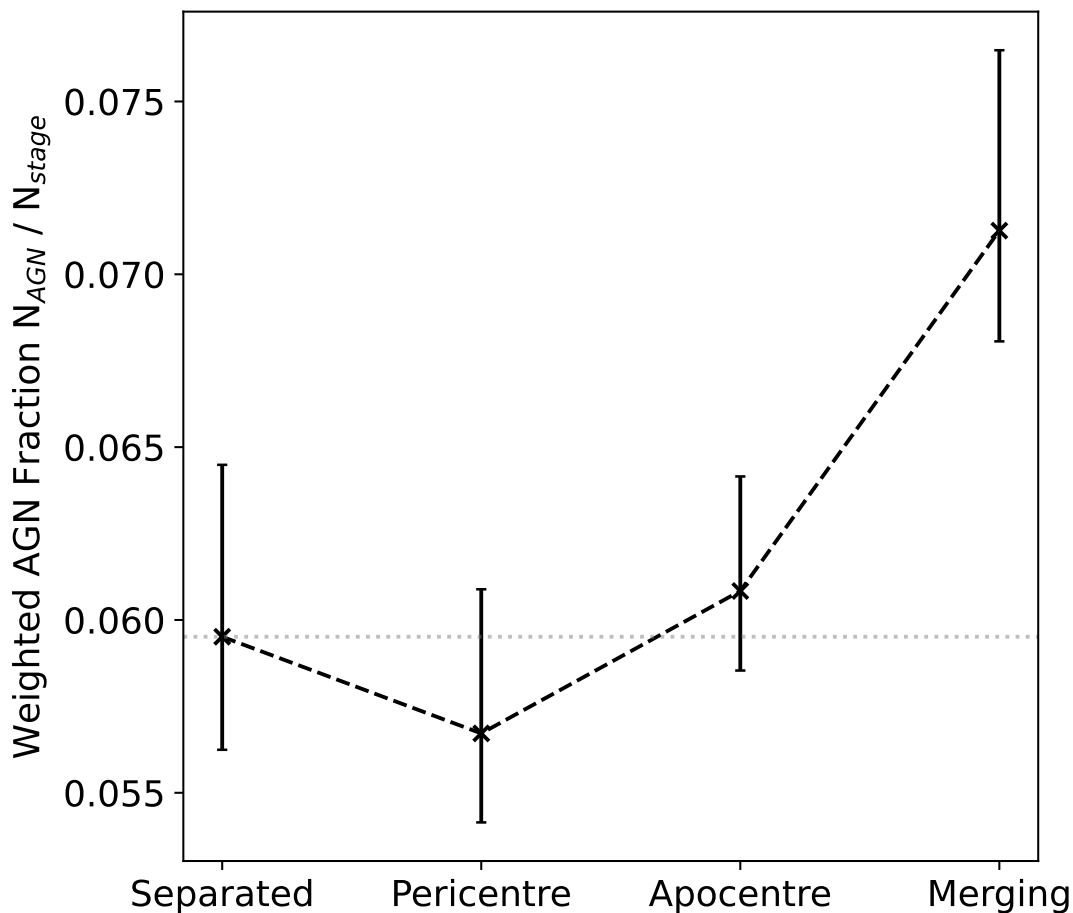
Applying KS or AD tests to these, however, reveals  $p$ -values close to 1 and therefore these distributions are consistent with being drawn from the same parent sample. However, due to the low counts of AGN and SFGs in our sample, using KS and AD tests to verify this is not optimal. Therefore, we instead investigate the global AGN fractions in our sample across different stages. We apply a weighting, as in our SFR and stellar mass distribution examples, to account for the various counts across the different stages. We then take a second weighting of the measured AGN fraction from the total size of the different samples we have. Thus, we have assumed that we have equivalent counts in each mass bin of our sample as well as approximated having the same sample size in each stage bin.

Figure 3.23 shows the changing AGN fraction with interaction stage. The dotted line shows the AGN fraction in the separated stage, which will have little effects of AGN. We find that the AGN fraction generally remains this fraction through the separated to apocentre stages. There is a small decrease from the separated to pericentre stage, followed by the fraction mostly remaining unchanged until the apocentre stage. Then, in the merging stage we measure a large increase in the AGN fraction from  $0.059 \pm 0.004$  to  $0.071 \pm 0.005$ . However, before we discuss this result further, we must point out that the large error bars on our measurements. We are only at the  $3\sigma$  threshold of detecting this enhancement of our merging AGN fraction. The errors on these distributions are calculated using the methodology of Cameron (2011). Rather than assume a Poisson distribution to calculate the error based on the confidence interval, we assume the underlying distribution is the  $\beta$ -function. We use this as, found in Cameron (2011), we retain an accurate measure of the error even with the very low number counts in our AGN samples, making interpretation difficult.





**Figure 3.22:** The distribution of AGN through stage with SFR and stellar mass. We find that the AGN populate every part of the SFR- $M_*$  parameter space probed in the pair sample.



**Figure 3.23:** The change in AGN fraction with stage. The dashed line shows the AGN fraction in our separated sample, representing a control non-interacting sample to compare to. We define the AGN fraction as the ratio of number of confirmed AGN divided the number of sources in that stage. The weights used are the mass weights described previously. Errors on each fraction are found as the confidence intervals defined via the beta distribution. We find a drop in AGN fraction from the separated to pericentre stage, followed by a rapid increase from the apocentre to merging stage.

It is also difficult to use interaction stage as a proxy for the projected separation in this context. As shown previously, the pericentre and apocentre stages have some overlap in the range of projected separations we have classified them into. Therefore, we also investigate any overlap between our confirmed pairs and the AGN fractions we see here. We find 104 AGN and 180 SFGs overlap with our confirmed pairs. Figure 3.24 shows the change in density of AGN classifications and SFGs with increasing projected separation. As expected, we find that with increasing projected separation the number of confirmed AGN and SFGs decreases. In the AGN distribution, we find two different components. The first is a peak in the projected separation distribution is from 0kpc-25kpc. The only contribution here is from pericentre stage galaxies. The second peak, from a projected separation of 30kpc - 60kpc is dominated by apocentre stage galaxies, although some separated stage AGN are in this peak as well. Finally, the third peak from 85 - 125kpc is representative of a mixture of the separated and apocentre stage galaxies. None of our merging stage galaxies which had their secondaries identified overlapped with our AGN and SFG identified sample.

We find the AGN fraction only increases at the point of coalescence in interaction: the merging stage. This indicates that the mechanism driving AGN ignition in interaction is primarily at the point of the closest approach between the two systems. When we investigate the AGN number counts with respect to the projected separation of systems, we find that it gradually declines over the projected separation. However, we find two peaks; first clearly in the pericentre of the interaction where the galaxies are overlapping and secondly in the early parts of the apocentre stage. This could be evidence of a delayed AGN ignition depending on the underlying parameters of the interaction. Thus, we find that the AGN fraction is generally unchanged with stage, although the mechanisms responsible for an increase in the fraction primarily occur when the two systems are actually merging. We find evidence of a delay of ignition, as there is a peak in AGN counts at a small projected separations in the apocentre stage.

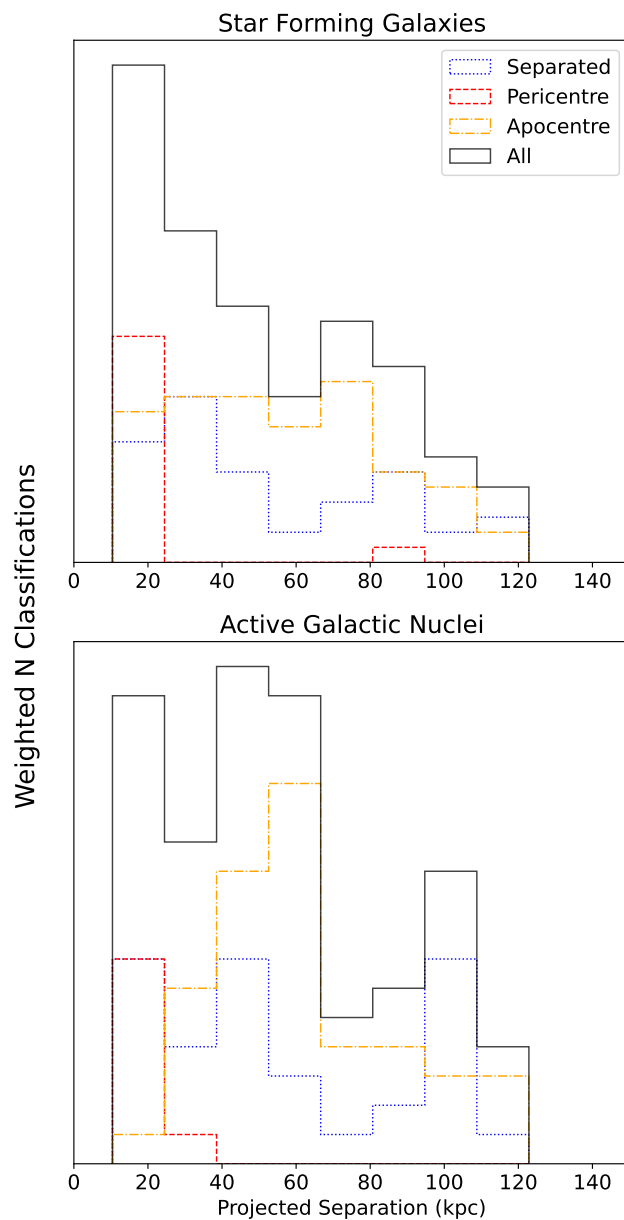


**Figure 3.24:** The distribution of both AGN and SFGs which have matched our confirmed galaxy pairs. These are 104 galaxies containing AGN and 180 classified as SFGs. While we find, as expected, the number of AGN and SFGs decreases with projected separation we find an interesting double peak in the AGN sample. The first peak, between a projected separation of 0 and 25kpc is primarily from pericentre stage galaxies (in red) while the second peak of 40 to 65kpc is of apocentre stage galaxies (in yellow) in our sample. As shown in Figure 3.23, we expect the fraction of AGN to be similar in these two stages despite being at different parts of the dynamical timescale in interaction. The third peak, from 75 to 125kpc is only from separated and apocentre stage galaxies.

## 3.6 Discussion

### 3.6.1 Interaction Stage and Projected Separation

Finding evolution with interaction stage is not a new idea in the field. Multiple works have found increases in SFE and SFR as a function of projected separation of pairs of galaxies (Barton et al., 2000; Ellison et al., 2008; Patton et al., 2013). Projected separation is often seen as a proxy for the point in the dynamical time of the interaction that is being measured. It is likely that, when the galaxies in the pair are closer together, they are closer to coalescence in the dynamical time and can be thought of as a linear progression in the interaction from being close pairs to coalescence. However, what this fails to capture is the larger complexity of interaction. Without morphological consideration, we are unable to tell whether galaxies at small projected separations are actually at the closest point of flying by each other or about to coalesce.

We find that throughout the different stages of interaction the SFR within the systems is increasing. Observations of interacting galaxies at various stages have found increased gas inflows into the nuclear regions of the galaxies which lead to enhancement in the SFR at the galactic core over their outer reaches (Barrera-Ballesteros et al., 2015). This is often confirmed with deep observations of individual systems, which capture snapshots of different parts of the dynamical timescale of the interaction (Karera et al., 2022). Our study utilises numerous snapshots of the dynamical time of interaction in attempt to build a full picture of the change in SFR. We have found that this process increases the SFR of galaxies and that being driven to starburst begins from the pericentre of interaction. Multiple simulation works, which have the ability to model the entire dynamical history, show that this is to be expected (Di Matteo et al., 2007; Hopkins et al., 2013; Karman et al., 2015; Moreno et al., 2021). Often, these works show an initial dramatic increase in the SFR of interacting systems followed by an exponential decline through the dynamical time before increasing dramatically again at either a second passage or coalescence. Moreno et al. (2015) is a direct example of this SF history through the interaction.

Our results differ here as we do not find an exponential decrease in the SFR in the pericentre systems to the apocentre systems. As stated previously, observational work does support a continued increase in SFE in galaxies to projected separations of out to 80kpc - well into our defined apocentre stage systems (for further examples, see Li et al., 2008a; Scudder et al., 2012). However, it is important to note that our apocentre stage defined classification is a ‘wide net’ that captures many systems that may be very soon after the initial passage in the dynamical timescale (recall Figure 3.7). The criteria defining pericentre and apocentre stages are simply that the galaxies must be no longer connected or overlapping morphologically with tidal features. They must only be distinct and separate galaxies. Therefore, our found large enhancement in the apocentre stage may be from interacting systems which are only just out of the pericentre passage and not enough time has passed for the rapid decline in SFR to begin.

Nonetheless, we still find a disappearance of the red sequence in the apocentre systems which may come as unexpected to when compared to simulations. It is important to note, however, that this is not the same as saying that a large proportion of the apocentre systems are classified as starbursting galaxies. While previously mentioned simulations approximate an initial large starburst before rapid decline, we find the interacting galaxy population is pushed from being quiescent / sub-main sequence to being on the star forming main sequence. Therefore, it may be more likely that the impact of interaction on star formation is not to suddenly cause rapid star formation in the aforementioned starburst before declining, but rather to gradually increase a galaxy’s SFR up and into the blue cloud of galaxies. This could be supported by the lack of rapidly quenched post-interaction galaxies found in both observations (Weigel et al., 2017) and simulations (Hani et al., 2020; Quai et al., 2021). Thus, the impact of interaction on star formation may not be a catastrophic increase in star formation that leads to quenching but, rather, a small increase in galaxies to use whatever gas they have into star formation.

This idea can be brought further forward by considering the large increase in starbursting galaxies we find when going from pericentre / apocentre stage to the merging galaxies. The merging stage represents, in our sample, galaxies that are undergoing the final coalescence of the two systems involved. We find that the

point of final coalescence leads to a large increase in the fraction of starbursting galaxies as well as the almost complete disappearance of the quiescent and sub-main sequence fraction of galaxies. Thus, from this result we can conclude that during coalescence galaxies use whatever gas they have into star formation which will quickly lead to their quenching. This is also supported by works such as Ellison et al. (2022), which find that galaxies post-coalescence are 30-60 times more likely than control galaxies to have rapidly shut down star formation.

Thus, we can conclude that, for merging galaxies, if gas is present within them, star formation will increase and change our classification of the galaxy. We will observe a sudden increase in the star formation rates of these systems followed by a rapid quenching as the gas is used up entirely. This differs from galaxies that move into the apocentre stage and do not merge. These apocentre stage systems will then slowly lose their enhancement over a long period of time, and return to star forming at their expected rate, whereas only moving into a merging stage galaxy will lead to a starburst which may incur rapid quenching.

Such a conclusion would also, therefore, explain the often quite large divide in the literature between whether interaction actually leads to enhancement or not. The only part of the interaction which causes the enhancement, and is the forking point, is the pericentre stage. From this point, if the galaxies then move off to the apocentre stage and escape, we will see a gradual decline in the SFE with the apocentre stage galaxy only having a minor increase in its star formation classification, whereas if the galaxies move into the merging stage of the interaction and coalesce we see the results of a major starburst and the complete using and of all the gas in the systems. Thus, this leads to a large fraction of quenched post-merger galaxies, but only after the initial coalescence.

### **3.6.2 Interaction Stage and AGN**

The evolution of the AGN fraction in interacting galaxies is similar to that of the evolution of star formation. It has often been found with projected separation the AGN fraction increases. There are multiple observational works that show this (Alonso et al., 2007; Ellison et al., 2013; Shah et al., 2020) as well as works on cosmological simulations which support these conclusions (Byrne-Mamahit

et al., 2023). In simulations, the increased likelihood of AGN activation comes from the sudden increase in gas density in the galactic core which naturally leads to increased black hole feeding, growth and nuclear activity. To satisfy these conditions, actual coalescence of the two systems are required. Observations of interacting galaxies are often interesting, as they contain examples of dual AGN and individual examples (e.g. Ellison et al., 2017; Stemo et al., 2021) or investigate the increase in the AGN fraction in only the merger / post-merger stage (Gao et al., 2020).

We find peaks in the AGN fraction with projected separation, before the galaxy merging and coalescence takes place. This is supported with other works which specifically look at AGN fraction with projected separation (Ellison et al., 2011; Steffen et al., 2023). However, we specifically find that the AGN fraction increases rapidly in the merging stage and holds quite constant between the separated to apocentre stages. This shows two distinct effects of interaction which can colour our interpretation of the link between AGN and interaction. It appears from our results that the AGN fraction is driven up during the points in the dynamical time when the inner parts of the galaxy are majorly disturbed, and not by the simple movement of gas and dust into the core during the two galaxies passing each other. There is evidence that the onset of nuclear ignition from interaction may be delayed (Ellison et al., 2011), or even flicker (Schawinski et al., 2015) after ignition. Both of these possibilities are reflected in the double peaked distributions of AGN fraction with projected separation and the different times in the dynamical time these represent.

Again, it is important to note the rather ‘wide net’ that our stage classification takes. There is overlap between our pericentre and apocentre stage classifications at high pericentre projected separation and low apocentre projected separations. However, these stages naturally lead onto one another. Therefore, what we see in the bi-modal distribution of AGN fraction with projected separation in Figure 3.24 are two peaks. The second of these peaks is at the cross over point of pericentre to apocentre; the point at which (if the two galaxies have just flown by each other) a delayed AGN ignition could take place. This is also reflected in Figure 3.22 where we see a slight increase in AGN fraction in the apocentre stage. This



is likely from the ignition of nuclear activity taking place over a large period of time with a delay being involved from the initial flyby.

We see an increase in AGN fraction in the merging stage systems, where coalescence is just beginning or has occurred. Byrne-Mamahit et al. (2023) has used cosmological simulations to show that we expect a large increase in AGN fraction at coalescence, and even for sometime into the post-merger phase. This is supported by measured AGN fractions in post-merger galaxies. This matches both what we find and what observations mentioned previously of increased gas densities in nuclear regions and cores, and that the merging stage is when this really occurs in earnest.

However, to more fully study this, we would need a larger sample of confirmed AGN and star forming galaxies from existing photometry or catalogues to make more decisive conclusions based on stage. In this Section, we were limited to a small number of AGN and star forming galaxies across each stage. When compared to our paired sample, we do not have the numbers to also divide into stage again. Therefore, Figure 3.24 shows the global AGN number count with projected separation. We show that the two peaks are due to different stages of the interaction, however, these are using very low number counts and should be treated carefully.

## 3.7 Conclusions

In this work, we investigate the evolution of multiple parameters and processes in galaxy interaction with interaction stage. We use the interacting galaxy catalogue created in Chapter 2 and match it with the COSMOS survey to gain ancillary data. This gives us a flux limited sample of 4,181 interacting galaxies of which 982 have a confirmed secondary from available photometric redshift data. We apply a mass limit to our sample, reducing it to 3,384 galaxies with 607 pairs. We use visual morphology as well as angular separation to split our sample into four distinct stages: (1) close pair, (2) morphologically disturbed and overlapping, (3) morphologically disturbed and distinct, (4) merging. Each stage is designed to capture a different part of the dynamical timescale of the interaction. We then

match these samples with existing catalogues of environment and active galactic nuclei for further study.

We first split our sample of galaxies into their different stages and investigate their evolution with stellar mass and star formation rate. We conduct Kolmogorov-Smirnov and Anderson-Darling tests to show the mass distribution of our sample does not change with stage, while the star formation rate changes dramatically. This change in star formation rate from the separated to merging stages is found in the red sequence of galaxies reducing to the point of disappearance. This is further confirmed by sub-classifying each sampled stage into starbursting, main sequence and quiescent galaxies. We find that as the galaxies move from the separated to pericentre stages the fraction of starbursting galaxies increases while the quiescent galaxy fraction reduces. In the merging stage, the starbursting fraction increases dramatically while almost no quiescent galaxies exist in the sample. This implies that the mechanisms responsible for enhancement in star formation in interacting galaxies is dominant from separated to pericentre stages and in the final coalescence of the system. We find that, for all of our galaxies, some enhancement in star formation is observed.

To further investigate this change in enhancement, we investigate our subsample of galaxy pairs and compare it to a mass and redshift matched control sample. We bin our projected separations and measure the ratio between the average interacting SFR and control SFR in each bin. We find, across the whole subsample, a general increase in this ratio as we move to smaller projected separation. The highest found SFR enhancement is below 10 kpc. However, when broken down into their constituent stages, we find different behaviour in the SFR ratio. This is best seen in the pericentre stage enhancement, which does not seem to change with projected separation while remaining enhanced. There is a dramatic decrease in the pericentre stage enhancement from 2.2 at 10 kpc down to 1.0 at 100 kpc. This shows that just using projected separation as a proxy for stage will leave out crucial information to the underlying causes and mechanisms fuelling star formation enhancement. To confirm that the effects observed here are not related to biases in the environment, we investigate its relation to our staged sample. We find that the environment is consistent between all stages, with no biases existing.

Finally, we investigate the change in AGN activity across our whole sample. We find that, on average, the AGN fraction remains constant with stage until the point of coalescence. However, when looking at project separation, we find an almost bi-modal distribution. This could be evidence for a delayed ignition in the AGN present in those systems undergoing an interaction. However, it is difficult to draw this conclusion definitively due to small number counts. We also find that the AGN fraction is highest in merging and merged galaxies.

While the results with projected separation are not unexpected, those with the different stages are. We have shown the use of projected separation of interacting galaxies as a proxy for the stage of the interaction may miss crucial information. We find very different behaviour in the star forming behaviour of interacting galaxies based on stage which are at in the dynamical timescale of the interaction. We find the beginning of an enhancement in star formation occurs in the pericentre stage. Then, through to the apocentre stage, the enhancement remains although with no further increase. There is then another dramatic starburst in the merging stage, where the two galaxies actually begin to undergo the coalescence processes.

Our work shows the importance of considering morphological stage when considering interaction, and that there is a fine interplay between underlying processes and dynamical timescale of an interaction. We require larger samples of correctly staged galaxies to further understand and exploit what these relations are, and how to best investigate when and where star formation and its enhancement occurs. This is also particularly true of the relation between active galactic nuclei and the interaction stage, where we are unable to have the sample size to definitively draw conclusions from our results. We also require numerical models to better identify the point in the dynamical timescale an interacting system is. This would lead to reliable constraints on the relations we have explore in this Chapter. We present our work on building such an algorithm in the following Chapter. This algorithm is focused on constraining both the dynamical timescale of the interaction and the full set of underlying parameters needed to describe a galaxy interaction.

## Chapter 4

# An Infrastructure to Constrain Underlying Interacting Galaxy Parameters

### 4.1 Introduction

The precise interplay between the observed processes we have discussed in this thesis and the underlying physical parameters of the involved galaxies is difficult to quantify. Using large scale observational datasets allows us to probe this relation, but without the ability to constrain the dynamical timescale the precision of our constraints on it remains limited. Algorithms have been developed to match the underlying parameters of an interaction and its dynamical timescale by directly modelling the expected final morphology. If a simulation of an interaction can reproduce the final morphology, then it has likely correctly inferred the interaction over the dynamical time.

Examples of algorithms designed to make this matching include Identikit by Barnes & Hibbard (2009) or the Stellar Particle Animation Module (SPAM) by Wallin (1990). However, finding the best fit underlying parameters for more than a handful of systems is often seen as unfeasible. There are often greater than 10

different parameters which contribute to different observed morphologies. This leads the underlying parameter space to be greater than 10-dimensional and complex. Exploring even a sub-space of this parameter space fully requires tens of thousands of models to be run. This is also hindered by its degeneracy. For example, Smith et al. (2010) found that four of their best-fit models were able to accurately match morphology of the Arp 284 system. Therefore, it is often preferable to use large cosmological simulations (e.g. Schaye et al., 2015; Hopkins et al., 2018; Hani et al., 2020) to create large samples of synthetic interacting galaxies where analogues to the observed system can be found. This, however, limits our capability to explore observational parameter space beyond the limitations of such cosmological simulations. By their nature, cosmological box simulations have finite scope and size; meaning the rarest (and likely most interesting) interacting systems will remain unexplored without significant further computational expense.

This limitation of directly comparing numerical simulations to observations was solved in a novel way by Holincheck et al. (2016) in the Galaxy Zoo: Mergers (GZM) project (for details on Galaxy Zoo, see Lintott et al. (2008)). GZM worked with citizen scientists to run simulations of interaction and visually compare the simulated morphology to observations. GZM studied a sample of 62 interacting galaxies from the Arp catalogue of interacting galaxies (Arp, 1966). Citizen scientists' were given a selection of simulation outputs around an observation and would select the one which appeared most alike. The simulations would then be run again with tweaked underlying parameters with the citizen scientist selecting the new the best fit output. With enough citizen scientists on the project, enough new simulations run and enough time GZM were able to find the best fit parameters for their interacting galaxy sample across a 14-dimension parameter space. This created the largest fully constrained interacting galaxy samples to date. In the era of the Vera C. Rubin Observatory such an approach will not be practical, with statistically significant samples of thousands of interacting galaxies potentially being produced every week, a new approach is required.

In this Chapter, we present an automated methodology to constrain the underlying parameters of interaction. We combine a fast restricted numerical simulation code with a Markov-Chain Monte Carlo (MCMC) framework. We con-

struct the flux distribution of interacting systems from different sets of underlying parameters. This allows us to map these underlying parameters to interacting system morphologies we then compare to an input image via pixel-to-pixel comparison. We apply our methodology over a 13D parameter space and constrain the probability distribution and find the likely parameter values describing an interacting galaxy system. This approach allows us to marginalise over each parameter, provide the best fit value as well as the error on each measurement. First, we apply this to a set of synthetic interacting galaxy observations created from a restricted N-body simulation where we have input the 13 underlying parameters. This provides us with diagnostics of our methodology. We then apply our process to five real observations of interacting galaxies and discuss how our methodology could be applied to real data, and the limitations therein. We also discuss the more general limitations of this approach, with a particular emphasis on the computational expense required, and the potential future solutions.

The layout of this Chapter is as follows. In Section 4.2, we describe the sample of 51 galaxies we will study and our approach to observation preparation. Section 4.3 will summarise our simulation code and how it has been updated from previous iterations. We also describe how we build our sample of synthetic interacting galaxies and the parameter space we will explore with this simulation. A full discussion of our results will be given in Section 4.5 followed by our conclusions and future work in Section 4.6.

## 4.2 Data

### 4.2.1 Sample of Major Interacting Galaxies

In this work, we test our Markov-Chain Monte Carlo (MCMC) process on idealised, mock observations of 51 major interacting systems. These mock observations are created using our numerical simulation where we have input the underlying parameter values directly. As we know what the true underlying parameters of each interaction are, we can test the accuracy of our MCMC. To create these mock observations, we use the underlying parameters found in the GZM project for 62 interacting galaxies.

Of the 62 systems, we create synthetic images of 51 of them to act as our idealised observational sample. As we are including the flux distribution of each system, we require an accurate redshift of each system. 3 of the 62 systems do not have a redshift measurement in the NASA Extragalactic Database (NED), the Sloan Digital Sky Survey (SDSS) or Simbad databases. Therefore, we discard these. We create each mock observation as though it was observed using SDSS. Of our remaining 59 interacting systems with reliable redshift measurements, eight had not been observed with SDSS. Therefore, we also discard these systems. This leaves us with the GZM best-fit parameters of 51 systems with which to create our synthetic observations. The details of the real systems are displayed in Table 4.3, including the target coordinates, the SDSS ID and the redshift measurements we use. How we create our synthetic images is described in Section 4.3.2 after we have described our simulation.

### 4.2.2 Observation Preparation

To robustly test our MCMC algorithm, we will constrain the underlying parameters of observations of a subset of the systems described in Table 4.3. Therefore, we describe how we build such observational images here. We downloaded the FITS files from SDSS Data Release 16 which contained the full system of interacting galaxies. These were then used to create smaller cutouts of the systems. The coordinates of the primary galaxy are used as the centre of the image. We judged the size of the cutout by the size of the full interacting system, most often between 600 - 1000 pixels. We created cutouts in each SDSS filter ( $u, g, r, i, z$ ).

We convert each observational image into counts from the native unit of nanomaggies using the conversion value in each FITS header. Each filter image was then stacked into white image by simply summing them together. This gave us a higher signal-to-noise in the tidal features of the interacting systems. Then, we took these native resolution white images and block reduced them to a  $100 \times 100$  thumbnail. Each cutout was visually inspected to ensure that, even with the reduced resolution, the tidal features were still clear and prominent in the image.

Name	SDSS ID	RA	Dec	Redshift
Arp 240	587722984435351614	204.980417	0.835278	0.02250
Arp 290	587724234257137777	30.946317	14.72365	0.01171
Arp 142	587726033843585146	144.429583	2.763056	0.02329
Arp 318	587727177926508595	32.380516	-10.158508	0.0132
Arp 256	587727178988388373	4.710417	-10.369167	0.02730
UGC 11751	5877272224711131318	322.247796	11.382539	0.02909
Arp 104	587728676861051075	203.037083	62.733889	0.01082
Double Ring, Heart	587729227151704160	238.287292	54.147861	0.040
Arp 285	587731913110650988	141.040000	49.226111	0.00967
Arp 214	587732136993882121	173.145221	53.067922	0.00331
NGC 4320	587732772130652231	185.740516	10.548328	0.02668
UGC 7905	587733080814583863	190.952917	54.900278	0.01648
Arp 255	587734862680752822	148.290000	7.870000	0.04106
Arp 82	587735043609329845	122.811250	25.193056	0.01368
Arp 239	587735665840881790	205.423852	55.672324	0.02489
Arp 199	587736941981466667	214.265833	36.573333	0.01024
Arp 57	587738569246376675	199.198750	14.424444	0.048
(HWB2016)Pair 18	587738569249390718	206.209583	13.921361	0.089
Arp 247	587739153356095531	125.889478	21.342976	0.01108
Arp 241	587739407868690486	219.461958	30.481222	0.03472
Arp 313	587739505541578866	179.418333	32.285556	0.01045
Arp 107	587739646743412797	163.069583	30.065278	0.03318
Arp 294	587739647284805725	174.931624	31.920108	0.00892
Arp 172	587739707420967061	241.389583	17.597222	0.029
Arp 302	587739721376202860	224.251667	24.612222	0.03286
Arp 242	587739721900163101	191.544583	30.727222	0.02205
Arp 72	587739810496708646	236.733750	17.878333	0.01100
Arp 101	587739845393580192	241.124946	14.800192	0.026
Arp 58	587741391565422775	127.990209	19.211523	0.03722
Arp 105	587741532784361481	167.804167	28.724722	0.021
Arp 97	587741534400217110	181.439583	31.068889	0.02305
Arp 305	587741602030026825	179.655833	27.490833	0.004
Arp 106	587741722819493915	183.902522	28.173576	0.02199
NGC 2802/3	587741817851674654	139.172619	18.963463	0.02914
Arp 301	587741829658181698	167.470000	24.259722	0.02059
Arp 89	587742010583941189	130.665852	14.285624	0.00687
Arp 87	587742014353702970	175.185000	22.437778	0.02373
Arp 191	587742571610243080	166.834167	18.431111	0.02739
Arp 237	587745402001817662	141.933458	12.286750	0.02899
Arp 238	588011124116422756	198.886667	62.126944	0.03106
MCG +09-20-082	588013383816904792	181.161667	52.956111	0.078
Arp 297	588017604696408086	221.330417	38.761389	0.0298
NGC 5753/5	588017604696408195	221.328663	38.805889	0.01374
Arp 173	588017702948962343	222.869434	9.328297	0.028
Arp 84	588017978901528612	209.649167	37.438889	0.01158
UGC 10650	588018055130710322	255.060770	23.106346	0.00986
Arp 112	758874299603222717	0.368333	31.437778	0.024
Arp 274	587736523764334706	218.786250	5.356389	0.02890
Arp 146	587747120521216156	1.685000	-6.635833	0.07544
Arp 143	588007005230530750	116.72333	39.019444	0.01374
Arp 70	758877153600208945	20.864583	30.778333	0.03500
Arp 218	587739720308818095	238.397500	18.607222	0.075

**Table 4.1:** The names, SDSS ID, right ascension, declination (in degrees) and redshift for the 51 interacting systems we will examine. All redshifts are as found on the NASA Extragalactic Database.



We take the 0.396'' pixel scale of SDSS on the sky with the measured redshift to calculate its physical size. From the pixel-to-distance conversion for each image, the position of each secondary galaxy was calculated from the central pixel. No attempt was made to approximate the  $z$ -position of the secondary galaxy, as this is a parameter to constrain. In total, there are 13 parameters that we must constrain over our synthetic and observation images. These parameters are detailed in the following chapter. The observation image preparations were made using the Astropy Python package (Astropy Collaboration et al., 2013b, 2018b).

## 4.3 Simulating Galaxy Interaction

We require a method of mapping underlying parameters to our observed systems morphology and calculating how likely it is they are representative. We input our set of underlying interaction parameters into a restricted three-body simulation which predicts the morphology and flux distribution of the interacting system. In this chapter, we describe our simulation code, its previous iterations and how we add in additional flux information.

### 4.3.1 APySPAM

#### 4.3.1.1 Restricted Three-Body Simulation

The simulation code we use is the Java Stellar Particle Animation Module (JSPAM) (Wallin et al., 2016). For an in-depth description of the underlying code, we direct the reader to Wallin (1990); Wallin et al. (2016) but provide a summary here. JSPAM is a restricted three-body code focused on recreating the morphology of interacting systems. It approximates the interaction as two massive bodies each being orbited by a set of massless test particles. The gravitational potential of the two massive bodies and the resultant forces upon the massless test particles is calculated and used to predict the particles position and velocity at different timesteps. The size and number of time steps can be input by the user. JSPAM is computationally efficient, approximating the morphology of an interacting system using thousands of particles in seconds on a regular work PC at a reasonable time

resolution. The primary particle integrator is a fourth-order Runge-Kutta which applies backwards integration to calculate the position and velocity of the massive bodies from  $t=0$  to the time set by the user. The test particles are then added to the simulation, and forward integration is conducted to find their position and velocity in each timestep through the trajectory of the massive bodies. In this way, a flyby of the two galaxies is simulated with the test particles representing the extended morphology of the two galaxies.

The user has the option to choose a N-body approximation or a softened point mass approximation. Each of these slightly changes the way that the integrator calculates the forces on each particle. Therefore, there will be slight discrepancies between the final morphology of systems interacting with the same underlying parameters but different force approximations. We elect to utilise the softened point mass approximation, as this has improved computational efficiency over the higher accuracy of N-body approximation (for more on this see Wallin et al., 2016).

The base code of **JSPAM** was purely a morphology matching code. Attempting to extract underlying parameters of interaction from morphology matching alone has been shown in prior works to be difficult (e.g. Barnes & Hibbard, 2009). **JSPAM** itself has been used in genetic algorithms to find the best fit parameters of different systems (e.g West et al., 2023). However, this lacks the exploration of parameter space and the quantification of uncertainties we aim to achieve in our approach. Using both morphology and flux matching between simulations and observations improves accuracy of recovered parameters (Miller & van Dokkum, 2021) and we have therefore enhanced the original **JSPAM** algorithm with the ability to model population evolution with star formation/star bursts to approximate the flux distribution of the interacting system. We have created this enhanced version in Python 3.7.4 (hence, we shall refer to this algorithm as Advanced Python Stellar Particle Animation Module, **APySPAM**).

To approximate the flux distribution of the galaxies in the simulation we calculate luminosity of each particle while minimising the computational cost. We incorporate the evolution of the underlying stellar populations of each galaxy over the time taken in the interaction. We also incorporate the formation of new stellar populations in potential starbursts, and approximate the impact this will

have on the galaxy flux distribution. To preserve the computational efficiency, we build a semi-analytic model and define a global stellar population to assign a luminosity to each particle based on its assigned, hypothetical mass. In this way, we ‘paint on the stars’ of each galaxy without having to directly model stellar evolution and star formation. This process is detailed in the following two subsections.

#### 4.3.1.2 Stellar Population Evolution

To model the underlying stellar populations, we utilise a Bruzual & Charlot (2003) (BC03) simple stellar population. These contain SEDs generated from flux libraries from a Chabrier (2003) initial mass function. We set this stellar population model to have a delayed exponentially declining star formation rate (Johansson et al., 2009; Pacifici et al., 2013; Simha et al., 2014; Boquien et al., 2019). However, to capture any star formation due star formation enhancement in the interaction, we increase the star formation based on the conditions in the interaction. We assume an e-folding time for star formation of  $\tau = 1.7\text{Gyrs}$ . This value is chosen as it matches field, massive galaxies found in the literature (e.g Peng et al., 2010b) and used in hydrodynamical simulations (e.g. Jeon et al., 2022). Our simulation outputs a spectrum normalised to  $1M_{\odot}$  with each particle initially assumed to be the same age as the galaxy.

This spectrum must then be scaled to the stellar mass present at each particle. We follow the prescription as stated in Wallin et al. (2016) to distribute the mass between the three components of the galaxy, and then to each test particle. The galaxy in the JSPAM simulation has its mass distribution as  $M_{\text{bulge}} = 0.05M_{\text{galaxy}}$ ,  $M_{\text{disk}} = 0.14M_{\text{galaxy}}$  and  $M_{\text{halo}} = 0.81M_{\text{galaxy}}$ . We take the total mass assigned to the galaxy (input by the user) and divide it into these three components. We then assume that the bulge and disk masses are fully baryonic, with the remaining mass being non-baryonic dark matter. We further divide the calculated baryonic mass into two components: stellar and gas. The total stellar mass of each particle is used to scale our final output SEDs from our model while total gas mass of each particle is used to calculate the star formation rate. The gas and stellar mass to be distributed to the particles is then defined by a gas fraction parameter that the

user can alter. By default, this value is 0.15 for both the primary and secondary galaxies.

We assume the initial ages of the galaxies (both 10 Gyrs by default) at initialisation and calculate the final age of the SEDs based on the number of time units the user wishes to run the simulation. This age is then used to extract the normalised spectra from the BC03 templates. These output SEDs are then convolved with given telescope filters of the users choice and integrated, giving a colour flux value to each particle. However, this process only outputs the final flux values at each particle of the initial stellar population. During the interaction, we assume that the galaxy begins to form new stars at a rate significantly higher than is modelled in the BC03 templates. Therefore, we account for this by modelling newly created stellar populations as the interaction progresses.

To incorporate the increase in star formation in our simulations, we manually enhance the expected star formation rate through the simulated interaction. In high-resolution simulations which also model the evolution of gas, starbursts occur naturally (Saitoh et al., 2009). However, in our simulations we must approximate this behaviour in a semi-analytic fashion. The change in star formation is heavily dependent on the mass ratio and the kinematics of the interaction and, therefore, we implement an enhancement parameter based on these parameters. We calculate the excess star formation due to the interaction compared to what is already expected in the SED, and distribute this to each particle based on the initial gas mass. Approaching the problem in this semi-analytic way is similar to what is done in the CIGALE (Boquien et al., 2019) algorithm. Here, we detail this enhancement parameter.

At any given timestep the enhanced SFR is given by

$$SFR_{\text{enhancement}} = \beta \left( \frac{t}{\tau} \right) \exp \left( -\frac{t}{\tau} \right) M_{\text{baryonic}} M_{\odot} \text{yr}^{-1}. \quad (4.1)$$

Here,  $\tau$  is the e-folding time of star formation,  $M_{\text{baryonic}}$  is the baryonic mass of the galaxy and  $t$  is the age of the galaxy at the given timestep. This is the star formation at any time given by the BC03 template. However, we include the  $\beta$  parameter, which is our enhancement value. This is a dimensionless value given

by

$$\beta = M_{\text{ratio}} D_{\text{ratio}}^2. \quad (4.2)$$

$M_{\text{ratio}}$  is the mass ratio between the galaxy being enhanced and the galaxy causing the interaction.  $D_{\text{ratio}}$  is the ratio of each galactic radius to the distance between the galactic cores. In a system with a high mass galaxy interacting with a low mass galaxy, the high mass galaxy will have relatively little star formation enhancement while the less massive galaxy will have significant enhancement. This is similarly true for the ratio of the radius and separation. If the galaxies are interacting in such a way that the distance of closest approach is less than each galactic radius, then this ratio will rapidly increase above one, enhancing star formation further. This represents a significantly more violent interaction. It is important to note, however, that this has significantly less impact on strengthening star formation than that of the mass ratios.

These parameters successfully reflect the findings of the current astrophysical literature, where mass ratio has a significantly higher role on star formation enhancement than impact parameter (Barton Gillespie et al., 2003; Lotz et al., 2008a; Li et al., 2008a). We base our semi-analytic approach on the star formation histories found in a range of high resolution N-body simulations (Mihos & Hernquist, 1996; Springel, 2000; Rodríguez Montero et al., 2019) which measure the change in star formation directly from the Kennicutt-Schmidt (Kennicutt, 1998) relation. These simulations directly model the star forming gas through the interaction, measuring the change its evolution which we are able to approximate. Thus, we achieve an accuracy comparable to directly-modelled simulations at a fraction of the computational cost.

The output of Equation 4.1 is global star formation of each interacting galaxies at any given timestep. However, the aim of our model is to be able to match the flux distribution across the entire galaxy (particularly the tidal features) to any observation that the code is given. Therefore, we must distribute the star formation throughout the particles. To keep computational efficiency, we utilise weights which have been assigned to each particle. These weights are based on the ratio of the gas mass of the particle which has been assigned at initialisation to the total gas mass of the galaxy. So, to find the star formation rate of a single

particle at any given timestep, the following equation is applied:

$$SFR_{\text{Particle}} = \frac{M_{\text{gas,Particle}}}{M_{\text{gas,Galaxy}}} SFR_{\text{Galaxy}}. \quad (4.3)$$

After every time step, the gas within each particle is reduced by the mass converted into stars. Once this drops below a user defined value, the particle is cut off from star formation and is considered quenched. Currently, each particle is assigned equivalent gas mass at initialisation of the simulation. Therefore, when a particle is quenched in this example, every particle in the galaxy will also be quenched. The user can define a gas distribution model, which will lead to particles being quenched at different times.

There are limitations to this approximation. We assume that each galaxy is a disk galaxy prior to the interaction when we assign gas masses to each particle. We assume that all of the gas mass assigned can be used in star formation, i.e. all the gas is cold molecular gas. We make no account of gas ionization or the turbulence in the ISM that likely occurs during these interactions. We also assume that the disruption occurring to the test particles represents what would occur to the gas disk of galaxies within an interaction. However, we find that with these assumptions, the output star formation histories mimic those simulations which directly calculate these values.

Upon finding the star formation rate at the position of each particle, we convert this into a stellar mass formed through the timestep taken. We then compare this formed mass to the expected mass formed in the initial underlying stellar population. If excess stellar mass has been formed, we assign an SED to it and its age is recorded. Once the simulation is completed, each new stellar population age is used to extract the relevant BC03 SED and multiplied by the total mass of the new stellar population. We then stack all of the SEDs together. This gives us the total extra emission we expect from the stars formed during the starburst throughout the simulation. This is then added to the initial stellar population emission defined at the beginning of the simulation. This gives us the total SED of each particle throughout the simulation. Each particle SED is then convolved with user inputted telescope filter responses and integrated. This gives a total flux that would be measured from each particle as if observed.

Thus, starting with the underlying JSPAM code approximating the positional distribution of particles to the observed system, we paint on the flux and find the flux distribution with APySPAM. This allows us to directly compare the pixel in a simulation image to an input observational image. However, in doing so, a limitation was found due to using a particle number that was significantly less than the number of pixels.

#### 4.3.1.3 Extending Flux Distribution

One remaining challenge in the simulations is that we are attempting to model full interacting systems with a number of particles significantly less than the number of pixels in each image. This is to maximise computational efficiency. The resulting effect is that large gaps can appear in the tidal features that form or within the disks themselves as the interaction progresses. To mitigate this effect, we calculate the flux at each particle position and then use the procedure described below to distribute it through each pixel of our image. This results in more realistic images of galaxies compared to binning the particle flux based on position.

First, we calculate the flux at each particle described in the previous sections. We take each particle SED, and convolve it with the filter(s) of the user's choice. These convolved SEDs are then integrated to give a value of the flux in counts at each particle. We then create a grid of pixels and calculate the physical distances between each of their centres. We then calculate the contribution of flux from each particle to each pixel centre. Once the 2D flux distribution has been found across the pixel grid, we then use the measured redshift of the galaxies to find the measured fluxes as if the system had been observed.

The result of this is a well distributed galaxy image where there are no empty spaces in the tidal features nor in the disk. However, it does have a limitation when particles are not within the galaxy. When a particle is flung out to different parts of the image during the interaction the particle flux is smeared into seemingly larger orbiting systems to the interaction. When doing our pixel matching, this can lead to much to a calculated excellent reproductions of the primary tidal

features being labelled as unrepresentative. As a result, we set the value of any particle with no neighbour within  $5 \times 5$  pixels to zero.

The process described above successfully creates continuous, synthetic images of the galaxies flux distribution with a limited number of particles in the simulation. However, this approach does impose two limitations on our constraining methodology. These limitations are related to the existence of tidal features at the very limits of detectability of our telescopes. The first is when a galaxy has a ‘hidden’ tidal feature that hasn’t been detected. In this example, the correct underlying parameters would lead to the formation of the tidal feature that would be measured in the synthetic image. When compared to the observational image, this would be identified as a mis-match between the morphologies of the observed and simulated images. It is important to be aware of all the tidal features within the image and understand the limiting flux and surface brightness of all images in a sample. Here, we have selected major mergers in SDSS with very clear tidal features which are far from the low surface brightness regime. Thus, we do not encounter this issue here.

The second is with tidal features at the very limit of our detectability, where a single isolated particle could be representative of the tidal feature but we now remove it with our  $5 \times 5$  neighbour criteria. Primarily, in testing, we find that this is a lesser problem than the first. The  $5 \times 5$  criteria is a very lenient one, and often such tidal features are close enough to the galactic disk in our images that they remain in the image. They often form continuous features which then incur the first limitation. This can be rectified by selecting lower resolution and getting more flux into larger pixels.

#### 4.3.1.4 Impact on Computation Time

The new algorithms to calculate flux have been added to the original JSPAM code while preserving computational efficiency. The choice to create an interaction constraining code which uses flux distribution rather than morphology matching is due to the prior difficulties of using such a method. Therefore, the introduction of extra algorithms which require extra computation time has been necessary. The runtimes of JSPAM and APySPAM are shown in table 4.2. As shown here, even with



N Particles	JSPAM (s)	APySPAM (s)
10	0.062	0.250
100	0.45	0.338
1000	4.22	1.090
2500	10.535	2.392
5000	21.104	4.458
10000	42.796	8.625

**Table 4.2:** Timing comparison between the original JSPAM code (as used in Galaxy Zoo: Mergers) and the advanced version of PySPAM we are using here. These timings were taken using Python 3.7.4 on an Intel(R) Core i7-8665U CPU. Our version of APySPAM significantly outperforms that of the original JSPAM by many times, even with the added architecture of approximating the flux distribution. This is because in our re-write of the underlying simulation code we take advantage of Python’s efficiency with vectorization and array multiplication over that of for loops. These tests were performed by running the simulation for seven hundred steps fifty times and then taking the average run time of each iteration.

our extra flux calculations, for reasonable particle counts our new code APySPAM outperforms JSPAM by at least a factor of four. When we have translated JSPAM into Python, we have also re-written the underlying code to take full advantage of Numpy and Python’s speed with vectorization over for loops. As shown, the computational efficiency impact only becomes noticeable at very low particle number, where the overheads of Python’s vectorization is comparable to the base runtime of a for loop.

To explore the full parameter space we must run APySPAM many thousands of times. Therefore, we need to use the simulation specified with the fastest runtime possible for the smallest trade off in resolution of the tidal features. We elect to use 2,500 particles throughout our run. This is still relatively fast, taking approximately 2 seconds, but also maintains high resolution of the tidal features. This is still five times faster than using the original JSPAM code with this many particles.

By using the flux distribution method described in Section 4.3.1.3, we mitigate the effect of lower particle compared to pixel number. This is at the cost, however, the adding the largest computational overhead. We find that this part of the algorithm is much more sensitive to image size than particle number. The timing calculations shown in Table 4.2 use an output image size of  $100 \times 100$ . When

increased to  $500 \times 500$ , the computation time for 2,500 particles increased to over 30s. Therefore, it is imperative that the user keeps this in mind when selecting cutout size.

### 4.3.2 Creating Test Images

With the descriptions of our simulation completed, we now describe how we build our idealised observations. We use the APySPAM three-body algorithm described in Section 4.3.1.1 to create these images. These images are measured in counts, as if observed in the SDSS. We utilise the best fit parameters which were found in the GZM project, and re-create their best fit images for each named interacting system. The parameters to create these images are shown in Table 4.3. We run our APySPAM with 20,000 particles and a high time resolution of 0.057Myrs per timestep. The resultant images are shown in Figure 4.1. Each image is white, created by the stacking of *ugriz* filters of SDSS. We find the original SDSS observations of each system, and extract the conversion from nanomaggies (native SDSS flux unit) to counts and apply them to the native standard units our simulation outputs the flux distribution in. By stacking, we increase the signal in the tidal features, as well as other points in the disk.

Each test image is centred on the ‘primary’ galaxy, with the *xyz*-position of the secondary galaxy being used to calculate the size of the cutout. The primary galaxy is the galaxy with most mass in the pair, as defined in H16. These images were then reduced from their native resolution to  $100 \times 100$  cutouts. This image size was found to be the best compromise between detail in the tidal features. As we will be matching the flux distribution of each system, it requires the redshift of the interacting system. As stated previously, the redshifts for our sample were found from the NASA Extragalactic Database. The full range redshift range of our sample is  $0.003 < z < 0.113$ .

## 4.4 Constraining Interaction

We now require a method to compare our simulation images to our synthetic images. This comparison acts as a way to map the set of underlying parameters to

## 4.4 Constraining Interaction

Names	x(kpc)	y(kpc)	z(kpc)	$v_x(\text{kms}^{-1})$	$v_y(\text{kms}^{-1})$	$v_z(\text{kms}^{-1})$	$\log M_{T,1}(M_\odot)$	$\log M_{T,2}(M_\odot)$	$R_1(\text{kpc})$	$R_2(\text{kpc})$	$\phi_1$	$\phi_2$	$\Theta_1$	$\Theta_2$
Arp 240	-149.08	-68.71	231.50	-260.83	-504.46	794.60	12.54	12.47	44.69	63.75	301.00	35.50	310.81	321.99
Arp 290	16.22	-25.02	-31.02	-31.22	-67.22	-4.94	10.71	10.56	14.11	6.58	12.97	135.12	97.54	305.01
Arp 142	-7.40	-21.57	0.90	12.44	-173.23	152.27	11.04	11.19	19.16	5.01	48.79	43.80	50.07	135.06
Arp 318	14.10	2.70	39.98	0.00	-71.83	196.50	10.56	11.01	9.87	9.21	6.21	95.00	200.00	289.23
Arp 256	-6.12	-28.88	29.37	-194.60	-173.47	132.02	11.10	11.10	14.11	8.16	97.79	60.52	144.60	216.50
UGC 11751	10.00	-31.91	24.23	-31.46	-39.20	34.96	10.28	10.19	12.22	11.34	15.00	87.50	203.48	22.36
HEART	-1.89	5.25	50.36	-21.98	94.78	680.87	10.89	10.99	4.58	6.18	152.78	195.63	147.23	138.43
NGC 4320	-1.58	2.14	-3.10	-339.22	-30.34	101.96	10.90	11.05	7.07	2.57	117.88	147.04	326.46	65.76
Arp 255	-18.50	21.49	17.61	-40.64	-89.59	126.67	11.36	10.64	15.20	11.73	140.38	-4.88	317.52	221.37
Arp 82	-7.30	-21.75	-9.39	68.90	-90.15	7.84	11.17	10.87	5.90	2.89	26.65	49.48	342.60	232.84
Arp 199	-4.10	2.85	11.17	218.16	176.37	84.61	10.25	10.05	4.55	4.63	96.61	49.83	152.65	109.12
Arp 57	-69.44	-52.30	128.05	-173.38	-160.84	440.18	11.15	10.99	17.70	9.77	176.94	71.08	337.85	335.44
Arp 247	7.14	-10.80	-41.04	26.09	-53.22	-43.00	10.87	10.55	7.17	3.33	55.45	45.65	319.41	335.29
Arp 241	-4.54	-8.23	-0.55	-74.39	79.62	0.00	10.20	10.37	3.72	5.17	96.08	107.20	191.08	229.44
Arp 107	-29.43	33.42	-9.48	0.20	19.43	46.26	10.99	10.86	16.49	6.55	82.03	271.03	191.08	296.27
Arp 294	-4.61	13.67	-62.09	-122.55	-52.72	-25.10	10.63	10.82	8.69	8.20	70.38	178.66	59.54	109.24
Arp 172	-6.62	-18.38	-30.98	-42.56	-33.24	-52.22	11.26	11.12	8.81	8.09	213.74	67.31	203.50	241.01
Arp 302	2.76	-25.61	74.51	-196.00	-305.20	97.39	10.75	10.32	14.16	9.52	6.24	36.33	283.48	345.34
Arp 242	-6.47	-13.90	-26.85	4.19	60.44	-3.14	10.52	10.74	10.69	5.86	7.45	57.97	85.88	212.75
Arp 72	16.78	-8.81	26.86	8.24	-23.74	171.19	10.12	9.98	9.18	2.59	6.80	90.49	224.26	228.89
Arp 58	-28.91	-25.10	-15.37	20.13	-158.10	11.60	11.32	10.55	19.35	2.85	173.29	45.58	44.63	230.34
Arp 105	-1.53	-31.87	80.03	37.05	-3.92	265.62	10.77	11.45	9.23	11.88	-34.38	141.75	306.34	0.00
Arp 106	-6.39	-12.55	-28.98	-73.92	1.21	-185.26	11.12	10.30	8.98	2.94	108.93	39.06	319.92	160.84
NGC 2802	15.95	15.68	24.54	169.82	53.15	263.10	10.75	10.36	13.78	7.52	108.04	30.31	327.91	146.78
Arp 301	-17.28	-4.91	-19.08	-314.96	25.19	-3.15	11.05	11.17	10.24	16.68	9.19	78.00	160.99	252.67
Arp 89	-14.81	-9.89	-36.98	21.05	-81.46	-20.52	10.71	10.49	12.05	4.66	149.19	110.69	78.26	70.43
Arp 87	-3.46	26.92	-38.84	-42.32	45.27	-106.64	10.16	10.23	8.08	5.42	116.69	65.78	32.05	249.08
Arp 191	9.03	-5.50	-47.81	-2.88	34.73	-272.22	10.87	11.09	7.37	8.22	101.88	53.06	2.24	216.89
Arp 237	-8.24	1.92	1.88	85.13	-141.79	48.60	11.04	10.65	7.85	5.18	86.86	55.83	348.72	148.42
Arp 173	11.63	-26.45	-54.92	75.32	5.69	-139.47	12.04	10.56	6.95	6.87	83.54	329.68	310.01	317.61
Arp 84	7.61	23.25	2.26	-24.13	44.84	26.11	10.67	10.06	17.24	4.08	11.06	65.56	111.80	290.68
UGC 10650	-1.64	-16.00	-26.56	43.91	30.74	5.69	10.59	10.61	8.50	6.96	73.19	-63.69	346.58	187.83
Arp 112	-9.47	9.57	4.03	-170.75	-32.95	71.45	10.96	10.98	4.37	4.09	97.25	-4.75	194.53	35.78
Arp 274	19.50	-4.72	55.56	226.62	154.11	-150.67	10.75	10.24	17.75	12.69	126.88	51.38	296.59	232.55
Arp 146	18.05	10.10	9.61	72.89	85.41	73.70	10.70	10.78	8.83	12.91	72.50	48.81	111.80	67.08
Arp 143	-3.91	-16.09	24.25	53.06	-21.88	84.27	10.62	10.15	7.35	7.75	45.23	32.38	236.54	61.02
Arp 70	9.24	-30.53	-29.87	42.03	-128.45	-0.41	10.78	10.67	13.72	7.80	149.90	136.19	50.40	38.01
Arp 218	35.55	-20.53	3.84	74.29	-59.10	-25.77	10.74	10.12	11.07	6.38	148.30	49.41	231.50	261.45
Violin Clif	-15.21	-33.86	-16.08	-15.95	-70.31	-186.56	10.59	10.78	10.47	7.86	142.49	65.29	258.15	238.65
Arp 104	0.89	-9.61	-9.34	32.76	-26.66	-53.61	10.94	10.68	1.44	0.88	78.09	87.64	36.70	347.77
Arp 285	-16.66	21.33	25.37	-84.45	86.28	14.76	9.20	10.50	5.01	5.71	51.19	-35.00	295.16	249.32
Arp 214	-43.09	13.54	0.93	-57.28	31.96	-21.48	10.07	10.01	8.01	6.31	135.70	354.86	140.82	138.14
UGC 7905	1.32	-9.53	16.47	-112.54	-80.94	67.17	10.31	11.07	4.19	5.03	14.93	68.72	103.69	239.11
Arp 239	-12.19	4.02	21.45	-104.37	16.96	58.77	10.97	10.27	7.45	2.21	58.82	94.31	235.38	335.40
PAIR18	-12.44	32.72	-18.36	14.70	-38.05	-156.67	10.96	11.36	11.02	16.62	153.57	43.84	168.63	326.13
Arp 313	-13.42	11.35	-39.17	-142.02	-61.52	-303.92	10.71	10.44	4.64	11.10	7.92	42.80	115.72	304.23
Arp 101	14.52	-39.46	-33.44	27.22	-132.95	-143.42	10.71	10.78	6.60	4.45	45.10	358.74	62.34	207.08
Arp 97	-0.57	27.13	4.51	-40.93	31.86	45.10	9.98	10.09	8.14	3.62	53.18	146.65	46.34	24.76
Arp 305	44.52	54.29	-1.86	50.93	115.06	12.07	10.53	10.27	10.51	7.03	45.81	166.88	286.21	234.78
Arp 181	-3.11	-1.81	-7.72	-199.27	-63.32	-201.94	10.69	10.94	1.56	1.73	96.00	65.69	127.45	221.37
MCG 09-02-082	8.67	-5.60	-16.64	197.24	16.52	-228.72	11.10	10.77	2.97	3.49	85.43	97.51	317.60	4.75
Arp 297	11.55	-2.79	-35.87	38.79	-62.45	20.98	10.84	10.48	10.76	5.24	51.44	136.06	199.01	243.73
NGC 5753	-24.85	-34.94	-21.60	-59.57	-86.24	-5.50	10.64	10.40	4.62	5.77	141.06	110.25	138.63	26.83

**Table 4.3:** The best fit parameters found the GZM project to represent each of the named interacting systems. We use these best fit parameters to create idealised images of each interacting system using APySPAM. Each of these parameters are the final parameters of the galaxy at the point of the observation. The positional and velocity vectors are of the secondary galaxy in the frame of the primary. The masses are the total mass of the system. The radii is that of the disk initialised to create the final morphology. Finally, the four orientation parameters are with respect to the  $y$ - and  $z$ - axis and allows the disk to be rotated in 3D with respect to the sky. The resultant simulation cutouts are shown in Figure 4.1.

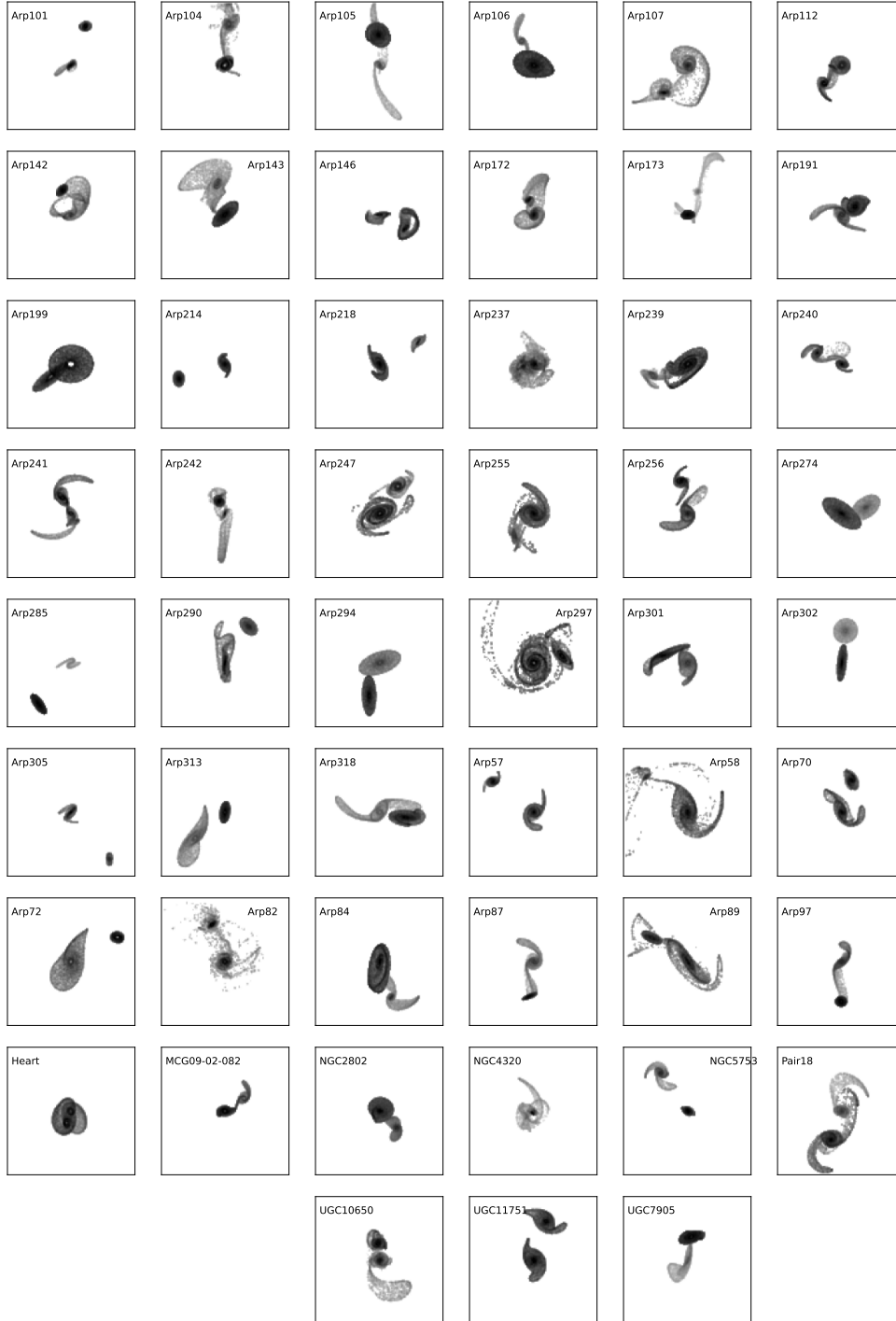


**Figure 4.1:** Our mock observations of each interacting system. These act as an idealised observation, which is completely noiseless. We also know the underlying parameters which formed these outputs. Therefore, this forms an excellent test-set to see if we can recover the underlying parameters when searching over a large parameter space.

an output morphology that we can then constrain by comparing to observations. However, we need a framework to conduct this comparison and to explore the parameter space of our interactions. To do this, we use an Markov-Chain Monte Carlo (MCMC) algorithm. In this chapter, we first describe the parameter space we explore, followed by our MCMC algorithm, how we quantify the similarity between simulation and synthetic images and how we find the parameters which are best fit.

### 4.4.1 The Parameter Space of Interaction

We aim to explore the underlying parameter space of interaction and find the best fit parameters which describe an input observation or test image. The parameters we constrain are the required parameters in the APySPAM three-body simulation algorithm. To function, APySPAM requires 15 different parameters. These are: the 6 positional and velocity vectors of the secondary galaxy, the total masses of both galaxies, their radius, 4 orientation parameters and the dynamical timeframe to model. We now also require the redshift measurement of the system to correctly estimate the flux distribution of the system. However, some of these parameters we can find before we begin exploring the underlying parameter space.

The first two parameters we find are the projected 2D position of the secondary from the primary. These are measured from the observational image of the system by converting between pixel and physical coordinates in the image. We take this position as the centre of the secondary disk. We also provide the redshift of the interacting system. The redshift not only directly impacts the flux distribution of the input image, but its scale and resolution. Therefore, we assume that this parameter is known and provided. Work is currently being conducted to making this a free parameter that can also be constrained based on the interacting systems flux distribution and size.

Thus, there are 13 different free parameters to recreate an interacting systems morphology and are the 13 parameters we will constrain over. A description of these parameters and the size of the parameter space explored are shown Table 4.4. We choose the limits of the parameter space based on the maximum values of the parameters we used to build our test images in Table 4.3. Table 4.4 provides

Parameter	Description	Conversion(Spec. Units)	Parameter Range(Spec. Units)
$z$ -position	Secondary $z$ -position	15kpc	-300kpc - 300kpc
$v_x, v_y, v_z$	Secondary velocities	$169.34 \text{kms}^{-1}$	$-1693 \text{kms}^{-1} - 1693 \text{kms}^{-1}$
$M_1, M_2$	Total Masses of Galaxy	$10^{11} M_\odot$	$1 \times 10^9 M_\odot - 4 \times 10^{12} M_\odot$
$R_1, R_2$	Radii of Galaxies	15kpc	0.15kpc - 150kpc
$\phi_1, \phi_2$	Y-axis orientation	deg	$0^\circ - 360^\circ$
$\theta_1, \theta_2$	Z-axis orientation	deg	$0^\circ - 360^\circ$
$t$	Time of Min. Separation	57.7Myr	0Myr - 500Myr

**Table 4.4:** The thirteen parameters used in both JSPAM and APySPAM to recreate an interaction. Each of these parameters must be found to consider an interaction constrained. The Parameter column shows how each parameter will be described throughout the rest of this paper. The third column then gives the conversion required to go from simulation units to SI units.

the size of the parameter space as well as the conversion between the simulation units and physical units. The conversions are found from Wallin (1990).

The  $z$ -position parameter is the distance of the secondary from the primary in the plane of the sky. Without accurate redshift information, this is very difficult to estimate and we, therefore, leave it as a free parameter. The  $v_x$ ,  $v_y$  and  $v_z$  are the three dimensional velocity components of the secondary in the frame of the primary galaxy. The two mass parameters are the total masses of the galaxies. The radii parameters are the maximum distance from each galactic core that a particle can be initially placed to represent the flux within the galaxy. In practice, the particles are distributed across different rings between the galactic core and the value of the radii parameter. The particles are distributed following an exponential disk. The  $\phi$  and  $\theta$  parameters are the orientations of the disks with respect to the sky. Finally, the time parameter is a measure of the time since the closest approach of the two galaxies.

## 4.4.2 Defining the Likelihood Function

### 4.4.2.1 MCMC & Bayes Theorem

We define framework by which to explore our parameter space, and identify areas where the parameter set successfully represent the input image. We combine APySPAM with a MCMC methodology in order to fully explore the underlying parameter space. In an MCMC, a set of walkers are created and are then moved

through parameter space in an ensemble. Each walker position is a set of parameters in our 13D parameter space. At each point, we calculate the likelihood that the output simulation is representative of the input interacting system. We then compare the likelihood between the old and new position, and if the likelihood is higher at the new position the walker moves there. If not, the walker remains in place and makes another attempt to find a higher likelihood. The walkers form their own chain of steps which gradually move toward the areas of highest likelihood. In our case, the likelihood is a measurement of the similarity in flux distribution between a simulated image with parameters of the walker position and an observed image of unknown underlying parameters. Therefore, the walkers are moving from a set of underlying parameters that poorly describe the observed system to a set of underlying parameters which describe the observed system well.

We use the well known Python package `emcee` (Foreman-Mackey et al., 2013) for our MCMC. This is an ensemble MCMC package with numerous predefined moves and algorithms to make getting to the area of high likelihood more efficient. We construct contours of walker mass and use these to calculate the errors and probability distribution of our best fit measurement; i.e. we can construct a posterior for each of our parameters. For full details of `emcee` and the different modes that it can use, see the extensive `readthedocs`<sup>1</sup>, but here we will briefly state the hyper parameters that we use.

For each observed image, an ensemble of six hundred walkers was initialised which would explore a total chain length of 7500 steps. Following the advice in the documentation regarding potentially complex and multi-model parameter spaces we utilised two different walker move proposals in our algorithm. These were the Differential Evolution (DE) Move (Nelson et al., 2014) and the Snooker Differential Evolution (DES) Move (ter Braak & Vrugt, 2008). An identical version of our setup can be found on GitHub<sup>2</sup>. Here, a user can download our setup to reproduce our results, or to update the model for their own purposes.

We define a likelihood function to compare the input images to our simulation outputs. By Bayes Theorem, the probability that a set of underlying parameters

---

<sup>1</sup><https://emcee.readthedocs.io/en/stable/>

<sup>2</sup><https://github.com/AstroORyan>

which produced a simulation also describe a test image follows Equation 4.4,

$$P(H_i|D_{obs}, C) = P(H_i|C) \frac{P(D_{obs}|H_i, C)}{P(D_{obs}|C)}. \quad (4.4)$$

$P(H_i|D_{obs}, C)$  is the probability that some hypothesised set of underlying parameters,  $H_i$ , successfully describes some observational data,  $D_{obs}$ , under some prior constraints,  $C$ . Applying this to our hypothesis,  $H_i$ , allows us to utilise the prior knowledge that we have about the interacting system in question and can be used to put constraints on the parameter spaces we explore to shorten computation time. This is described by the expression  $P(H_i|C)$ . This is multiplied by the likelihood that the observation is defined by the hypothesised parameters given the constraints,  $P(D_{obs}|H_i, C)$ , all divided by a normalisation constant,  $P(D_{obs}|C)$ .

#### 4.4.2.2 Simplifying the Prior

In order to simplify this expression, we make assumptions about the underlying parameter space to increase efficiency and simplify our computations. We first assume uniform priors for each of our 13 parameters. Therefore, we define a range of parameter values that if a walker moves beyond, we set the probability immediately to zero. The ranges we allow for each parameter are specified in Table 4.4. These ranges can be tweaked, or a different prior function defined, by the user. Here, we elect to set the priors part of Equation 4.4 to one.

We improve efficiency in our code further by adding to the prior based on the likelihood that tidal features will form in any given interaction. This is defined by a filter parameter,  $\gamma$ , and is fully described in Holincheck et al. (2016, where it is called  $\beta$  but we call it  $\gamma$  here to not be confused with our star formation enhancement parameter of Equation 4.2):

$$\gamma_{min} = \frac{M_1 + M_2}{r_{min}^2 V_{r_{min}}}. \quad (4.5)$$

Here,  $r_{min}$  is the closest approach distance,  $V_{r_{min}}$  is the relative velocity at the time of closest approach and  $M_1$  and  $M_2$  are the primary and secondary masses, respectively. This parameter is designed to capture two important quantities: the



mutual gravitational attraction and the inverse of the closest approach velocity. Each of which is important for the resultant gravitational distortion of the interacting system. By maximising the total mass of the system, while minimising the distance of closest approach and maximising the time of closest approach (i.e. minimising  $V_{r_{min}}$ ) we would expect stronger tidal distortion.

In our case, we use it to inform our prior as the MCMC continues. This significantly enhances the computational efficiency and pushes the walker ensemble to areas of high likelihood quickly. In each step of the MCMC, running the simulation itself is the highest computational cost, so we calculate  $\gamma$  first and then make a decision on whether to run the simulation. This decision is based on an exponentially declining probability dependent on the value of  $\gamma$ . This probability, or prior, is defined as

$$C = \begin{cases} \exp(0.5 \frac{\gamma}{\gamma_{min}}), & \text{if } \gamma < 0.5 \\ 0, & \text{if } \gamma \geq 0.5 \end{cases} \quad (4.6)$$

Here,  $\gamma$  is a user defined cutoff, 0.5 in our case. Taking the log of this, we can directly add it to prior. If the prior is initially calculated above 100, we do not run the simulation and move the walker to a new set of parameters.

#### 4.4.2.3 Simplifying the Likelihood Function

To further simplify the likelihood function, we can assume our probability distribution is Gaussian. This is a reasonable assumption to make as a starting point for our constraining attempts. However, as will be described in Section 4.5 this is found to not always hold true, particularly for the orientations of the system. However, making this assumption allows us to utilise the following Equation to compare our mock observations to our observed data:

$$P(D_{obs}|H_i, C) = (2\pi\sigma_j^2)^{-n} \exp(-\frac{1}{2\sigma_j^2} \sum_{j=1}^n (x_j - \mu)^2) \times C. \quad (4.7)$$

Here  $\sigma_j$  is the uncertainty in the observed image,  $x_j$  is our mock observation and  $\mu$  is the observed image. The above expression can be simplified further by noting

that the expression in the exponential function is just a half of the  $\chi^2$  difference between the observational image and the mock observational image. This is the same  $\chi^2$  function that is used in the code GALFIT (Peng et al., 2002), where  $\chi^2$  is given by;

$$\chi^2 = \frac{1}{N - n_{dof}} \sum_0^{N_x} \sum_0^{N_y} \frac{(p_{x,y} - q_{x,y})^2}{\sigma_{x,y}^2}. \quad (4.8)$$

Here,  $N$  is the number of pixels in the observed image, which has the number of degrees of freedom subtracted from it,  $n_{dof}$ .  $p_{x,y}$  and  $q_{x,y}$  are the flux values of the ( $x$ th,  $y$ th) pixel in the observed and simulated images respectively.  $\sigma_{x,y}$  is the  $\sigma$  value of the ( $x$ th, $y$ th) pixel; this is the uncertainty in the observed images pixel value and follows the  $\sigma_{x,y}$ -image definition from GALFIT (Peng et al., 2002; Peng et al., 2010a). This is then summed over all pixels in the image, giving us a single  $\chi^2$  value between each simulated image and observed image.

Finally, to help computation time the log is taken of our likelihood function. This leaves us with a final expression that a given set of parameters describing a simulation image also describe the observed image input into the algorithm,

$$\log_{10}(P(H_i|D_{obs}, C)) = \log_{10}(L) = -\frac{\chi^2}{2} + \log_{10}(C). \quad (4.9)$$

This is used at every step of our MCMC chain, with a simulation have to be run for each.

Thus, we now have a method by which to quickly predict the resultant morphology and flux distribution that the user would observe in a set of given filters. We also have a means of exploring the likely parameter space of an interaction, given an existing observation.

## 4.5 Results & Discussion

We now apply our MCMC algorithm to our set of synthetic interacting galaxy images. To reduce the number of repetitive figures in this paper, we focus here on a specific system as a representative sample, and publish the results of all

systems online. They are presented online on Zenodo<sup>1</sup>. As these input images are created from APySPAM, they provide us with a set of synthetic images of interacting pairs with no noise and where the underlying parameters are known. Initially, we explore the results of running this on the synthetic image of Arp 240. We discuss how the constraints could be improved, and discuss improvements on our constraints with extra, 3D information. We then plot the results for the entire dataset, and discuss trends we see in the parameters we recover.

We apply our methodology to a set of real, observed images of interacting galaxies. We select the five which are at different stages and various levels of constraint from our test dataset. We apply our MCMC to only a subset as the computational expense is significantly increased to make constraints on the observational systems and for our MCMC to reach convergence. We compare our found best fit values with those of our synthetic system, and discuss the difference between applying this to best fit simulations and observations. Finally, we describe the applicability of our approach to other systems, keeping an emphasis on those in the low surface brightness regime and the limitations this would introduce.

### 4.5.1 Testing on a Synthetic Image

We apply our MCMC to a single image from our mock dataset described in Section 4.3.2. We elect to use this system as it is composed of two clear and distinct disks, with a tidal bridge connecting them and tidal tails forming on the opposite side. The tidal features lie in the high surface brightness regime, and have an inclination close to 0. The observation and synthetic image are shown in Figure 4.2. There are clear differences between the morphology of our mock image and the observation of Arp 240. Therefore, testing on the synthetic image is not the same as constraining the Arp 240 system. However, the synthetic image is an ideal scenario to test our methodology on. We elect to test our MCMC on the Arp 240 system first, as it has a high mass in our sample meaning the tidal features will contain more flux and should be easier for our MCMC to constrain.

---

<sup>1</sup>All results are found on Zenodo with DOI: 10.5281/zenodo.11532157

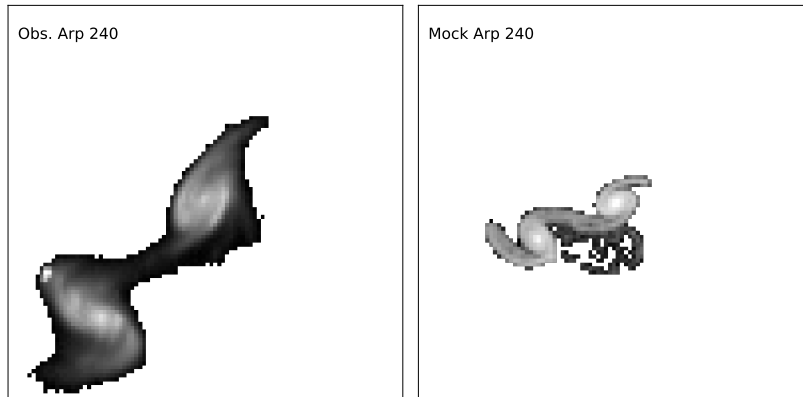
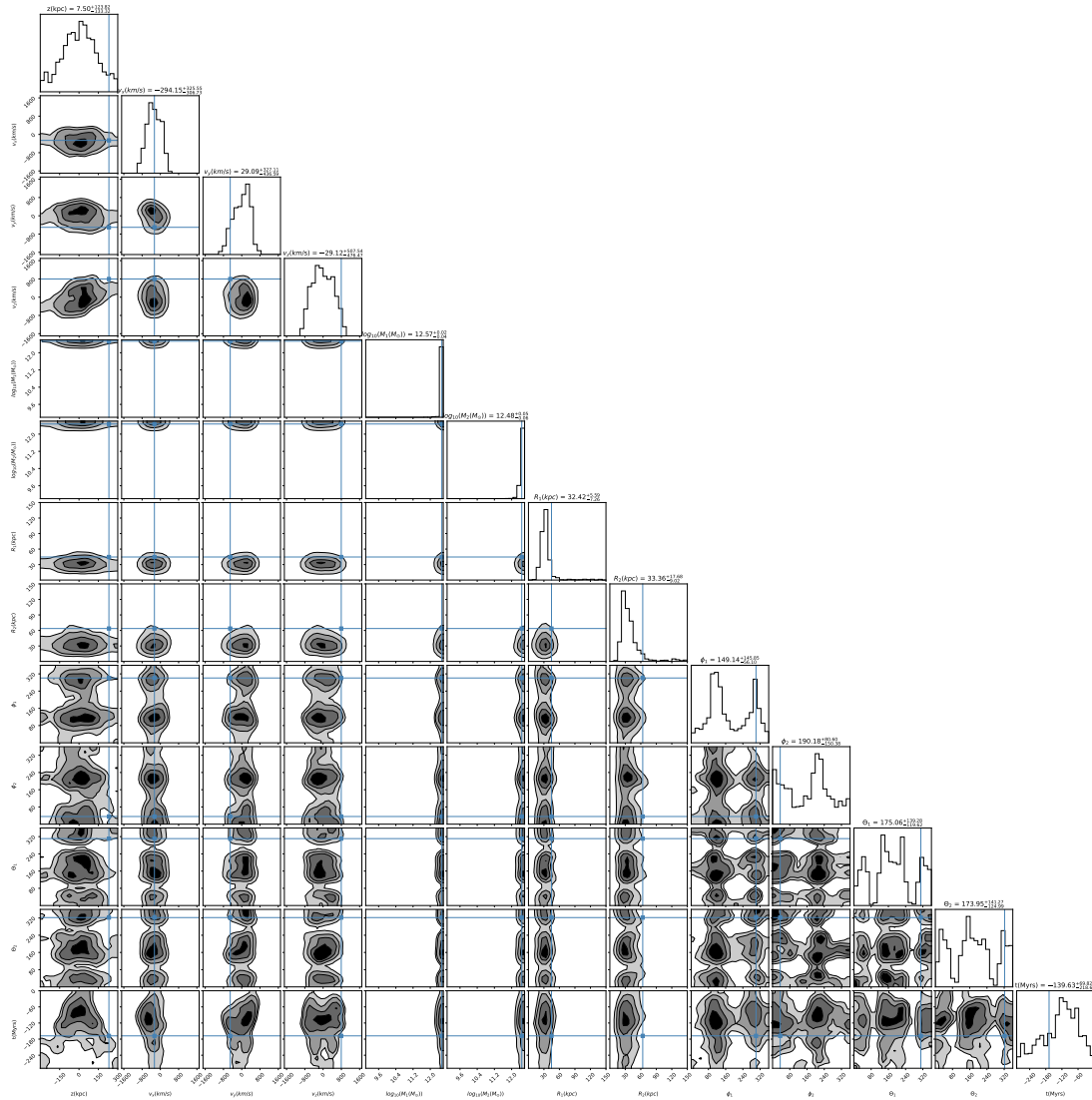


**Figure 4.2:** The example system used to test our MCMC: the Arp 240 interacting system. This system is considered an easy one to constrain. It is composed of two clearly distinct galaxies, with strong tidal features that our MCMC can match. These tidal features are the two tidal tails formed in the interaction and the tidal bridge linking the two systems. *Left:* The prepared observation image of the Arp 240 system created from SDSS DR16 observations. *Right:* The synthetic observation of Arp 240 used in our pipeline. It is created by using the best fit parameters found by Holincheck et al. (2016). The different in scale and orientation are discussed below.

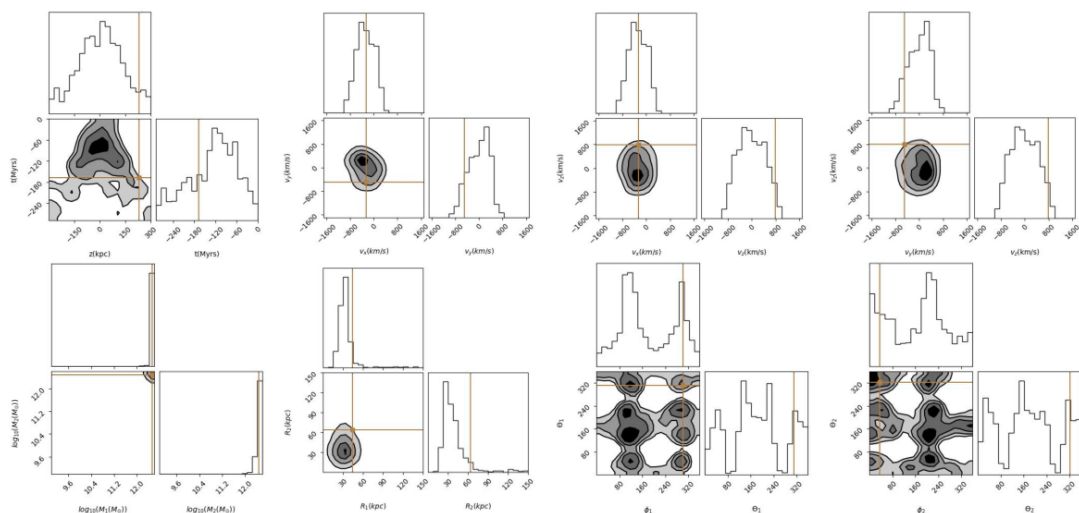
We constrain the synthetic Arp 240 image by running our simulation with 2,500 particles with 600 walkers and 7,500 steps in the MCMC. An example of our full results is shown in Figure 4.3. This corner plot is created using the **Corner** Python Package (Foreman-Mackey, 2016). However, displaying our results as is shown in Figure 4.3 will be difficult as we will be discussing multiple different systems throughout this chapter. This larger corner plot also uses a lot of space. Therefore, we will present and discuss our results using reduced corner plots as shown in Figure 4.5.

Figure 4.5 shows the constraints we have found on each parameter from our MCMC. The golden lines then show the true values used to create the synthetic image, and are those described in Table 4.3 for Arp 240. The contour levels correspond to 11.8%, 39.3%, 67.5% and 86.4% of the samples across all walker chains (these are default values), indicating the confidence level (CI). For reference, we have set up the corner plots here such that the contours containing 68% of the walkers roughly corresponds to  $1\sigma$ <sup>1</sup>. However, this assumes a Gaussian probabil-

<sup>1</sup>Full explanation in Corner plot Docs: <https://corner.readthedocs.io/en/latest/>



**Figure 4.3:** Corner plot showing the constraints made on all thirteen parameters we are exploring. Each contour level contains 11.8%, 39.3%, 67.5% and 86.4% of the samples across all walker chains. The blue lines show the true values used to create our synthetic observation. Displaying our results using the full corner plot is difficult in a paper because of the high dimensional results that we obtain. Therefore, we elect to show all remaining results in this paper as reduced corner plots like Figure 4.5. We elect to put the parameters which are most likely to correlate together in different corner plots.



**Figure 4.4:** Same as Figure 4.3, but reduced to only corresponding parameters. Gold lines indicate truth values.

ity distribution, which is not strictly true for the results we find here. The blue lines in each contour plot correspond to the true parameter value used to create the synthetic observation of Arp 240. Figure 4.5 shows that each of these truth values is within a 67.5% CI of the probability distribution with the exception of the  $z$ -position and time.

We get excellent constraints on the masses of the two galaxies. This system is the most massive system in our sample, and therefore we expect the mass at the very limits of the range we are exploring. We find that the MCMC first converges on the two masses of the disks, and are the easiest for us to constrain. We provide the algorithm with the secondary 2D position, and therefore it only has to fit the flux distribution of the inner disk correctly to get good constraints on the galactic masses. The largest gains in likelihood maximisation come from matching the flux distribution in the inner parts of the primary and secondary. While the formation of the tidal features depends on the mass ratio, they also depend heavily on the orientation of the interaction as well as the relative sizes.

The relative sizes of the disks is important for the constraining the tidal features as it is the outer parts of the disk that are sheared off to form them.

The primary radius is constrained very well, and is primarily expected to be smaller than the true value of this system. This is, again, due to the  $\chi^2$  nature of calculating the distance between the two images. The likelihood, on average, is lower with some pixels within the galaxy being missed than a pixel containing the central disk in it when it should not. We therefore have a bias effect where the peak of probability drifts to just below the true value of the radius. However, the true value of the radius remains within 86.4% CI of the found contours.

The recovery of the radius of the secondary is worse than that of the primary. We find the peak in the probability distribution is far lower than the true value. This is from a limitation of our simulation as well. While the output simulations of the MCMC are always centred on the primary, the secondary galaxy central position is not so certain. Due to the backwards integration and trajectory calculated here, the secondary does not always end in the exact same image bin in the output simulation image. Therefore, the secondary disk likely moves slightly per simulation. This change transfers further uncertainty in the secondary disk size, and a preference for the secondary to be smaller to improve the likelihood calculation. The size of the secondary disk also contributes much more to the tidal debris formed in the interaction. The simulation is conducted in the frame of the primary, leading to the 3D velocity of the secondary being higher than that of the primary. Therefore, the particles in the secondary are much more likely to be ejected during the encounter than the simply orbiting primary particles. This adds further uncertainty to the secondary radius. However, once again, the best fit values found are within 84.6% CI of the true value from the base simulation.

There will also be some uncertainty involved in this measurement from the formation of the tidal features. The flux distribution of the tidal features that form are inter-dependent on multiple parameters, primarily the mass ratio, the size ratio and the orientation of the galaxies in the interaction. The significant degeneracy in the orientation constraints undoubtedly has some effect on the fitness of the resultant system. Due to a lack of three dimensional information, our algorithm cannot discern which way the galaxy is rotating or which way the tidal features should be orientated in the line-of-sight. Therefore, degeneracy at  $\pm 180^\circ$  of the true parameter values for  $\phi$  and  $\pm 180^\circ$  for  $\theta$ . Figure 4.5 shows this with several different peaks in both measurements of  $\phi$  and  $\theta$ . However, we

recover the true parameters in one of the peaks of the marginalised posterior for each orientation parameter.

It is important reiterate here that  $\phi$  is the orientation of the galactic disk with respect to the  $y$ -plane while  $\theta$  is the orientation with respect to the  $z$ -plane. With 3-dimensional information, such as the direction of rotation of the disks or the line of sight (LOS) velocities of the tidal features, we would be able to resolve the degeneracy in the  $\phi$  parameter. However, the source of the degeneracy in  $\theta$  has a different source. The tidal features can form in the opposite direction from the mock observation and still be found to have high likelihood. This is a result of our likelihood being based on flux matching on pixels. There is no knowledge provided of the direction the tidal features should be moving or forming, only if the pixels contain the correct flux. Therefore, this gives a significant degeneracy in the  $\theta$  parameter. Therefore, while the disk can be flipped in the  $z$ -direction and still match the observation, it can also be flipped in the  $y$ -direction as well. While the degeneracy in  $\phi$  can be solved with velocity information, the  $\theta$  orientation will require information on the rotation of the disk itself. Having rotational information will allow us to constrain the bulk motion within the galaxy and the direction the inner disk should be rotating as well. These two pieces of 3D information will remove the 4-fold degeneracy in each parameter.

The lack of 3D information also affects our constraints in the  $z$ -direction: the  $z$ -position and the  $z$ -velocity. As seen in Figure 4.5, the finds the peak in the posterior distribution for both parameters as much lower than they truly are. First, the  $z$ -position is difficult to constrain as we lack 3D information. The simulation is run in the reference plane of the primary galaxy, therefore the secondary can only be behind or in front of it. There will be change in the flux of the secondary based on whether it is in front or behind of the primary galaxy. However, this change in flux is completely dominated by the distance due to the redshift of the galaxy. Therefore, there is little to no observable change in the absolute values of flux unless the true value of the  $z$ -position was very large.

The constraint of the  $z$ -velocity remains far from the true parameters due to similar reasons as above. The true value lies at the very edge of the probability distribution found, at approximately 86.4%. This would, again, be rectified readily by introducing velocity information into our constraints. The simulation



works so that the secondary galaxy is always at the same  $x$  and  $y$  position that is defined by the user. Therefore, an output simulation with a positive or negative LOS velocity will have the same flux distribution. Hence, this constraint simply peaks about zero for the  $z$ -velocity.

Our MCMC works significantly better, however, with the  $x$ - and  $y$ -velocity of the secondary galaxy. We find the truth value of this is within 67.8% CI of our found distribution. The velocity values are directly related to the strength of the interaction, and therefore indirectly relate to the tidal features which form. Thus, our MCMC is informed by the flux distribution of the resultant simulated image and gives an excellent constraint on the parameters.

Finally, we discuss attempting to constrain the time of the interaction. We show the time since closest approach, not the total interaction time. The underlying simulation utilises backwards integration to calculate the trajectory of the interaction. Therefore, the time we input into the simulation simply tells it how far back in said trajectory to put the secondary galaxy. Therefore, the same interaction will occur whether we input -10 time units or -100 time units. The algorithm will require more computation time to calculate the particle positions in the lead up to the interaction. It is important to note that the total integration time will only affect the output system when we make it too small. In other words, if the secondary starts after the point of closest separation or at closest separation, our simulation breaks down and gives nonphysical results.

We calculate the time of closest approach for all of our walker steps and then present this as a measure of the time posterior distribution. Our measured value is significantly smaller than the true value of our best fit simulation, although it does lie within the region of 86.4% CI. This parameter is highly dependent on the velocity and position constraints that we have made, and these are skewed to significantly smaller values than the truth. Therefore, it is unsurprising that our time of closest approach value is also found to be much smaller.

To fully put this result into context, we explore the simulations that lie in the areas of highest probability within these posteriors. To select which simulations to present, we take those walkers that were within the 11.8% CI throughout each walker chain and take the top 5 as an illustration here. Our MCMC is not able to precisely reproduce the input image. It is often able to reproduce the tidal features

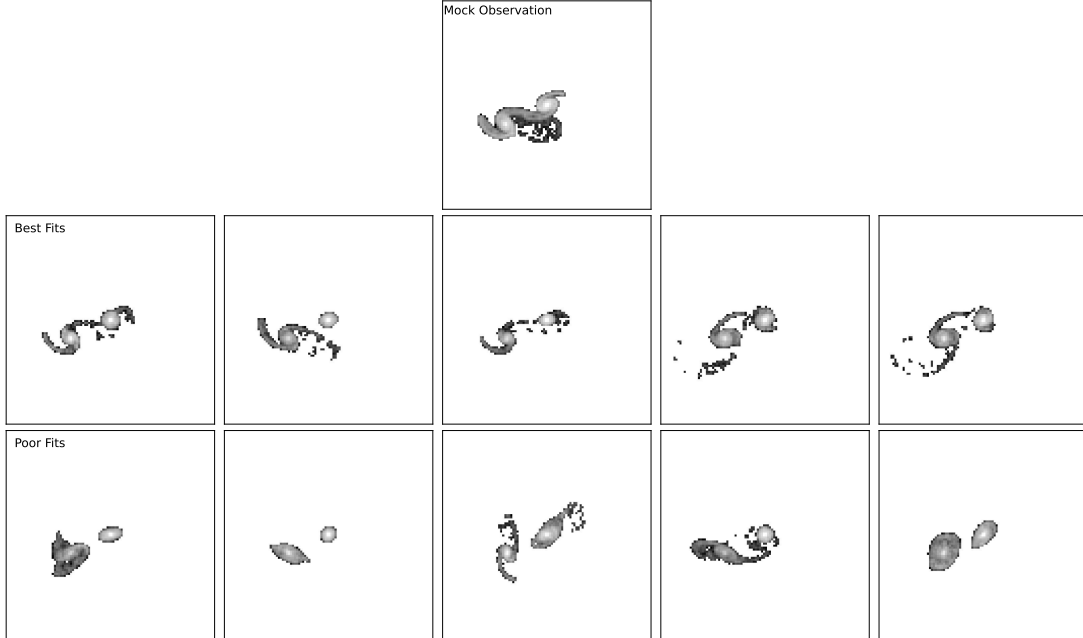


**Figure 4.5:** Simulations from the areas of parameter space that lay within the 11.8% CI of our constraints. *First Row:* The synthetic image we are attempting to constrain. *Second Row:* The best fit simulations from this parameter space. *Bottom:* The worst fit simulations from this parameter space. Our MCMC found those parameters which cause the formation of the correct tidal features, as well as the tidal bridge connecting the two systems. However, it has been unable to fully identify the tidal features of the secondary. There is also a lot of noise in this posterior distribution, with many systems with different tidal features in the areas of high probability. Therefore, identifying specific systems with the sought after tidal features requires manual intervention.

of the primary as well as the tidal bridge connecting the two systems. This appears to be where the MCMC has centred the posterior upon. The likely reason for this is actually due to the filtering parameter that we use on the simulation. The Arp 240 simulation lies in an unlikely area of tidal features to form -  $\gamma = 0.259$ . Therefore, using our  $\gamma$  parameter as a filter is suppressing the likelihood measured in this particular parameter combination. However, the  $\gamma$  parameter remains a necessity in our MCMC. Without the ability to filter the simulations quickly, we begin to approach very large requirements of computational expense. Therefore, for this particular example the  $\gamma$  parameter is a hindrance.

In the surrounding area of probability space, however, we find some interesting

constraints. Changing each parameter by small amounts based on the posteriors of each parameter space leads to variation in the simulation outputs and tidal features. Due to the disks being well defined and aligned, this can often lead to them being weighted highly. Therefore, the question remains, how would one use this code to find their best fit simulation and actually make constraints using it? This algorithm is best used as an indication of where in parameter space the true parameters lie in recreating the tidal features observed in an observation. This reduces the size of parameter space to explore dramatically, and could be an indication of where to search with more accurate simulation models for true interacting galaxy parameters.

Overall, from our example of Arp 240, we are able to recover nearly all the true values of the input simulation to within an 86.4% CI of the true parameters. The only missing parameter is the time since the flyby. There is significant degeneracy in constraining the orientations of this interaction, but this is expected. While our results appear like they have converged in the MCMC, we will also describe the diagnostics with which to prove this.

### 4.5.2 Diagnostics of Pipeline

It is important to ensure our results are reliable by using diagnostics to investigate the MCMC chains. We investigate three different diagnostics of our MCMC run. First, we check that they have truly converged with the Geweke diagnostic. The Geweke diagnostic is a Z-test of equality of means where the autocorrelation in the flattened samples is taken into account as the standard error is measured. We compare the means of the first 10% and last 50% of each chain in each parameter, and require the resultant Z-score to be  $< 1$  for convergence. We use the Geweke diagnostic as written in the ChainConsumer (Hinton, 2016) Python package. For this case, every parameter passes this convergence test, with the exception of the orientation parameters (although, this is likely the result of converging on multiple best-fit values).

Figure 4.5 clearly shows that each orientation has incredibly complex, multi-model structure in the parameter space. We have a 2- or 4-fold degeneracy in the output models due to three dimensional information not being available.

This disrupts our Geweke diagnostic measure, which is looking for a single peak in parameter space. Therefore, by folding the parameter space over and only exploring over  $0^\circ - 180^\circ$ , we achieve a single peak in parameter space. These results then pass the Geweke diagnostic test.

The second diagnostic we use is that the walkers have fully explored parameter space and that we have removed enough of the steps at the beginning of the run to consider the MCMC burnt-in. Once again, using ChainConsumer, we can plot out each walker step throughout parameter space. Figure 4.6 shows the flattened walker chains through parameter space. We have removed the first 200 steps of each walker chain before thinning the chain and flattening it. By flattening we have taken each walker chain and combined them into one chain for every parameter. Discarding the first 200 steps has been enough for the burn in of the MCMC, as the walkers have already moved mostly through parameter space and are centring on a central value of high probability. The structure in the orientation parameters is also interesting. The degeneracy structure in the parameter space has already formed by the end of the burn-in and then the walkers move within those areas of high probability. This is for two reasons. First, they affect the flux distribution of the disks primarily if they are face-on or edge-on. The MCMC quickly converges on face-on systems in our case. Second, when they are in that degenerate space, the slight changes in inclination of the disks given does not change the likelihood calculation significantly enough to reduce this degenerate space further. Hence, the degenerate areas are very large with very flat areas of probability at their peak.

We have tested resolving this problem by running further steps in our MCMC to achieve convergence naturally within the parameter space. We find that increasing the number of steps does improve convergence on the orientation parameters, but at a much larger computational cost and without substantial improvement on the other parameters. Therefore, we elect to fold our resultant degenerate solutions into a smaller parameter space. This achieves convergence, and gives us excellent estimates on the orientation for these systems.

A second solution to this problem would be involving velocity information into our models. Knowing the bulk motion of the tidal features would allow us to constrain the tidal features based on which way they were rotating. This

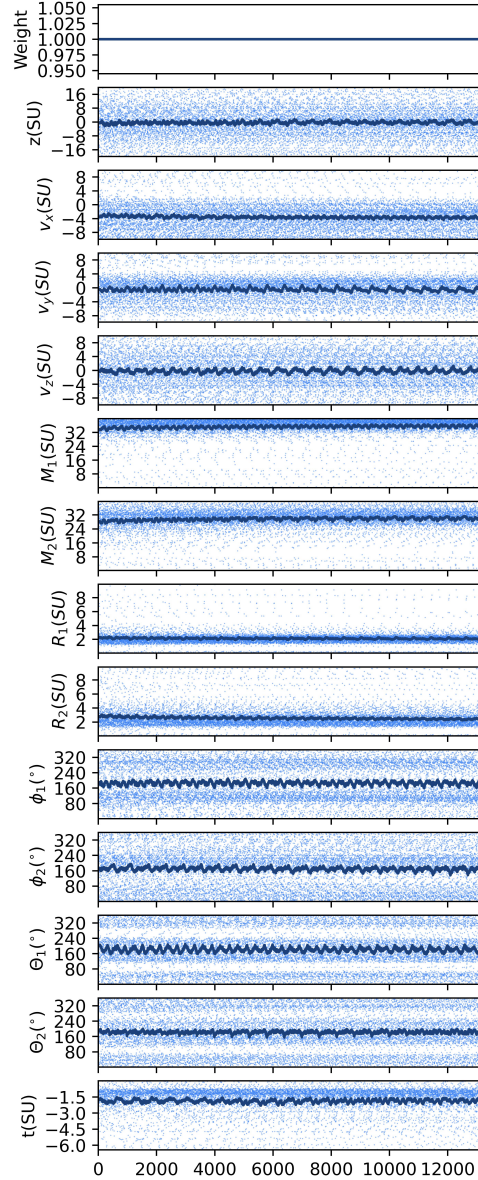


**Figure 4.6:** Steps taken by each walker in our MCMC chain to constrain the Arp 240 best fit simulation. Note, the  $y$ -scales here do not extend over the full parameter space for some galaxies, and only show where the walkers have stepped after the burn-in phase. The deeper the blue, the more walkers have stepped at that point. This figure shows that our MCMC has successfully burnt in and very quickly goes to high areas of probability for parameter space. They then oscillate around the best fit values while searching the remaining parameter space. The  $z$ -position,  $z$ -velocity and  $\phi_2$  parameters show significant uncertainty as the walkers move around the entire parameter space. In the  $\phi_1, \theta_1, \theta_2$ , we can see the two fold degeneracy form very early on and then the walkers do not explore across them at any point.

would eliminate part of the degenerate space. However, as stated previously, little spectroscopic data exists of our sample of interacting galaxies. Therefore, we run this test using the our synthetic Arp 240 image and including the LOS velocity of the particles and creating a velocity grid to constrain over.

### 4.5.3 Inputting 3D Information

Very few of the systems described in Table 4.3 have associated integral field spectroscopy (IFU) data in order to get LOS velocities to incorporate 3D information into our fitting process. This is because they are very large in the field-of-view of many instruments, and therefore we can only achieve measurements of their inner disks and not their tidal features. We, therefore, map the velocity distribution of our synthetic Arp 240 image. This map is created by summing the  $z$ -velocities of each particle in the bin and then create a total LOS velocity map for which to compare to simulations. This has little impact on the measurements of mass, size and  $x$ - and  $y$ -velocity measurements. However, it completely changes our measurements of the  $z$ -position and time of interaction as well as improves our constraints on all three velocity vectors dramatically.

Figure 4.7 shows the new measurements of the constraint on the  $z$ -position,  $y$ - and  $z$ - velocities. The constraints on each of these parameters is significantly improved. This is with the same number of MCMC walkers and steps as without 3D information. For the  $y$ - and  $z$ -velocities, the constraints are improved to the point where we completely recover the true underlying parameter values within 39.3% CI. With the  $z$ -position, we also gain significant constraint. We are able to recover which side of the primary the secondary lies, with a sharp drop in the marginalised posterior over the negative part of the  $z$ -position parameter space. We also significantly improve our constraint on the time of the interaction, and approximately recover the true parameter. We are able to constrain the final velocity expected in the observation, and therefore, means the galaxy cannot be moving too fast at in the final timestep. This has the effect of shifting the expected time of contact back significantly.

Interestingly, we lose a significant amount of constraint on the relative sizes of the two systems. Adding the velocity information in the way we have likely

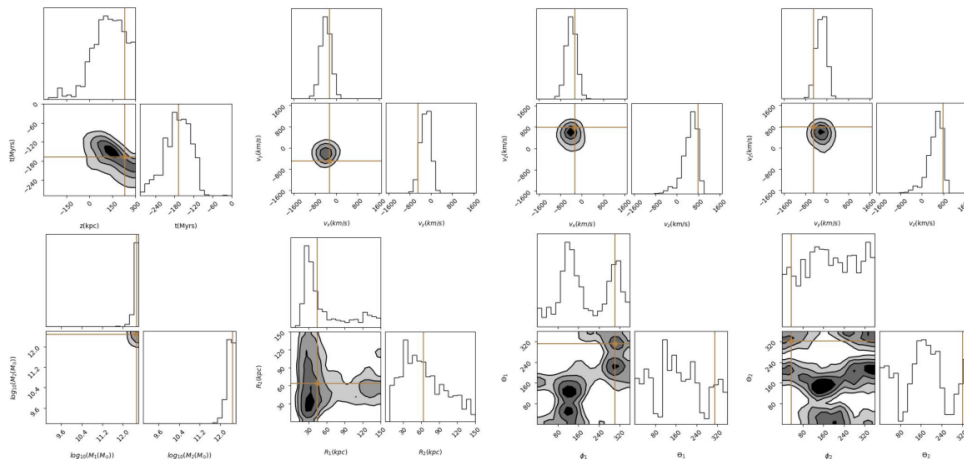


**Figure 4.7:** The reduced corner plot of the synthetic Arp 240 system with a velocity map also used for constrained. To add this extra information, we created a mock velocity map of our Arp 240 synthetic image and summed the LOS velocity ( $z$ -velocity) in each pixel of our image. Comparing between here and Figure 4.5, we see we make different constraints on the  $z$ -position and the time as well as resolve one of the degeneracies in the orientation space.

increases the required size of the disks so the LOS velocities match within them. Therefore, more particles are stripped from the secondary galaxy and cause further uncertainty in the final image. We also find the removal of some of the degeneracy in the orientation parameters, as expected. It is important to note that, in this example, we have only used the LOS velocities to achieve this improvement in constraint. To better get constraint on orientation, we likely need further velocity and 3D information of the system. For instance estimates of the internal rotation, and accurate measures of the bulk motion of the tidal features in the galaxy. Currently, the simulation is not able to accurately reproduce this and simply assumes circular velocities at different radii from each galactic centre. Finally, the mass constraints remain the same as was found without velocity information as they are dependent primarily on the flux distribution and dominated by the inner disk of the system.

This shows the improvement that adding velocity information to our MCMC could bring, and how far interacting galaxy simulation and constraint can go once we incorporate IFU spectroscopy over more systems. In the sample we are using here, of the most massive, large, major interacting systems, only three have

got any IFU data. This data is from the MaNGA (Bundy et al., 2015) IFU spectrograph, whose field of view is only able to capture the central disk of these systems. While having velocity information on even a subset of the pixels of the galaxy would improve constraints, to significantly improve them we will need this of the full tidal features of the systems. IFUs with larger fields of view are soon to come online, such as WEAVE (Dalton et al., 2014).

#### 4.5.4 Running on Full Idealised Sample

With constraints being ascertained on nearly all parameters of our synthetic Arp 240 image, we then applied our MCMC to the remaining 50 synthetic images. The reader is invited to see the resultant corner and reduced corner plots of each system on the website. Here, we will detail describe our best and worst three corner plots, and then discuss the trends throughout applying the MCMC to the dataset. First, our ability to constrain is highly dependent upon the stage of interaction. Our tightest constraints, the ones with narrowest posteriors, were on those interacting galaxies which were only just past the point of closest approach. I.e., they were the systems which had highly distinct tidal features and disks were fully separate. Our best three fits were those of synthetic images of Arp 172, Arp 240 and Arp 290. The ‘best fits’ have been judged by those with the smallest FWHM of their marginalised probability distribution in mass. The reduced corner plots are shown in here in Figures 4.5, 4.8 and 4.9. Each of these systems is clearly in stage 2 or 3 of the interaction, where tidal features have formed clearly, and there are two distinct disks.

The worst fits we achieved were of those systems which were close to the merging stage. They were systems where the two cores were close to coalescence, very little tidal features were visible or the position of the secondary galaxy was very unclear. Our worst three fits and examples of this were Heart, NGC4320 and Arp 57. The reduced corner plots are shown in Figures 4.10, 4.11 and 4.12. Each of these systems represent the three limitations, respectively. First, is the issue with constraining a stage 4 system. If two cores are close to coalescence, the flux distribution will appear similar to two overlapping disks. Therefore, our  $\chi^2$  calculation will lead to a maximised likelihood which is equivalent between



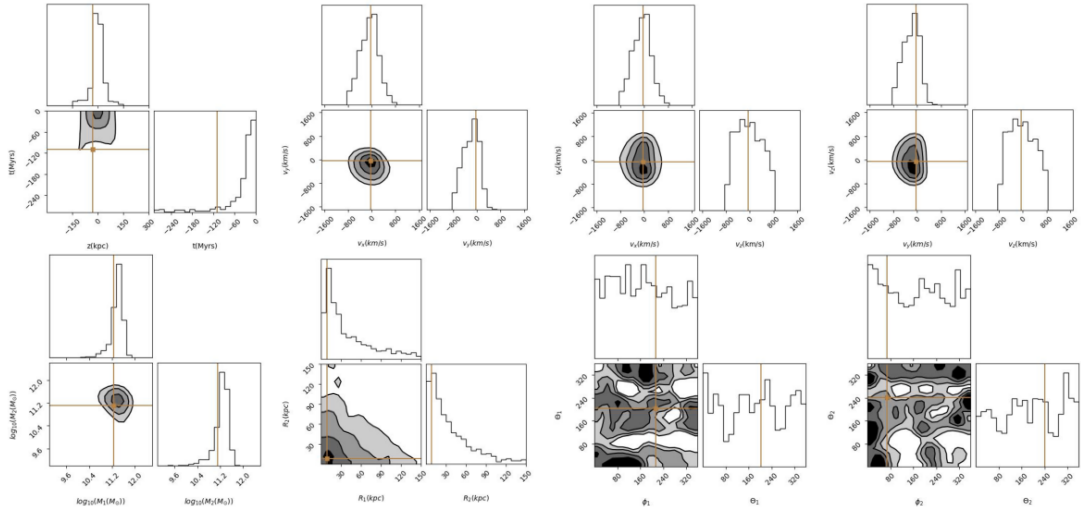


**Figure 4.8:** Second example of our best fits from our methodology is representative of the simulated image of Arp 172, a stage 3 system. Gold lines represent the true values.

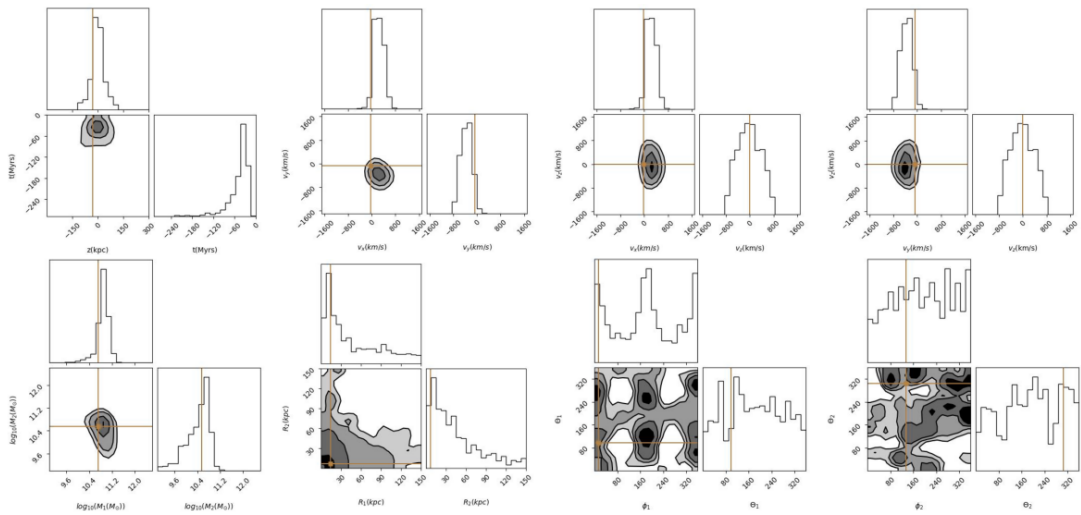


**Figure 4.9:** Third example of our best fits from our methodology is representative of the simulated image of Arp 290, a stage 2 system.

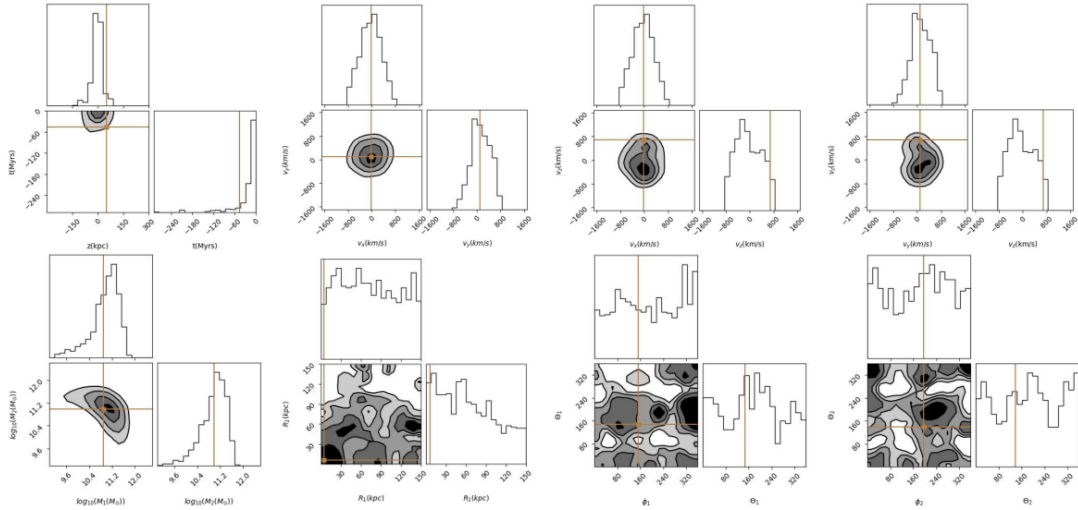


**Figure 4.10:** First example of our worst fits. This shows our constraints of the simulated image of the Heart system, a stage 4 system.

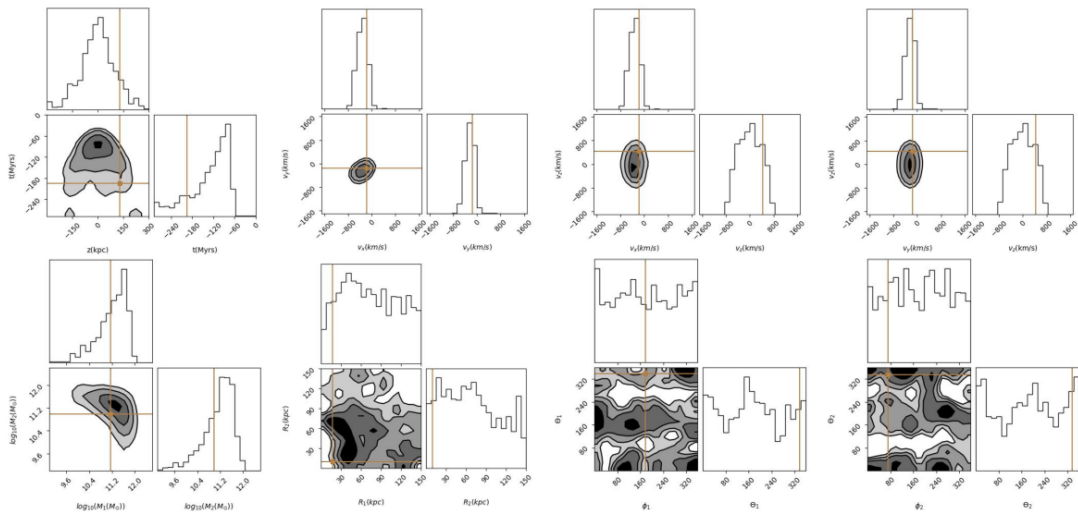


**Figure 4.11:** Second example of our worst fits. This shows our constraints on the simulated image of NGC 4320, a stage 4 system.

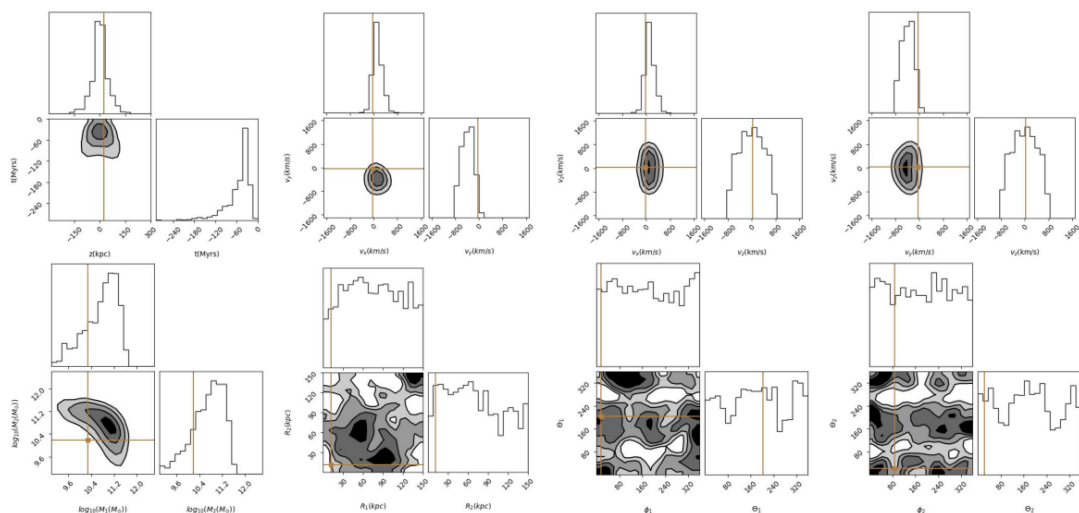


**Figure 4.12:** Third example of our worst fits. This shows our constraints on the simulated image of UGC 11751, a stage 3 system.

systems with little to no interaction and a merger with multiple flybys undergoing coalescence. This would be improved by including velocity information, where the velocity distribution will be very different between two overlapping disks and coalescing galaxies. Our process is also not yet designed to account for multiple flybys, which is likely to have occurred in a merging system. To make accurate constraints on many parameters, we require clear and distinct tidal features. UGC 11751 is a system where we have reduced the resolution so much that we lose spatial resolution in the flux distribution of the tidal features. Therefore, we insert a significantly higher uncertainty into our constraints. Finally, our MCMC requires a secondary galaxy to make reasonable constraints on the underlying parameters. The example of NGC 4320 is a final stage merger where a large tidal feature has formed as a result of the coalescence.

Throughout every system we put constraint on, the parameter we are able to get reliable constraints on are the masses of the systems. This is shown above as even our worst fit systems still hold excellent constraints, with the values confined to small areas of parameter space. However, our worst constraints lie in the orientation and time since the interaction. We show the relation between the true parameter used to create the synthetic image and our recovered best fit parameter with errors included. Figure 4.13 shows this distribution. We

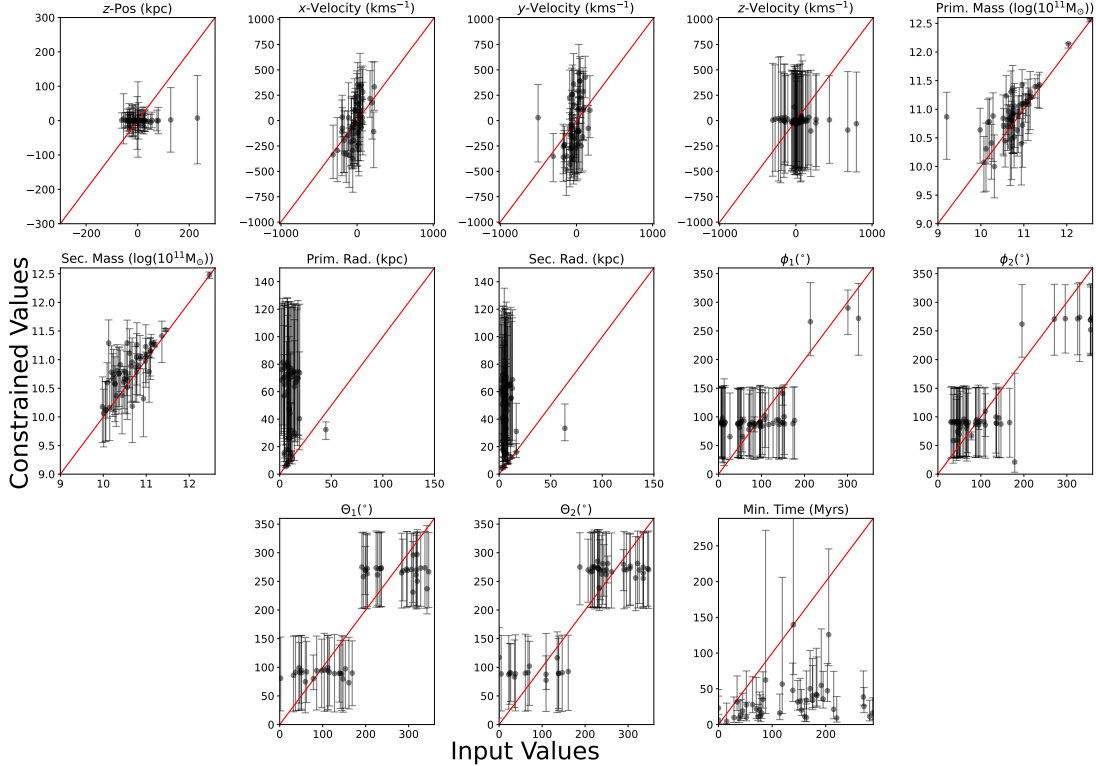


**Figure 4.13:** The distribution of parameter values used to create our synthetic interaction images and the best-fit values we recover from our algorithm. The constrained values are taken as the 50th percentile of our walker distribution. Our lower and upper errors are then calculated as the difference from our best found value and the 16th and 84th percentiles, respectively. This gives an idea of the extent of our walker distribution in 1D. The red lines show a 1-1 relation and where our points would lie if the 50th percentile represented the exact input value found. Parameter names and units are found in the title of each subplot.

define the best fit value from our MCMC as the 50th percentile of our walker distribution. This is represented by each point in Figure 4.13. The upper and lower error bars are calculated from the difference between the 50th percentile value and the 84th and 16th percentile values, respectively. The red lines in each subplot represent a 1-to-1 relation between the true parameter value and the recovered value.

Figure 4.13 clearly shows where our MCMC has made excellent constraints and where it has not. The best constraints are on the masses of the interacting systems, where each best-fit value approximately follow the 1-to-1 relation.

Where there is some discrepancy, the true values are within our errors. There is a trend here, however, that the total mass of the system is over estimated when compared to the true value. We also find excellent constraints on the majority of the positional and velocity vectors of the interaction, where the 50th percentile value approximates the true value. However, in these parameters we have explored a very wide parameter space when the majority of the true values are clustered around the centre of the parameter space. We will require further investigation with interacting systems more representative of the full parameter space we have explored.

We also have reasonable constraints on our orientation parameters. As we often have two areas of high probability due to degeneracy, we opt to only plot the 50th percentile and errors of the high probability space near the input value. This would not be possible with an observational system with unknown parameters. Therefore, the user will either need to make a choice of what area of parameter space to explore, or input some prior on the orientation / inclination of the system. Once we have accounted for the degeneracy, we find that our 50th percentile value is representative of the true value, with the true value being within error of it.

There are three parameters remaining where we find poor constraints or struggle to recover the true parameter value in general. The first are the radii of the two galaxies. We find that these are often over-estimated. Upon inspection of many of the output simulations, we find this is likely an effect of the distribution of particles and that we are using idealised synthetic images with no noise in the image. The way in which the particles are distributed is with an exponentially declining disk. This is achieved by creating a disk of particles which are sectioned into rings. Each ring has an exponentially declining probability of particles appearing within it based on the radius from the centre. Therefore, we find the outer rings of the galaxy are diffuse of particles, and do not dominate the likelihood function at high radius. This, in turn, means that galaxies with large angular size can be calculated as likely if the inner parts of the galaxy, with high particle numbers, match the flux of the inner disk. This also explains the over-estimate of the mass of each system. There are likely fewer particles than expected still within the galactic disk, and therefore more mass (ergo, luminosity) is required to keep the flux matched in the disk.

We also find we often under-estimate the time since the closest point of the encounter - i.e., the time of the passage - by a large margin. While those synthetic images whose underlying parameters had their point of passage very recently we recover very well, those at larger values we fail to. This is due to the likelihood function finding equivalent, high probability values between systems with correct tidal features and simple disks which match the inner disk of the interacting system. The former, tidal feature formation, requires a high  $\gamma$  parameter with low velocity and low impact distance. However, if the system is fast and does not form tidal features, but ends the simulation in the right place with the correct flux, the calculation will be dominated by the inner disk. Thus, we find a radius that covers the inner parts of the galactic disk successfully, with little disturbance that matches the flux of a large part of the galaxy. Therefore, the  $\gamma$  parameter is of the utmost importance to filter out these galaxies and give weight to higher  $t_{\min}$  values.

Aside from the points that have already been raised regarding our MCMC constraining each parameter, a further problem was that the likelihood calculation is dominated by contributions from the mass and velocity parameters. Therefore, to continue improvements on other parameters further walkers and a longer chain must be run, incurring a cost of far more computation time. For the purposes of this work, we show the full degeneracy, limitations and difficulties of our model and what is to be expected in the most general case. Many of these limitations and problems can be resolved from tighter priors with more information regarding the systems being investigated.

The true power of this approach will be when investigating large populations of interacting galaxies and combining and marginalising over many different posteriors. When combining the parameter spaces of many different systems, it will be possible to identify those areas of parameter space which lead to the formation of certain features across populations of interacting galaxies. Our method will allow more intense simulations to sample smaller parameter spaces and be more efficient when finding systems with specific features. However, how to combine the posteriors is somewhat up for debate. We have ensured that the parameter spaces we are exploring are equivalent in size and that the prior is equal across parameter space. This introduces the question of the  $\gamma$  parameter in filtering

simulations which, indirectly, changes the prior based on the trajectory of the interacting system. To conduct this combination, we would recommend that the  $\gamma$  parameter was not utilised when building the different posteriors if the increased computational cost is viable.

However, all of our results so far have been in the best-case scenario of a noiseless best fit simulation. The translation from simulation to observation in previous algorithms such as these is never an easy one. We, therefore, use our top three best fit systems here (Arp 172, Arp 240 and Arp 290) and apply our pipeline to their reduced observations.

### 4.5.5 Applying to Observations

We apply our MCMC to the reduced observational data of Arp 172, Arp 240, Arp 256, Arp 290 and Heart. Cutouts were created as described in Section 4.2.2. We reiterate here that the cutout resolution is reduced from its native resolution to cutouts of  $100 \times 100$  pixels. Before we input the images into the pipeline, we find the central pixel of the secondary galaxy and convert this into a physical  $x$ - and  $y$ -position. We also find the total size physical size of the cutout in kpc, convert it to simulation units and provide this to the pipeline. We find that the physical size of the cutouts are significantly different from those of our synthetic dataset. As an example, we create the cutout of Arp 240 at  $600 \times 600$  pixels at native resolution. With SDSS data, this corresponds to a physical size of  $111.50\text{kpc} \times 111.50\text{kpc}$  at the redshift of Arp 240. The synthetic image we previously used of Arp 240 is  $785.35\text{kpc} \times 785.35\text{kpc}$ . Figure 4.2 clearly shows a very different scaling between the observation and simulation, however, it is not enough to be seven times zoomed in on the system. We also find that the secondary positions are very different between the observation image and that used previously. As a result, the parameters we will find for constraining the observation will likely be very different.

We apply our MCMC to those outputs which had varying constraint. We only investigate these five systems as we find the computational expense is significantly higher when constraining the observations compared to the best fit simulations. We find the reasons for these are two fold. First, we must run each walker for

twice the number of steps than when constraining the synthetic images to reach convergence. This is from increased noise contributions in the observation images. Second, due to the smaller scale size of our images, the defined  $\gamma$  parameter is much stronger than with the synthetic images. This is due to the smaller scale of the images, and therefore we have a much smaller impact distance. We will also have a smaller velocity at closest approach measurement because the final point of the secondary has been moved closer to the primary. These reasons lead to a higher computational expense as the  $\gamma$  parameter filters out less candidate systems and runs the base simulation code more often.

Figure 4.14 shows the reduced corner plot for the observed Arp 240 system. The constraints on the velocity parameter have significantly worsened when compared to the constraints on the best fit simulation. They are also in a different area of parameter space when compared. The velocity and spatial parameters are the most likely to be affected by the change in scale between the two input images. As the secondary galaxy position has been completely altered the best fit trajectory of the interaction has also completely changed. The secondary is significantly closer to the primary, therefore meaning the secondary velocity must be significantly slower than previously. Due to the increase in noise in the observational image, and the extent of the tidal features of the primary and secondary galaxies, the constraint has also significantly weakened.

However, for the remainder of the parameters the level of constraint remains similar even with the change in the best fit values. We retain the two- and four-fold degeneracy in the orientation parameters. This follows on that the pipeline outright rejects disks which are edge on and loses accuracy when attempting to pin point the precise inclination of each galaxy. We are unable to make any constraint on the  $\theta$  parameters, while the degeneracy of the  $\phi$  parameters is still visible. The radius parameter is well constrained at 11.8% CI, although with large tails in the probability space for both the primary and secondary galaxies. These tails are significantly larger here than when using the best fit simulation as the input. This is due to the observation image having no hard cutoff of the edge of the galaxy, and simply moving into more noise. The outer edges of our simulated galaxies also moves to very low signal, and therefore, there is lots of uncertainty surrounding the true radius of the galaxy.



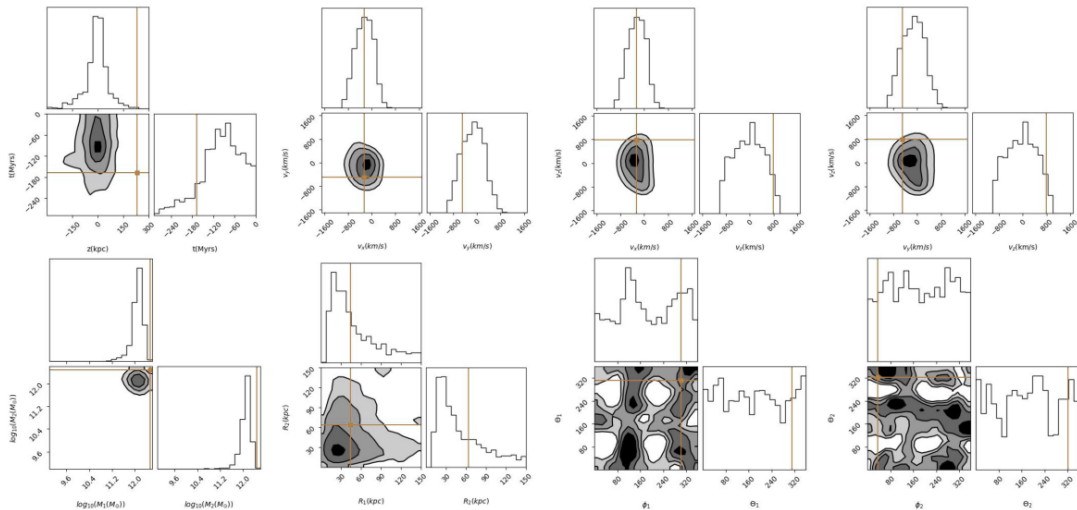


**Figure 4.14:** Reduced corner plot of the constraints made on the observational image of Arp 240. As shown, there is significant additional uncertainty in these measurements than those of the best fit simulation. However, we are able to make constraints on almost all parameters in the sample. The degeneracy in the orientations remains. The gold lines represent the true values we used in to create the synthetic image.

We, again, make excellent constraints on the mass parameters. The accuracy in the flux distribution of the primary and secondary disk is what dominates here, and therefore, we find this value incredibly quickly. The found value is comparable to the best fit simulation, although slightly lower. We also compare our constrained values to what is found in the literature. Using the criteria described previously, we recover total masses of  $\frac{M_1}{10^{11}M_\odot} = 7.97 - 15.9$  and  $\frac{M_2}{10^{11}M_\odot} = 8.1 - 16.2$  which correspond to stellar masses between  $\frac{M_{1,*}}{10^{11}M_\odot} = 0.94 - 1.89$  and  $\frac{M_{2,*}}{10^{11}M_\odot} = 1.0 - 1.9$  in our simulations. These are slightly higher than literature values, with a recent work quoting the stellar mass as  $\frac{M_{1,*}}{10^{11}M_\odot} = 0.94$  and  $\frac{M_{2,*}}{10^{11}M_\odot} = 1.05$  (He et al., 2020). Thus, while our 50th percentile value is higher than the measured values, we do recover them within error.

We find similar constraints on the other observations we input into our MCMC. Figures 4.15, 4.16, 4.17 and 4.18 show these constraints with the gold lines being the best fit parameters to create our test images. The variability across our constraints is greater than on the synthetic images. We often find degeneracy in the

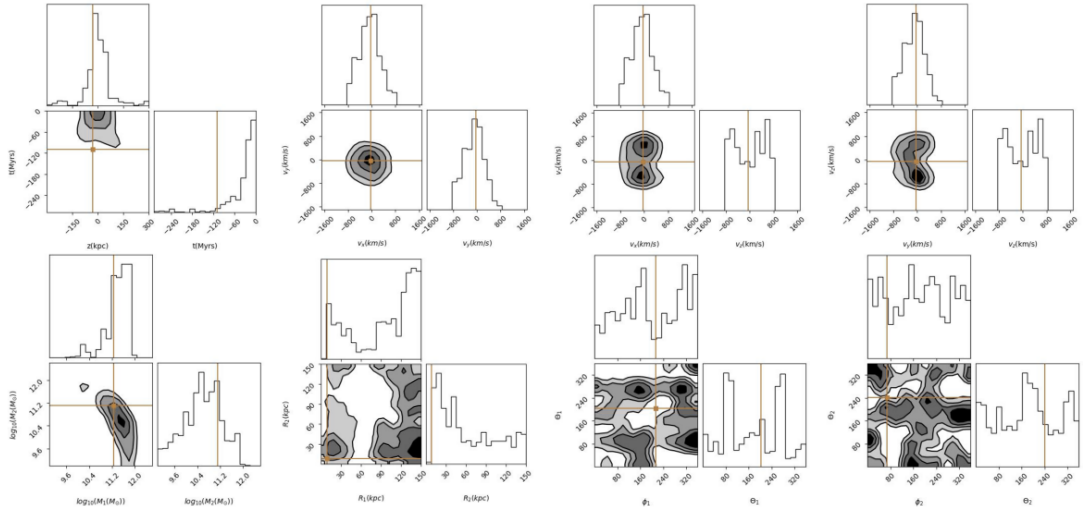


**Figure 4.15:** Reduced corner plot of the constraints made on the observational image of Arp 172.

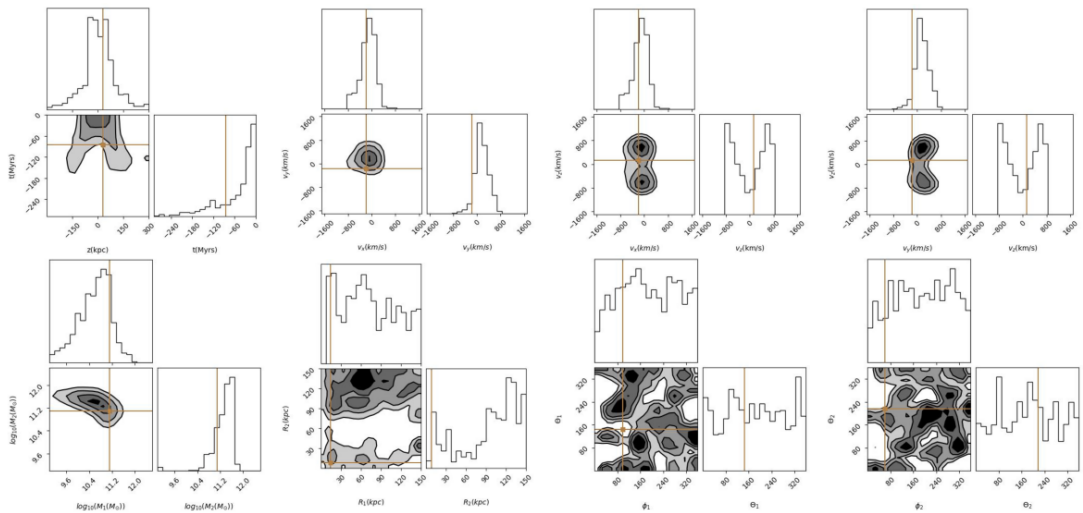


**Figure 4.16:** Reduced corner plot of the constraints made on the observational image of Arp 256.

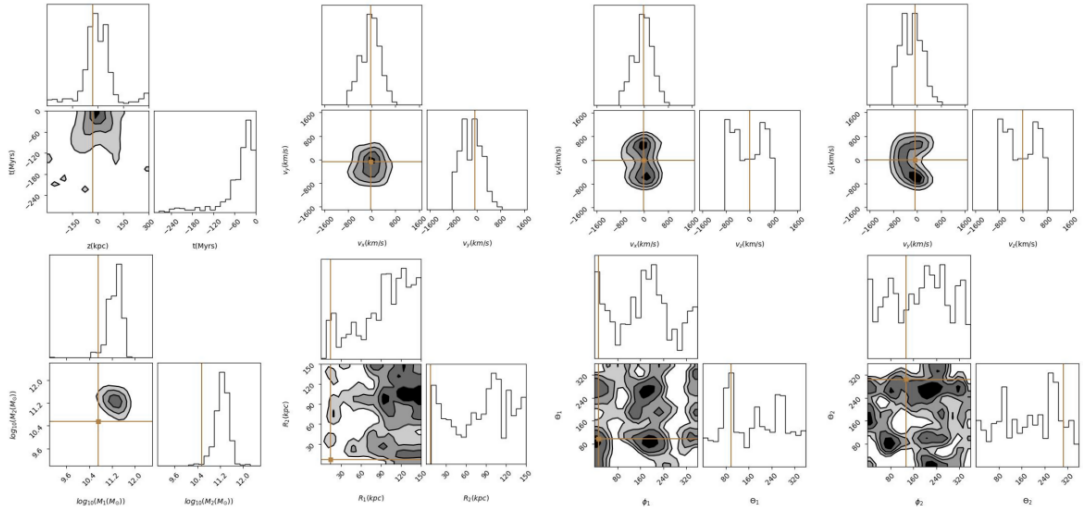


**Figure 4.17:** Reduced corner plot of the constraints made on the observational image of Arp 290.

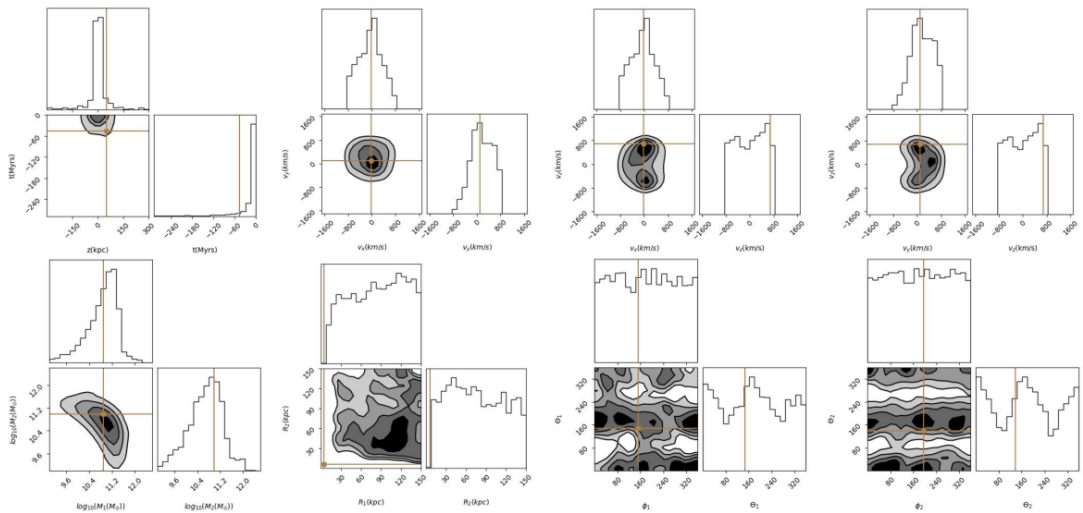


**Figure 4.18:** Reduced corner plot of the constraints made on the observational image of the Heart system.

velocity parameters, as expected, but also appear to lose much of the constraint on the radius parameters. The constraints we do make are often different from those of our synthetic images representing these systems. The primary reason for this is the synthetic images we have used are at a different scale when compared to the the SDSS observations. We therefore find similar constraints to the different parameters, however with significant variation in the spatial parameters. The uncertainties in the radius parameters are significantly increased, while the constraint on the  $\theta$  and  $\phi$  parameters are lost. In fact, for the same number of steps compared to constraining the best fit parameters, our MCMC fails the Geweke diagnostic. Therefore, due to the added noise, and more complex flux distribution, running longer chains is imperative which drives up computational expense.

This leads us onto the limitations of this process to constraining galaxy interaction. While it has been very successful for many of the underlying parameters, there are many different parameters which must be provided to the pipeline so it is able to make those constraints. We discuss the limitations of applying this methodology to large interacting galaxy datasets, and how these can be offset in the short term but a long term solution is still required.

### 4.5.6 Limitations

While this methodology does show promise in being able to constrain underlying parameters across populations of interacting galaxies, it is important to note that at its base is a restricted numerical interaction code with limited resolution. There may be some interacting systems that simply cannot be modelled realistically using three-body approximations, and may therefore cause a skew in results. However, there are also some more subtle limitations which may affect how a user wishes to use this MCMC approach.

#### 4.5.6.1 Resolution & Depth Effects

One of the fundamental parameters that must be provided for this methodology to work is the redshift of the system. This is used to calculate the distance to the

system and then converted to an assumed resolution for the scale of the image. If this is input incorrectly the simulation images will be created at an incorrect resolution, and the MCMC will likely not reach convergence. This is also true of providing and calculating correctly an approximation of the position of the secondary galaxy. Significant computation power can be wasted if these parameters are incorrect, and will give spurious results. The reduction in resolution of the images is also an important limitation. This toy model needs small, thumbnail size images with a reasonable number of degrees of freedom as to reach convergence. Therefore, input images can only be of limited resolution which will affect the quality of the constraints we can actually make on different systems.

The redshift is also used in scaling the fluxes calculated for each particle in the simulation. The base SED is calculated for a  $1 M_{\odot}$  system at a distance of 10pc. This is then scaled to the mass assigned to a particle and then put at the distance calculated from the redshift. If the redshift is incorrect (or even slightly off) then this could lead to a bad fit for the mass of the two galaxies in the system. A flag exists in the algorithm to give it the freedom to slightly vary the redshift (and therefore the distance and resolution) by 0.001 with each step. It will then attempt to fit the redshift and resolution of the system. Note, however, this is untested and currently significantly increases computational expense.

Depth effects also play a significant role in the ability of our algorithm to fit a system which may have ‘unseen’ tidal features. For this Chapter, we used primarily synthetic images, meaning we were not at risk of this. Our observational examples were of major interacting systems which resided in the high surface brightness regime, where we retained the full extent of the tidal features and could provide better fitting. However, for systems that lie closer to the low surface brightness regime, our algorithm will become less efficient and require more computational expense to make effective constraints.

This also has the opposite effect in terms of tidal features formed. For example, if a system is being fit but at the true parameters a tidal feature exists which has not been detected due to its low surface brightness then our MCMC pipeline will not be able to converge on the true values. The algorithm would instead converge on those parameters where the disks were at the correct flux rather than getting the tidal features correct. Therefore, when exploring the parameter space

of interacting systems with our pipeline, it is imperative that the full structure is within detection of the observing instrument.

There must be a trade off between the resolution of our simulation and the observations. In this work, we used cutouts of  $100 \times 100$  pixels. This was so that we could still get consistent system outputs from our simulations using only 2500 particles. If many pixels are used, then using a low number of particles can lead to many ‘unphysical’ output simulations. I.e. these are simulation systems where the disks will have large holes in them where there haven’t been enough particles to fill the disk. To mitigate the effect of potentially using low particle numbers, we distribute the flux as described in Section 4.3.1.3, which is an imperfect solution. It is recommended for any user to make a balanced trade off between resolution and computational expense.

#### 4.5.6.2 Computational Expense

The main drawback of this methodology is that of computational expense required to run such an MCMC over a the full parameter space. In the case of this work, the simulation was set up with 2500 particles on a High End Computer Cluster with 50 CPUs. Each simulation took approximately two seconds, with the full sample run taking approximately 40 days to complete. Each galaxy was given 600 walkers to move through parameter space with each walker moving 7,500 steps. The highest memory requirement of any system was 6GB. Therefore, the runtime is very high but the memory required for it is approximately 122MB per core.

This methodology was successful in constraining 51 different interacting galaxy synthetic images. Achieving the same in prior work projects, such as Galaxy Zoo: Mergers, took months to complete. We have reduced the runtime required of it to 40 days on a powerful High End Computer Cluster. However, this is not the solution to the large scale dataset problems that we will be seeing when LSST comes online. If we are to run this methodology on a much larger galaxy sample - such as thousands of galaxies - then we will need to find ways to significantly improve the runtime of this method.

## 4.6 Conclusions & Future Work

In this Chapter, we have introduced a new algorithm based on a MCMC framework to apply constraints on the underlying parameters of interacting galaxies. We have made these constraints, and explored the underlying parameter space, through directly comparing input images to output simulations. This maps the underlying parameters that define interaction to an output morphology that we compare for similarity with a synthetic or observation image. We have introduced an updated version of the restricted three body simulation **JSPAM** and modified it to calculate and match the flux distribution of interacting galaxies based on thirteen underlying parameters. This updated algorithm, **APySPAM**, calculates the flux distribution by assigning particles with a spectral energy distribution and accounting for star formation throughout the interaction.

To test our MCMC, we applied it to a set of synthetic images of interacting systems created from the parameters found in the Galaxy Zoo: Merger project for a set of real interacting systems. We were able to recover the true parameters used to create these images, with associated error measurements on each. We have explored the specific results of a single synthetic image: that of the Arp 240 system, and shown the corner plots and full posteriors of each parameter. We have taken the 50th percentile value as the best fit value for our synthetic dataset, and used the 16th and 84th percentile to define the errors on our measurements. We then presented the distribution of our recovered underlying parameters and the true values, describing the general trends in our methodology as well as its limitations.

Every parameter was recoverable, however there was significant degeneracy in the orientation angles of the two galactic disks. This was expected as works such as Smith et al. (2010) found significant degeneracy between systems, but not a direct cause. In this work we found, without taking account of kinematic information, multiple orientation angles can recreate observed tidal features as well as limitations in the pixel matching method of constraint. When tested on observational data of our best fit synthetic systems, we were able to retain the excellent constraints on nine of the thirteen parameters, but lost any constraint

on the orientations. However, we were able to maintain a tight constraint on the masses of the two systems.

There are limitations to this method that any users must be aware of. First, the core simulation of this process is a restricted three-body code with a highly optimised flux distribution calculation and approximation. It is probable that there are systems that this approach can not constrain, or may give nonphysical results for. The required reduction in the parameter space of the images, such as reducing the degrees of freedom and limiting individual pixel resolution in favour of computation time, also may lead to constraints only on the disks of the galaxies and not the tidal features themselves. There is also limited time and spatial resolution within the simulation itself. When using true observations, they had to be artificially scaled up so our simulation could maintain the resolution to have constraint. In terms of the temporal and spatial parameters, this scale up can be accounted for. However, in terms of the masses of the flux distribution, this can be significantly hindered. Therefore, a user must be careful when choosing the image scales to use when attempting to constrain individual systems.

We have demonstrated the power of this methodology, and that it is capable of recovering the underlying parameters of interaction in idealised examples. The next serious test of this MCMC approach will be to use it on a set of observed interacting systems, where the underlying parameters are known to properly diagnose the results. However, completely constrained interacting galaxy samples are only of a small scale and few exist. We will apply our MCMC to the observed dataset of our 51 interacting systems in SDSS.

This is an initial step towards developing the methodology to serve the field as large scale surveys - such as LSST - come online. Large scale automation where we can constrain interaction, make diagnostics and estimates about parameter space are not only important for inferences about individual datasets but for the interacting galaxy population as a whole. The main limitation of this method is the computational expense associated with it. To run this on 51 systems, the total run time was thirty days; an unusable timescale when being applied to interacting galaxy samples in the thousands. Therefore, future works with this algorithm and methodology will also be focused on increased computational efficiency and working on larger interacting galaxy datasets.



The bottleneck for computational efficiency lies in the time spent running the APySPAM simulation. While incredibly cheap individually, this is exceptionally expensive when having to be run in an MCMC chain. With the growing power of graphical processing units, and their ability to run numerical simulations significantly more efficiently than CPUs, a pathway to solve this limitation may already exist. This, combined with further developments in methodologies such as simulation based inference, machine learning and Gaussian Processes could begin to reduce computation time.

# Chapter 5

## Summary and Future Work

### 5.1 Summary

This work has focused on the role of galaxy interaction with respect to galaxy evolution. We have shown a new and novel way of creating large interacting galaxy samples, used it to explore the relation between galactic parameters and interaction and presented the initial pilot of a MCMC algorithm to definitively link the parameters of galaxies to the tidal features that form. The novel process of creating a large catalogue of interacting galaxies was detailed in Chapter 2. By using newly developed data-access architecture with the newly developed Bayesian CNN, Zoobot, the largest catalogue of interacting galaxies to date was created. Along with this, we demonstrated how the new data-access architecture, ESA Datalabs, can be used to explore archival data volumes easily and efficiently. To make concrete links between galaxy evolution and interaction in the local volume, this catalogue was cross-matched to catalogues of ancillary data. This was done using the catalogues created from deep observations of the COSMOS field. This provided us with a flux limited sample of 4,181 and volume limited sample of 3,378, interacting galaxies to explore.

In Chapter 3 we conducted this exploration of our cross-matched sample in the context of interaction stage. We investigated whether conflicting theories about galaxy interaction were a result of not accounting for interaction stage

based on observed morphology. We confirmed that interaction stage does have a significant impact on the underlying processes and enhancements that result from interaction. It was immediately found that the SFR increases dramatically through stage - from close pair to merger. This was demonstrated by measuring the distributions of stellar mass and SFR through stage and comparing them. We found that for distributions of stellar mass drawn from the same parent sample, the distribution of SFR changes. This was in the form of the disappearance of the red sequence, as our samples SFR was enhanced. We compared this with existing works which utilise the projected separation between systems as an approximation of the stage of interaction in the two systems. We found a complete disconnect with the projected separation and stage, noting that conflicting results can emerge from only looking at the projected separation without properly accounting for the interaction stage from the morphology.

This degeneracy in the projected separation was particularly true of the change in the fraction of active galactic nuclei with stage, a topic the literature is particularly divided upon. We found that AGN fraction remained consistent with the separated stage at  $0.059 \pm 0.004$  to throughout the interaction until coalescence where the fraction increased to  $0.071 \pm 0.005$ . Breaking down our AGN counts with projected separation, we found two peaks in AGN count. Thus, we find evidence for a delay in the activation of the AGN which is difficult to account for when only using projected separation. While this methodology shows how we can use ancillary data to connect the underlying parameters of galaxies to interaction, and fundamental processes we attempted to conduct this in a more general way and to bring in linking to tidal feature formation.

Chapter 4 saw the development of an algorithm to find the underlying parameters of the galaxies involved in interaction from their flux distribution. We combined a fast, efficient restricted numerical simulation with a MCMC methodology and Bayesian statistics and placed constraints on the underlying parameters of 51 synthetic images of interacting systems. While our uncertainties increased when applied to observational data, constraints were nonetheless able to be made upon the majority of the parameters. Constraints only failed on the orientation parameters. The creation of this MCMC algorithm paves the way to apply this

to large interacting galaxy datasets such as the one described in Chapter 2. However, the limitations in the runtime of the algorithm; taking approximately 15-20 hours per interacting galaxy, leads this to not be feasible. Therefore, methods of further improvement in efficiency of the underlying numerical simulation must be explored. There is particular promise in this regard with the development of numerical simulations on GPUs, and the massive acceleration they provide to such projects.

We have created a large interacting galaxy dataset and demonstrated its capability in the context of how the progression of a galaxy changes the underlying properties of galaxies. We have introduced a method by which further examination of these systems could be explored, although further advances in its efficiency must be made for this approach to be viable. Potential methods, plus descriptions of future works in Chapters 2 and 3, are discussed in the final subsection of this thesis.

## 5.2 Future Work

### 5.2.1 Catalogues of Galaxy Morphology with Ancillary Data

Chapter 2 demonstrated that new data access architecture is now ready for us to conduct source classification at a scale rarely seen to this point. We can now directly access millions of sources across multiple filters, instruments and observatories to yield unprecedented sample sizes. These can be combined with novel machine learning algorithms requiring small training set sizes to fine-tune making them versatile and accurate across many different observatories. Since the publication of the paper underlying Chapter 2, the *Zoobot* algorithm has been updated many times. Not only is it now trained upon *HST* data, but part of the representations of galaxies it learns is if a galaxy is interacting or not. By redoing the work conducted in Chapter 2, one could classify galactic morphologies across the Galaxy Zoo workflow rather than just on an individual question.

The fundamental component of this which makes it possible is the ESA Datalabs platform. This platform has also been updated to provide access to many different observatories archives within it (such as *JWST* and *Euclid*) and also has access to much larger storage spaces and GPUs. Therefore, the entire work of Chapter 2 can be done on the platform with no requirement for data transfer (in our case, data had to be moved from ESA Datalabs to the Lancaster computer cluster for classification, taking the bulk of the project time). ESA Datalabs now allows us to conduct a project similar to the one outlined in Chapter 2 with much greater efficiency. Not only could this classification be applied for interacting vs non-interacting, but we can also begin to consider creating larger catalogues of much broader morphology classifications. The recent Galaxy Zoo: DESI release contained 9.7 million galaxies with full morphology classification. Applying this to just the sources created in Chapter 2 would find 126 million morphology classifications, which is over a factor of 10 greater than previously achieved.

We can also take this further and not limit the opportunity here to only large catalogues of morphology classification. With the all-sky photometry that will be available from *Euclid*, or survey scale photometry that will be available from ground based observatories like the Legacy Survey of Space and Time, it will be possible to get broad-band photometry for millions of overlapping sources. By applying well-known astrophysical software such as **FAST**, **EaZY** or **LePhare**, it will be able to estimate many galactic parameters. These include the stellar masses, the photometric redshifts or, in some cases, the presence of AGN. By creating such large morphology catalogues, combined with this ancillary data, we will be able to robustly link different galaxy parameters to their physical morphologies. This can then be expanded out to include linking to the source environments across the sky.

The development of algorithms like those proposed and tested in Chapter 4 will also provide excellent methods for constraining the underlying parameters of sources. While Chapter 4 focused on such an algorithm in the context of interacting galaxies, algorithms such as **GALFIT** are able to find morphological parameters purely from comparison to flux distributions and images. Even without further broad band photometry from other observatories, we will be able to explore the

---

underlying parameter spaces of galaxies and link this to their morphologies using these data access architectures.

### 5.2.2 Constraining Interacting Galaxy Parameters

In Chapter 4, we made direct links between the flux distribution of interacting galaxies and the parameters of those galaxies. We made constraints and revealed degeneracies across multiple parameters. However, the limitation of this approach was the computational expense, taking between 15-20 hours per system with the associated run time cost for this. For the large scale surveys or the catalogues such as those created in Chapter 2, this efficiency is not enough. Making constraints on the entire sample selected in Chapter 2 would take between 37 and 50 years. However, there are multiple development routes that could be taken in future to boost computational efficiency. The first is to take full advantage of the next generation of GPUs. Many cases of accelerating numerical simulations have been written about and analysed, particularly from the GPU developer NVIDIA. These have demonstrated striking improvements in efficiency up to a factor of 3, especially in the context of numerical models of fluid dynamics (recent examples include Mantas et al., 2016; Costa et al., 2021). Thus, reworking the code in this way would remove this limitation and have constraint being made in a matter of minutes: much more feasible for applying to large scale samples.

A second approach would be to move away from the direct method of MCMC and into utilising simulation based inference (SBI), often called likelihood free inference. Work has been conducted into SBI, and its massive increases in efficiency when constraining over large and complex parameter spaces (for an excellent description of likelihood free inference, see Jeffrey et al., 2021). In this context, rather than running a MCMC and directly comparing simulation outputs to an observational image, a machine learning algorithm trained on simulation outputs is used to explore the parameter space. By running an initial set of simulations and feeding this into a rudimentary CNN, a low dimensional representative vector can be created of each image. This is then applied to the observational image. The CNN then approximates the posterior through parameter space, achieving

constraints comparable to a direct MCMC exploration. However, while this approach has been very successful for small parameter spaces defining 1D cases, applying to cases of images - especially one defined by a 13D parameter space presented here - is in its infancy.

Once this is evolved, however, it would succeed in significant improvements in the efficiency of our constraining algorithms. We could take advantage of the amortisation of SBI, and be able to apply our initially trained network and posterior distribution to many different systems instead of having to explore parameter space directly every time. This has the effect of front-loading the computational expense of our constraining process, running thousands to millions of simulations across parameter space initially to train the neural network and then being able to use the model in multiple cases, albeit with some caveats. Amortisation of the trained model across parameter space would be very sensitive to many different fundamental parts of our analysis process. For instance, changing the position of the secondary galaxy, the changing resolution of the images, the number of particles in the simulation, etc, all could be attempted. Changing any of these would mean amortisation is not valid, and the model would have to be retrained - re-introducing the problem of computational efficiency.

However, if these caveats can be resolved, this would open the way for large-scale application of SBI and our direct inferencing methodology to large samples. These will be our next steps in the development of this algorithm, and to then make it widely accessible to the community, with the application of our sample of interacting galaxies from Chapter 2. We will then be able to apply the process as conducted in Chapter 3, and link the effects of interaction to further underlying parameters than the stellar mass, interaction stage and SFR.

# Appendix A

## Model Diagnostics & Further Identified Objects

### A.1 Further Model Diagnostics

In Section 2.5 we present diagnostic properties of our model. These include the accuracy measurements, purity measurements as well as confusion matrices at different cutoffs of our model. Here, we present the Receiver Operating Characteristic (ROC) curves, the precision-recall (PR) curves, and measures of true and false positive rates vs the cutoff threshold.

Figure A.1 shows the ROC and PR curves of the final Zoobot model we applied to the the *Hubble* archives. The ROC shows the rate of change of finding true positives and false positives with changing cutoff. The PR curve shows the changes of precision against recall. Precision is the ratio of true positives (interacting galaxies correctly predicted as so) to the sum of true and false positives (non-interacting galaxies incorrectly predicted as interacting). The recall is then the ratio of true positives to the sum of true positives and false negatives (interacting galaxies that have been misclassified as non-interacting). The red crosses in both plots shows how the model was behaving when we use a cutoff of 0.95.

These are both as expected. Both curves show that the model behaves well, and are much better than a random classifier (which would have a 1:1 relation).



The ROC plot shows that we are minimising our false positive rate when using a prediction score cutoff of 0.95. However, we are misclassifying approximately 50% of interacting galaxies as non-interacting galaxies. The contamination rate in our final catalogue (False Positives rate) will be very low (close to zero in this ideal validation set). The PR curve shows a similar result. Here, we are operating with a high precision (finding a pure catalogue) while keeping our recall minimal.

We also present the changing F1 score for the model used in this work, shown in Figure A.2. The F1 score is twice the ratio of precision multiplied by recall upon precision summed to recall. This combines our measure of accuracy and purity into a single metric. The cutoff we use in this work is at the point where the F1 score has began to decline. This is because we are beginning to lose recall rapidly, but gaining significantly in precision. As discussed in Section 2.5, this was an acceptable trade off in this work for a very large, pure interacting galaxy catalogue.

## A.2 Examples of Sources with 3-Band Information

Of the full catalogue of 21,926 interacting systems, only 1336 of them had got all 3-band information. Six examples are shown in Figure A.3. These were created using the Lupton et al. (2004) algorithm, with a scaling factor  $Q = 2$  and  $\alpha = 0.75$ , with ( $F814W$ ,  $F606W$ ,  $F475W$ ) as RGB channels and multiplicative factors of (1.25, 0.95, 2).

## A.3 Unknown Objects

From the final catalogue, there were six sources which we could not visually identify. These objects were also not referenced anywhere in the astrophysical literature.  $F814W$  cutouts of the six objects are shown in Figure A.4. Their Source IDs are shown in the upper left of each image, and a separate catalogue

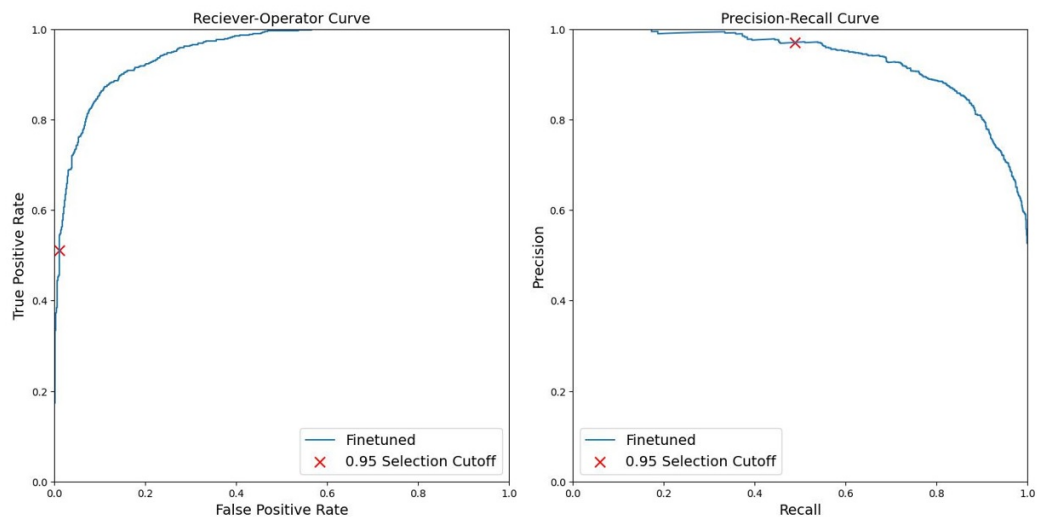


**Figure A.1:** The Receiver-Operator and Precision-Recall Curve for the Zoobot model that was used to explore the Hubble archives. The blue curves are the measured curves. These curves measure the relevant rates or characteristics based on the changing cutoff applied to how Zoobot defines an interacting galaxy. The red crosses are where the prediction score cutoff is for this work. We can see in the Receiver-Operator Curve that the prediction score cutoff we use would have an incredibly low false positive rate, while it would be misclassifying  $\approx 50\%$  of interacting galaxies. This is also shown in the precision recall curve where our recall is  $\approx 50\%$ .

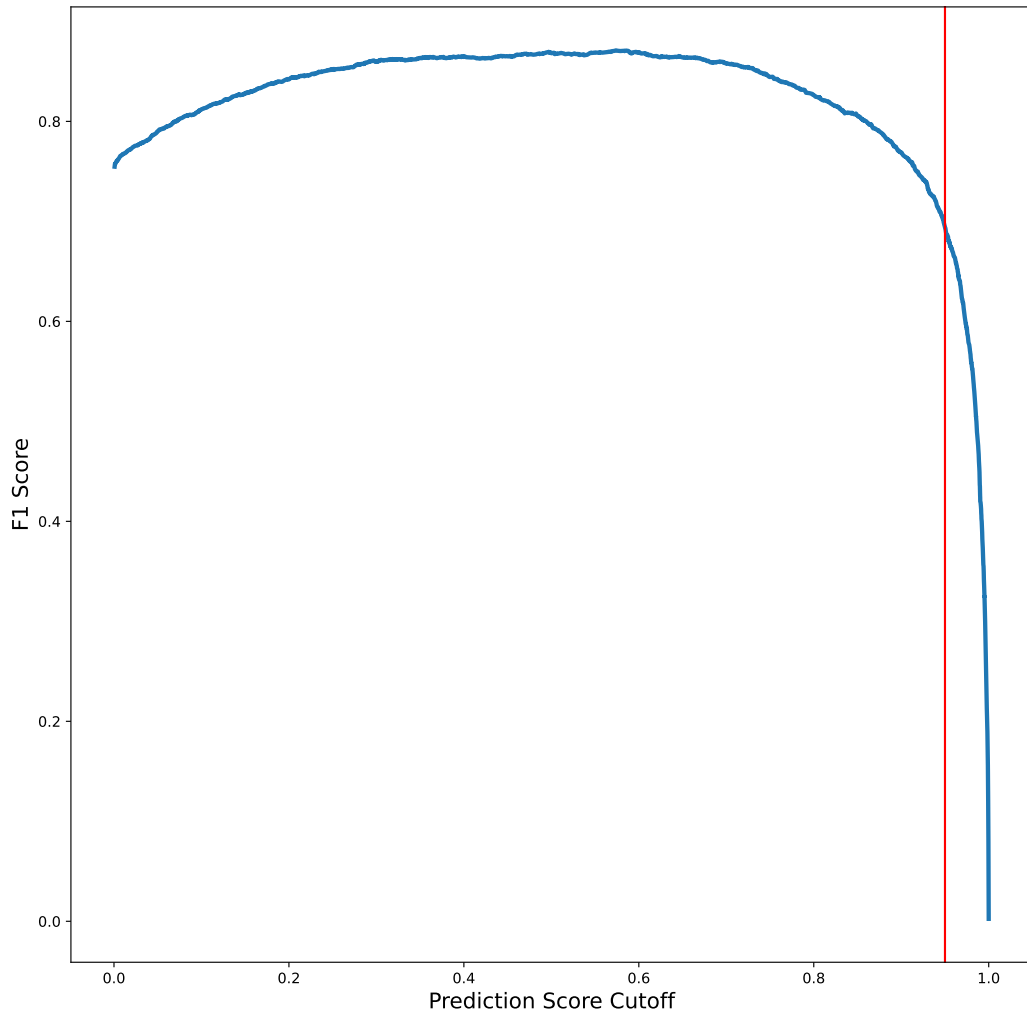


**Figure A.2:** The F1 score found during the diagnostics of the model used in this work. The F1 score is a measure combining the measure of accuracy and purity into one metric. The cutoff we use is at the point where the F1 score begins to rapidly decline. This point is shown by the red vertical line.



**Figure A.3:** Example of six interacting systems in the catalogue with full 3-band imagery.

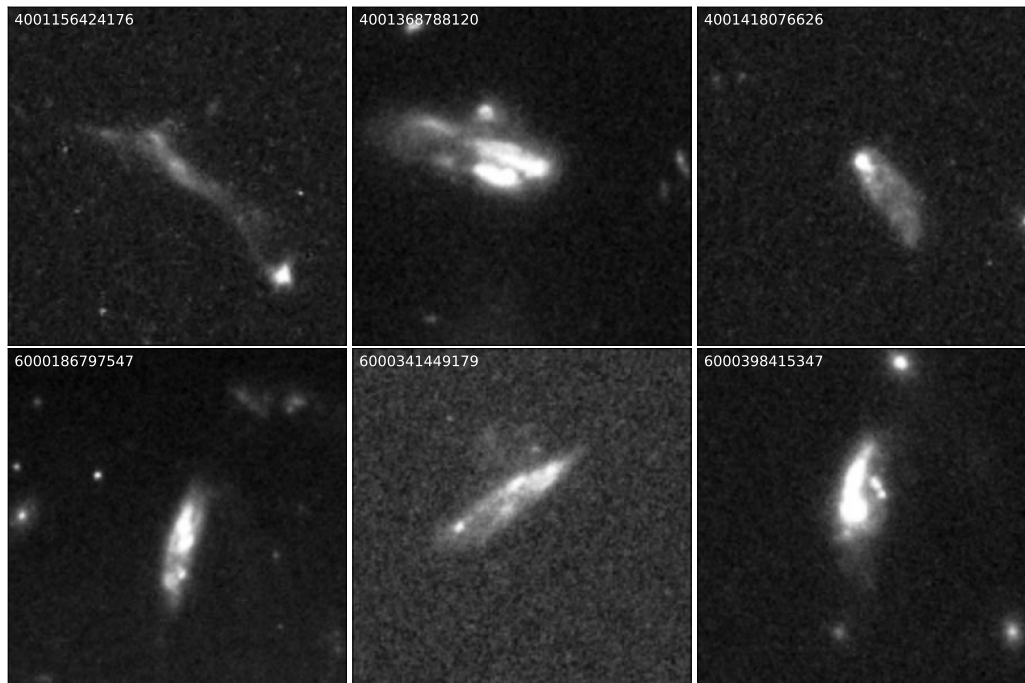


**Figure A.4:** The six unknown systems found in this work. These have no reference in Simbad or in NED, and their morphology could not be classified by the authors. Investigation into these six objects are presented to the community, with the authors hoping that future work and investigation of them can be conducted by them.

has been released of these with all other objects. This catalogue can be found at the data release on Zenodo.

Four of the six objects (40001156424176, 4001368788120, 4001418076626 and 6000398415347) have a bright central source, followed by a low-surface brightness tail. Initially, it was assumed that these were solar system objects such as comets. This, however, could not be confirmed. The first of these four sources is also thought to potentially be a highly disrupted system with a significantly elongated tidal feature. The final two unknown sources (6000186797547 and 6000341449179) have no clear central source, though there is extended structure to them. These are likely to be highly irregular galaxies, but no confirmation could be found.

These objects are released to the community for identification and investigation, as the authors cannot find definitive agreement on what they are.

Proposal ID	Observation ID	Observation Date	DOI	references
8183	hst_8183_54_acs_wfc_f814w_j59l54	18/07/2002	<a href="https://doi.org/10.5270/esa-88k8vcj">https://doi.org/10.5270/esa-88k8vcj</a>	
9075	hst_9075_2a_acs_wfc_f814w_j6ff2a	24/07/2002	<a href="https://doi.org/10.5270/esa-gsxhb4b">https://doi.org/10.5270/esa-gsxhb4b</a>	
9351	hst_9351_11_acs_wfc_f814w_j8d211	31/03/2003	<a href="https://doi.org/10.5270/esa-5lba8bo">https://doi.org/10.5270/esa-5lba8bo</a>	
9361	hst_9361_03_acs_wfc_f814w_j8d503	22/07/2003	<a href="https://doi.org/10.5270/esa-ecmnqgh">https://doi.org/10.5270/esa-ecmnqgh</a>	
9363	hst_9363_09_acs_wfc_f814w_j8d809	02/07/2002	<a href="https://doi.org/10.5270/esa-ethtec5">https://doi.org/10.5270/esa-ethtec5</a>	
9367	hst_9367_02_acs_wfc_f814w_j8ds02	10/06/2003	<a href="https://doi.org/10.5270/esa-3j404ll">https://doi.org/10.5270/esa-3j404ll</a>	
9373	hst_9373_02_acs_wfc_f814w_j6la02	05/07/2002	<a href="https://doi.org/10.5270/esa-ztsq94u">https://doi.org/10.5270/esa-ztsq94u</a>	Rejkuba et al. (2005)
9376	hst_9376_02_acs_wfc_f814w_j8e302	13/07/2002	<a href="https://doi.org/10.5270/esa-h90iavd">https://doi.org/10.5270/esa-h90iavd</a>	Keel et al. (2006)
9381	hst_9381_02_acs_wfc_f814w_j8fu02	13/03/2003	<a href="https://doi.org/10.5270/esa-vlapyea">https://doi.org/10.5270/esa-vlapyea</a>	
9400	hst_9400_04_acs_wfc_f814w_j6kx04	29/05/2003	<a href="https://doi.org/10.5270/esa-39rmout">https://doi.org/10.5270/esa-39rmout</a>	
9403	hst_9403_02_acs_wfc_f814w_j8fp02	09/07/2002	<a href="https://doi.org/10.5270/esa-k5mv9ct">https://doi.org/10.5270/esa-k5mv9ct</a>	
9405	hst_9405_6k_acs_wfc_f814w_j8iy6k	22/05/2003	<a href="https://doi.org/10.5270/esa-zy9phm1">https://doi.org/10.5270/esa-zy9phm1</a>	
9409	hst_9409_03_acs_wfc_f814w_j6n203	29/06/2003	<a href="https://doi.org/10.5270/esa-vjngw7r">https://doi.org/10.5270/esa-vjngw7r</a>	Goudfrooij et al. (2004)
9411	hst_9411_09_acs_wfc_f814w_j8dl09	11/02/2003	<a href="https://doi.org/10.5270/esa-debpiln">https://doi.org/10.5270/esa-debpiln</a>	
9427	hst_9427_13_acs_wfc_f814w_j6m613	21/10/2002	<a href="https://doi.org/10.5270/esa-bw1b97v">https://doi.org/10.5270/esa-bw1b97v</a>	
9438	hst_9438_01_acs_wfc_f814w_j6me01	16/01/2003	<a href="https://doi.org/10.5270/esa-c5eaam5">https://doi.org/10.5270/esa-c5eaam5</a>	Gregg & West (2017)
9450	hst_9450_02_acs_wfc_f814w_j8d402	25/08/2002	<a href="https://doi.org/10.5270/esa-9ttmykz">https://doi.org/10.5270/esa-9ttmykz</a>	York et al. (2005)
9453	hst_9453_02_acs_wfc_f814w_j8f802	03/12/2002	<a href="https://doi.org/10.5270/esa-1xvyjfy">https://doi.org/10.5270/esa-1xvyjfy</a>	Brown et al. (2003)
9454	hst_9454_11_acs_wfc_f814w_j8ff11	23/03/2003	<a href="https://doi.org/10.5270/esa-xsdowj9">https://doi.org/10.5270/esa-xsdowj9</a>	

**Table A.1:** Twenty example of the accompanying data table of observations used.

## A.4 Acknowledging PIs

In the final section of this work, we wish to acknowledge all of the PIs whose observations we have used. A machine readable table containing the proposal IDs, the DOIs and the references (if provided/found) is presented with this work. Table A.1 shows the first twenty observations used in this work and is an example of this table.

# References

- Abadi M. G., Navarro J. F., Steinmetz M., Eke V. R., 2003, *ApJ*, 591, 499
- Abazajian K. N., et al., 2009, *ApJS*, 182, 543
- Abd El Aziz M., Selim I. M., Xiong S., 2017, *Scientific Reports*, 7, 4463
- Ackermann S., Schawinski K., Zhang C., Weigel A. K., Turp M. D., 2018, *MNRAS*, 479, 415
- Adams D., Mehta V., Dickinson H., Scarlata C., Fortson L., Kruk S., Simmons B., Lintott C., 2022, *ApJ*, 931, 16
- Aird J., Coil A. L., Georgakakis A., 2017, *MNRAS*, 465, 3390
- Aird J., Coil A. L., Georgakakis A., 2019, *MNRAS*, 484, 4360
- Alonso M. S., Tissera P. B., Coldwell G., Lambas D. G., 2004, *MNRAS*, 352, 1081
- Alonso M. S., Lambas D. G., Tissera P., Coldwell G., 2007, *MNRAS*, 375, 1017
- Ardizzone E., Di Gesù V., Maccarone M. C., 1996, *Vistas in Astronomy*, 40, 401
- Arnouts S., Cristiani S., Moscardini L., Matarrese S., Lucchin F., Fontana A., Giallongo E., 1999, *MNRAS*, 310, 540
- Arp H., 1966, *ApJS*, 14, 1
- Arp H. C., Madore B., 1987, *A catalogue of southern peculiar galaxies and associations*

- 
- Astropy Collaboration et al., 2013a, *A&A*, 558, A33
- Astropy Collaboration et al., 2013b, *A&A*, 558, A33
- Astropy Collaboration et al., 2018a, *AJ*, 156, 123
- Astropy Collaboration et al., 2018b, *AJ*, 156, 123
- Atkinson A. M., Abraham R. G., Ferguson A. M. N., 2013, *ApJ*, 765, 28
- Avila R. J., Hack W., Cara M., Borncamp D., Mack J., Smith L., Ubeda L., 2015, in Taylor A. R., Rosolowsky E., eds, *Astronomical Society of the Pacific Conference Series Vol. 495, Astronomical Data Analysis Software and Systems XXIV (ADASS XXIV)*. p. 281 ([arXiv:1411.5605](https://arxiv.org/abs/1411.5605)), doi:10.48550/arXiv.1411.5605
- Baldry I. K., Balogh M. L., Bower R. G., Glazebrook K., Nichol R. C., Bamford S. P., Budavari T., 2006, *MNRAS*, 373, 469
- Balogh M. L., Schade D., Morris S. L., Yee H. K. C., Carlberg R. G., Ellingson E., 1998, *ApJL*, 504, L75
- Balogh M. L., Baldry I. K., Nichol R., Miller C., Bower R., Glazebrook K., 2004, *ApJL*, 615, L101
- Banerji M., et al., 2010, *MNRAS*, 406, 342
- Barchi P. H., et al., 2020, *Astronomy and Computing*, 30, 100334
- Barnes J. E., 1992, *ApJ*, 393, 484
- Barnes J. E., Hibbard J. E., 2009, *AJ*, 137, 3071
- Baron D., et al., 2018, *MNRAS*, 480, 3993
- Barrera-Ballesteros J. K., et al., 2015, *A&A*, 579, A45
- Barton Gillespie E., Geller M. J., Kenyon S. J., 2003, *ApJ*, 582, 668
- Barton E. J., Geller M. J., Kenyon S. J., 2000, *ApJ*, 530, 660
- Baugh C. M., Cole S., Frenk C. S., 1996, *MNRAS*, 283, 1361



- 
- Beckmann V., Shrader C. R., 2012, *Active Galactic Nuclei*
- Bell E. F., et al., 2004, *ApJ*, 608, 752
- Bell E. F., et al., 2006, *ApJ*, 640, 241
- Bell E. F., Monachesi A., Harmsen B., de Jong R. S., Bailin J., Radburn-Smith D. J., D'Souza R., Holwerda B. W., 2017, *ApJL*, 837, L8
- Bergvall N., Laurikainen E., Aalto S., 2003, *A&A*, 405, 31
- Bertin E., Arnouts S., 1996, *A&AS*, 117, 393
- Bickley R. W., et al., 2021, *MNRAS*, 504, 372
- Bluck A. F. L., Conselice C. J., Bouwens R. J., Daddi E., Dickinson M., Papovich C., Yan H., 2009, *MNRAS*, 394, L51
- Blumenthal K. A., et al., 2020, *MNRAS*, 492, 2075
- Bolatto A. D., et al., 2013, *Nature*, 499, 450
- Boquien M., Burgarella D., Roehlly Y., Buat V., Ciesla L., Corre D., Inoue A. K., Salas H., 2019, *A&A*, 622, A103
- Bottrell C., et al., 2019, *MNRAS*, 490, 5390
- Bournaud F., Jog C. J., Combes F., 2005, *A&A*, 437, 69
- Bournaud F., Jog C. J., Combes F., 2007, *A&A*, 476, 1179
- Bower R. G., Lucey J. R., Ellis R. S., 1992, *MNRAS*, 254, 589
- Brammer G. B., van Dokkum P. G., Coppi P., 2008, *ApJ*, 686, 1503
- Brinchmann J., Charlot S., White S. D. M., Tremonti C., Kauffmann G., Heckman T., Brinkmann J., 2004, *MNRAS*, 351, 1151
- Brown T. M., Ferguson H. C., Smith E., Kimble R. A., Sweigart A. V., Renzini A., Rich R. M., VandenBerg D. A., 2003, *ApJL*, 592, L17

- 
- Brown M. J. I., Dey A., Jannuzi B. T., Brand K., Benson A. J., Brodwin M., Croton D. J., Eisenhardt P. R., 2007, *ApJ*, 654, 858
- Bruzual G., Charlot S., 2003, *MNRAS*, 344, 1000
- Buck T., Wolf S., 2021, arXiv e-prints, p. arXiv:2111.01154
- Bundy K., Ellis R. S., Conselice C. J., 2005, *ApJ*, 625, 621
- Bundy K., et al., 2015, *ApJ*, 798, 7
- Burstein D., Ho L. C., Huchra J. P., Macri L. M., 2005, *ApJ*, 621, 246
- Bushouse H. A., 1987, *ApJ*, 320, 49
- Byrne-Mamahit S., Hani M. H., Ellison S. L., Quai S., Patton D. R., 2023, *MNRAS*, 519, 4966
- Calvi V., Stiavelli M., Bradley L., Pizzella A., Kim S., 2014, *ApJ*, 796, 102
- Cameron E., 2011, *PASA*, 28, 128
- Chabrier G., 2003, *PASP*, 115, 763
- Chang Y.-Y., Lin L., Pan H.-A., Lin C.-A., Hsieh B.-C., Bottrell C., Wang P.-W., 2022, *ApJ*, 937, 97
- Cheng C., et al., 2020, *MNRAS*, 499, 5241
- Cheng T.-Y., Huertas-Company M., Conselice C. J., Aragón-Salamanca A., Robertson B. E., Ramachandra N., 2021, *MNRAS*, 503, 4446
- Cheung E., et al., 2016, *Nature*, 533, 504
- Christlein D., Zabludoff A. I., 2004, *ApJ*, 616, 192
- Cicone C., et al., 2014, *A&A*, 562, A21
- Ćiprijanović A., Snyder G. F., Nord B., Peek J. E. G., 2020, *Astronomy and Computing*, 32, 100390

- 
- Colless M., et al., 2001, MNRAS, 328, 1039
- Comerford J. M., Pooley D., Barrows R. S., Greene J. E., Zakamska N. L., Madejski G. M., Cooper M. C., 2015, ApJ, 806, 219
- Conselice C. J., Arnold J., 2009, MNRAS, 397, 208
- Conselice C. J., et al., 2007, MNRAS, 381, 962
- Conselice C. J., Yang C., Bluck A. F. L., 2009, MNRAS, 394, 1956
- Costa P., Phillips E., Brandt L., Fatica M., 2021, Computers & Mathematics with Applications, 81, 502
- Cowan N. B., Ivezić Ž., 2008, ApJL, 674, L13
- Cox T. J., Jonsson P., Somerville R. S., Primack J. R., Dekel A., 2008, MNRAS, 384, 386
- Curtis H. D., 1917, PASP, 29, 206
- Dalcanton J. J., et al., 2012, ApJS, 200, 18
- Dalton G., et al., 2014, in Ramsay S. K., McLean I. S., Takami H., eds, Society of Photo-Optical Instrumentation Engineers (SPIE) Conference Series Vol. 9147, Ground-based and Airborne Instrumentation for Astronomy V. p. 91470L (arXiv:1412.0843), doi:10.1117/12.2055132
- Darg D. W., et al., 2010a, MNRAS, 401, 1043
- Darg D. W., et al., 2010b, MNRAS, 401, 1552
- Darvish B., Mobasher B., Sobral D., Scoville N., Aragon-Calvo M., 2015, ApJ, 805, 121
- Darvish B., Mobasher B., Martin D. C., Sobral D., Scoville N., Stroe A., Hemmati S., Kartaltepe J., 2017, ApJ, 837, 16
- Das A., Pandey B., Sarkar S., 2023a, Research in Astronomy and Astrophysics, 23, 095026

- 
- Das A., Pandey B., Sarkar S., 2023b, *Research in Astronomy and Astrophysics*, 23, 115018
- De Lucia G., Blaizot J., 2007, *MNRAS*, 375, 2
- De Lucia G., Springel V., White S. D. M., Croton D., Kauffmann G., 2006, *MNRAS*, 366, 499
- Delvecchio I., et al., 2017, *A&A*, 602, A3
- Dey A., et al., 2019, *AJ*, 157, 168
- Di Matteo P., Combes F., Melchior A. L., Semelin B., 2007, *A&A*, 468, 61
- Eisenstein D. J., et al., 2003, *ApJ*, 585, 694
- Ellison S. L., Patton D. R., Simard L., McConnachie A. W., 2008, *AJ*, 135, 1877
- Ellison S. L., Patton D. R., Mendel J. T., Scudder J. M., 2011, *MNRAS*, 418, 2043
- Ellison S. L., Mendel J. T., Patton D. R., Scudder J. M., 2013, *MNRAS*, 435, 3627
- Ellison S. L., Secrest N. J., Mendel J. T., Satyapal S., Simard L., 2017, *MNRAS*, 470, L49
- Ellison S. L., et al., 2022, *MNRAS*, 517, L92
- Elmegreen B. G., Elmegreen D. M., 2005, *ApJ*, 627, 632
- Emsellem E., et al., 2011, *MNRAS*, 414, 888
- Faber S. M., Gallagher J. S., 1976, *ApJ*, 204, 365
- Fensch J., Bournaud F., 2021, *MNRAS*, 505, 3579
- Ferreira L., et al., 2022, *ApJL*, 938, L2
- Foreman-Mackey D., 2016, *The Journal of Open Source Software*, 1, 24

- 
- Foreman-Mackey D., Hogg D. W., Lang D., Goodman J., 2013, *PASP*, 125, 306
- Gabor J. M., Davé R., Finlator K., Oppenheimer B. D., 2010, *MNRAS*, 407, 749
- Gadotti D. A., Kauffmann G., 2009, *MNRAS*, 399, 621
- Gao F., et al., 2020, *A&A*, 637, A94
- Garay-Solis Y., Barrera-Ballesteros J. K., Colombo D., Sánchez S. F., Lugo-Aranda A. Z., Villanueva V., Wong T., Bolatto A. D., 2023, *ApJ*, 952, 122
- Geach J. E., et al., 2018, *ApJL*, 864, L1
- Gebhardt K., et al., 2001, *AJ*, 122, 2469
- Gehrels N., 1986, *ApJ*, 303, 336
- Ghosh A., Urry C. M., Wang Z., Schawinski K., Turp D., Powell M. C., 2020, *ApJ*, 895, 112
- Giavalisco M., et al., 2004, *ApJL*, 600, L93
- Goldreich P., Lynden-Bell D., 1965, *MNRAS*, 130, 97
- Gordon Y. A., et al., 2017, *MNRAS*, 465, 2671
- Goudfrooij P., Gilmore D., Whitmore B. C., Schweizer F., 2004, *ApJL*, 613, L121
- Goulding A. D., et al., 2018, *PASJ*, 70, S37
- Gregg M., West M., 2017, in *Early stages of Galaxy Cluster Formation*. p. 13, doi:10.5281/zenodo.831767
- Guo Q., White S. D. M., 2008, *MNRAS*, 384, 2
- Guo Y., et al., 2015, *ApJ*, 800, 39
- Guo Y., et al., 2018, *ApJ*, 853, 108
- Hani M. H., Gosain H., Ellison S. L., Patton D. R., Torrey P., 2020, *MNRAS*, 493, 3716

- He H., Wilson C. D., Sliwa K., Iono D., Saito T., 2020, *MNRAS*, 496, 5243
- He C., Xu C. K., Domingue D., Cao C., Huang J.-s., 2022, *ApJS*, 261, 34
- Helou G., Madore B. F., Schmitz M., Bica M. D., Wu X., Bennett J., 1991, in Albrecht M. A., Egret D., eds, *Astrophysics and Space Science Library Vol. 171, Databases and On-line Data in Astronomy*. pp 89–106, doi:10.1007/978-94-011-3250-3\_10
- Hernández-Toledo H. M., Avila-Reese V., Conselice C. J., Puerari I., 2005, *AJ*, 129, 682
- Hinton S. R., 2016, *The Journal of Open Source Software*, 1, 00045
- Hogg D. W., et al., 2002, *AJ*, 124, 646
- Holincheck A. J., et al., 2016, *MNRAS*, 459, 720
- Hopkins P. F., Hernquist L., Cox T. J., Kereš D., 2008, *ApJS*, 175, 356
- Hopkins P. F., Cox T. J., Younger J. D., Hernquist L., 2009, *ApJ*, 691, 1168
- Hopkins P. F., et al., 2010, *ApJ*, 715, 202
- Hopkins P. F., Cox T. J., Hernquist L., Narayanan D., Hayward C. C., Murray N., 2013, *MNRAS*, 430, 1901
- Hopkins P. F., et al., 2018, *MNRAS*, 480, 800
- Hubble E. P., 1926, *ApJ*, 64, 321
- Hubble E. P., 1936, *Realm of the Nebulae*
- Huertas-Company M., et al., 2015, *ApJS*, 221, 8
- Ilbert O., et al., 2006, *A&A*, 457, 841
- Ivezić Ž., et al., 2019, *ApJ*, 873, 111
- Jackson R. A., Kaviraj S., Martin G., Devriendt J. E. G., Noakes-Kettel E. A., Silk J., Ogle P., Dubois Y., 2022, *MNRAS*, 511, 607

- Jacobs C., et al., 2019, *ApJS*, 243, 17
- Jeffrey N., Alsing J., Lanusse F., 2021, *MNRAS*, 501, 954
- Jeon S., et al., 2022, *ApJ*, 941, 5
- Johansson P. H., Naab T., Burkert A., 2009, *ApJ*, 690, 802
- Kant I., 1755, *Allgemeine Naturgeschichte und Theorie des Himmels*
- Karera P., Drissen L., Martel H., Iglesias-Páramo J., Vilchez J. M., Duc P.-A., Plana H., 2022, *MNRAS*, 514, 2769
- Karman W., Macciò A. V., Kannan R., Moster B. P., Somerville R. S., 2015, *MNRAS*, 452, 2984
- Kauffmann G., et al., 2003, *MNRAS*, 341, 33
- Kaviraj S., 2014a, *MNRAS*, 437, L41
- Kaviraj S., 2014b, *MNRAS*, 440, 2944
- Kaviraj S., Devriendt J., Dubois Y., Slyz A., Welker C., Pichon C., Peirani S., Le Borgne D., 2015, *MNRAS*, 452, 2845
- Keel W. C., White Raymond E. I., Owen F. N., Ledlow M. J., 2006, *AJ*, 132, 2233
- Keel W. C., et al., 2022, *AJ*, 163, 150
- Kennicutt Robert C. J., 1998, *ApJ*, 498, 541
- Khalid A., Brough S., Martin G., Kimmig L. C., Lagos C. D. P., Remus R. S., Martinez-Lombilla C., 2024, *MNRAS*, 530, 4422
- Kingma D. P., Ba J., 2014, arXiv e-prints, p. arXiv:1412.6980
- Kolmogorov A., 1933, *Giorn Dell'inst Ital Degli Att*, 4, 89
- Koss M., Mushotzky R., Treister E., Veilleux S., Vasudevan R., Trippe M., 2012, *ApJL*, 746, L22

- Lacey C., Cole S., 1993, MNRAS, 262, 627
- Lambas D. G., Tissera P. B., Alonso M. S., Coldwell G., 2003, MNRAS, 346, 1189
- Lambas D. G., Alonso S., Mesa V., O’Mill A. L., 2012, A&A, 539, A45
- Li C., Kauffmann G., Heckman T. M., Jing Y. P., White S. D. M., 2008a, MNRAS, 385, 1903
- Li C., Kauffmann G., Heckman T. M., White S. D. M., Jing Y. P., 2008b, MNRAS, 385, 1915
- Lintott C. J., et al., 2008, MNRAS, 389, 1179
- López-Sanjuan C., Balcells M., Pérez-González P. G., Barro G., García-Dabó C. E., Gallego J., Zamorano J., 2009, A&A, 501, 505
- Lotz J. M., Primack J., Madau P., 2004, AJ, 128, 163
- Lotz J. M., Jonsson P., Cox T. J., Primack J. R., 2008a, MNRAS, 391, 1137
- Lotz J. M., et al., 2008b, ApJ, 672, 177
- Lotz J. M., Jonsson P., Cox T. J., Croton D., Primack J. R., Somerville R. S., Stewart K., 2011, ApJ, 742, 103
- Lupton R., Blanton M. R., Fekete G., Hogg D. W., O’Mullane W., Szalay A., Wherry N., 2004, PASP, 116, 133
- Lynds R., Toomre A., 1976, ApJ, 209, 382
- Malin D. F., Carter D., 1983, ApJ, 274, 534
- Mantas J. M., De la Asunción M., Castro M. J., 2016, An Introduction to GPU Computing for Numerical Simulation. Springer International Publishing, Cham, pp 219–251, doi:10.1007/978-3-319-32146-2\_5, [https://doi.org/10.1007/978-3-319-32146-2\\_5](https://doi.org/10.1007/978-3-319-32146-2_5)
- Marchesi S., et al., 2016, ApJ, 817, 34



- 
- Marian V., et al., 2020, *ApJ*, 904, 79
- Martig M., Bournaud F., 2008, *MNRAS*, 385, L38
- Martig M., Bournaud F., Croton D. J., Dekel A., Teyssier R., 2012, *ApJ*, 756, 26
- Martin G., et al., 2022, *MNRAS*, 513, 1459
- Masters K. L., et al., 2010, *MNRAS*, 405, 783
- Mathieu A., Merrifield M. R., Kuijken K., 2002, *MNRAS*, 330, 251
- McInnes L., Healy J., Melville J., 2018, arXiv e-prints, p. arXiv:1802.03426
- McKernan B., Ford K. E. S., Reynolds C. S., 2010, *MNRAS*, 407, 2399
- Merín B., et al., 2017, arXiv e-prints, p. arXiv:1712.04114
- Mihos J. C., Hernquist L., 1994, *ApJL*, 425, L13
- Mihos J. C., Hernquist L., 1996, *ApJ*, 464, 641
- Mihos J. C., Richstone D. O., Bothun G. D., 1992, *ApJ*, 400, 153
- Miller T. B., van Dokkum P., 2021, *ApJ*, 923, 124
- Moreno J., Torrey P., Ellison S. L., Patton D. R., Bluck A. F. L., Bansal G., Hernquist L., 2015, *MNRAS*, 448, 1107
- Moreno J., et al., 2019, *MNRAS*, 485, 1320
- Moreno J., et al., 2021, *MNRAS*, 503, 3113
- Morganti R., Garrett M. A., Chapman S., Baan W., Helou G., Soifer T., 2004, *A&A*, 424, 371
- Murata K. L., et al., 2014, *ApJ*, 786, 15
- Nair P. B., Abraham R. G., 2010, *ApJS*, 186, 427
- Nelson B., Ford E. B., Payne M. J., 2014, *ApJS*, 210, 11

- Netzer H., 2015, *ARA&A*, 53, 365
- Nevin R., Blecha L., Comerford J., Simon J., Terrazas B. A., Barrows R. S., Vázquez-Mata J. A., 2023, *MNRAS*, 522, 1
- Nielsen F., 2016, Hierarchical Clustering. pp 195–211, doi:10.1007/978-3-319-21903-5\_8
- O’Shea K., Nash R., 2015, arXiv e-prints, p. arXiv:1511.08458
- Ochsenbein F., Bauer P., Marcout J., 2000, *A&AS*, 143, 23
- Pacifici C., Kassin S. A., Weiner B., Charlot S., Gardner J. P., 2013, *ApJL*, 762, L15
- Patton D. R., Ellison S. L., Simard L., McConnachie A. W., Mendel J. T., 2011, *MNRAS*, 412, 591
- Patton D. R., Torrey P., Ellison S. L., Mendel J. T., Scudder J. M., 2013, *MNRAS*, 433, L59
- Pawlik M. M., et al., 2018, *MNRAS*, 477, 1708
- Pearson W. J., Wang L., Trayford J. W., Petrillo C. E., van der Tak F. F. S., 2019a, *A&A*, 626, A49
- Pearson W. J., et al., 2019b, *A&A*, 631, A51
- Pearson W. J., et al., 2022, *A&A*, 661, A52
- Peng C. Y., Ho L. C., Impey C. D., Rix H.-W., 2002, ] 10.1086/340952
- Peng C. Y., Ho L. C., Impey C. D., Rix H.-W., 2010a, *AJ*, 139, 2097
- Peng Y.-j., et al., 2010b, *ApJ*, 721, 193
- Petsch H. P., Theis C., 2008, *Astronomische Nachrichten*, 329, 1046
- Quai S., Hani M. H., Ellison S. L., Patton D. R., Woo J., 2021, *MNRAS*, 504, 1888

- Quinn P. J., 1984, *ApJ*, 279, 596
- Quirk W. J., 1972, *ApJL*, 176, L9
- Rejkuba M., Greggio L., Harris W. E., Harris G. L. H., Peng E. W., 2005, *ApJ*, 631, 262
- Ren J., Li N., Liu F. S., Cui Q., Fu M., Zheng X. Z., 2023, *ApJ*, 958, 96
- Rizzo F., Fraternali F., Iorio G., 2018, *MNRAS*, 476, 2137
- Rodríguez Montero F., Davé R., Wild V., Anglés-Alcázar D., Narayanan D., 2019, *MNRAS*, 490, 2139
- Rogers B., Ferreras I., Kaviraj S., Pasquali A., Sarzi M., 2009, *MNRAS*, 399, 2172
- Ross D., Lim J., Lin R., et al. 2008, *Int J Comput Vis*, p. 125–141
- Saitoh T. R., Daisaka H., Kokubo E., Makino J., Okamoto T., Tomisaka K., Wada K., Yoshida N., 2009, *PASJ*, 61, 481
- Salim S., et al., 2007, *ApJS*, 173, 267
- Salo H., Laurikainen E., 1993, *ApJ*, 410, 586
- Sánchez S. F., et al., 2004, *ApJ*, 614, 586
- Satyapal S., Ellison S. L., McAlpine W., Hickox R. C., Patton D. R., Mendel J. T., 2014, *MNRAS*, 441, 1297
- Schawinski K., et al., 2009, *MNRAS*, 396, 818
- Schawinski K., et al., 2014, *MNRAS*, 440, 889
- Schawinski K., Koss M., Berney S., Sartori L. F., 2015, *MNRAS*, 451, 2517
- Schaye J., et al., 2015, *MNRAS*, 446, 521
- Schiminovich D., et al., 2007, *ApJS*, 173, 315

- 
- Schmidt M., 1959, *ApJ*, 129, 243
- Schweizer F., Seitzer P., 1992, *AJ*, 104, 1039
- Scoville N., et al., 2007, *ApJS*, 172, 1
- Scoville N., et al., 2023, *ApJ*, 943, 82
- Scudder J. M., Ellison S. L., Torrey P., Patton D. R., Mendel J. T., 2012, *MNRAS*, 426, 549
- Shah E. A., et al., 2020, *ApJ*, 904, 107
- Shah E. A., et al., 2022, *ApJ*, 940, 4
- Silva A., Marchesini D., Silverman J. D., Martis N., Iono D., Espada D., Skelton R., 2021, *ApJ*, 909, 124
- Simha V., Weinberg D. H., Conroy C., Dave R., Fardal M., Katz N., Oppenheimer B. D., 2014, *arXiv e-prints*, p. arXiv:1404.0402
- Simmons B. D., et al., 2017, *MNRAS*, 464, 4420
- Smethurst R. J., et al., 2015, *MNRAS*, 450, 435
- Smethurst R. J., et al., 2018, *MNRAS*, 473, 2679
- Smethurst R. J., et al., 2022, *MNRAS*, 510, 4126
- Smith B. J., et al., 2010, in Smith B., Higdon J., Higdon S., Bastian N., eds, *Astronomical Society of the Pacific Conference Series Vol. 423, Galaxy Wars: Stellar Populations and Star Formation in Interacting Galaxies*. p. 227 ([arXiv:0908.3478](https://arxiv.org/abs/0908.3478)), doi:10.48550/arXiv.0908.3478
- Smolčić V., et al., 2017, *A&A*, 602, A6
- Sola E., et al., 2022, *A&A*, 662, A124
- Sparre M., Whittingham J., Damle M., Hani M. H., Richter P., Ellison S. L., Pfrommer C., Vogelsberger M., 2022, *MNRAS*, 509, 2720

- 
- Springel V., 2000, *MNRAS*, 312, 859
- Springel V., et al., 2005, *Nature*, 435, 629
- Steffen J. L., et al., 2023, *ApJ*, 942, 107
- Stemo A., Comerford J. M., Barrows R. S., Stern D., Assef R. J., Griffith R. L., Schechter A., 2021, *ApJ*, 923, 36
- Stephens M. A., 1974, *Journal of the American Statistical Association*, 69, 730
- Strateva I., et al., 2001, *AJ*, 122, 1861
- Suelves L. E., Pearson W. J., Pollo A., 2023, *A&A*, 669, A141
- Swinbank A. M., Smail I., Sobral D., Theuns T., Best P. N., Geach J. E., 2012, *ApJ*, 760, 130
- Tacconi L. J., et al., 2010, *Nature*, 463, 781
- Tarsitano F., Bruderer C., Schawinski K., Hartley W. G., 2022, *MNRAS*, 511, 3330
- Tian C., et al., 2023, *ApJ*, 944, 124
- Tolman R. C., 1930, *Proceedings of the National Academy of Science*, 16, 511
- Tolman R. C., 1934, *Relativity, Thermodynamics, and Cosmology*
- Toomre A., 1977, in Tinsley B. M., Larson Richard B. Gehret D. C., eds, *Evolution of Galaxies and Stellar Populations*. p. 401
- Toomre A., Toomre J., 1972, *ApJ*, 178, 623
- Vavilova I., Elyiv A., Dobrycheva D., Melnyk O., 2021, in Zelinka I., Brescia M., Baron D., eds, , Vol. 39, *Intelligent Astrophysics*. pp 57–79, doi:10.1007/978-3-030-65867-0\_3
- Vayner A., et al., 2023, *ApJ*, 955, 92

- 
- Violino G., Ellison S. L., Sargent M., Coppin K. E. K., Scudder J. M., Mendel T. J., Saintonge A., 2018, *MNRAS*, 476, 2591
- Vorontsov-Velyaminov B. A., 1959, *Atlas and Catalog of Interacting Galaxies*, p. 0
- Vorontsov-Velyaminov B. A., 1977, *A&AS*, 28, 1
- Wallin J. F., 1990, *The Astronomical Journal*, 100, 1477
- Wallin J. F., Holincheck A. J., Harvey A., 2016, *Astronomy and Computing*, 16, 26
- Walmsley M., et al., 2020, *MNRAS*, 491, 1554
- Walmsley M., et al., 2022a, *MNRAS*, 509, 3966
- Walmsley M., et al., 2022b, *MNRAS*, 513, 1581
- Walmsley M., et al., 2023, *The Journal of Open Source Software*, 8, 5312
- Weaver J. R., et al., 2022, *ApJS*, 258, 11
- Weigel A. K., et al., 2017, *ApJ*, 845, 145
- Wenger M., et al., 2000, *A&AS*, 143, 9
- West G., Ogden M., Wallin J. F., 2023, *Astronomy and Computing*, 42, 100691
- Whitaker K. E., Kriek M., van Dokkum P. G., Bezanson R., Brammer G., Franx M., Labbé I., 2012, *ApJ*, 745, 179
- White S. D. M., Frenk C. S., 1991, *ApJ*, 379, 52
- White S. D. M., Rees M. J., 1978, *MNRAS*, 183, 341
- Whitmore B. C., et al., 2016, *AJ*, 151, 134
- Wild V., et al., 2014, *A&A*, 567, A132
- Willett K. W., et al., 2013, *MNRAS*, 435, 2835

- Willett K. W., et al., 2017, MNRAS, 464, 4176
- Woods D. F., Geller M. J., Barton E. J., 2006, AJ, 132, 197
- York D. G., et al., 2000, AJ, 120, 1579
- York T., Jackson N., Browne I. W. A., Wucknitz O., Skelton J. E., 2005, MNRAS, 357, 124
- de Albarnaz Ferreira L., Ferrari F., 2018, MNRAS, 473, 2701
- de Mello D. F., Infante L., Menanteau F., 1997, ApJS, 108, 99
- de Vaucouleurs G., de Vaucouleurs A., Corwin Herold G. J., Buta R. J., Paturel G., Fouque P., 1991, Third Reference Catalogue of Bright Galaxies
- ter Braak C. J. F., Vrugt J. A., 2008, Statistics and Computing, 18
- van Dokkum P. G., 2005, AJ, 130, 2647
- van Dokkum P., et al., 2018, Nature, 555, 629
- van Dokkum P., et al., 2019, ApJL, 883, L32